STUDY OF TRANSFORMATION CHARACTERISTICS AND MICROSTRUCTURAL EVOLUTION IN 9Cr REDUCED ACTIVATION FERRITIC / MARTENSITIC STEEL USING ELECTRON MICROSCOPY, CALORIMETRY AND COMPUTATIONAL METHODS

By
RAVIKIRANA
ENGG02200904026

Indira Gandhi Centre for Atomic Research

A thesis submitted to the

Board of Studies in Engineering Sciences

In partial fulfillment of requirements
for the Degree of

DOCTOR OF PHILOSOPHY

of

HOMI BHABHA NATIONAL INSTITUTE

August, 2014

Homi Bhabha National Institute

Recommendations of the Viva Voce Committee

As members of the Viva Voce Committee, we certify that we have read the dissertation prepared by 'Ravikirana' entitled "STUDY OF TRANSFORMATION CHARACTERISTICS AND MICROSTRUCTURAL EVOLUTION IN 9Cr REDUCED ACTIVATION FERRITIC / MARTENSITIC STEEL USING ELECTRON MICROSCOPY, CALORIMETRY AND COMPUTATIONAL METHODS" and recommend that it may be accepted as fulfilling the thesis requirement for the award of Degree of Doctor of Philosophy.

Chairman	Prof. T. Jayakumar	**Date:** 16 feb. 2015
Guide / Convener	Prof. Saroja Saibaba	**Date:** 16/02/2015
Member 1	Prof. K. Laha	**Date:** 16. 2. 2015.
Member 2	Prof. G. Amarendra	**Date:** Feb 16, 2015
Technology Advisor	Dr. S. Raju	**Date:** 16/02/2015
Examiner	Prof. Indradev Samajdar	**Date:** 17/02/2015

Final approval and acceptance of this thesis is contingent upon the candidate's submission of the final copies of the thesis to HBNI.

I/We hereby certify that I/we have read this thesis prepared under my/our direction and recommend that it may be accepted as fulfilling the thesis requirement.

Date: 18/02/2015

Place: Kalpakkam

Guide

(SAROJA SAIBABA)

STATEMENT BY AUTHOR

This dissertation has been submitted in partial fulfillment of requirements for an advanced degree at Homi Bhabha National Institute (HBNI) and is deposited in the Library to be made available to borrowers under rules of the HBNI.

Brief quotations from this dissertation are allowable without special permission, provided that accurate acknowledgement of source is made. Requests for permission for extended quotation from or reproduction of this manuscript in whole or in part may be granted by the Competent Authority of HBNI when in his or her judgment the proposed use of the material is in the interests of scholarship. In all other instances, however, permission must be obtained from the author.

Ravikirana

DECLARATION

I, hereby declare that the investigation presented in the thesis has been carried out by me. The work is original and has not been submitted earlier as a whole or in part for a degree / diploma at this or any other Institution / University.

Ravikirana

List of Publications arising from the thesis

I. Journal

1. Microstructural modifications due to W and Ta in 9Cr Reduced Activation Ferritic Martensitic steels on creep exposure. R. Mythili, **Ravikirana**, J. Vanaja, K. Laha, S. Saroja, T. Jayakumar, M.D. Mathew, E. Rajendrakumar, *Proc. Eng*., 55 (3–4) (2013) 295–299.
2. Influence of W and Ta content on microstructural characteristics in heat treated 9Cr-Reduced Activation Ferritic / Martensitic steels, **Ravikirana**, R. Mythili, S. Raju, S. Saroja, T. Jayakumar, E. Rajendrakumar, *Mater. Charact*., 84 (2013) 196 – 204.
3. Effect of alloy content on microstructure and microchemistry of phases during short term thermal exposure of 9Cr-W-Ta-0.1C Reduced Activation Ferritic/Martensitic (RAFM) steels, **Ravikirana**, R. Mythili, S. Raju, S. Saroja, G. Paneerselvam, T. Jayakumar, E. Rajendra Kumar, *Bulletin Mater. Sci*., 37 (6) (2014) 1453–1460.
4. Decomposition Modes of Austenite in 9Cr-W-V-Ta Reduced Activation Ferritic Martensitic Steels, **Ravikirana**, R. Mythili, S. Raju, S. Saroja, T. Jayakumar and E. Rajendra Kumar, *Mater. Sci. Tech.,* 31 (4) (2014) 448-459

5. High Temperature Phase Stability of 9Cr-W-Ta-V-C Based Reduced Activation Ferritic-Martensitic (RAFM) steels: Effect of W and Ta additions, **Ravikirana**, S. Raju, R. Mythili, S. Saroja, T. Jayakumar and E. Rajendra Kumar, *Steel Res. Int.,(2014)* doi:10.1002/srin.201400183.

II. Manuscript under preparation

1. Evolution of secondary phases in 9Cr RAFM steels with varying W, Ta content - Experimental and computational studies
2. Identification of retained austenite in normalised 9Cr RAFM steels

III. Conference Proceedings

1. Effect of heating rate on transformation temperature of 9Cr-W TaV RAFM steels, Ravikirana, S. Raju, R. Mythili, S. Saroja, T. Jayakumar and E. Rajendra Kumar, Proc. 19th Symp. on thermal analysis (Thermans -2013), Mumbai, India, 2013, pp.414 – 419.
2. Effect of alloy content on microstructure and microchemistry of phases during short term thermal exposure in 9Cr-W-Ta-C RAFM Steels, Ravikirana, R. Mythili, S. Saroja, T. Jayakumar, E. Rajendrakumar, Proc. ISRS-2012, Chennai, December 13-15, 2012, 1.
3. Microstructural modifications due to W and Ta in 9Cr Reduced Activation Ferritic / Martensitic steels on creep exposure, R. Mythili, Ravikirana, J. Vanaja, K. Laha, S. Saroja, T. Jayakumar, M.D. Mathew, E. Rajendrakumar, Proc. 6th Int. Conf. on Creep, Fatigue and Creep-Fatigue Interaction (CF-6), Mamallapuram, India, January 22-25, 2012, pp.685-689.

IV. Conferences

1. Study of precipitation kinetics in W added 9Cr- RAFM steel, R. Mythili, Ravikirana, S. Saroja, 48th NMD-64th ATM, Nov.14-17, 2010, Bengaluru.
2. Study of microstructural evolution in 9Cr Reduced Activation Ferritic / Martensitic steels under the influence of temperature and stress, Ravikirana, R. Mythili, J. Vanaja, K. Laha, S. Saroja, 49th NMD- 65th ATM, Nov. 13-16, 2011, Hyderabad.
3. Role of W and Ta on transformation characteristics and microstructure development in 9Cr-W-Ta-C RAFM Steels, R. Mythili, Ravikirana, S. Raju, S. Saroja, T. Jayakumar, M.D. Mathew, E. Rajendrakumar, IAEA Topical Meeting, December 11-13, 2012, Gandhinagar.
4. Study of γ→α′ transformation in 9Cr-ferritic martensitic steel by Automated Crystal Orientation Imaging Microscopy, R. Mythili, Ravikirana, L. Herojit Singh, R. Govindaraj, S. Saroja and M. Vijayalakshmi, 52nd NMD- 68th ATM, Nov. 12-15, 2014, Pune, India.

Ravikirana

Ravikirana

This thesis is dedicated to

my Parents and Brother

ACKNOWLEDGEMENTS

I express my deep sense of gratitude to my Ph.D supervisor Prof. Saroja Saibaba, Head, MTPD for her guidance, support and motivation throughout the course of my research work. My heartfelt thanks are due to Dr. R. Mythili, MTPD for dedicating her time and efforts for my research work. This thesis would not have materialised but for the kind support from Prof. Saroja Saibaba and Dr. R. Mythili who supported me in all respects. I wish to express my gratitude to Shri S. Raju, Head, CMMS, MTPD, for his keen interest and support during the course of my thesis work.

I am grateful to the Chairman of my Doctoral Committee Prof. T. Jayakumar, Director, MMG, members Prof. G. Amarendra, Head, MPD, MSG, Prof. K. Laha, Head, MMD and Shri S. Raju, Technology Advisor for their valuable suggestions and encouragement.

I am extremely thankful to Dr. P. R. Vasudeva Rao, Director, IGCAR and former Directors, Dr. Baldev Raj and Shri S. C. Chetal, for enabling me to carry out my doctoral work at IGCAR. I wish to express my sincere thanks to Dr. T. Jayakumar, Director, MMG and Dr. M. Vijayalakshmi, AD, PMG for their support. I sincerely acknowledge the Department of Atomic Energy for the fellowship.

I thank Dr. G. Paneerselvam, CG, IGCAR, for XRD measurements, Dr. R. Govindaraj, MSG, IGCAR for Mossbauer Spectroscopy measurements, Dr. A. K. Sinha and M. N. Singh, for ADXRD at RRCAT, Indore and Dr. C. Sudha, MTPD, for her support for the JMatPro calculations. I express my gratitude to all members of PMG and fellow researchers for their timely support and assistance during various stages of the work.

I thank Dr. M. Saibaba, AD, RMG and members of BARC Training School at IGCAR for conducting the coursework and my comfortable stay at Research Scholars enclave.

I express the deepest gratitude to my parents and brother, whose love and support sustained me throughout my academic career, and whose encouragement and support brought me this far.

CONTENTS

TITLE **Page**

CHAPTER 1 **INTRODUCTION**

CHAPTER 2 **EXPERIMENTAL METHODS**

TITLE Page

CHAPTER 3 PHASE TRANSFORMATIONS IN 9CR RAFM STEELS

TITLE **Page**

CHAPTER 5 MICROSTRUCTURAL EVOLUTION IN 9CR RAFM STEELS ON LONG TERM EXPOSURE - EFFECT OF COMPOSITION, TEMPERATURE AND STRESS

CHAPTER 6 SUMMARY AND SCOPE FOR FUTURE WORK

Synopsis

1. Introduction

Reduced Activation Ferritic / Martensitic (RAFM) steels, are potential structural material for test blanket module (TBM) and first wall of the International Thermonuclear Experimental Reactor (ITER) due to their excellent resistance to radiation-induced swelling, He embrittlement and acceptable high temperature mechanical properties [1,2]. Though the general metallurgical characteristics of the steel is similar to P91 steel, the replacement of Mo by W and Nb by Ta exerts significant influence on the phase transformation characteristics of the steel [1]. An extensive data base exists for the 9Cr class of steels w.r.t the metallurgical characteristics of the steel [3]. However, there is limited literature on the physical metallurgy aspects like phase transformation and microstructural evolution of W and Ta added RAFM steels during thermal exposures and existing reports mainly deal with property evaluation [4, 5]. Further, for the Indian TBM, RAFM steels have been developed indigenously based on an extensive Research and Development effort involving optimisation of composition and processing window, developmental and industrial scale production of the steels, characterisation and structure – property correlations. Therefore, efforts have been made to evaluate the phase transformation characteristics and microstructural evolution of RAFM steels with varying W and Ta content and different thermal treatments.

The main aim of the present thesis is to obtain an in-depth understanding on thermodynamic and physical metallurgy aspects of indigenously developed 9Cr RAFM steels with different W and Ta content, which involves the study of $\alpha \leftrightarrow \gamma$ transformation characteristics using differential scanning calorimety (DSC), microstructural investigation through Analytical Transmission Electron Microscopy. Also, Orientation Imaging Microscopy (OIM) in TEM, a newly emerging technique has been used to study the martensite characteristics. The thesis highlights the role of alloy content and process parameters on the mechanism and kinetics of phase transformation by a systematic experimental investigation and simulation using JMatPro and Thermocalc software.

2. Scope of the Thesis

This thesis titled "STUDY OF TRANSFORMATION CHARACTERISTICS AND MICROSTRUCTURAL EVOLUTION IN 9Cr REDUCED ACTIVATION FERRITIC / MARTENSITIC STEEL USING ELECTRON MICROSCOPY, CALORIMETRY AND COMPUTATIONAL METHODS" presents the results of an extensive physical metallurgy study on 9Cr RAFM steels with W and Ta varying from 1–2 wt. % and 0.06 – 0.14 wt. % respectively. This study on microstructural aspects of four compositions of the RAFM steels forms a part of a large Research and Development program on indigenous development of RAFM steel as a structural material for ITER. The thesis addresses three major themes given below–

- Phase transformation in RAFM steels
- Decomposition modes of high temperature austenite and characteristics of martensite
- Microstructural evolution - Effect of alloy content, temperature and stress

A brief description of the above themes is discussed below.

2.1. *Phase transformation in RAFM steels*

2.1.1 Phase transformation characteristics using Differential Scanning Calorimetry

Based on DSC results, the following transformation sequence has been established on heating the normalised and tempered RAFM steels.

α-Ferrite (ferromagnetic) + $M_{23}C_6$ + MX → α-ferrite (paramagnetic) + $M_{23}C_6$ + MX → γ-austenite + $M_{23}C_6$ + MX $\rightarrow \gamma$ + MX $\rightarrow \gamma \rightarrow \delta + \gamma \rightarrow \gamma + \delta + L \rightarrow \delta + L \rightarrow$ Liquid.

The Ac_1, Ac_3, M_s and M_f temperatures have been evaluated for the four steels.

- An increase in Ac_1, Ac_3 was observed with heating rate in 1.4W–0.06Ta steel.
- The critical cooling rate for γ→α′ transformation was found to be close to 40 K min^{-1} for the 1.4W– 0.06Ta steel. The decrease in M_f with increase in cooling rate was more significant than M_s, suggesting that, though martensite nucleation takes place at same temperature, completion of martensite transformation requires higher undercooling.
- With increase in W content of the steel, Ac_1 and Ac_3 showed a small increase, while M_s and M_f showed a significant decrease.
- Sluggish dissolution of carbides in 1.4W–0.06Ta and 2W–0.06Ta steels was found to influence the kinetics of $\alpha \leftrightarrow \gamma$ transformation.

2.1.2 Phase transformation and precipitation behaviour - JMatPro® & Thermocalc® simulations

Phase equilibria simulations for all the steels were performed using JMatPro® and *Thermocalc*®. Figure 1 shows the phase fraction and transformation temperatures of different phases for the

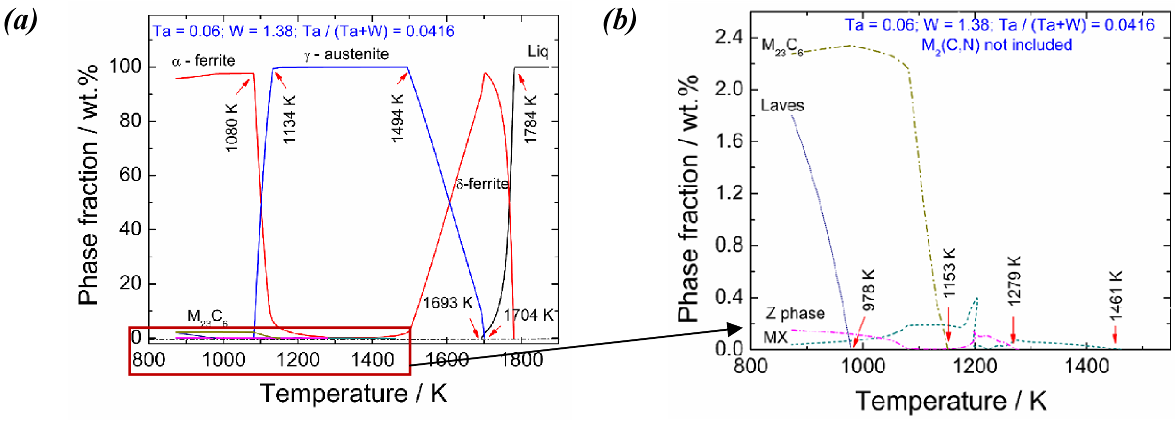

Figure 1. *Calculated (a) phase diagram for 1.4W–0.06Ta steel showing different transformation regimes (b) calculated minor phases showing different phases (M_2X phase not considered).*

steel containing 1.4 wt. % W. The equilibrium phases predicted and the computed values of Ac_1 and Ac_3 agreed with the experimental results. However, there is a mismatch between equilibrium simulation and experimental studies regarding the prediction of formation of secondary phases like M_2X, M_3C and Z phase due to the influence of kinetic factors. Computations showed no significant change in transformation/ dissolution temperature of phases with increase in W content of the steel, while the dissolution temperature of MX increased with Ta content.

2.2. Decomposition modes of high temperature austenite and characteristics of martensite

All the steels showed a martensitic microstructure after normalising from 1253 K and 1323 K, while furnace cooling resulted in a mixture of ferrite and martensite. A mixture of δ – ferrite and martensite formed after solutionising at 1553 K.

2.2.1 Effect of alloy content and solution treatment conditions

Normalising 1.4W steel at 1253 K showed predominantly martensite with an average lath size 200-300 nm, while fine needles of Fe rich precipitates were observed in a few wide laths measuring 1-2 µm (Fig. 2). Such precipitates are not expected in air hardenable 9Cr steels. The carbides identified as a function of solution treatment temperature and cooling rate for the three steels with varying W content are summarised in Table 1.

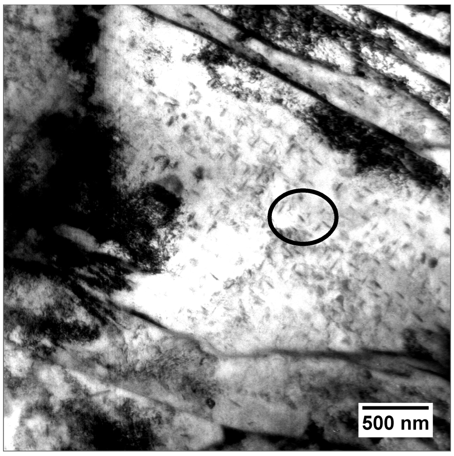

Figure 2. *Thin foil micrograph of normalised 1.4W steel showing needle like precipitates*

Table 1 Summary of microstructure of the austenitised steels

Steel	*1253 K / AC*	*1253 K / WQ*	*1323 K / AC*	*1323 K / WQ*
1W – 0.06Ta	α' + UC	α' + UC	α' + UC	α' + UC
1.4W – 0.06Ta	α' + UC + M_3C*	α' + UC	α' + UC+ $M_{23}C_6$*	α' + UC
2W – 0.06Ta	α' + UC + $M_{23}C_6$*	α' + UC + M_3C*	α' + UC+ $M_{23}C_6$*	α' + UC
1W – 0.14Ta	α' + UC	α' + UC	α' + UC	α' + UC

*UC – undissolved carbibes; *acicular intralath Fe rich carbides*

The present study has established that formation of Fe rich carbides is not due to para-equilibrium precipitation or by auto-tempering of martensite. Due to compositional inhomogeneity of austenite caused by the undissolved carbides, the solute lean austenite in the vicinity of undissolved carbides transform to ferrite + carbides above the M_s temperature, while solute rich austenite away from the undissolved carbides transforms to martensite. This has been confirmed by analysis of DSC profile during cooling of 1.4W–0.06Ta steel and detailed microstructural analysis.

2.2.2 Martensite Characteristics and optimisation of tempering parameters

Orientation imaging of normalised 1.4W-0.06Ta steel revealed random orientation of the martensite laths (Fig.3(a)) suggesting no variant selection due to a relatively high cooling rate. A low amount of retained austenite (~2%) was also found to be present as shown in fig. 3(b).

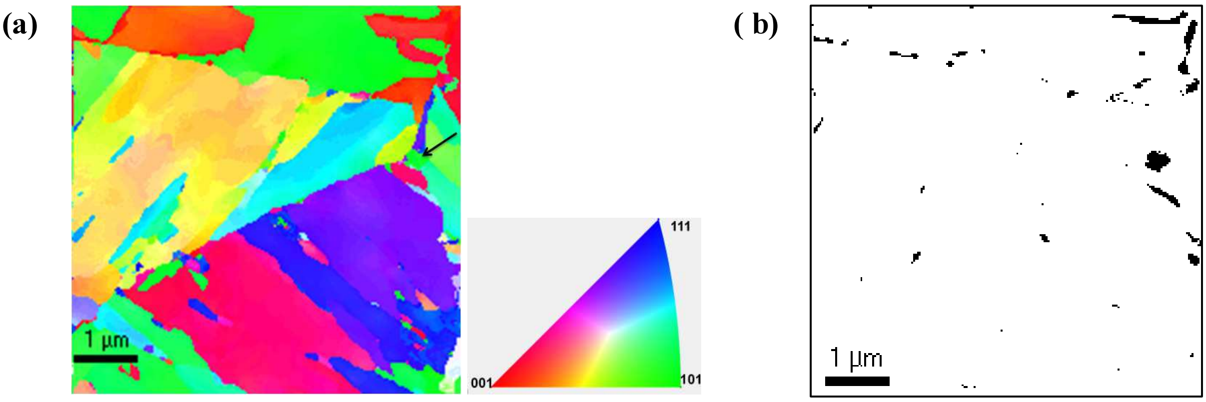

Figure 3. *(a) Orientation imaging of 1.4 W-0.06Ta steel showing random orientation of martensite laths, (b) phase map showing retained γ*

The mechanism and kinetics of tempering with W and Ta content has been studied. The activation energy (Q) was calculated by Arrhenius type of analysis using hardness and strain variation from XRD studies. The values of Q varied from 0.5 to 1 eV, corresponding to interstitial diffusion of C in α-ferrite.

Recovery of martensite and coarsening of precipitates was sluggish at 923 K. Fe rich intralath $M_{23}C_6$ carbides formed in the initial stages of tempering at 923 K were unstable, while Cr rich interlath $M_{23}C_6$ carbides formed at later stages. Tempering at 973 and 1033 K showed faster recovery than at 923 K. However subgrain formation and coarsening of precipitates was fastest at 1033 K. Microchemical variation of $M_{23}C_6$ showed a systematic change as a function of W content of the steel. Although $M_{23}C_6$ was Cr rich, it showed a large solubility for W. This also explains the sluggish dissolution of carbides with increase in W content discussed in section 2.1.

2.3. Microstructural evolution - Effect of alloy content, temperature and stress

2.3.1 Effect of temperature and stress exposure

1W – 0.06Ta steel aged at 773 K upto 5000h showed an insignificant hardness variation with time, whereas a significant decrease was observed at 823 K, which was correlated to the softening of matrix, due to the depletion of solute elements through the coarsening of $M_{23}C_6$ carbides. However, aging at 873 K showed a secondary hardening behaviour after 2 h of thermal exposure, due to fresh nucleation of fine MX precipitates. V and Ta rich MX precipitates were in the size range of 20 – 40 nm and did not coarsen with long term aging at any temperature. Microchemical variation of $M_{23}C_6$ precipitates showed an increase in Cr / Fe and W / Fe ratios beyond 823 K after long term thermal exposure.

Significant change in subgrain size was not evident with thermal exposure, due to effective pinning by the fine MX precipitates. However, the combination of thermal and stress exposure showed considerable coarsening of sub-structure and $M_{23}C_6$ precipitates [6].

2.3.2 Role of W and Ta on evolution of secondary phase

Replacement / addition of W in RAFM steel retards the coarsening of $M_{23}C_6$ precipitates as compared to P91/ T91 steel [7]. The present study showed the increase in amount of Laves phase with W and Ta content of the steel. Detailed TEM analysis revealed the formation of Laves phase around $M_{23}C_6$, suggesting that $M_{23}C_6$ acts as nucleation centre. X-ray mapping showed that the Laves phase is richer in Fe and W, with little solubility for Cr and Ta. The coarsening of Laves phase is accompanied by the exchange of Cr and W at the Laves phase / $M_{23}C_6$ interface. Influence of Ta on formation of Laves phase was also evident from the microstructural characterisation of 0.14 Ta steel after long term thermal exposure. The above result was also supported by JMatPro® calculations.

3. Organisation of the Thesis:

This thesis consists of six chapters and is organised as follows-

Chapter 1, **Introduction**, briefly presents a review of the existing literature on the RAFM steel, with emphasis on basis of alloy development, physical and mechanical properties of the steel. Chapter 1 also highlights the specific issues related to the physical metallurgy aspects of RAFM steels that need to be addressed.

Chapter 2 deals with the **Experimental Methodology** adopted in this study. Details of processing parameters, heat treatments and specimen preparation are given. Details of different experimental techniques, operating conditions, analysis procedures and sources of error are described. A brief description the computational methods namely JMatPro® and Thermocalc® are also presented.

Chapter 3 titled **"Phase transformation in RAFM steels"** discusses the thermodynamic studies carried out to establish the temperatures and enthalpy of the transformation. Simulation of thermodynamic data using JMatPro® and Thermocalc® software have been correlated with the experimental data. The kinetics of martensite transformation in the W added RAFM steels with variation in cooling rate has been discussed.

Chapter 4 titled **"Decomposition modes of high temperature austenite and characteristics of martensite"** describes the microstructures that evolve during the decomposition of austenite as a function of temperature and cooling rate. The role of alloy content in controlling the kinetics of martensitic transformation has been understood in terms of the heterogeneity of austenite at solution treatment temperatures, which is a consequence of the incomplete dissolution of the pre-existing carbides. The transformation products have been characterised using OIM in TEM. This chapter also discusses about the kinetics of tempering of martensite. The phase evolution and microchemistry of the phases, which varies with W content has been discussed extensively.

Chapter 5 titled **"Microstructural evolution - Effect of alloy content, temperature and stress"** provides a detailed description on the effect of prolonged exposure to high temperature and stress on recovery and recrystallisation of substructure and evolution of secondary phases. Extensive studies on the effect of W and Ta on evolution of secondary phases and the mechanism of formation of Laves phase are dealt with in this chapter.

Chapter 6 presents the summary of important findings of this study and also identifies the future directions for further studies.

The topics addressed in this thesis are summarised in Figure 4.

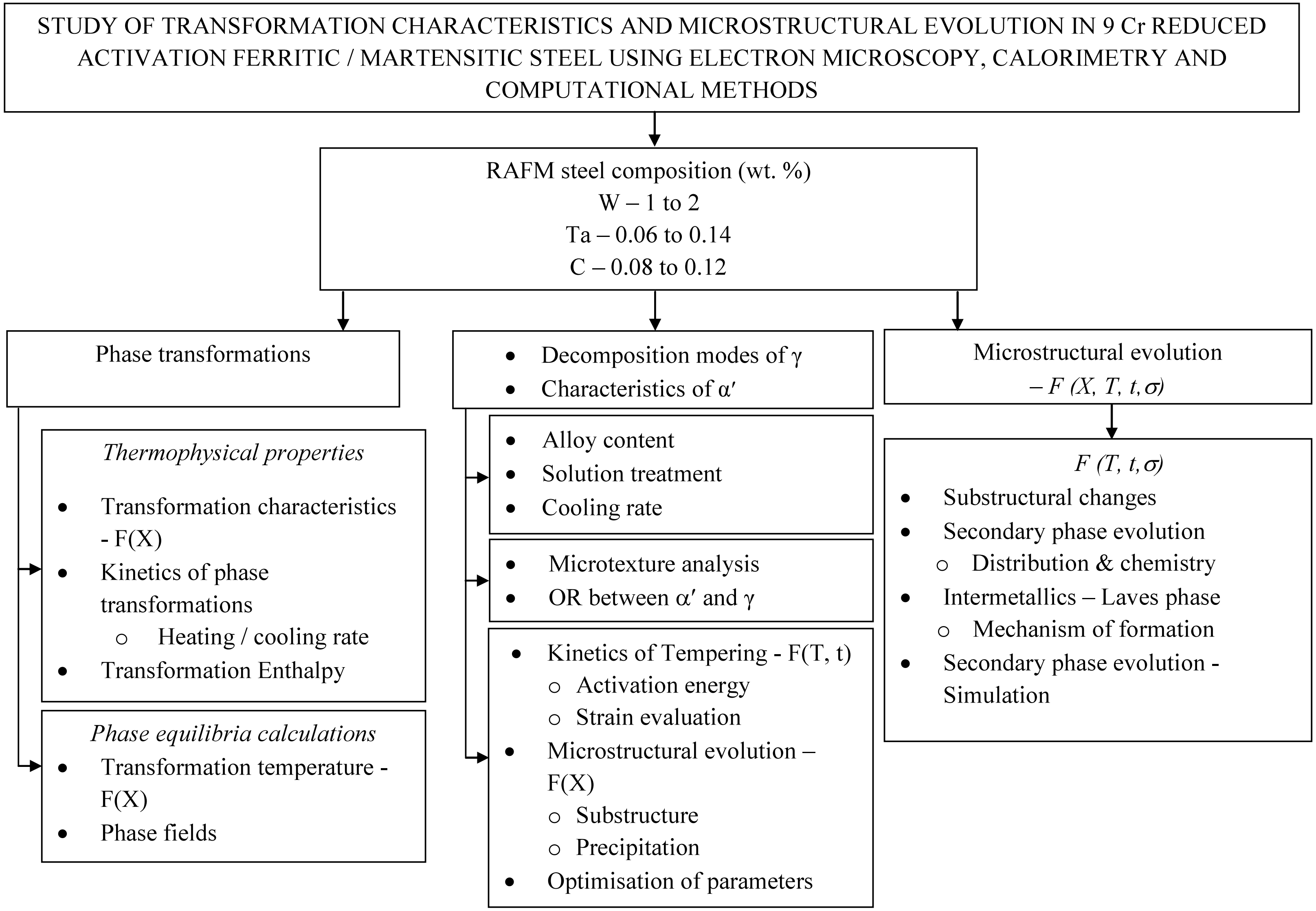

X, T, t and σ are composition, Temperature, time and stress respectively

Figure 4. Flow chart of the major themes of the thesis

References:

1. R.L. Klueh, *Int. Mater. Rev.* **2005**, 50(5), 287–310.
2. R.L. Klueh, D.R. Harries, *High-Chromium Ferritic and Martensitic Steels for Nuclear Applications*. ASTM Monograph, ASTM International: West Conshohocken **2001**; 3:1–38.
3. B. Jeyaganesh, S. Raju, A. K. Rai, E. Mohandas, M. Vijayalakshmi, K. B. S. Rao, B. Raj, *Mater. Sci. Tech.,* **2011**, *27*, 500 –512.
4. Huang Q, et al., *J. Nucl. Mater.* **2013**; 442, S2 – S8.
5. A. Danón , A. Alamo, *J. Nucl. Mater.,* **2002**, 307–311, 479–483.
6. R. Mythili, Ravikirana, J. Vanaja, K. Laha, S. Saroja, T. Jayakumar, M.D. Mathew, E. Rajendrakumar, *Proc. Engg.* **2013**, 55 (3–4), 295–299.
7. V. Thomas Paul, S. Saroja, M. Vijayalakshmi, *J Nucl Mater.*, **2008**, 378, 273–281.

List of Figures

List of Tables

List of Symbols and abbreviations

ADXRD	Angle Dispersive X-ray Diffraction
BSE	Back Scattered Electron
CCT	Continuous Cooling Transformation
DBTT	Ductile to Brittle Transition Temperature
DSC	Differential Scanning Calorimetry
ECD	Equivalent Circle Diameter
EDX	Energy Dispersive X-Ray
FWHM	Full Width at Half Maxima
ITER	International Thermonuclear Experimental Reactor
ODS	Oxide Dispersion Strengthened
OIM	Orientation Imaging Microscopy
PAGS	Prior Austenite Grain Size
RAFM	Reduced Activation Ferritic / Martensitic Steel
ROI	Region of Interest
SAED	Selected Area Electron Diffraction
SEM	Scanning Electron Microscopy
TBM	Test Blanket Module
TEM	Transmission Electron Microscopy
TTT	Time Temperature Transformation
XRD	X-ray Diffraction
Ac_1	Austenite Start temperature
Ac_3	Austenite finish Temperature
G	Gibbs free energy
H	enthalpy
K_{AB}	Cliff-Lorimer constant
L	Liquid
M_f	Martensite finish temperature
M_s	Martensite start temperature
Q	Activation energy
T_d	Disolution temperature
T_L	Liquidus Temperature
T_s	solutionising temperature
T_γ	Austenitisation temperature
α	Low temperature ferrite
α'	Martensite
β	Cooling rate
γ	Austenite
δ	High temperature ferrite
θ	Bragg angle
λ	Wave length

Chapter 1

An Introduction to Physical Metallurgy of Reduced Activation Ferritic-Martensitic Steels

1.1 Development of 9Cr ferritic martensitic steels for nuclear applications

The worldwide growing demand for energy and the limited fuel resources have thrown open a challenge, which can be met partly by enhancing the efficiency of conventional energy sources and by alternate energy sources, with high priority on the environmental aspects associated with the option. Although renewable energy sources such as solar, wind etc. can provide clean energy, their technology as a viable commercial option is still evolving. Nuclear energy is one of the environmentally safe and viable options among other alternate energy sources, with worldwide established technologies. The increasing number of operating reactors in the world stands testimony to this. Today the water moderated/ cooled thermal reactors and sodium cooled fast reactors have established the safety, reliability, economics and robustness of the technology for power production. The experience gained by different countries to build and operate the fission reactors has led to an international collaboration to build the first fusion reactor called the International Thermonuclear Experimental Reactor (ITER), and efforts towards this are in progress in various directions [1,2].

The selection of structural materials for critical components is of utmost importance to achieve both performance and the designed life of the plant. Selection of structural material for the plasma facing components in a fusion reactor namely the first wall and blanket is a bigger challenge and stems from the difference in the fission and fusion environments. A much higher energy and higher neutron flux in addition to the high rate of production of hydrogen and helium in a fusion reactor demand materials which can withstand such aggressive environments [1-4]. Austenitic stainless steels were the first to be considered as structural materials for both fast fission and fusion reactors. In order to achieve high operating temperatures exceeding 973K, superalloy and refractory alloys of Mo, Nb and V were also considered for fusion applications. The inhibition in employing ferritic steels was primarily due to a possible interaction of the ferromagnetic alloy with the high magnetic fields in a fusion reactor [1]. The refractory alloys of Mo or Nb are not considered due to their inadequate mechanical properties. Austenitic steels also have a limitation with respect to high rates of void swelling, low thermal conductivity and high thermal expansion coefficient. Intensive research over the last several decades have narrowed down the choice of materials to vanadium alloys, SiC/SiC composites and ferritic-martensitic (F-M) steels. Among these, the F-M steels possess an advantage over the other classes of materials for the present due to their well known metallurgical behaviour and industrial experience on fabrication and joining of components. Since the 1970s the ferritic steels became candidate materials for both the fission and fusion applications in view of their enhanced void swelling resistance [5,6] besides other attractive properties like good thermal conductivity, moderate high temperature creep strength and microstructural stability [1,7-9]. Ferritic-martensitic steels with 9-12%Cr containing about 0.1% carbon and about 1%Mo along with small amounts of V, Nb, W have been known to possess adequate elevated temperature strength including creep strength upto ~823K and good thermal properties with high resistance to thermal stresses along and have been employed in power plants, chemical and petrochemical industries. [1,9]. **Figure 1.1** illustrates the dependence of Cr content on creep strength and ductile to brittle transition temperature (DBTT) of ferritic martensitic steels. It is observed that the steel with 9% Cr possess the optimum combination of high creep strength, high toughness and low DBTT among all the other steels considered. Again, a decrease in creep strength, ductility and increase in DBTT is observed with increases in Cr concentration beyond 10% due to the formation of coarse δ- ferrite grains [2,3]. It is evident that 9Cr steels have an edge over other ferritic or F-M steels. It is also of interest to note that steels of the type of modified 9Cr-1Mo (9Cr-

1MoVNb steel) have been approved for design by code bodies in countries such as USA, Japan and Europe for applications in conventional power plants and steam generator circuitry in liquid metal cooled fast reactors.

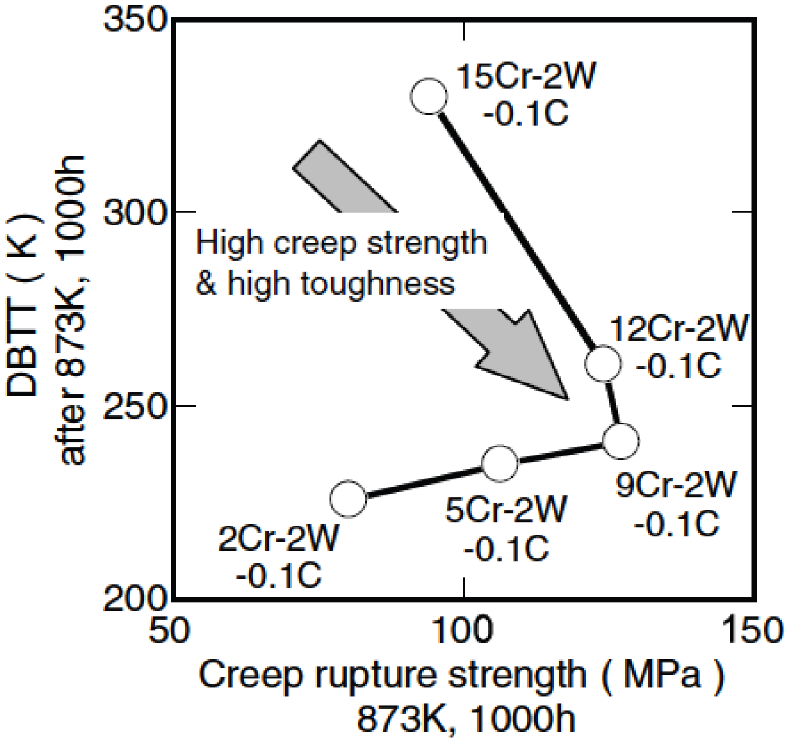

Figure 1.1. *Variation of DBTT and creep strength with variation in Cr content (unirradiated)[3]*

1.2 Development of Low and Reduced Activation F-M steels

As already discussed, 9Cr ferritic / martensitic steels with good mechanical properties [1-4] are proven structural material for steam generator circuits [10,11], due to the good thermal conductivity and low thermal expansion coefficient [12,13]. Modified 9Cr–1Mo with addition of V and Nb, showed superior mechanical properties, due to the formation of very fine particles of MX, which are stable [14-16] in the service temperature of 773–873 K [1,17] as compared to their unmodified counterparts [18]. 9Cr–1Mo steel variants are also selected as core structural material for the fast breeder reactors due to their excellent radiation swelling resistance and compatibility with liquid sodium [19,20].

However, in a nuclear plant in addition to the general performance criteria discussed above, it is important to have a 'low activation' material, which means that the structural material would not become radioactive or alternately would decay rapidly into nearly non-radioactive levels of activity [21,22]. Such a low activation material would provide the necessary protection from radioactive debris in the extreme case of an accidental situation. Under normal conditions maintenance of the plant and disposal of radioactive waste also call for "low activation" steel. It is well known that the elements like Mo and Nb in modified 9Cr–1Mo transmute on neutron irradiation to produce long lived isotopes [23-25] and do not satisfy the criterion of low activation. Environmental effects associated with disposal of fusion reactor components after replacement during operation or after decommissioning of the plant need to be borne in mind while selecting the material. Based on the constituent elements in the alloy the time for decay of induced radioactivity can be a few thousand years and requires deep geological storages.

No structural material has been developed so far which meets the criterion of 'low activation' i.e material does not activate or activates to very low levels. In view of this requirement, efforts were initiated internationally in the 1980s to produce a 'reduced activation' F-M steel, which can be disposed by shallow land burial or by suitable recycling methods after adequate cooling period of about hundred years [26]. Although guidelines exist for disposal of nuclear waste from fission reactors it remains yet to be seen as to how they can be applied to wastes from fusion reactors. It is imperative that the composition of the steel should be tailored to consist of only those elements whose radioactive products will decay relatively faster probably within hundreds of years rather than thousands of years. Based on calculations elements that need to be minimized or eliminated in Cr-Mo steel for a rapid decay of induced radioactivity after irradiation in a fast reactor have been determined. It is understood that elements such as Mo, Nb, Cu, Ni and N should be either eliminated or kept to very minimum levels [27].

Reduced Activation Ferritic / Martensitic (RAFM) steels without the addition of any of the above restricted elements have been developed for evaluation of the physical and mechanical properties and to demonstrate that their properties are comparable or superior to the Cr-Mo steels [28]. Besides these elements, it is also essential to restrict the level of other elements such as Co, Bi, Cd, Ag etc., that could appear as tramp impurities and pose difficulties to achieve reduced activation. It is also of importance to restrict the level of metalloids or residuals such as S, P, As, Sb which are embrittlement promoting elements. 9Cr RAFM steels have been developed where Mo and Nb are replaced by W and Ta in modified 9Cr–1Mo [23,25]. RAFM steels are considered for the first wall and test blanket module, which are plasma facing components in the International Thermonuclear Experimental Reactor (ITER). These steels are reported to show good thermophysical and mechanical properties in addition to the excellent resistance to void swelling [29-32] and He embrittlement [32-34]. The operative temperature of RAFM steel is 773 – 823 K, while oxide dispersoid strengthened (ODS) variants of the steel is expected to enhance the operating temperature to 923 K [35].

Worldwide efforts more notably from the European Union, USA, Japan, China and India have been made towards optimising the chemical composition of RAFM steels [36-47] and processing parameters. Many countries have developed RAFM steels based on the chemical composition of EUROFER 97, which has been taken as a reference for the development. The developments have aimed towards meeting the specifications of Eurofer 97 for the operating conditions of ITER, and intense research on materials for the future DEMO and PROTO reactors, having high operating temperature and neutron flux is in progress [21]. Chemical composition of the RAFM steels used worldwide is compared in **Table 1.1**.

Use of clean raw materials and melting practice has been adopted to minimise the impurities like Nb, Ni, Cu and Co [44,48]; with special emphasis on the Nb content. Chemical composition and heat treatment has been optimised for the desired mechanical properties and to obtain a stable microstructure during service exposure. Mechanical properties of the developed steels have shown to meet the requirement of ITER-TBM, with some data also generated on mechanical properties after irradiation [44,49,50].

Table 1.1. *Composition of RAFM steels developed in different countries*

Program	Designation	C	Si	Mn	Cr	V	W	N	Ta	Ref
USA	9Cr2WVTa	0.11	0.03	0.39	8.84	0.18	1.97	0.022	0.065	[38]
Japan	9Cr1WVTa	0.12			9.24	0.18	1.06	0.003	0.1	[39]
	9Cr3WVTa	0.17	-	-	9.16	0.16	3.08	0.003	0.10	[39]
	JLF1	0.10	0.05	0.52	8.70	0.18	1.91	0.028	0.08	[40]
	F82H	0.09	0.1	0.21	7.46	0.15	1.96	0.006	0.023	[40]
Europe	LA4Ta	0.14	0.03	0.78	11.0	0.23	0.72	0.041	0.07	[40]
	LA12Ta	0.16	0.03	0.88	9.86	0.28	0.84	0.043	0.1	[40]
	LA13Ta	0.18	0.04	0.79	8.39	0.24	2.79	0.048	0.09	[40]
	Eurofer 97	0.12	0.03	0.48	8.96	0.18	1.04	0.022	0.15	[41]
	Asturfer(AF1)	0. 12	0.05	0.39	8.9	0.19	1.4	0.01	0.10	[42]
	Asturfer(AF2)	0.11	0.04	0.44	8.8	0.19	1.1	0.007	0.12	[42]
	OPTIFER (Ia)	0.1		0.5	9.3	0.26	0.96	0.015	0.066	[43]
	OPTIFER (Ib)	0.12		0.49	9.5	0.23	0.98	0.006	0.163	[43]
	OPTIFER (II)	0.12		0.49	9.5	0.28	0.006	0.015	0.018	[43]
	OPTIFER (III)	0.12		0.49	9.32	0.24	0.023	0.017	1.60	[43]
	OPTIFER (IV)	0.11		0.57	8.5	0.23	1.16	0.06	0.15	[43]
China	CLF1	0.1		0.5	8.5	0.25	1.5	0.025	0.1	[44]
	CLAM	0.12		0.49		0.20	1.44		0.15	[45]
	CNS-1	0.1	0.4	0.4	9.3	0.05	2.2	0.043	0.05	[13]

Based on the data obtained the composition of RAFM steels considered by different countries varied within the narrow range of 1 – 2 wt. % W and 0.05 – 0.15 wt. % Ta. In India, a three stage alloy development program is in place for the indigenous development of RAFM steel to meet the international specifications and a unique composition has been identified, which is discussed subsequently.

Optimisation of heat treatment conditions showed that the steels in the normalised and tempered condition exhibits a good combination of strength, ductility and toughness [51,52]. It is well known that the alloy content plays an important role in the phase transformations, microstructural and mechanical properties of the steel. The effect of W and Ta on the mechanical properties of the steel is rather well studied [47,53,54]. However, the influence of microstructural changes on the mechanical properties stems from the various phase transformations, which in turn are dictated by the alloying elements. Hence a systematic study on the phase transformation characteristics with alloying elements is essential to understand the microstructural evolution in the steel. The general physical metallurgy aspects of the steel are discussed in **section 1.2**, addressing the phase transformation in RAFM steel and the microstructural characteristics on thermal exposure.

1.3. Physical metallurgy of RAFM steel

Figure 1.2 presents the pseudo binary diagram of Fe–Cr–C system with 0.1 % C. It is seen that the γ loop for the equilibrium diagram closes if the Cr content exceeds 12 %. Therefore the high Cr (9-12%) steels are austenitic or duplex in the temperature range of 1120 to 1470 K. Hence the normalising temperature for steel with 9% Cr is chosen to be below 1120 K to confine to single γ phase field. However, the actual phase diagram for the steel is also sensitive to other alloying elements which can be ferrite stabilisers like Cr, W, V, Ta etc or austenite stabilisers like C, N, Mn, etc., [1]. The constitution of the

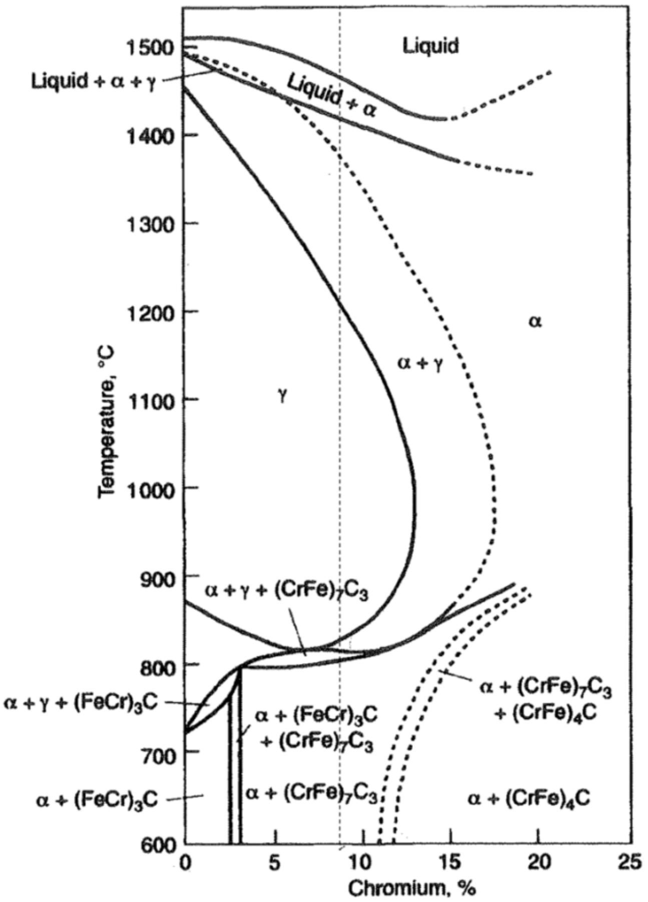

***Figure 1.2.** Pseudobinary diagram of Fe – Cr – C system with 0.1% C [1]*

steels with both ferrite and austenite stabilisers at room temperature on cooling from the γ phase field is predicted from the Schaeffler-Schneider diagram using the Cr and Ni equivalent of the steel [1]. To suppress the formation of δ-ferrite, the Cr equivalent element content should be ≤ 9 wt.%. The equation for Cr equivalent of such steels is written as-

$$Cr_{eq} = Cr + 6*Si + 4*Mo + 11*V + 5*Nb + 1.5*W + 8*Ti + 12*Al - 4*Ni - 2*Co - 2*Mn - Cu - 40*C - 30*N \quad (1.1)$$

where all the compositions are expressed in wt. % [1].

Cr equivalent for the RAFM steel developed world wide is in the range of 9-10 wt. %, which is well within the γ loop at the austenitisation temperature. Therefore, phase transformations in RAFM steel, is reported to be similar to that of other 9Cr steels [55].

However, replacement of Mo and Nb by W and Ta is expected to change the kinetics of phase transformation [56,57] which will have a significant impact on the microstructures and mechanical properties of the steel. As mentioned earlier, the steels are used in normalised and tempered condition [51,52], which has a lath martensitic microstructure with precipitates decorating the lath and grain boundaries and fine intra granular precipitates [4]. The steel derives its strength from the martensitic substructure and precipitation in this matrix [4,1,47]. Based on an extensive survey of literature, a brief description on the phase transformation and microstructural aspects is discussed in the following section.

1.3.1. Role of alloying elements on phase transformation in RAFM steel

Literature reports on phase transformations in a variety of steels studied showed the sensitivity of alloy content on phase transformation temperatures namely Ac_1 and Ac_3 [55-57,58-61] as an interplay between the ferrite and austenite stabilisers. It is known that the phase transformation characteristics of the 9Cr RAFM steel particularly, the Ac_1 and Ac_3 temperatures are sensitive to the W and Ta content [41,58-61]. The increase in Ac_1 and Ac_3 with ferrite stabilisers W and Ta content of the steel is reported [58]. Reports also show the variation of phase transformation temperatures (Ac_1, Ac_3, M_s and M_f) for the different steels [41,60].

Literature reports from Zheng et al., in 2011 [61] and Alamo et al., in 1998, [58] explained the development of Continuous Cooling Transformation (CCT) curve for CLAM (9Cr–2W–TaV) and F82H (7.5Cr-2WTaV) steel through dilatometric experiments. The CCT diagram for CLAM steel is presented in **Figure 1.3** [61]**.** It is evident from the diagram that the microstructure of the steel is either martensite or ferrite depending on the cooling rate. The critical cooling rate for the complete formation of martensite is 50-60 K min^{-1} **(Figure 1.3)**. The Time-Temperature-

Transformation (TTT) diagrams for different reduced activation steels have also been generated to show the dependence of $\gamma \leftrightarrow \alpha$ transformation, and the dependence of M_s as a function of C+N content [58]. Raju et al., reported that the transformation temperatures and $\gamma \leftrightarrow \alpha$ transformation kinetics [56,57] for RAFM steel, was sensitive to the heating and cooling rate. Although the precipitation behaviour in F-M steels is well studied in literature with respect to their type and microchemistry, only few have addressed the formation and dissolution temperatures of $M_{23}C_6$ and MX precipitates in 9Cr class of steels, which is useful in knowing the stability regime of these precipitates, since the steels derive strength from these precipitates [51,52].

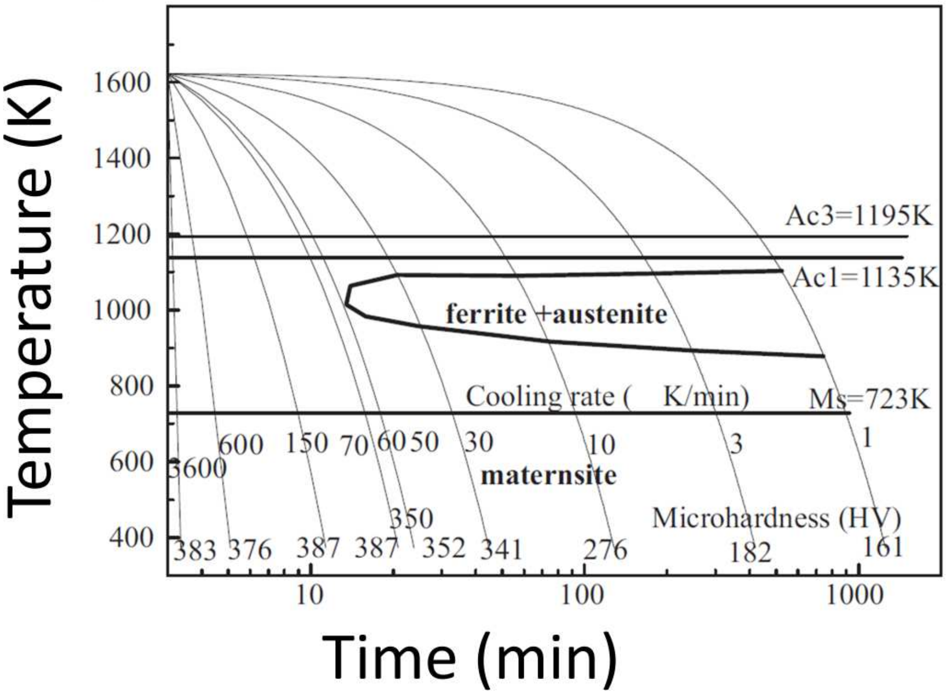

Figure 1.3. *CCT diagram for CLAM steel showing the transformations for different cooling rates [61]*

Simulation of phase transformations using Thermocalc® [62] and JmatPro® [63] software supported the experimental findings in RAFM steels. Simulations provided the necessary information on the formation / stability regime of different phases in the steels [64-68], which was in close agreement with the experimental data presented by Alamo et al. [58].

1.3.2. Evolution of secondary phases in 9Cr F-M steels and the role of alloy content

The role of alloy content on the mechanism and kinetics of phase transformation is very significant. It is also well known that the microstructural parameters of the steel primarily depend on the phase transformation characteristics, a one to one correspondence between them is apparent. Several researchers have reported a myriad of microstructures in 9Cr class of steel after different thermo-mechanical treatments [65,69]. The steels are generally air-hardenable resulting in a martensitic structure for a range of cooling rates when cooled from the austenite phase field [69-71] with high hardness ranging from 360 – 470 VHN [58]. The steels are employed after tempering, which brings down the hardness and improves the toughness [72-75]. Tempering of martensite is also reported to bring down the internal energy [76] in low C martensite steel, there by stabilising the microstructure. It is also reported that the presence of fine carbides after tempering stabilises the microstructure against recovery and recrystallisation [3,77]. In addition, prolonged thermal / creep exposure at 773 to 923 K is known to form Z phase and intermetallics like Laves phase [78,79], which are beneficial when they nucleate with a fine size, a fast growth of these phases degrades the mechanical properties [4,1]. Hence it can be inferred that the nature and kinetics of precipitation exert a significant influence on the microstructural stability of the steel, which in turn controls the mechanical properties. Therefore, it is necessary to possess a detailed knowledge of the different phases that can form in 9Cr F-M of steels and the effect of alloying elements, specially those related to the chemical composition of RAFM steels, which is discussed below-

M_3C

M_3C carbides are Fe rich with a complex orthorhombic structure. Formation of M_3C carbides are familiar in low chromium steel [80], while these carbides are not expected to form in 9Cr class of steels [81]. However, precipitation of Fe rich M_3C carbides has been reported in normalised steel [82]. However, according to thermodynamic calculations, M_3C is not a stable phase in 9Cr steels [48].

M_7C_3 and M_6C

Formation of M_7C_3 or M_6C during tempering of steel is reported [48, 77, 83] in low Cr steels. However Danon et al., [48] predicted the formation of M_7C_3 or M_6C in 9Cr RAFM steel also. Tamura et al., [77] experimentally showed the presence of Fe_7C_3 precipitate during tempering at 1023 K in 9Cr- 1Mo steel. Recent literature on CS25 steel with 8.5% Cr also reported [83] the formation of M_7C_3 in few grains at 873 K, as a consequence of repartitioning of W. Though such a precipitation can add to the high temperature strength, dissolution of these precipitates after prolonged thermal exposure suggested their metastable nature in high Cr steels [77].

$M_{23}C_6$

Formation of the faced cantered cubic $M_{23}C_6$ carbides is favoured in high Cr steels, which also remains stable phase during long term service [4,84] in the temperature range of 773 to 1033 K. However, considerable coarsening of the carbide phase is reported to soften the ferrite matrix [84]. The carbide mainly consists of $Cr_{23}C_6$; however solubility of other elements is also reported [85]. In RAFM steels $M_{23}C_6$ contains Cr, W and Fe as major elements [69,44,86], a small amount of V also is reported [2]. Enrichment of Cr is reported in 9 Cr class of steels as it grows [87,73]. Addition of W in RAFM steel is reported to control the coarsening of $M_{23}C_6$ [4]. Fine precipitates of $M_{23}C_6$ are beneficial in increasing the strength [88] by pinning the boundaries. However the coarsening of the carbides leads to the recovery of dislocations and coarsening of lath during creep, which results in a decrease in resistance to creep deformation [89].

MX

In many of V, Nb and Ta added creep resistant steels, a stable fine intralath NaCl type fcc monocarbides / carbonitrides are evident [1,4, 14,83,73]. Thermocalc calculations showed that these precipitates nucleate in the range of temperatures from 770 to 1300 K [65]. It is reported [90-92] that these carbides do not coarsen significantly during prolonged thermal exposure and even under creep exposure [93]. Hence, these carbides are responsible for the high temperature strength during prolonged service [90-92]. Two types of MX precipitates, namely V rich and Ta rich are possible in V and Ta added steels [90]. These carbonitrides are reported to be stable up to 1681 K [94].

M_2X

It is reported that tempering the high nitrogen steel at relatively lower temperature for longer time can favour the formation of a nitrogen rich M_2X phase [95,96]. Recent study on high Cr steel also showed the formation of Cr_2N; while it is unstable during longer durations of thermal exposure. Haribabu et al., [97] also showed the formation of M_2X phase in Eurofer 97 steel. However stability of M_2X in 9Cr steel tempered at 1033 K is less probable, which dissolves during further aging.

Z-phase

Z-phase, is known to be a complex tetragonal nitride with the general formula Cr(X)N, where X= Nb, Ta, V which forms simultaneously with the dissolution of the cubic MX-phase, precipitates and coarsens much faster than the MX phase. Hence, formation of Z-phase is reported to lead to a steep reduction in the creep strength of the 9–12% Cr ferritic steels [98], since the increased creep resistance is attributed to the presence of carbonitrides in the matrix [99]. The Z-phase was observed in the ternary CrNbN and CrTaN systems, but no Z-phase was found in the CrVN system [100], though Cr(V,Nb)N has been observed. However, in multicomponent steels containing Ta, the effect of Ta on Z-phase formation has not been experimentally reported [48].

Laves Phase

Other than carbides or nitrides Laves phase precipitation is reported in 9Cr creep resistant steels containing Mo or W, during low temperature thermal exposure, [101]. Tamura et al., [102], report that the presence of stress accelerates its formation and coarsening [103], based on the TTP diagram for Laves phase in RAFM steels developed by them. Fine precipitation of Laves phase is beneficial to increase the strength [4,104], while its rapid coarsening has shown a detrimental effect on mechanical properties of the steel, especially on the toughness [4,103]. In Mo added steels it is reported that, a Mo / C ratio greater than 5, can promotes the formation of Laves phase [105]. However, in RAFM steels the formation of Laves phase depends on the W content of the steel [48]. Increase in W content increases the formation of Laves phase [48]. Role of Ta on the formation of Laves phase is speculated based on the Fe-W-Ta ternary diagram [106], while no experimental evidences to this effect exist so far.

From the above description of the various phases, it is understood that phases like M_2X, M_7C_3, M_6C are metastable carbides that form at low temperatures at shorter durations of tempering. Typical tempered martensitic structure in high Cr steels consists of $M_{23}C_6$ precipitates decorated along the lath / grain boundaries with size varying from 100 to 300 nm [72,74] and fine intra lath MX precipitates with size 10 to 40 nm [74-75]. The formation of Z and Laves phase are important to be considered during long term thermal exposure more so under stress, due to their detrimental effect on mechanical properties.

1.4 Role of Microstructure on Mechanical properties

It is well known that the maximum service temperature of a structural material is decided by its stability in the operating environment and degradation of mechanical properties [1,35], specially creep properties. At a given temperature, the mechanical properties of the steel largely depend on the alloy content [47,107] and microstructural properties of the steel [35]. 9Cr steels as already discussed, derive their strength from the fine substructure and precipitates which pin the grain / lath boundaries [35,3]. However, during long term thermal or creep exposure, these precipitates coarsen, weakening the boundaries [104]. Furthermore, the appearance of intermetallics like Laves phase, on the grain boundaries offers a beneficial strengthening effect during initial stages of its nucleation [4,104]. However, the accelerated coarsening of Laves phase particles compared to the $M_{23}C_6$ [4,103,104] carbides decreases the grain boundary strength and hence the toughness of the steel [7].

As already discussed in the previous section, increase in W content retards the coarsening of $M_{23}C_6$, which in turn helps to retard the substructural recovery due to the pinning effect of carbides. This increases the long term stability of microstructure and hence the long term mechanical properties [103,108,109]. Also, addition of W from 1 to 3%, in 9Cr RAFM steel is reported to increase the creep strength of the steel considerably. However, further addition of W, above 4 % is reported [2] to form δ – ferrite, which decreases the creep strength. The tensile strength of the steel is reported to show an insignificant change with W content of the steel [35]. **Figure 1.4(a)** shows the dependence of the Ductile to Brittle Transition Temperature (DBTT) on W content of the steel. For the normalised and tempered steel a decrease in DBTT with addition of W is seen compared to a steel without W. However, large addition of W increases the

DBTT. A similar trend is observed in a steel aged at 873 K. This result shows that 1 – 2% W is optimum for the RAFM steel to achieve better mechanical properties.

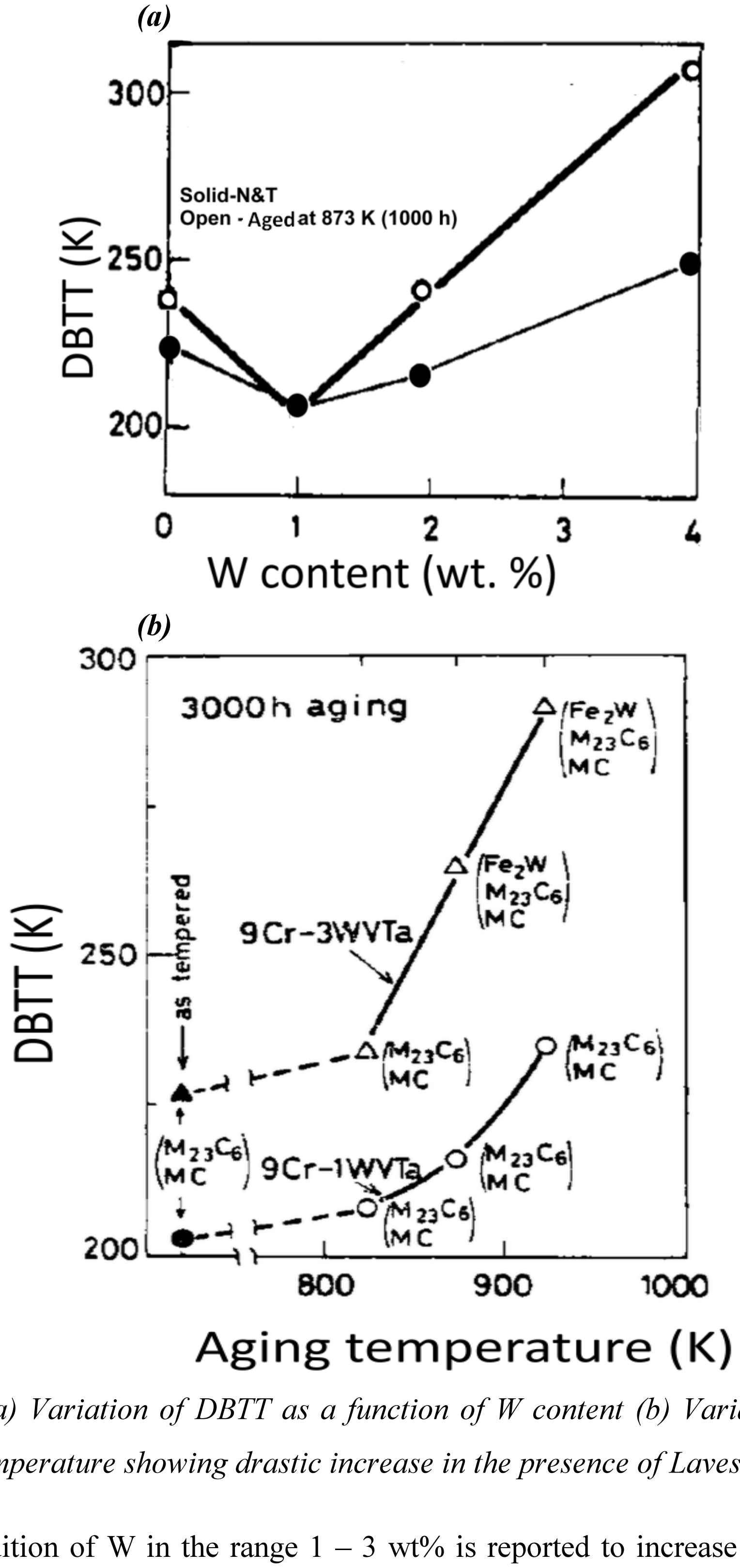

***Figure 1.4**. (a) Variation of DBTT as a function of W content (b) Variation of DBTT with aging temperature showing drastic increase in the presence of Laves Phase [2].*

However, addition of W in the range 1 – 3 wt% is reported to increase the δ – ferrite content in the weld and heat affected zone, which deteriorates the impact properties of the steel [110, 111]. Formation of delta ferrite is also reported to reduce the creep ductility of the steel [112]. The formation of delta ferrite and Laves phase due to the addition of W is also reported to influence DBTT [3,35]. Addition of W also favours the formation of coarse Laves phase in the steel during creep exposure [2]. **Figure 1.4(b)** shows the effect of $M_{23}C_6$ and Laves phase on DBTT in the W added 9 Cr steels. It is seen that coarsening of both $M_{23}C_6$ and Laves phase increase the DBTT, however, the increase is high in steel containing 3% W in the presence of brittle Laves phase compared to that in 1% W.

Addition of small amount of Ta was reported to be beneficial to reduce the grain size and improve the mechanical properties of the steel [54]. Addition of Ta from 0.05 to 0.08% is also reported to decrease the DBTT [54]. However, further increase in Ta up to 0.16% is reported to increase the DBTT [113]. A decrease in tensile and creep rupture strength of the steel is reported with increase in Ta content from 0.06 to 0.14 wt.% [47].

1.5 Development of India specific RAFM steel

In India, considerable R&D efforts have been made on various aspects of material development and establishment of fabrication technologies as a part of ITER-TBM program [114,115]. A three-phase alloy development program on the 9Cr RAFM steel is in progress [47,114], The three stage program includes, (a) demonstration of India’s capability to produce RAFM steel, with physical and mechanical properties comparable to the internationally produced RAFM steels, (b) optimisation of chemical composition of the steel through mechanical property evaluation and (c) development of RAFM steel in commercial scale. Efforts to indigenously develop an RAFM steel with a specific composition for the Indian Test Blanket Module, as a part of second phase of the program, has been successful [47]. This has been possible by a systematic alloy development program as a collaborative venture between several organisations like Institute of Plasma Research, Gandhinagar, MIDHANI, Hyderabad, and Indira Gandhi Centre for Atomic Research, Kalpakkam, India[47,116-128]. Four heats of 9Cr-W-Ta RAFM steel having different tungsten (1, 1.4 and 2 wt. %) and tantalum (0.06 and 0.14wt. %) contents were produced. By a detailed characterization of physical and mechanical properties, the chemical composition with optimum combination of impact, tensile, low cycle fatigue and creep properties has been arrived at [47,116-119,122-128]. India-specific RAFM steel designated as Indian Reduced Activation Ferritic Martensitic (INRAFM) steel conforms to a composition of 1.4 wt. % of W and 0.06 wt. % of Ta which meets the property requirements of ITER. The third stage of the development, namely production of the INRAFM steel at a commercial scale and into various product forms is in progress. Establishment of fabrication technologies for the TBM by different welding methods HIPing is also in progress [129-132].

1.6 Objective of the thesis

The objective of this thesis is to obtain an in-depth understanding on thermodynamic and physical metallurgy aspects of indigenously developed 9Cr RAFM steels with different W and Ta content, which involves the study of $\alpha \leftrightarrow \gamma$ transformation characteristics using differential scanning calorimetry (DSC) and microstructural investigation through Analytical Transmission Electron Microscopy and related techniques. The thesis highlights the role of alloy content and process parameters on microstructure by a systematic experimental investigation and simulation using JMatPro and Thermocalc software.

1.7 Scope of the thesis

This thesis presents the results of an extensive physical metallurgy study on 9Cr RAFM steels with W and Ta varying from 1–2 wt. % and 0.06 – 0.14 wt. % respectively.

These microstructural aspects studied in four compositions of the RAFM steels forms a part of a large Research and Development program on indigenous development of RAFM steel as a structural material for ITER. The thesis addresses three major themes, namely

- $\alpha \leftrightarrow \gamma$ phase transformation in RAFM steels
- Decomposition modes of high temperature austenite and characteristics of martensite
- Microstructural evolution **-** Effect of alloy content, temperature and stress

1.8 Organisation of the thesis

This thesis consists of six chapters and is organised as follows-

Chapter 1, **Introduction**, briefly presents a review of the existing literature on the RAFM steel, with emphasis on basis of alloy development, physical and mechanical properties of the steel. Chapter 1 also highlights the physical metallurgy aspects of RAFM steels and defines the objective and scope of the thesis.

Chapter 2 deals with the **Experimental Methodology** adopted in this study. Details of processing parameters, heat treatments and specimen preparation are given. Details of different experimental techniques, operating conditions, analysis procedures and sources of error are described. A brief description the computational methods namely JMatPro® and Thermocalc® are also presented.

Chapter 3 titled **"Phase transformation in RAFM steels"** discusses the thermodynamic studies carried out to establish the temperatures and enthalpy of the transformation. Simulation of thermodynamic data using JMatPro® and Thermocalc® software have been correlated with the experimental data. The kinetics of martensite transformation in the W added RAFM steels with variation in cooling rate has been discussed.

Chapter 4 titled **"Decomposition modes of high temperature austenite and characteristics of martensite"** describes the microstructures that evolve during the decomposition of austenite as a function of temperature and cooling rate. The role of alloy content in controlling the kinetics of martensitic transformation has been understood in terms of the heterogeneity of austenite at solution treatment temperatures, which is a consequence of the incomplete dissolution of the pre-existing carbides. The transformation products have been characterised using Mossbauer Spectroscopy and Orientation Imaging Microscopy in TEM, a newly emerging technique. This chapter also discusses about the kinetics of tempering of martensite. The phase evolution and microchemistry of the phases, which varies with W content has been discussed extensively.

Chapter 5 titled **"Microstructural evolution - Effect of alloy content, temperature and stress"** provides a detailed description on the effect of prolonged exposure to high temperature and stress on recovery and recrystallisation of substructure and evolution of secondary phases. Extensive studies on the effect of W and Ta on evolution of secondary phases and the mechanism of formation of Laves phase are dealt with in this chapter.

Chapter 6 presents the summary of important findings of this study and also identifies the future directions for further studies.

Chapter 2

Experimental Methods

2.1 Introduction

The details of experimental methodology adopted in the present study are discussed in this chapter. Experimental methodology includes pre-history, chemical composition and processing parameters of RAFM steels, details of heat treatments employed in this study, methods of sample preparation for microscopy and calorimetry analysis. The details on the operating conditions of instruments, their calibration are also presented along with the procedure used for analysis of the data and sources of error. Thermodynamic computations and simulations have also been performed using Thermocalc® and JmatPro®, to study the phase transformation characteristics and phase evolution in the RAFM steels. Further details on the experimental procedure are discussed in subsequent sections.

2.2 Alloy preparation and chemical composition

Present study used four different compositions of the RAFM steels with W varying from 1 to 2 wt. % and Ta from 0.06 to 0.14 wt. %. The steels used in this study were supplied by M/s MIDHANI Hyderabad, India. Four different compositions / heat have been received, the chemical compositions of which are listed in **Table 2.1**. Alloys were produced by vacuum induction melting followed by vacuum arc refining. Steels were remelted three or four times to ensure a high degree of homogeneity. Pure raw materials have been used to ensure the purity of the end product. A strict control over radioactive tramp elements (Mo, Nb) and elements which promote embrittlement (S, P) was practiced during the process. The ingots obtained in this process were subsequently rolled and hot forged into 12 mm thick plates. These hot forged plates have been subjected to a heat treatment conforming to an industrial practice of a normalization treatment at 1253 K for 30 minutes followed by tempering at 1033 K for 60-90 minutes.

Table 2.1. *Chemical composition of the RAFM steels*

Steel	Element (wt%)										
	Cr	**C**	**Mn**	**V**	**W**	**Ta**	**N**	**O**	**P**	**S**	**Fe**
1W-0.06Ta	9.04	0.08	0.55	0.22	1	0.06	0.0226	0.0057	0.002	0.002	Bal.
1.4W-0.06Ta	9.03	0.126	0.56	0.24	1.38	0.06	0.03	0.002	<0.002	<0.001	Bal.
2W-0.06Ta	8.99	0.12	0.65	0.24	2.06	0.06	0.02	0.0024	0.002	0.0014	Bal.
1W-0.14Ta	9.13	0.12	0.57	0.22	0.94	0.135	0.033	0.0041	<0.002	0.0015	Bal.

2.3 Heat treatments

Specimens of ~10 x 10 x 10 mm were cut from the ‘as received’ (normalized and tempered) steel plates to carry out the heat treatments. Different sets of heat treatments using a muffle furnace were carried out for the four steels, details of which are presented in **Table 2.2**. Heat treatments were carried out in the uniform temperature zone of well calibrated furnaces with a temperature accuracy of ±5 K. For phase transformation studies with calorimetry reported in **Chapter 3**, steels of mass 50-100 mg and dimensions 2 x 2 x 2 mm were used.

2.4 Specimen preparation

Standard metallographic specimen preparation methods were employed for XRD studies, optical microscopy, Scanning Electron Microscopy and Hardness measurements. Flat surface was obtained by successive grinding with SiC abrasive discs, Further a mirror finish of the surface was obtained by polishing with 1 micron diamond paste with kerosene as the lubricant / coolant. The polished samples were etched with Villela’s reagent to reveal the microstructural features. Vilella’s reagent used for the sample preparation contained 1 g of picric acid and 5 ml of HCl in solution of 100 ml in methanol.

Table 2.2. *Heat treatment schedules used in the present study*

S. No	Theme	Chapters concerned	Heat treatment conditions		
			Temperature	**Holding time**	**Heating / Cooling rate**
1	$\alpha\leftrightarrow\gamma$ Transformation	3	RT- 473 K		5 K min^{-1}
			473-1473 K		1-99 K min^{-1}
			1473 K	15 minutes	
			1473 K- RT		1-99 K min^{-1}
2	Decomposition modes of γ	4	1253, 1323 and 1553K	30 minutes	WQ, AC, FC
3	Tempering kinetics	4	1253K	30 minutes	AC
			923, 973 and 1033 K	30 minutes to 10 h	AC
4	Microstructural changes on long term exposure	5	773, 823, 873 K (1W – 0.06Ta steel)	30 minutes to 10,000 h.	AC
			923 K	5,000 h and 10,000 h	

**WQ, AC and FC stands for water quenching, air cooling and furnace cooling respectively*

Two types of specimens were used for the TEM characterization of the steels namely thin foil and carbon extraction replica. To prepare thin foils, bulk samples were pre-thinned to about 100 μm, from which 3 mm discs were punched out. The punched discs were again ground to reduce the thickness to about 80μm, prior to electrochemical polishing, using a twin jet polisher "Struers Tenupole-5". 10 % perchloric acid in methanol was used as electrolyte for polishing at 238 K and 15 V.

Carbon extraction replica specimens were prepared from the metallographically prepared samples, to study the precipitate characteristics without matrix interference. Polished samples were very lightly etched with Vilella's reagent, followed by a thin carbon coating using BAL-TEC MED 020 coating system. The coating was extracted along with the precipitates attached to the carbon film from the bulk sample using the same etchant and collected over a copper grid. The film with the secondary phases was further studied in TEM.

2.5 Experimental techniques and analysis procedure

The steels were characterized by employing a variety of the techniques, which included X-ray diffraction (XRD), optical microscopy, Scanning Electron Microscopy (SEM), Transmission Electron Microscopy (TEM) and Mossbauer Spectroscopy. The phase transformation temperatures and enthalpy were measured by Differential Scanning Calorimetry (DSC). The operating conditions and procedure adopted for analysis for the techniques employed in the present study are given below:

2.5.1 X-ray diffraction

XRD spectra of the specimens were recorded with a Philips X'pert pro diffractometer in θ-2θ geometry, (θ range: 30-85^{o}) at room temperature, with Cu Kα as the incident radiation at a scan rate of 0.5°/ min. The intensity and 2θ values were calibrated with a standard pellet of powdered Si, prior to acquisition of the spectra on the specimens. Evaluation of microstrain was performed by measuring full width at half maximum (FWHM) of the predominant α-Fe peaks from the XRD spectrum. The equation used for the strain evaluation is given below

$$S = (\Delta FWHM / FWHM_{ref}) X\ 100 \qquad\text{-----------(2.1)}$$

where, ΔFWHM refers to the difference in FWHM value between the heat treated steel and reference, $FWHM_{ref}$ refers to that of normalized and tempered steel.

Synchrotron XRD experiments were carried out using Angle Dispersive X-Ray Diffraction (ADXRD) beamline (BL-12) at Indian Synchrotron Source (Indus 2), at RRCAT, Indore for the same samples. Monochromatic x-ray beam ($\lambda/\Delta\lambda$ = 8000 at

~8keV) of photon energy 13.081 KeV (λ=0.9478A°), photon flux (>10^9 photons/s) and beam size 300 x 300μm^2 was used. The high brilliance of synchrotron source compared to conventional source enabled the identification of minor phases like MX and $M_{23}C_6$, whose volume fraction is very low. In addition, with the area detector employed at synchrotron XRD, the integration of scattered intensity was for 15 minutes compared to laboratory source, where the integration is typically, for few seconds, which improved the signal to noise ratio. NIST LaB_6 powder was used for calibration of wavelength in transmission mode. The XRD pattern was recorded using thin foil specimen of thickness of about 0.08 mm in the transmission mode using MAR Research image plate (MAR 345 DTB). Image plate data was further processed with an automated software FIT2D [133] by integrating over full circle, to obtain the XRD spectrum. The center of the pattern has been fixed carefully to minimize the possible error. Phase identification was carried out by comparison with JCPDS data [134], within a $\Delta\theta$ ($\theta_{observed}$- $\theta_{expected}$) of 0.2°. Due to the fast saturation of the image plate with the major peaks of α-Fe and other experimental difficulties, only qualitative analysis of the ADXRD data was carried out.

2.5.2 Microscopy techniques

Operating conditions and analysis of different microscopy techniques namely optical microscopy, SEM and TEM are explained in the following paragraphs.

(a) Optical microscopy

Optical microscopy was carried out using Leica MeF4A optical microscope fitted with a Leica digital camera along with image analysis software Leica QWin and MW Workstation and Vicker's indentor. The magnification calibration of the objective lenses was carried out with a standard micrometer stage insert with 1000 lines / mm.

The RAFM steel consists of martensite / ferrite microstructure depending on the heat treatment condition. In this study, the grain size was measured using linear intercept method [135] using an automated Java based software, ImageJ® [136]. The standard deviation of several readings is taken as the error.

(a) Scanning Electron Microscopy

Scanning Electron Microscopy was carried out using a Philips XL-30 ESEM, on etched specimens for microstructural observations in the Secondary Electron (SE) and Back Scattered Electron (BSE) imaging modes. The magnification was calibrated with standard cross grating samples of 20 lines / mm and 2160 lines / mm. A standard sample with nanocrystalline oriented gold on holey carbon film with the separation between particles being of the order of 20 Å was used to perform the high resolution test. Accelerating voltage in the range of 20-30 kV and spot size ranging from 100 to1000 Å were used.

Energy dispersive analysis of X-rays was carried out using an Energy Dispersive Spectrometer attached to the SEM, for qualitative identification of elements with atomic number >10 or to establish relative changes in concentration level of any element across different regions. Energy calibration was carried out with pure elements with a detector resolution of 132 eV at Mn Kα.

(c) Transmission Electron Microscopy

TEM studies were carried out using a Philips CM200 Analytical Transmission Electron Microscope fitted with Oxford X-Max SDD detector for microstructural and microchemical analysis. The operating voltage used was 200 kV. The images were acquired by a bottom mounted on axis TVIPS CCD camera with a resolution of 2048 x 2048 pixels. Magnification calibration was carried out with a cross grating of 2160 lines/ mm with a separation of 469 nm between two lines. Camera length was calibrated with standard nanocrystalline oriented gold in holey carbon film at different accelerating voltages. The same standard sample was also used to perform the high resolution test with a line resolution of 2.3 Å. Analysis of selected area electron diffraction (SAED) or micro-diffraction patterns and dark field microscopy was carried out to identify the presence of different phases. An aperture of 10 µm size was used for obtaining the SAED pattern and dark field images. Rotation of SAED pattern with respect to magnification was calibrated using MoO_3 crystals. A spot size of ~50 nm was used to collect the characteristic X-rays from the constituent phases for determining the composition. A low background single tilt holder was used to reduce the noise due to spurious X-rays. In-hole spectra were collected periodically to ensure the absence of spurious X-ray sources in the column of the microscope. The conditions for acquisition of the EDS spectra are listed in **Table 2.3**. A large number of spectra were acquired from several regions of the specimen for a statistically meaningful analysis of the composition.

Thin foil TEM micrographs were used to measure martensite lath and subgrain width. Micrographs of carbon extraction replica of the sample were used for analyzing the frequency distribution of the precipitates as a function of size using automated image analysis software ImageJ. The size the precipitates is quoted in terms of the equivalent circle diameter (ECD), which was arrived at from the conversion of the measured projected area of the particle, based on the approximation of the particles being nearly globular. In all the steels, two types of precipitates MX and $M_{23}C_6$ were found, which were generally fine and coarse respectively. However, for analyzing the frequency distribution of the precipitates, no distinction between the two types of carbides could be made as the coarse ones highly dominated over the fine ones, which were few and sparsely distributed. The standard deviation of several readings is taken as the error. It is also to be mentioned that the error can originate from artifacts such as unextracted particles, agglomeration of two or more particles and orientation of the particle with respect to the beam direction. The volume fraction of the precipitates has been calculated based on area fraction analysis of a large number of regions from extraction replica samples. However, the error associated with this measurement of volume fraction was generally high, and over estimated due to the practical difficulties of extracting the precipitate from a single plane, but from different layers of the sample.

For indexing electron diffraction patterns, the angles and d-spacing were measured with an accuracy of <1° and 0.2Å respectively. The measured d-spacing values are compared with standard JCPDS data, the angle between the planes were calculated [134] and matched to the measured values.

Composition of $M_{23}C_6$ and MX phases with size ranging from 20 to 400 nm were determined using Analytical TEM. This method involved acquisition of Energy Dispersive X-ray (EDX) spectra from the respective phases from many regions (~ 30 – 40) in one or two samples. The performance of the equipment and the reliability of the measurements were monitored by the periodical checking of the energy calibration carried out with pure Al and Cu and the energy resolution with Mn Kα.

Composition analysis was carried out assuming the thin foil criterion based on the observation that the intensity difference was less than 10% between the in-hole spectrum and that on the specimen. For quantification purposes, only Fe Kα, Cr Kα, W Mα, Ta Lα and V Kα peaks were chosen as the Region of Interest (ROI) and quantified using the Cliff – Lorimer method [137]. The library values of Cliff – Lorimer constants, (i-e) K_{AB}'s were used for 200kV and verified for the correctness with samples of known composition. The following Cliff-Lorimer equation was used for quantification of the spectra.

$$\frac{C_A}{C_B} = K_{AB}\frac{I_A}{I_B} \qquad \text{----------------} \ (2.2)$$

where C_A and C_B refer to the concentration of elements A and B in the region of interest and I_A and I_B refer to their respective intensities in the X-ray spectrum. The conditions for acquisition and input parameters used for quantification of EDX spectra are listed in **Table 2.3**. One of the main sources of error is the acquisition time, which can be minimized by increasing the collection time. Therefore, a collection time of ~100s 'live time' was used. It is assumed that collection of the spectra is from within the beam size and volume of the sample encloses only the region of interest without overlapping of phases, though in some cases it was difficult to ensure this condition. The average composition of each type of precipitate was calculated from the average of about 30 measurements. The statistical error for 99% confidence limit in the compositional analysis was within ±3 wt%. The stoichiometry of the precipitates from the measured composition was arrived at based on the procedure detailed in [138].

Table 2.3. *Conditions for quantification of EDX spectra*

Parameter	**Value**
Operating voltage	200kV
Angle of tilt	30°
Beam diameter	30- 50 nm
Thickness of the sample	100 nm
Density	8.05 g/cc
Collection time	100 s

Orientation Imaging Microscopy (OIM) in TEM

To study the martensite characteristics in 1.4 W-0.06Ta steel normalized at 1253 K, automated orientation mapping experiments were carried out in TEM with an experimental setup and analysis software supplied by Nanomegas, Belgium. The conditions for acquisition of orientation maps are given in **Table 2.4.** The micro-diffraction patterns were acquired by scanning a precessing electron beam across the region of interest and recorded with an external camera fitted on the viewing screen of the TEM. Prior to acquisition of diffraction patterns of the sample, diffraction pattern from a standard [001] oriented gold specimen was used for the calibration of angle of precession and camera length. The distortion correction for the diffraction pattern collected by the off-axis tilted camera was carried out using a dewarping procedure. The area of the region of interest was calibrated with the image of the scanned region with the TVIPS camera. After the acquisition of the diffraction patterns, they were indexed with the templates generated for the expected phases with known crystallographic details like the lattice parameters and the space group. The reliability of the solution was ascertained with the cross correlation index and reliability values [139]. From the orientation maps generated, it was possible to derive phase map from the Euler angles of orientation of the constituent phases.

Table 2.4. *Conditions for acquisition of OIM maps*

Parameter	**Value**
Operating voltage	200kV
Precession angle	0.4°
Beam size	30-50nm
Condenser aperture size	50 μm
Diffraction pattern acquisition rate	25-30 frames per second
Camera length	12 to 17 cm
Magnification	8800 X

2.5.3 Mossbauer Spectroscopy

Mossbauer spectroscopy studies were carried out to identify the magnetic and nonmagnetic phases in 1.4W-0.06Ta steel normalized at 1253 K and also after tempering at 1033 K. Mossbauer spectrometer was operated in constant acceleration mode and in transmission geometry. ^{57}Co dispersed in Rh matrix with a specific activity of 50 mC has been used as the source. Each spectrum has been acquired in 1024 channels. Spectra were fitted to Lorentzian line shapes using a non linear least squares program to obtain hyperfine parameters such as isomer shift, quadrupole splitting and magnetic hyperfine fields experienced by relative fractions of distinct ^{57}Fe absorber atoms, based on which the phase fraction details were derived.

2.5.4 Differential Scanning Calorimetry

Differential Scanning Calorimetry (DSC) is a technique which measures the difference in heat flow between the sample and a reference material (usually an empty alumina crucible used as reference), when both are heated or cooled at a preset heating or cooling rate. The absorption or evolution of heat due to the phase change in the material induces a change in the differential heat flow between the sample and reference, which appears as an uncompensated temperature differential ΔT. Present study used Setaram® Setsys 1600 heat flux DSC, employing plate type DSC transducer [140] for all the experiments.

Determination of phase transformation temperature

Difference in ΔT mentioned above, associated with the thermal arrest results in a differential signal in the base line. A typical DSC signal obtained for α→γ transformation in RAFM steel is presented in **Figure 2.1** where Y-axis represents the difference in heat flow (μV) which is

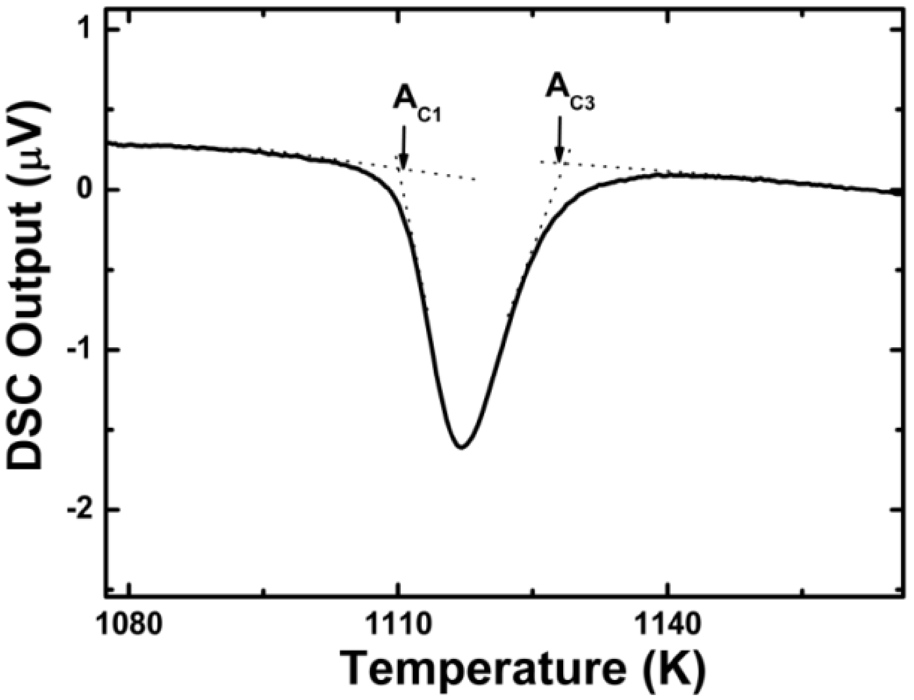

Figure 2.1. *Typical DSC thermogram for RAFM steel showing α→γ transformation*

the output of the instrument and X-axis represents temperature or time. To determine the phase transformation start (Ac_1) and transformation finish (Ac_3) temperatures, tangents to the baseline and from the inflection point of the peak are drawn and their intersection point is taken as the transformation temperature.

Determination of phase transformation enthalpy

An exothermic or endothermic peak is observed during phase transformation in a non-isothermal DSC experiment. The measured area of this signal is assumed to be directly proportional to the enthalpy change

$$\Delta H_{tr} = k(T) \times \text{Peak Area} \tag{2.3}$$

where, ΔH_{tr} is the enthalpy change accompanying phase transformation, k(T) is the temperature dependent calibration constant. The calibration constant k(T) is obtained by measuring the peak area recorded with the melting or fusion reactions of primary or secondary standards like pure aluminium, zinc, tin, copper and iron of known enthalpy

[141-144]. The sensitivity of calibration constant k(T) is influenced by many factors like the heating or cooling rate, the hydrodynamic nature of the ambience and the nature of calibrant which introduces error in the measurement. It is also desirable to employ a calibrant that has similar thermophysical characteristics as the alloy under investigation. Hence, pure Iron has been used as the calibrant for accurately characterizing the enthalpy effects of RAFM steel.

Uncertainty associated with the measured peak area also can give rise to error in the estimation of the enthalpy. This error arises due to the difficulty in unambiguously fixing the transformation start and finish temperatures. This situation arises due to the wrong selection of the base line, which in the present investigations is minimized by accurate baseline calibration. The baseline calibration is performed by subtracting a nil sample empty run signal from the actual run recorded with the sample in position. Also, identical pair of crucibles, gas flow rate and scanning rate conditions etc., are employed to minimize spurious factors from affecting the accuracy.

Temperature calibration

Temperature calibration has been carried out using the melting points of pure metals such as Al, Zn, Sn, Cu, Au and Fe standards [145]. The start temperature of melting is determined for different heating rates, and the result obtained was extrapolated to hypothetical cooling rate of 0 K min^{-1} to determine equilibrium onset temperature [145]. The values obtained are compared with the literature values in order to estimate the correction to be employed for obtaining the true transformation temperature. Temperature calibration of DSC for the cooling cycle is comparatively difficult due to varying degree of under cooling associated with the phase change; therefore the calibration is performed only for heating cycle.

2.5.5 Hardness Testing

Vicker’s hardness test was used, to evaluate the hardness of the steels after different heat treatments. Hardness measurements were carried out in a FIE VM-50 PC based Vickers hardness tester at a load of 10 Kg, which lies in the load independent region of the load vs diagonal length plot. Flat, polished samples with thickness greater than approximately 10 times the indentation depth were used for all measurements. A standard test block of known hardness with prescribed load of 10 Kg was used for calibration. Vickers Hardness number was evaluated after about 20 measurements on every sample to get reproducible and reliable values. The possible sources of error could be measurement error w.r.t diagonal length estimation, presence of more than one phase with different hardness within the volume of indentation. The scatter was found to be within ±5 HV 10.

Similar method is used to measure the microhardness of different phases in etched samples employing Leitz Miniload-2 microhardness tester at a load of 50 or 100 g depending on the grain size of the phase studied.

The operating conditions of different instruments employed in the present study are summarised in **Table 2.5**.

2.6. Simulation of Phase transformation / Phase fields

Thermocalc$^{®}$ and JMatPro$^{®}$ software are extensively used for the equilibrium and kinetic simulation of phases at different temperatures. Thermocalc$^{®}$ used TCFE6 database for the calculation of equilibrium phases that can co-exist at different temperatures. Thermocalc$^{®}$ also predicts the composition of different phases. The main disadvantage of the TCFE6 database is that, it does not take into account the addition of Ta content to the steel. However, based on the report by Prat et.al., [64] present calculation considered the substitution of Nb instead of Ta during the calculation. Thermocalc calculations did not consider the kinetic aspects of phase transformations.

Table 2.5. *Summary of the experimental techniques employed in this thesis*

Technique	Instrument	Operating conditions	Measurement performed
Optical Microscopy	Leica MEF4 A	Bright field	Prior austenite grain size
Hardness	FIE VM-50 PC based Vickers hardness tester	Load 10 Kg for 15 sec.	Vickers hardness number
	Leitz Miniload-2 microhardness tester	50 or 100 g depending on the experiment.	
Differential Scanning Calorimetry	Setaram® Setsys 1600heat flux DSC	Heating / cooling rate is mentioned in respective chapters	Transformation temperature and enthalpy
X-ray Diffraction	Philips X'pert pro	θ-2θ geometry, (θ range: 30-85^{o}); with Cu Kα radiation	Phase identification & Microstrain Analysis
	ADXRD at BL12	16 kV synchrotron radiation	
Mossbauer Spectroscopy	Wissel	Source: ^{57}Co dispersed in Rh in constant acceleration mode	Phase identification
Scanning electron microscopy	Philips XL-30 ESEM	Operated at 20 kV (SE and BSE detector)	Microstructural and microchemical characterization
Transmission electron microscopy	Phillips CM 200 ATEM with Oxford X-Max SDD detector	Operated at 200 kV	

JMatPro® uses a CALPHAD based internal database for the calculation of thermodynamic properties [62,63]. Present study used *'General steel'* module in JMatPro® version 7.0 for the thermodynamic calculations. Equilibrium calculations evaluated the properties such as stability regime of phases, phase fraction and the composition of phases in different temperature domains. The phases that can form during equilibrium conditions were carefully chosen based on the experimental data. The kinetic properties like CCT/ TTT diagram, precipitate evolution during tempering / thermal aging were predicted based on the Johnson-Mehl-Avrami equation [146]. It is important to mention that the kinetic simulation of the phases is largely influenced by the initial conditions of the alloy, which determines the microstructure. The inputs for the calculations were steel composition, temperature of austenitisation, PAGS and aging temperature. The selection of phases was not possible during kinetic simulation using JMatPro. A reasonable estimation of phase fraction for different conditions of heat treatment could be obtained. The result obtained was correlated with the experimental findings, wherever conditions were similar. It was noted the phase fraction obtained in different steels from the JMatPro calculations was in weight percentage for equilibrium simulations while it was volume percentage for the kinetic simulations.

CHAPTER 3

Phase Transformations In 9Cr RAFM Steels

3.1 Introduction

It is well known that the physical, mechanical and welding characteristics of a steel are largely dictated by the alloy content and the microstructure [124,147-149]. This essentially arises from the variety of phase transformations that the steel can undergo depending upon the thermal history and processing conditions. [59,150-152] High temperature austenite (γ) in martensitic steels undergoes transformation to martensite (α') or ferrite (α) + carbides depending on the austenitisation conditions such as temperature, soaking time and cooling rate. [147,153-155] Hence, it is essential to study the nature of phase transformations in the indigenously developed 9Cr RAFM steels and understand the influence of the alloying elements and process parameters on the transformation characteristics.

The present chapter describes the mechanism and kinetics of phase transformation and the crucial role of tungsten and tantalum on the above, when the steels are subjected to heating and cooling at various rates. Characterisation of microstructure by conventional metallography was carried out to support the results, which are discussed in the appropriate sections. In addition to the experimental studies, simulations have been carried out using JMatPro and Thermocalc software. The results in this chapter are presented in the following sequence.

The preliminary characterisation of 9Cr-W-V-Ta RAFM steels to understand the effect of solutionising temperature (T_s), and the cooling rate (β) on microstructure and to identify the critical cooling rate for martensitic transformation is given in **Section 3.2**. **Section 3.3** presents the results of a detailed study on various phase transformations in four steels using Differential Scanning Calorimetry (DSC). In **Section 3.4,** the kinetics of $\alpha \leftrightarrow \gamma$ transformations in 1.4W-0.06Ta steel (designated as INRAFM) are studied in detail by varying the heating and cooling rates. **Section 3.5** describes the results of equilibrium simulations of phase transformations using JMatPro and Thermocalc simulation software. The results of the equilibrium simulations and the empirically evaluated martensite start temperature (M_s) are compared with the experimental values. The summary of the findings is listed in **Section 3.6.**

3.2 Preliminary characterisation of RAFM steels

3.2.1 Effect of solution treatment temperature on microstructure of 9Cr -W-V-Ta steels

The microstructure of the ferritic – martensitic steels is dictated by the solution treatment temperature T_s and cooling rate. **Figure 3.1(a and b)** shows optical micrographs of 1W-0.06Ta steel, solutionised at 1253 and 1323 K respectively, followed by water quenching. A fully martensitic structure is observed suggesting a complete austenite phase (γ) at these temperatures. A similar observation was made with respect to 1.4W-0.06Ta, 2W-0.06Ta and 1W-0.14Ta steels. Evaluation of Prior Austenite Grain Size (PAGS) as a function of T_s showed a monotonic and significant increase for the four steels as seen from **Table 3.1.** This is in agreement with the expected enhanced diffusion of substitutional, interstitial solutes and also self diffusion of Fe in austenite with increase in temperature. At any T_s, the 1W-0.06Ta steel showed the highest PAGS, while 1.4W-0.06Ta, 2W-0.06Ta, and 1W-0.14Ta steels showed a lower grain size, which is attributed to the effective pinning of grain boundaries by the heavy solutes namely W and Ta.

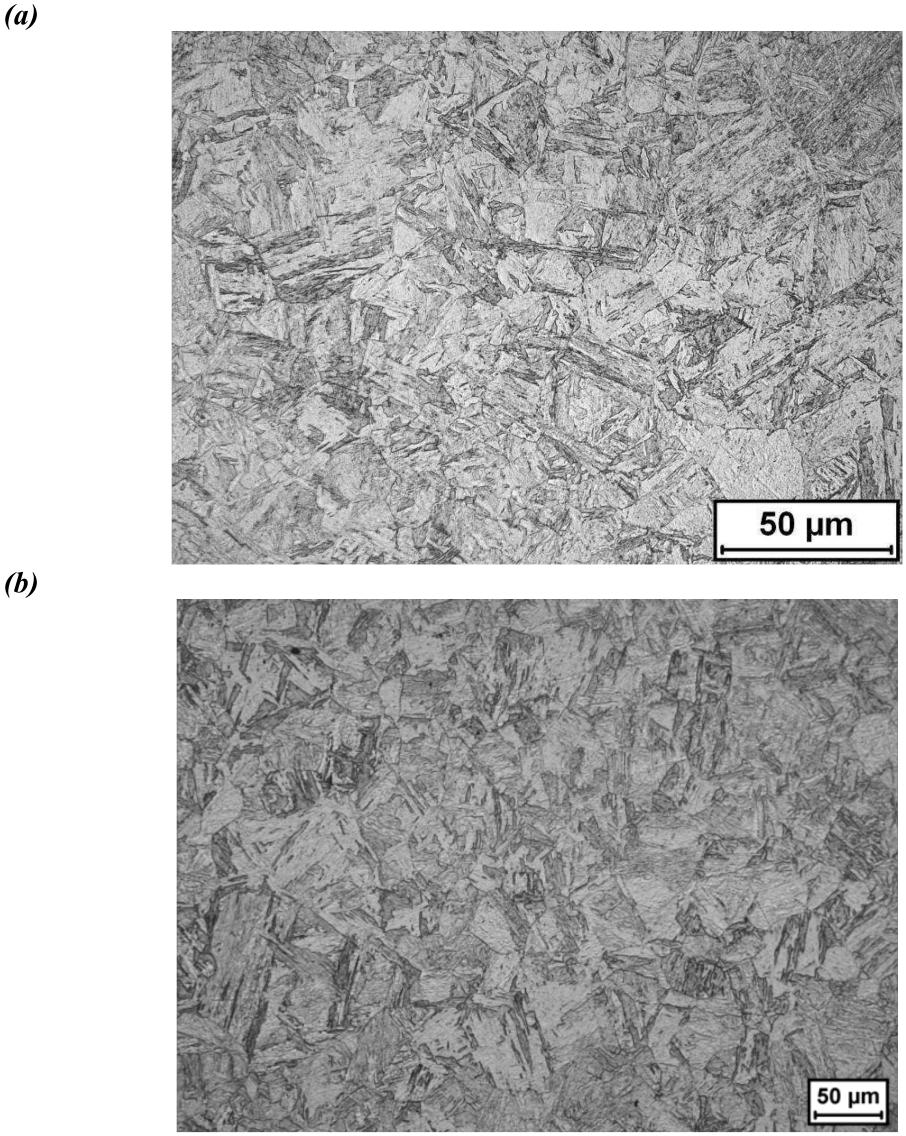

Figure 3.1. *Optical micrographs of 1W-0.06Ta steel showing martensite structure on quenching from (a) 1253 K (b) 1323 K*

Table 3.1. *Effect of austenitisation temperature on Prior Austenite Grain Size*

Steel	**PAGS ±4 (µm)**	
↓ T_s→	*1253K*	*1323K*
1W-0.06Ta	25	35
1.4W-0.06Ta	13	26
2W-0.06Ta	12	22
1W-0.14Ta	11	24

The Secondary Electron (SE) image in **Figure 3.2** shows the presence of coarse undissolved carbides (indicated by arrow mark) in 1.4W-0.06Ta steel solutionised at 1253K. These carbides restrict the γ grain growth by Zener pinning [156,157]. The number density of such undissolved carbides increased with W and Ta concentration of the steel, while it decreased with increase in T_s. In fact, the number density of undissolved carbides was very low even in the 2W-0.06Ta steel austenitised at 1323K. A detailed description of these aspects is provided in subsequent sections.

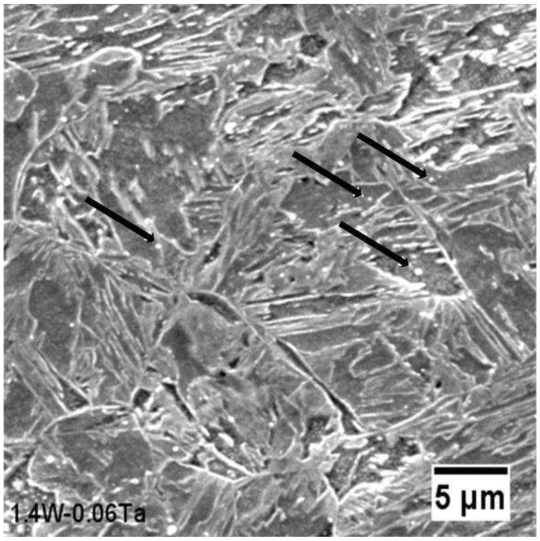

Figure 3.2. *SEM micrograph of 1.4W–0.06Ta steel solutionised at 1253 K showing martensite structure and undissolved carbides*

It is also to be noted that the C concentration of 1W-0.06Ta steel is only 0.08%, while the other two steels with higher W concentration possess a C concentration of 0.12%, which could also be responsible for the increased amount of carbides. Hence the decrease in PAGS of 1.4W-0.06Ta and 2W-0.06Ta steels is attributed to the combined effect of solute drag by heavy solutes and pinning due to undissolved carbides.

Figure 3.3((a) and (b)) shows microstructure of 1W–0.06Ta steel subjected to solution treatment at 1553 K followed by water quenching. A two phase structure is clearly

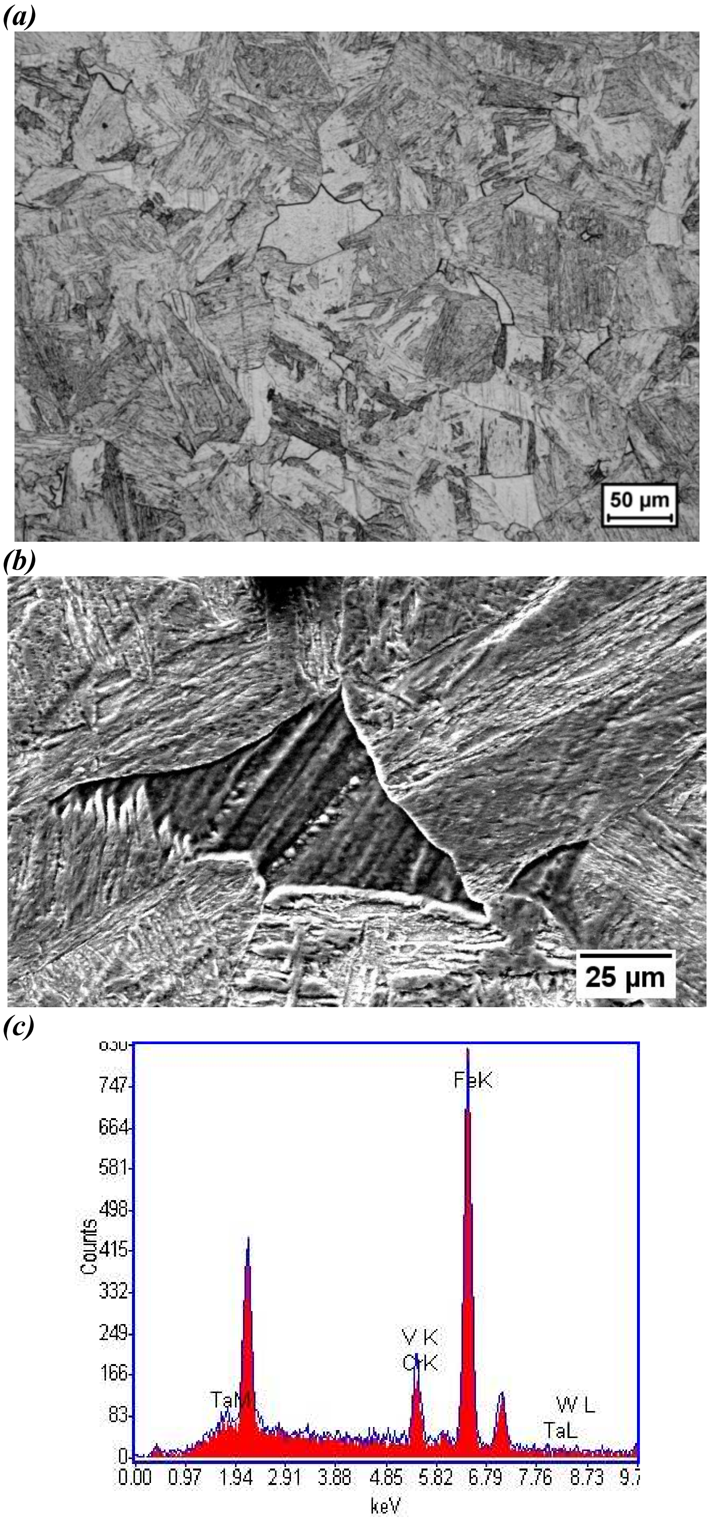

Figure 3.3. *(a, b) Microstructure of 1W-0.06 Ta steel solution treated at 1553 K showing α′ and δ ferrite (c) EDX spectra showing a higher enrichment of Cr in δ ferrite than α′*

observed with islands of lath free grains and grains with martensite substructure. The steel also showed a higher value of PAGS than at 1323 K. The hardness value measured (100 g load) in the two regions are 190 and 427 VHN respectively, which suggests the presence of ferrite in addition to martensite. The high cooling rate adopted precludes the formation of proeutectoid ferrite. Hence, these lath free grains should correspond to the high temperature δ–ferrite. The EDX spectra from the two regions are compared in **figure 3.3(c)**. The enrichment of Cr in the ferrite grains as compared to martensite confirms the repartitioning of Cr between δ and γ phases at 1553 K, which provides further evidence for the presence of δ-ferrite.

Based on the above preliminary results, it is clear that the α→γ transformation temperature is below 1253 K and that for γ→δ is below 1553 K. Detailed Differential Scanning Calorimetry studies have been carried out to determine accurate values of transformation temperatures, which is discussed in the next section (Section 3.3).

3.2.2 Effect of cooling rate on transformation of austenite in 9Cr-W-V-Ta steels

Austenite in ferritic steels can decompose into a variety of products such as martensite, bainite and pearlite depending on alloy composition and cooling rates. Parameswaran et al. [158], showed that the free energy of formation of bainite from austenite in 2.25Cr-1Mo is favourable during air cooling while it is not favourable in 9 Cr steels. The same studies have also reported that the driving force for formation of martensite is higher in 9Cr-1Mo as compared to 2.25Cr-1Mo steel during air cooling. The effect of cooling rate on microstructure has been predicted by JMatPro simulations and the simulated CCT diagram for 9Cr–1W–0.06Ta steel is shown in **Figure 3.4**. It is observed that the cooling curve corresponding to air cooling (~2K s^{-1}) lies above the nose of the C-curve for the formation of ferrite + carbides. It is recognized that JMatPro considers the formation of M_3C precipitate alone while calculating CCT diagram. Pearlite or bainite is not expected to form in this steel which contains carbide forming alloying elements.

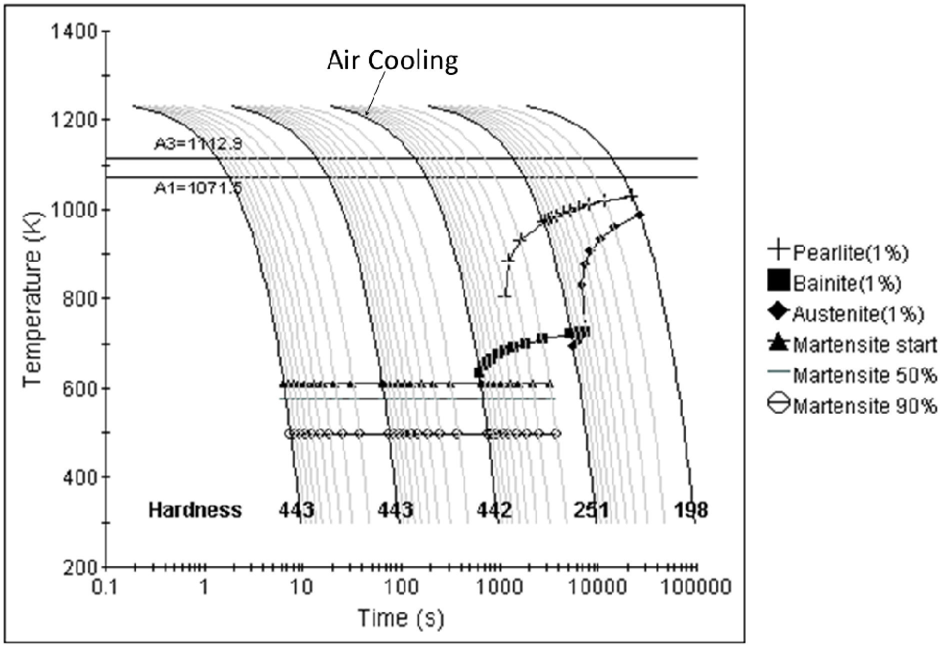

Figure 3.4. *Computed CCT diagram for 1W-0.06Ta steel austenitised at 1253K*

Figure 3.5 presents the microstructural variation in 1W-0.06Ta steel with cooling rate after solutionising at 1253K. It is observed that water quenching (**figure 3.5 (a))** and air cooling (**figure 3.5 (b)**) resulted in martensitic structure, while furnace cooling (**figure 3.5 (c)**) resulted in a mixed microstructure. For the furnace cooled steel, hardness values measured in the two phases are 200 and 430 VHN respectively. This indicates that the phases correspond to ferrite and martensite. The low cooling rate employed shows that it is proeutectoid ferrite that forms due to the diffusional transformation of austenite.

In order to study the effect of cooling rate the steels with higher W and Ta content were austenitised at 1253 and 1323 K, followed by air cooling and water quenching. It was observed that martensite was the resultant product of the athermal transformation of austenite under all these conditions. **Figure 3.6** presents the TEM thin foil micrographs

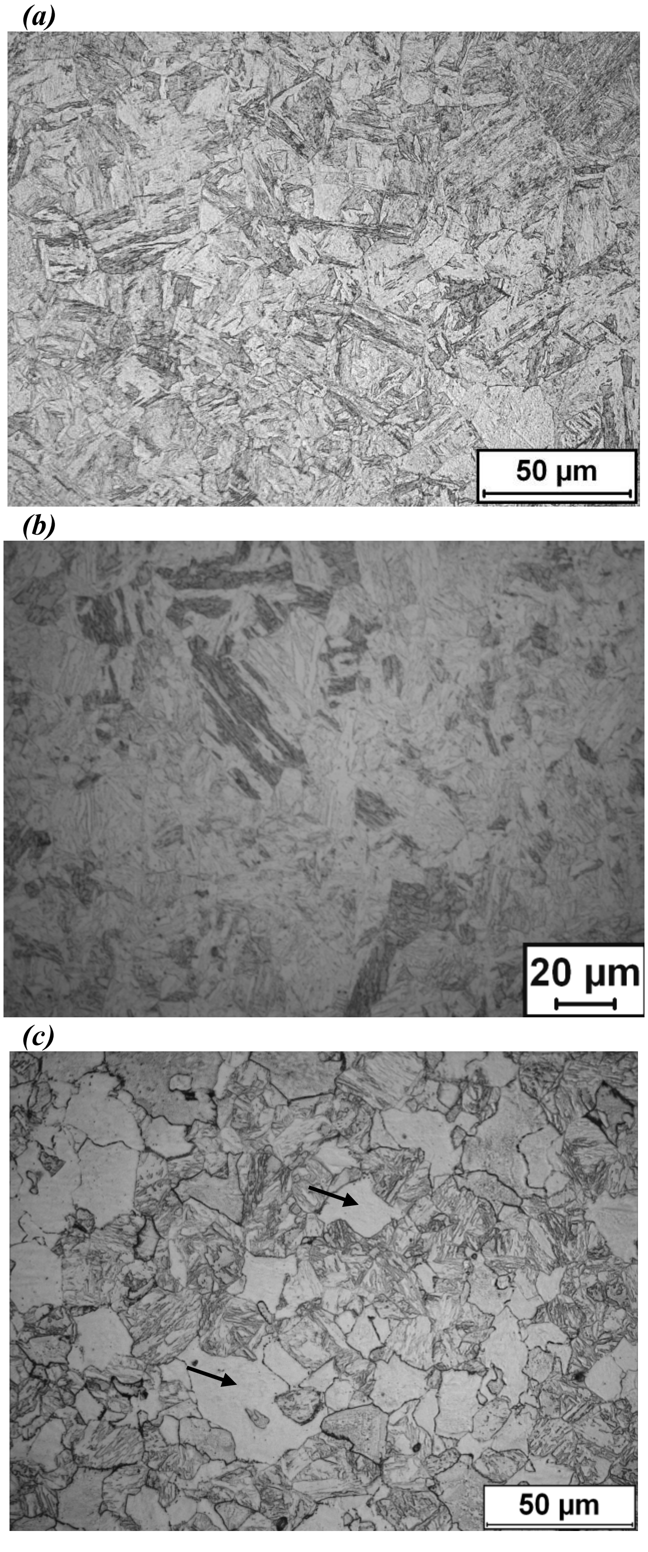

Figure 3.5. *Microstructure of 1W-0.06Ta steel austenitised at 1253 K after (a) water quenching, (b) air cooling showing full martensite structure and (c) furnace cooling showing mixture of α-ferrite (arrow marked) and martensite*

of all the steels normalised at 1253 K showing a martensitic lath structure, with a few undissolved carbides. The lath width was measured and found to be in the range of 250 – 400 nm. However, the average lath width was found to decrease from 400 to 250 nm as the W content increased from 1 to 2% W.

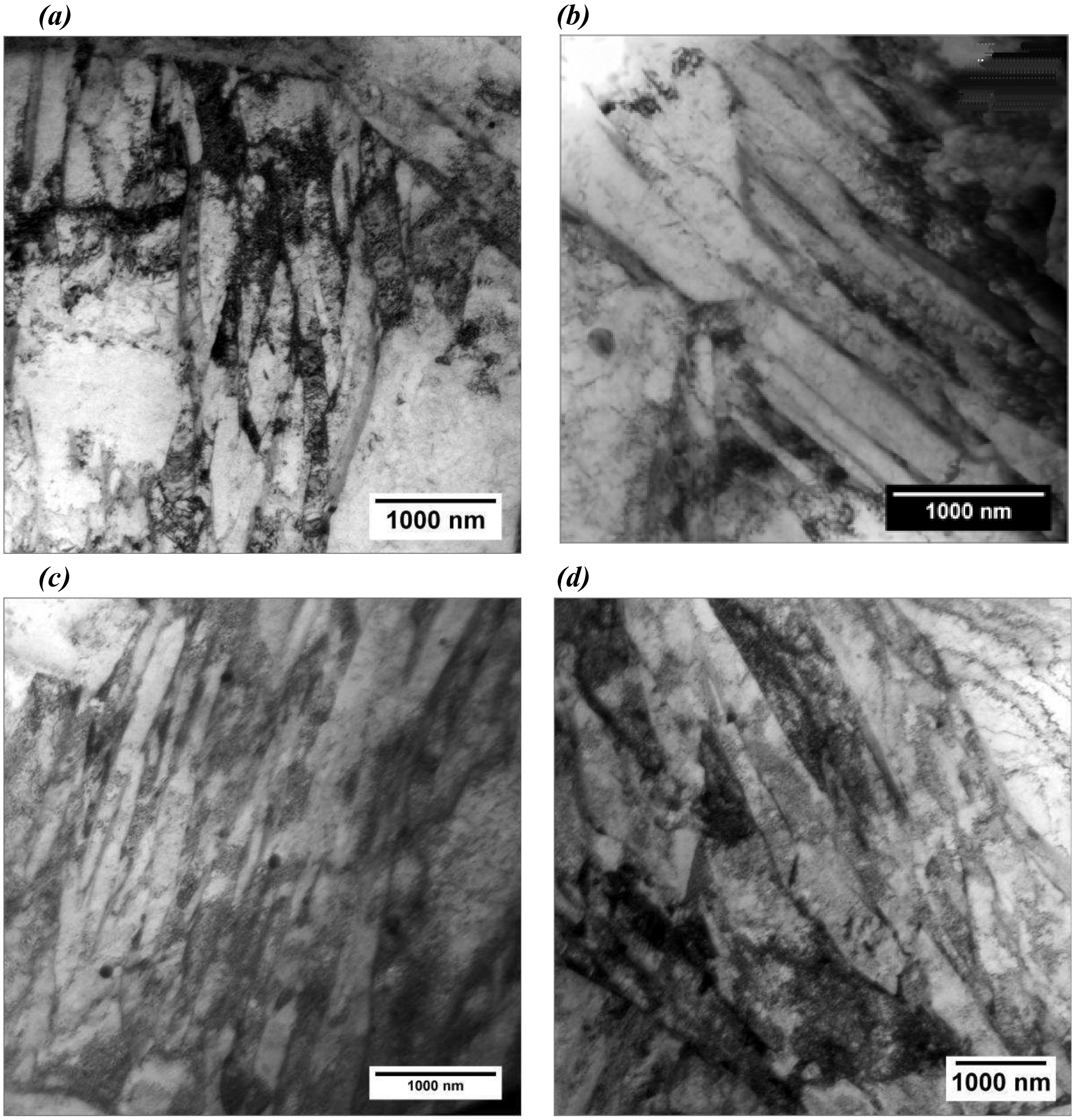

Figure 3.6. *Bright field TEM micrographs of steels normalised at 1253 K (a) 1W–0.06 Ta, (b) 1.4W-0.06 Ta, (c) 2W-0.06 Ta and (d) 1W-0.14 Ta steel, showing lath martensitic structure*

The average lath size of martensite in the 1W-0.06Ta steel was measured to be in the range of 400 nm and was found to decrease with increase in cooling rate. A similar observation was made for the other steels with higher W and Ta content, at both T_s. Thus high T_s and low cooling rate resulted in coarser laths, while finer laths were observed for low T_s and higher cooling rate. Such a decrease in lath width with increase in cooling rate or lower grain size is understood in terms of increased nucleation kinetics of martensite [159-163]. The decrease in lath width of martensite in steels with higher W, Ta and C content for any cooling rate from γ phase field is attributed to decrease in PAGS.

The above changes in microstructural parameters also manifested in the variation of hardness of the steel under different austenitisation conditions, which is listed in **Table 3.2**. It is observed that a lower T_s and a higher cooling rate has resulted in the highest hardness in all the steels, as expected due to the finer PAGS and lath size. On the other hand, the hardness of martensite for a high cooling rate decreases with increase in PAGS. It is observed that the hardness of 1.4W – 0.06Ta steel is higher than that of other steels at all conditions of austenitisation and cooling, which can be attributed to the solid solution strengthening due to W and C. However, the decrease of hardness of 2W – 0.06Ta steel compared to that of 1.4W – 0.06Ta steel with the same C content, could only be attributed to the increased number of coarse undissolved carbides, which overrides the solid solution strengthening effect of W.

These studies show that the four steels with different W and Ta content are air hardenable. Further studies have been carried out to understand the effect of cooling rate and alloy content on martensite transformation kinetics, which will be discussed later in this chapter.

Table 3.2. *Variation of hardness with austenitisation conditions*

Steel	**Hardness ±5 (HV 10)**			
Condition	***1253K(AC)***	***1253K(WQ)***	***1323K (AC)***	***1323K (WQ)***
1W-0.06Ta	363	416	352	415
1.4W-0.06Ta	417	483	420	445
2W-0.06Ta	406	476	400	443
1W-0.14Ta	399	472	405	435

It is observed that the normalised steels have high hardness due to the martensite structure. It is well known that the martensitic steels are tempered to obtain good toughness. Therefore the steels used for this study were tempered at 1033 K for 1 h. This is the tempering adopted in industrial practice and the microstructural characterisation of the normalised and tempered steel is presented below.

3.2.3 Microstructural characterisation of normalised and tempered RAFM steel

The starting samples for the DSC studies were drawn from normalised and tempered steels with W and Ta content varying from 1 – 2 wt. % and 0.06 – 0.14 wt. % respectively. The phases present in the normalised and tempered RAFM steels have been identified using Angle Dispersive X-ray Diffraction (ADXRD). **Figure 3.7 shows the** room temperature XRD profile for four steels. Analysis of the XRD pattern revealed the presence of α- ferrite, $M_{23}C_6$ and TaX phase in the steel. The formation of VX type of precipitate could not be unambiguously confirmed due to the overlap of the VX peak with that of $M_{23}C_6$. Analysis of the results is tabulated in **Table 3.3**. The lattice parameter calculated using Nelson – Riley function [164] for each phase did not show considerable variation with W and Ta content, in the tempered steels.

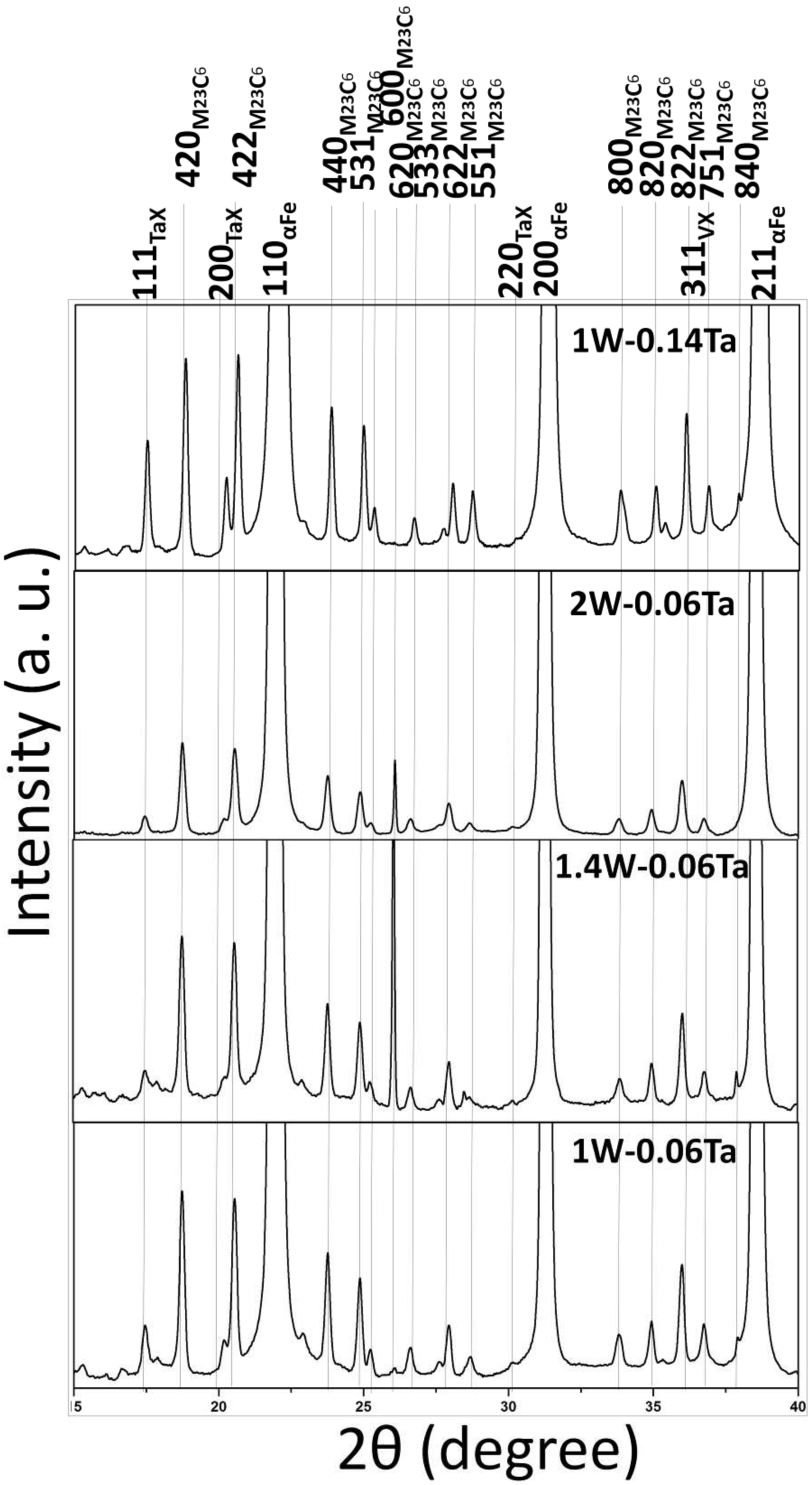

Figure 3.7. *ADXRD patterns for normalised and tempered steels obtained from synchrotron radiation source, showing the presence of α-Fe, $M_{23}C_6$ and TaX phases.*

Table 3.3. *Lattice parameter of different phases investigated by ADXRD analysis*

Steel	**1W-0.06Ta**			**1.4W-0.06Ta**		**2W-0.06Ta**		**1W-0.14Ta**	
Phases detected	a (Å)	hkl	d (Å)	a (Å)	d (Å)	a (Å)	d (Å)	a (Å)	d (Å)
α-Fe	2.88	110	2.0259	2.88	2.0248	2.87	2.0278	2.87	2.0271
		200	1.4351		1.4358		1.4339		1.4343
		211	1.1717		1.1720		1.1713		1.1711
$M_{23}C_6$	10.65	420	2.3668	10.73	2.3660	10.64	2.3702	10.69	2.3692
		422	2.1612		2.1598		2.1640		2.1638
		531	1.7919		1.8736		1.8751		1.8740
		600	1.7664		1.7923		1.7926		1.7913
		620	1.6723		1.6810		1.6756		1.6705
		622	1.5993		1.6034		1.6003		1.5978
		800	1.3271		1.3282		1.3272		1.3305
		662	1.2234		1.2232		1.2189		1.2215
		822*	1.2559		1.2557		1.2523		1.2543
Ta(C,N)	4.46	111	2.529	4.49	2.5253	4.44	2.5380	4.43	2.5448
		200							2.2048
		220							1.5616
		311	1.3308		1.3339		1.3300		1.3305
		222	1.2792		1.2827		1.2793		1.2761
V(C,N)	4.18	311*	1.2618	4.14	1.2503	4.14	1.2499	4.14	1.2497

*Identified peak for V(C,N) is overlapping with the (822) Peak of $M_{23}C_6$

Figure 3.8(a) shows the bright field thin foil micrograph of normalised and tempered 1.4W-0.06Ta steel, clearly revealing the presence of lath martensitic structure along with precipitates. The micrograph presented in **figure 3.8 (a, b)** shows the presence of coarse interlath and fine intralath precipitates. The SAED patterns obtained from the two types of precipitates are shown in **figure 3.8 (c and d)**. Analysis of the SAED

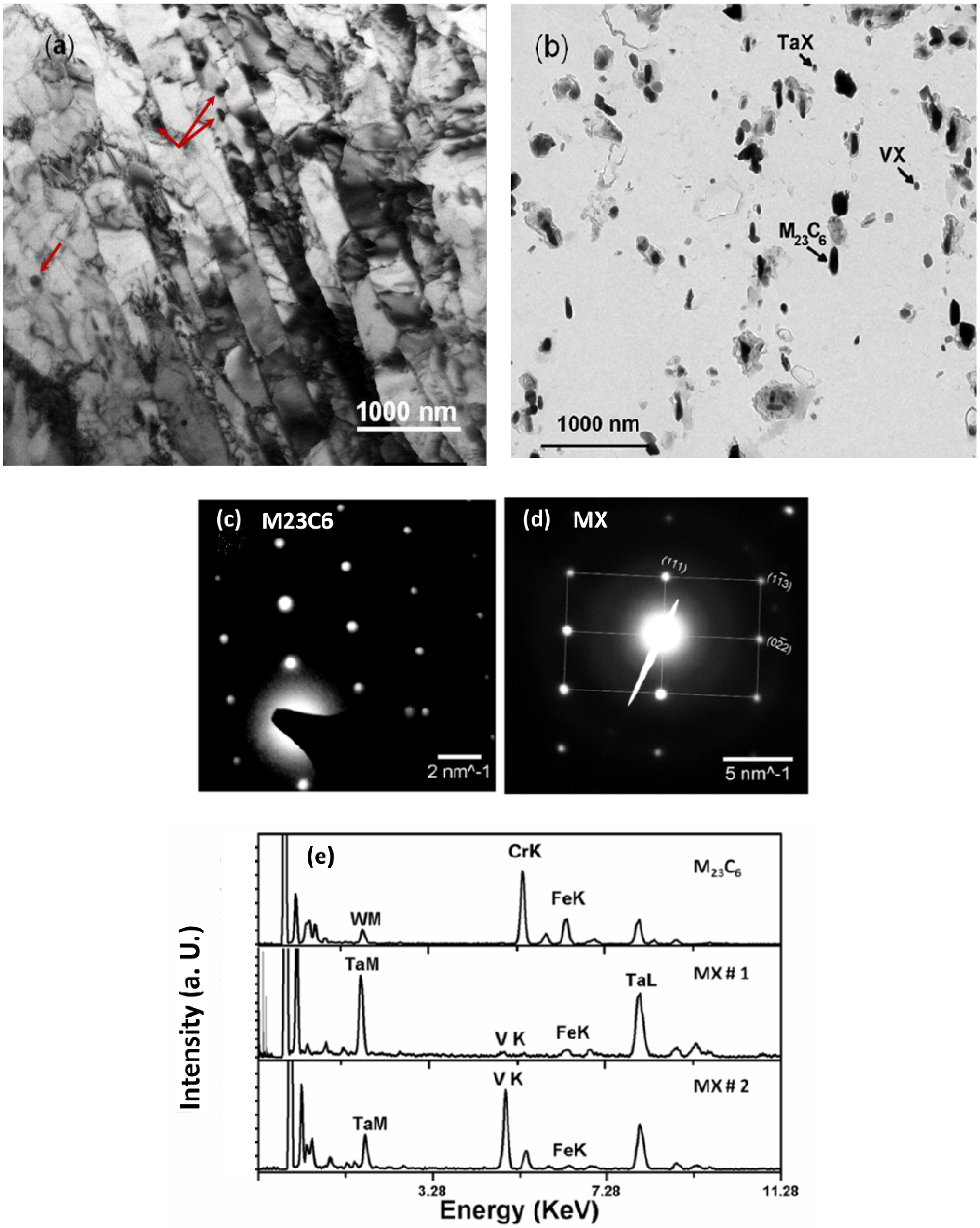

Figure 3.8. *(a) Bright field transmission electron micrograph of normalised and tempered 1.4W-0.06Ta steel showing martensitic lath structure; arrows point to intra-lath and lath boundary precipitates; (b) Carbon extraction replica micrograph of the same steel showing the distribution of precipitates; (c, d) SAED patterns to identify* $M_{23}C_6$ *and MX carbides; (e) EDX spectra obtained from* $M_{23}C_6$ *and two types of MX precipitates.*

patterns confirmed the presence of $M_{23}C_6$ and MX type of precipitates. The EDX spectra in **figure 3.8(e)** shows that the interlath $M_{23}C_6$ was Cr rich with solubility for Fe and W, while solubility for V was also observed in few cases. Formation of MX precipitates with two types of composition is evident from the EDX spectra, one type being V rich with considerable solubility for Ta and the other Ta rich with negligible solubility for V and Fe. It is obvious that the precipitation of $M_{23}C_6$ and MX carbides depletes the solute atoms from the ferrite matrix, although the presence of fine precipitates contribute to the strength of the steel.

The other three steels also showed similar features though minor variations in microstructure and microchemistry of precipitates was observed, the details of which will be discussed in **Chapter 4**.

3.3 Phase transformations in 1.4W – 0.06Ta (INRAFM) steel

A typical DSC thermogram for 1.4W – 0.06Ta steel for a slow heating and cooling rate of 3 K min^{-1} is presented in **Figure 3.9**. The following transformation sequence was observed during heating.

α*-ferrite (ferromagnetic)* + $M_{23}C_6 + MX \rightarrow$ α*-ferrite (paramagnetic)* + $M_{23}C_6 + MX \rightarrow$ γ*-austenite* + $M_{23}C_6 + MX \rightarrow \gamma + MX \rightarrow \delta + \gamma + MX \rightarrow \gamma + \delta \rightarrow \gamma + \delta + L \rightarrow \delta + L \rightarrow$ *Liquid*

On slow cooling, the reverse transformation was observed. Transformation temperatures were also found to be a function of heating and cooling rates.

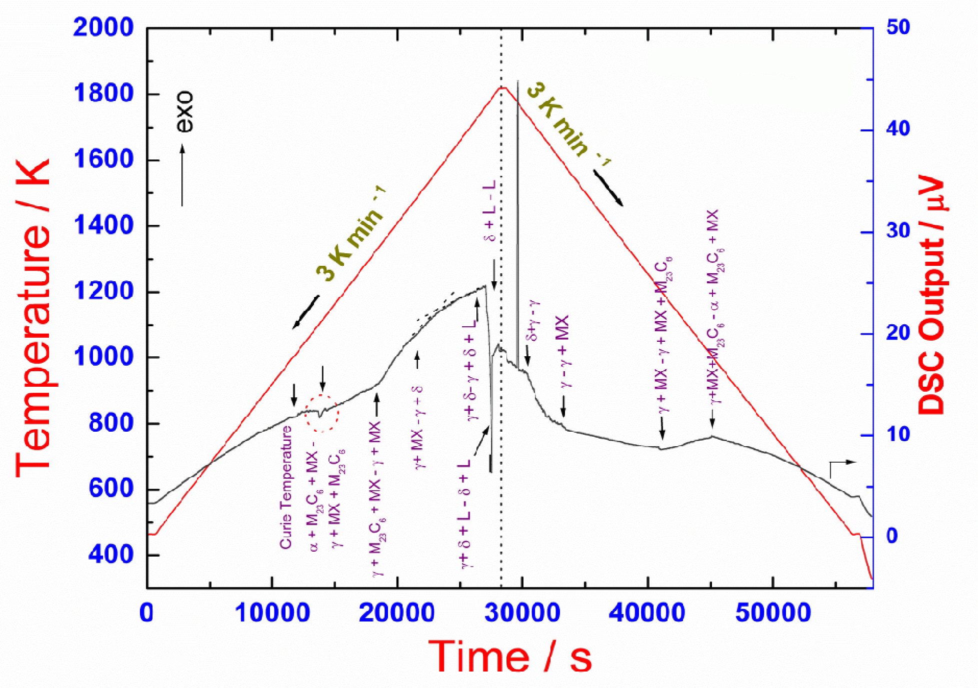

Figure 3.9. *DSC profile for 1.4W-0.06Ta steel showing the transformation sequence during heating and cooling at the rate of 3 K min^{-1}*

3.3.1 α→γ transformation on heating

An expanded view of **Figure 3.9** is presented in **Figure 3.10(a)** representing the on heating transformation profile for 1.4W-0.06Ta steel. The various transformations and the corresponding temperatures obtained for a heating rate of 3 K min^{-1} are elaborated below –

i. *α-ferrite* (ferromagnetic)+$M_{23}C_6$+MX → *α-ferrite* (paramagnetic)+$M_{23}C_6$+MX; T_c =1027 ± 5 K

ii. *α-ferrite* (paramagnetic) + $M_{23}C_6$ + MX → *α-ferrite* + $M_{23}C_6$ + MX + γ-*austenite;* Ac_1 = 1091 ± 5 K

iii. *α-ferrite* + $M_{23}C_6$ + MX + γ-*austenite* → $M_{23}C_6$+ MX + γ-*austenite;* Ac_3 = 1130 ± 5 K

iv. $M_{23}C_6$+ MX + γ-*austenite* → γ-*austenite* + MX; $T_{d,\ M23C6}$ = 1342 ± 5 K (T_d –Dissolution temperature)

v. γ-*austenite* + MX → δ-*ferrite* + γ-*austenite* + MX ; 1494 ± 10 K

vi. γ-*austenite* + δ-*ferrite* + MX → γ-*austenite* + δ-*ferrite;* $T_{d,\,MX}$= 1563 ± 5 K

vii. γ-*austenite* + δ-*ferrite* → γ-*austenite* + δ-*ferrite* + Liquid*;* 1762 ± 5 K

viii. γ-*austenite* + δ-*ferrite*+ Liquid → δ-*ferrite* + Liquid; 1767 ± 15 K

ix. δ-*ferrite* + Liquid → Liquid; T_L= 1791 ± 15K

It is to be noted that the dissolution of $M_{23}C_6$ and MX was not complete below Ac_3 for this steel. Considerable amount of super heating above Ac_3 is essential for the complete dissolution of $M_{23}C_6$ and MX precipitates. Thus, the dissolution reactions of both $M_{23}C_6$ and MX in γ-austenite are decided more by kinetics, that is, the diffusional mobility of substitutional solutes like, Cr, W, Ta and V in γ-austenite. An important point to be noted from the above mentioned transformation sequence is that the existence of a three phase domain (γ-*austenite* + δ-*ferrite* + Liquid) between 1762 and 1767 K. The width of the transformation (ΔT) in practice will be a function of W content. **Figure 3.10(b) and (c),** shows the expanded views of the same graph around α+carbides→γ transformation region and melting respectively. The transformation enthalpy was found to be 21.3 and 318 J g^{-1} for α + carbides → γ transformation and melting respectively.

A comparison of transformation temperatures for the four steels is presented in **Table 3.4**. A mild increase in Ac_1 with increase in W from 1.4 to 2 % is evident from **Table 3.4**. These findings are in reasonable agreement with the results obtained by Brachet et al. [60]. The reason for the observed increase in Ac_1 is attributed to the increase in the ferrite stabilisers (W and Ta) in the composition of steel. However, as mentioned earlier, it should be noted that the C content of 1.4W-0.06Ta steel is higher (0.12%) compared to that of 1W-0.06Ta steel (0.08%), which could be responsible for the observed decrease in Ac_1 despite the increase in W content. A similar argument holds good for the steel with higher Ta content also (1W-0.14Ta steel). Further there was a considerable increase in the solidus temperature of the steel. The enthalpy of transformations did not show considerable change with W and Ta.

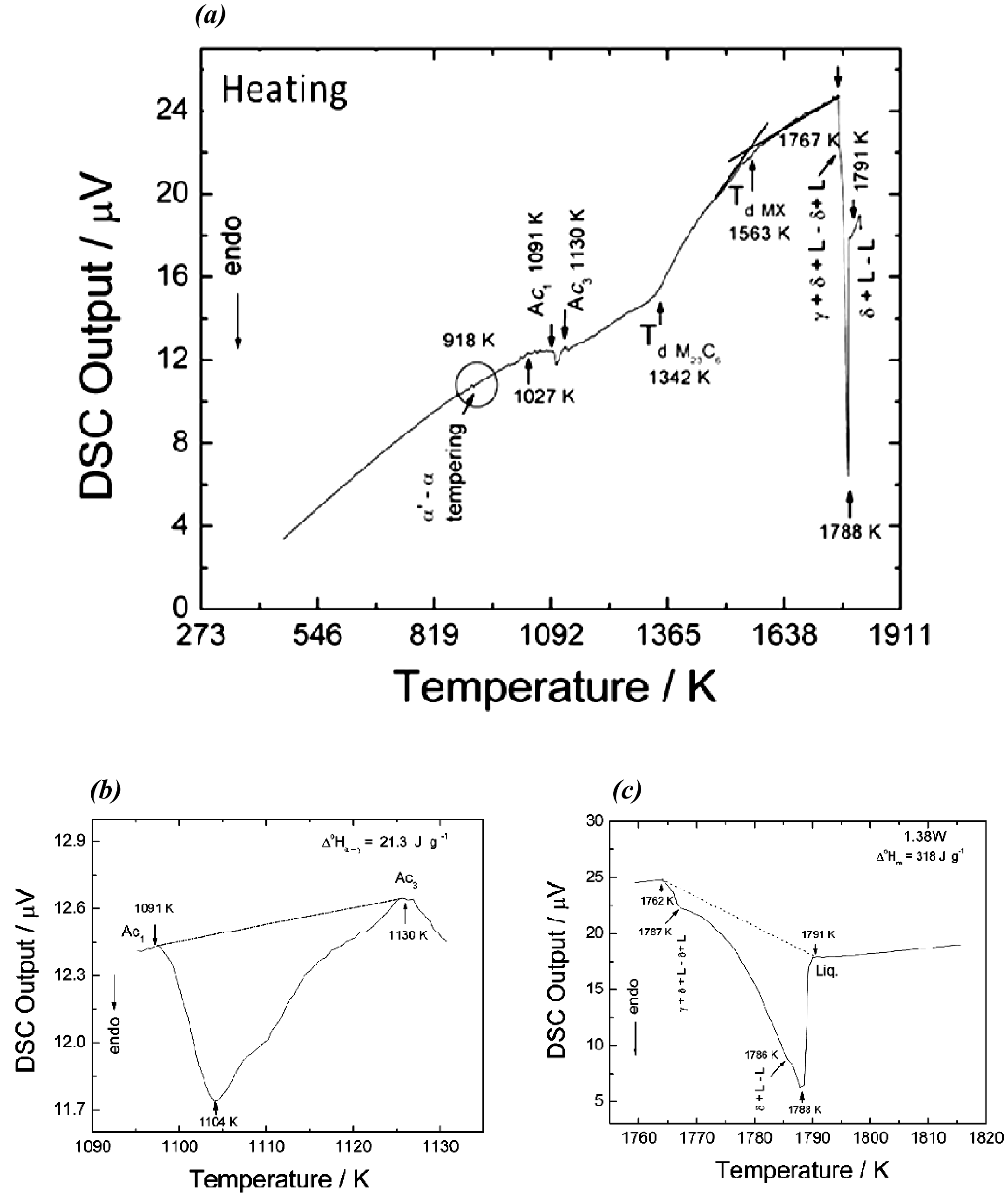

***Figure 3.10**. (a) DSC profile of 1.4W -0.06Ta steel showing the transformation sequence during heating (b) expanded view of thermal arrest from α→γ transformation regime, (c) melting regime.*

Table 3.4. *Transformation temperatures of RAFM steels at a heating rate of at 1 K min*$^{-1}$

Description of phase change	**Transformation Temperature (K)**			
	1W-0.06Ta	**1.4W-0.06Ta**	**2W-0.06Ta**	**1W-0.14Ta**
α' (martensite) → α (ferrite)+ $M_{23}C_6$	937±5	918±5	917±7	919±4
T_C,*Curie temperature*	1018±5	1027±5	1025±5	1024±5
$\alpha + MX + M_{23}C_6 \rightarrow \alpha + \gamma + MX + M_{23}C_6$ (Ac_1)	1104±5	1091±5	1108±5	1086±5
$\alpha + \gamma + MX + M_{23}C_6 \rightarrow \gamma + MX + M_{23}C_6$ (Ac_3)	1144±5	1130±5	1135±5	1114±5
$\gamma + MX + M_{23}C_6 \rightarrow \gamma + MX$ *$M_{23}C_6$ dissolution*	1350±5	1342±10	1342±10	Not very clearly detected
$\gamma + MX \rightarrow \delta + \gamma + MX$ *δ-ferrite formation*	1575±5	1494±10	1499±10	1495±10
$\delta + \gamma + MX \rightarrow \delta + \gamma$ *MX dissolution*	1581±15	1563±15	1570±15	1565±15
δ+ γ → Liquid + γ+δ *(solidus)*	1730±15	1762±15	1788±15	1784±15
Liquid + γ +δ → Liquid + δ	1753±15	1767±15	1791±15	1792±15
Liquid + δ → Liquid *(liquidus)*	1805±15	1791±15	1794±15	1796±15
$\Delta^{o}H_f$, enthalpy of melting(J g^{-1})	364±25	318±25	357±25	343±25
$\Delta^{o}H_{\alpha\ \gamma}$, (J g^{-1})	14±5	14±5	13±5	16±5

3.3.1.1 Microstructural analysis of samples subjected to DSC

Post-calorimetry samples quenched from different phase field domains revealed interesting microstructural features at various stages of transformation. The metallographic examination of the samples cooled from different phase field domains is presented in **Figure 3.11**. Optical micrograph (**figure 3.11(a)**) of slow cooled specimen (1 K min^{-1}) from the melt showed the development of coarse grains of *α*-ferrite. It is speculated that few large carbides (indicated by arrows) embedded in it and also few smaller ones dispersed in the matrix could be present but has not been confirmed. There

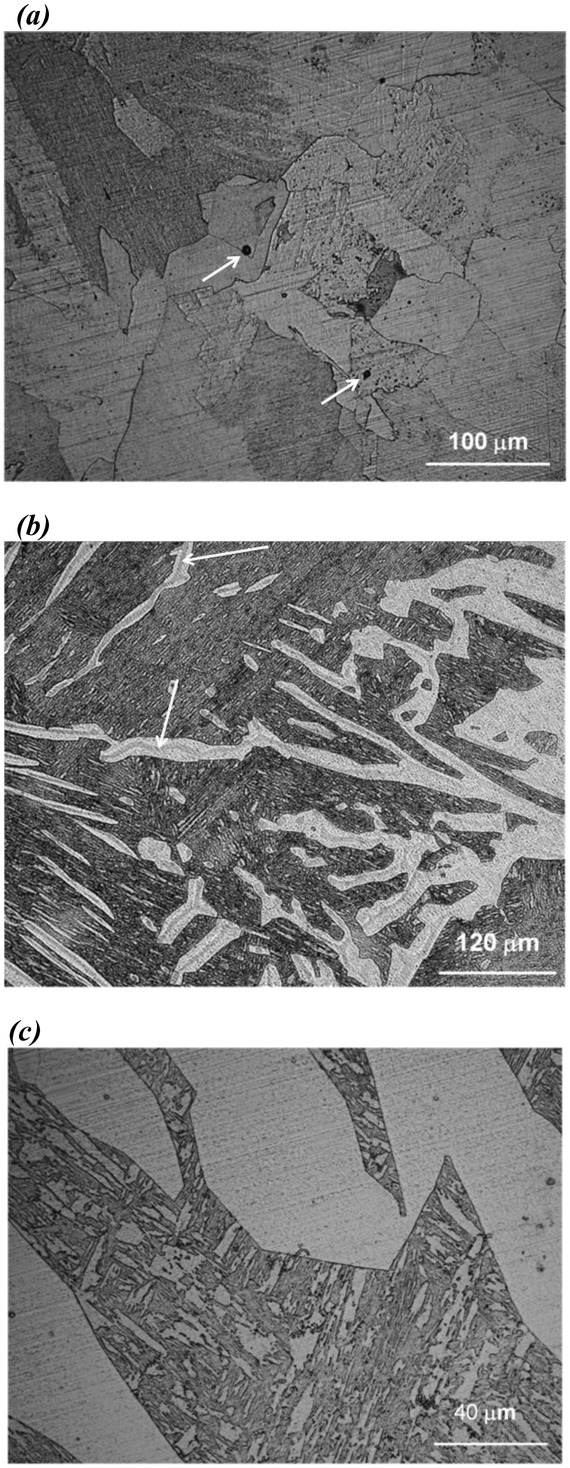

Figure 3.11 *Microstructure of 1.4W-0.06Ta steel cooled from (a) liquid at 1 K* min^{-1} *showing coarse grains; (b) Liquid to* $L+\delta$ *region at 1 K* min^{-1} *and quenched to room temperature showing* $\delta+\alpha'$ *structure; (c) intercritical zone at 99 K* min^{-1} *showing* α' *and untransformed* α

was no evidence for the formation of martensite (α') in slow cooled specimens, suggesting the formation of complete diffusional *α*-ferrite phase. Microstructural features observed in slow cooled DSC sample (1 K min^{-1}) from the liquid up to the L+δ region, held there for a minute and quenched thereafter at 99 K min^{-1} is presented in **figure 3.11(b)**. It is interesting to note the development of long interdendritic channels of the solid phase first to form from liquid, namely the nonmagnetic δ-ferrite (white etching feature in **figure 3.11(b**). But the observed segregation tendency in and around the δ-channels is found to be more remarkable; a distinct midrib like feature (indicated by arrows) running all along the length of δ-phase dendrites and further accompanied by a gradual gradient in the grey-level contrast in the surrounding region. This suggests that the formation of δ-ferrite upon slow cooling is accompanied by considerable partitioning of solute elements, notably W in this case, to the growing solid. This segregation would leave the remaining liquid suitable for the formation of γ-austenite. Although it would be useful to investigate the solidification morphology as a function of cooling rate, to understand about the extent of segregation taking place during solidification reaction, it has not been included as it is beyond the scope of this work. **Figure 3.11(c)** presents the microstructure of the sample cooled from T= 1100 K, that is in the intercritical zone ($Ac_1 \leq T \leq Ac_3$), at 99 K min^{-1} to room temperature. The presence of two phase microstructure consisting of *α′*-martensite and untransformed *α*-ferrite is observed.

3.3.1.2 Effect of prior microstructure on α→γ transformation

The transformation temperatures Ac_1 and Ac_3, especially Ac_3 are reported to be sensitive to the starting microstructure. In order to study this, the transformation temperatures of the N&T steel have been compared with those obtained from the steel with different microstructures mainly consisting of different amount of $M_{23}C_6$ precipitates, typically studied in the 1W- 0.06Ta steel. These microstructures were obtained by long term thermal exposure of the steel at 773 and 873 K for durations ranging from 30 minutes to 5000 h. The details of the microstructural evolution due to aging are presented in **Chapter 5**. The effect of aging on microstructure and its consequence on the α→γ transformation was studied by DSC employing a heating rate of 10 K min^{-1}. **Figure 3.12** presents the variation of the α→γ transformation temperature for 1W-0.06Ta steel after thermal exposure at 773 and 873 K. It is observed that Ac_1 did not show any significant variation, while Ac_3 showed a minor increase with exposure time. The increase in Ac_3 in the present case is due to the depletion of carbon in the matrix caused by the undissolved carbides. This arises due to the precipitates in the aged steel, whose dissolution kinetics is slow. It is well known that the amount, size and chemistry of $M_{23}C_6$ precipitate vary with aging time, particularly the increase in Cr and W in 9Cr steels [165]. The sluggish diffusion of alloying elements (Cr and W) slows down the dissolution of these precipitates during heating to γ phase field. It is also known that (**table 3.4**) that the complete dissolution of $M_{23}C_6$ occurs at temperature higher than Ac_3. The delay in C release to the matrix increases as a result of precipitate evolution during aging. This causes the Ac_3 to increase as the extent of aging increases in the starting structure for calorimetry studies.

3.3.2 γ → α transformation on cooling

The DSC profile for 1.4W–0.06Ta steel, slow cooled (1 K min^{-1}) from liquid phase is presented in **Figure 3.13**. The transformation sequence observed during heating is duplicated during cooling. However, there is a considerable degree of undercooling effect noticed in the case of solid state transformations, such as precipitation of cubic MX and $M_{23}C_6$ secondary phases, and the diffusional formation of α-ferrite from γ.

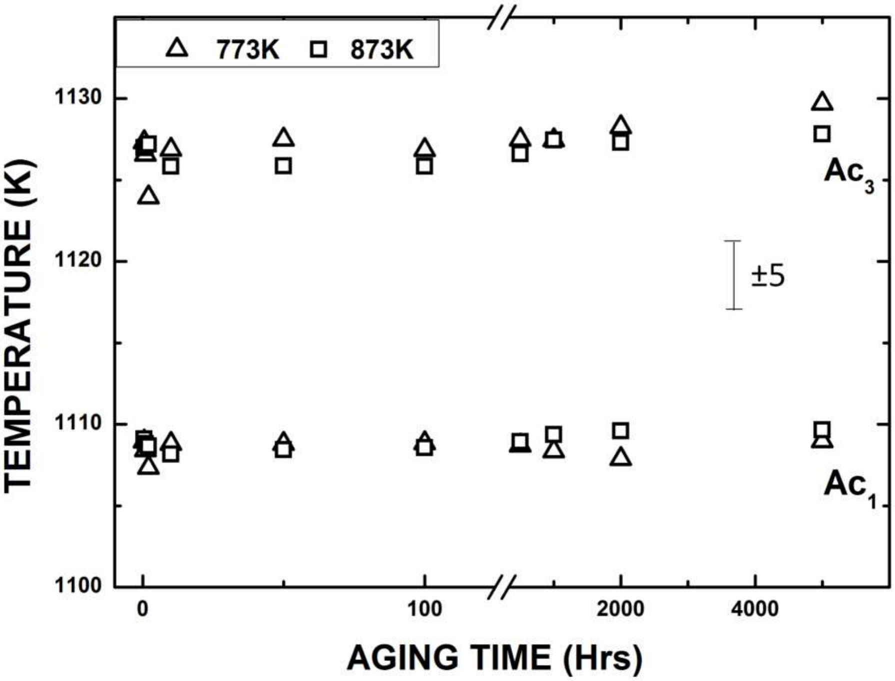

Figure 3.12. *Variation of Ac_1 and Ac_3 for 1W-0.06 Ta steel after aging at 773 and 873 K showing a small increase in Ac_3 with aging time.*

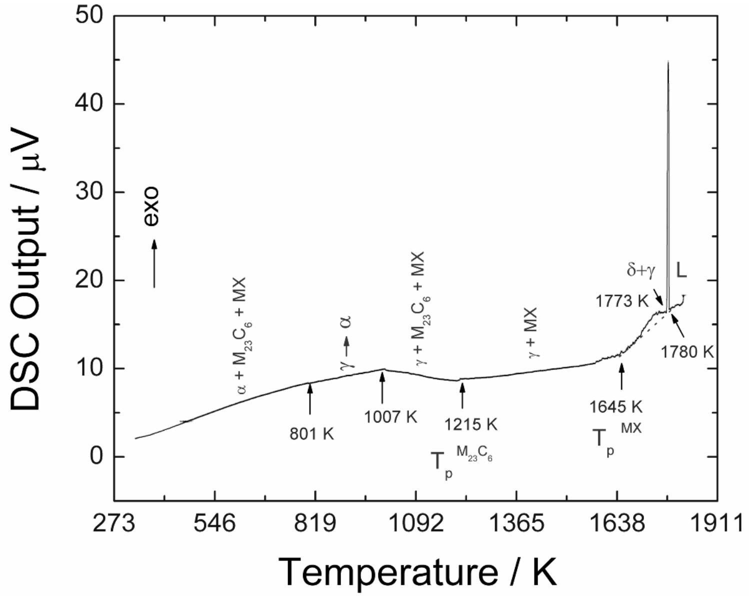

Figure 3.13. *DSC profile obtained during cooling at 1 K min^{-1} showing different transformations for1.4W–0.06Ta steel*

Another interesting observation is the high temperature three phase equilibrium during heating that is, Liquid + $\delta + \gamma \rightarrow$ Liquid+δ reaction is not clearly defined in the cooling profile. It is possible that this suppression could be due to kinetic factors; the formation of δ-ferrite as the first solid product from liquid is accompanied by the segregation of W to the solidifying δ-phase, leaving the remaining interdendritic liquid rich in Ta, V and C. This is conducive to the primary precipitation of fcc structured MX phase, that is TaC directly from liquid through the reaction, $L+\delta \rightarrow L+\delta+MX$. In reality, there could be an overlap of $L+\delta \rightarrow L+\delta+\gamma$ and subsequent $\gamma \rightarrow \gamma+TaC$ reactions. This is however not clearly resolved in the cooling cycle thermogram obtained in this study. Further, this phenomenon is also a function of the cooling rate, since fast cooling of liquid can prevent or delay the nucleation of primary MX. This in turn serves to expand the width of L+δ and L+$\delta+\gamma$ domains. It is necessary to note that the solidification aspects of high Cr ferritic steels have not been as extensively studied as that of austenitic steels [166]. It would be useful to understand the effect of cooling rate in influencing solidification and post solidification microstructures in highly alloyed ferritic-martensitic steels from welding point of view.

3.3.2.1 Effect of W and Ta content on M_s and M_f

The experimentally measured M_s and M_f temperatures for different RAFM steels are listed in **Table 3.5**. It is important to mention that, all the steels studied are subjected to the same austenitising temperature, (1253 K for 30 minutes) and the cooling rate employed is 99 K min^{-1}. A slight decrease in M_s and M_f is evident with increase in W and Ta content of the steel. However, it is difficult to give a clear interpretation to the result obtained, due to the uncertainty of having the same austenite composition. This uncertainty arises due to the presence of varied amount of undissolved carbides in different steels and their effect on PAGS. This difference in PAGS and austenite composition could be the reason for the observed change in M_s and M_f within a narrow range of composition selected in this study. However, the transformation enthalpy did not change significantly with W and Ta content of the steel as seen from **table 3.5**.

Table 3.5. *Experimentally determined martensite start and finish temperatures of the RAFM steels*

Steel designation	M_s (±5) (K)	M_f (±5) (K)	$\Delta H^{\gamma\rightarrow\alpha'}$ J g^{-1}
1W-0.06Ta	701	610	74±15
1.4W-0.06Ta	645	503	79±15
2W-0.06Ta	618	562	69±15
1W-0.14Ta	654	605	73±15

3.4 Kinetics of α↔γ transformation

3.4.1 Kinetics of α→γ transformation: effect of heating rate

Figure 3.14 presents the effect of heating rate on Ac_1 and Ac_3 temperatures. It is found that both Ac_1 and Ac_3 increase nonlinearly with heating rate. The present study estimated the equilibrium transformation temperature of the steel by extrapolating the curve to the hypothetical zero scan rate. The measured Ae_1 and Ae_3 for the steel was 1092 and 1106 K respectively, which was in agreement with the dilatometry results of Eurofer 97 obtained and the calculated results from the literature [60,166-167]. The nonlinear increase in Ac_1 and Ac_3 is attributed to the presence of undissolved carbides, which requires over heating for its dissolution. Thus, higher heating rate implies higher amount of undissolved carbides in the matrix, which reduces the availability of C in the α-ferrite matrix and thereby increasing the stability of ferrite. This increases the α→γ transformation temperature. In other words, the gradual diffusion controlled dissolution of carbides shifts Ac_3 to progressively higher temperatures.

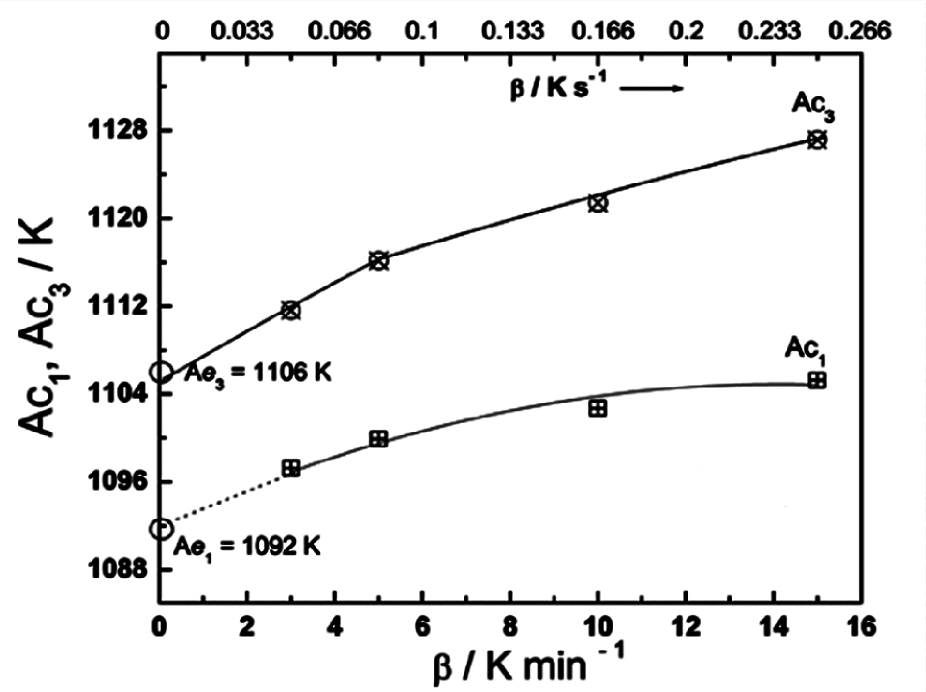

Figure 3.14. *Variation of Ac_1 and Ac_3 with heating rate*

3.4.2 Effect of cooling rate on M_s and M_f

Thermo-kinetic characteristics of $\gamma \rightarrow \alpha'$-martensite transformation in steels depends on several factors listed below –

(i) Solution temperature and time in γ-austenite state, which effectively determines the composition and grain size of austenite

(ii) Rate of heating to austenitization temperature

(iii) Rate of cooling from the austenite phase field

(iv) Presence of stress

In the present study, the steels were normalised at 1253 K for 30 minutes, which is on the lower side of single phase γ-austenite region and is not adequate to dissolve [165] the pre-existing $M_{23}C_6$ and MX completely after austenitisation. These carbides, particularly the intragranular fine dispersion of MX precipitates can serve to pin the free growth of austenite grains [156], resulting in a situation that is favourable for promoting heterogeneous austenite grain size distribution [168]. This heterogeneous state of austenite can play a decisive role in subsequent kinetics of martensite formation upon fast cooling.

Variation of martensite start (M_s) and finish (M_f) temperatures with cooling rate (β) is presented in **Figure 3.15**. The holding temperature is kept constant at 1253 K for all the experiments. It may be mentioned that only for cooling rates of above ~6 K min^{-1}, martensite conversion is noticed in small sized samples used in calorimetry studies. This is also supported by metallography and hardness studies (**figure 3.15 (b)**). The martensite hardness was found to be between 410 to 420 VHN, which did not vary significantly with the cooling rate. In the present study, the critical cooling rate for martensite formation is estimated to be above 6 K min^{-1}, for samples that are austenitised at 1253 K, the microstructural characteristics of which is discussed later. This is also not found to vary appreciably within the narrow range of W- content investigated.

Figure 3.15(c) presents the microstructure of the sample cooled from 1253 K (γ-austenite region) at 5 K min^{-1}. The cooling rate for the metallography is chosen to be lower than the critical cooling rate for the martensite formation. Microstructure consisting of α – ferrite and martensite (α′) is observed (**Figure 3.15(b))**. The areas etched in white in **Figure 3.15(c)** stand for *α*-ferrite that forms through the diffusional transformation of *γ*-austenite, while dark etching regions correspond to the athermal martensite.

From **figure 3.15**, it is observed that M_s, the start temperature of martensite is invariant to the cooling rate, where as M_f the finish temperature of martensite formation is more

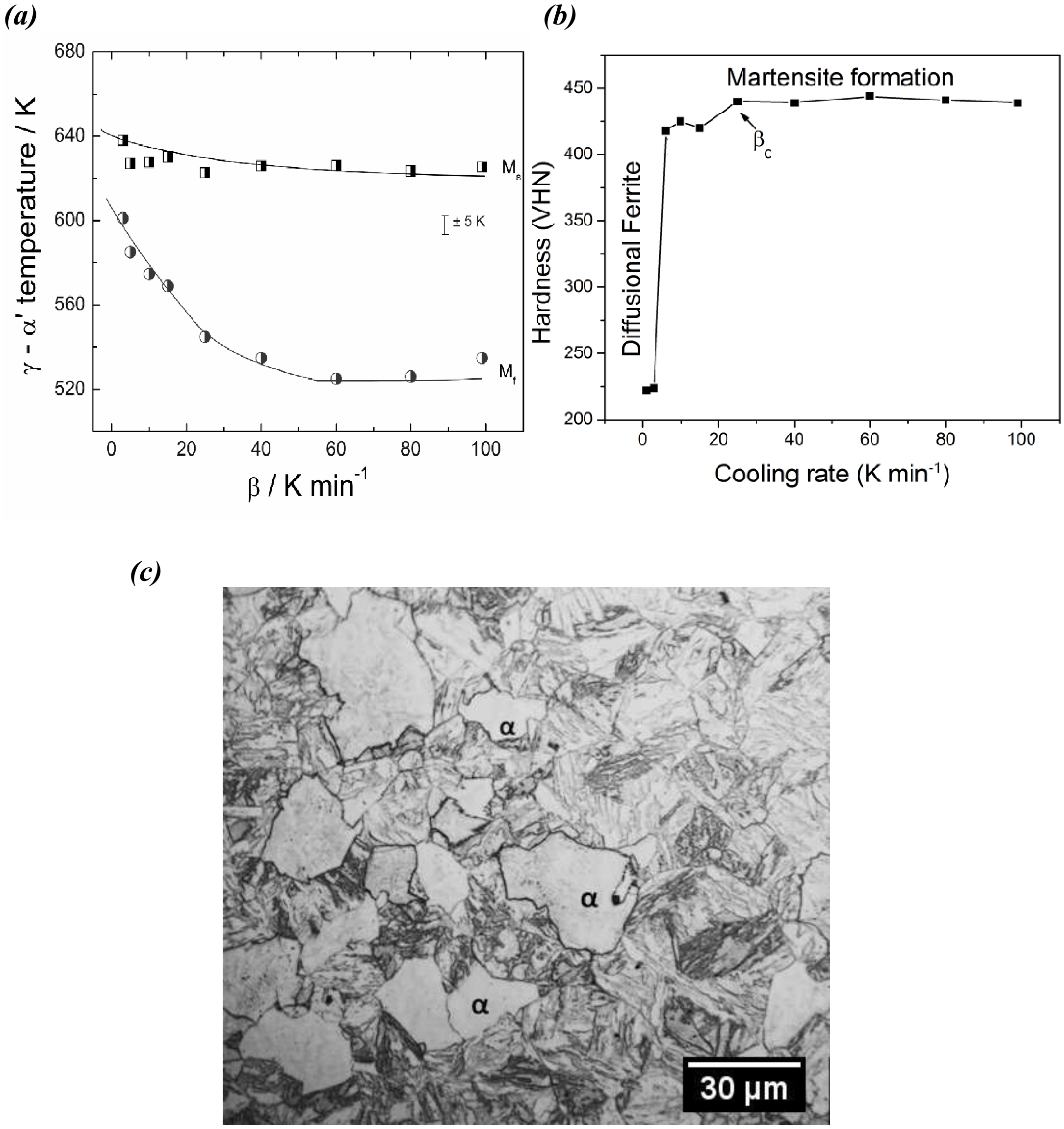

Figure 3.15. *(a) Cooling rate dependence of M_s and M_f temperatures (b) micro-hardness profile showing the variation of hardness of samples cooled at different rates (c) microstructure of the sample cooled from 1253 K (γ-austenite region) at 5 K min^{-1}.*

sensitive to the cooling rate, especially at low cooling rates. This behaviour is rather unexpected for standard athermal martensite transformation. It is observed that though the nucleation of martensite gets initiated at about the same temperature (M_s) for different cooling rates (6-100 K min^{-1}), the subsequent progress of transformation to reach near 100% requires cooling rates higher than about 40 K min^{-1}, at which point, M_f

becomes insensitive to further rise in cooling rate suggesting that critical cooling rate (β_c) lies close to 40 K min^{-1}. It emerges that the transformation rate of $\gamma \rightarrow \alpha'$ reaction happens to be a strong function of thermal history for low cooling rates. It is reported in literature that the athermal martensite transformation is nucleation controlled and growth may be taken as almost instantaneous [169]. Further it is also clear that at any chosen instant of time after martensite start M_s temperature has been reached, a higher cooling rate should result in the availability of an increased driving force for the athermal movement of γ/α' transformation interface. If this scenario is extended to the present RAFM steel, then it follows that the M_s-M_f gap, or the martensite transformation width should exhibit a mild decrease with increasing cooling rate, or at the least, it should remain constant with regard to cooling rate, as it is indeed so for cooling rates exceeding 40 K min^{-1} (**Figure 3.15**). Against this background the present findings on the cooling rate sensitivity of M_s and M_f at low cooling rates is surprising.

The martensite laths once nucleated at temperatures below M_s, their volume fraction increases, till the limit ($f_{\alpha'}$) has been realized for the concerned temperature T ($M_s \leq T \leq M_f$). If for some reason, the propagation of martensite laths encounters some mechanical hindrance, either due to the pinning of carbide particles or other effects, further branching of the propagating laths or even the nucleation of fresh laths are required for the further progress of transformation. [170] This requires the availability of additional driving force, which can come only from further lowering of temperature. It is believed that this may happen in the low cooling rate regime of $\gamma \rightarrow \alpha'$ transformation in RAFM steels. Once adequate thermodynamic driving force ($\Delta G^{\gamma \rightarrow \alpha'}$) for full extent of martensite conversion has been attained, which to a first order of approximation can be taken as proportional to (T-M_s), the martensite finish temperature begins to exhibit a near constancy with further change in cooling rate. However, caution must be exercised in extending this interpretation, for more experiments, especially with regard to the influences of varying austenitization temperature, heating rate to the austenite regime and holding times in the γ-austenite phase field are required, before a conclusive mechanism for the kinetics of athermal $\gamma \rightarrow \alpha'$ displacive transformations in W-added RAFM steels can be arrived at.

3.4.3 Empirical Calculation of M_s

Figure 3.16 shows the comparison of measured M_s temperatures against the estimated values using the empirical formula proposed by Finkler and Schirra **(Equation 3.2)** [171].

$$M_S/\mathrm{K} = 908 - 474\,\{C + 0.86(N-0.15[Nb+Zr]) - 0.066Ta\} - \{17Cr + 33Mn + 21Mo + 20Ni + 39V + 5W - 45Mn^2 - 25Ni^2 - 100V^2 + 10Co + 20Cu\} - 47.4Si. \qquad (\mathbf{3.2})$$

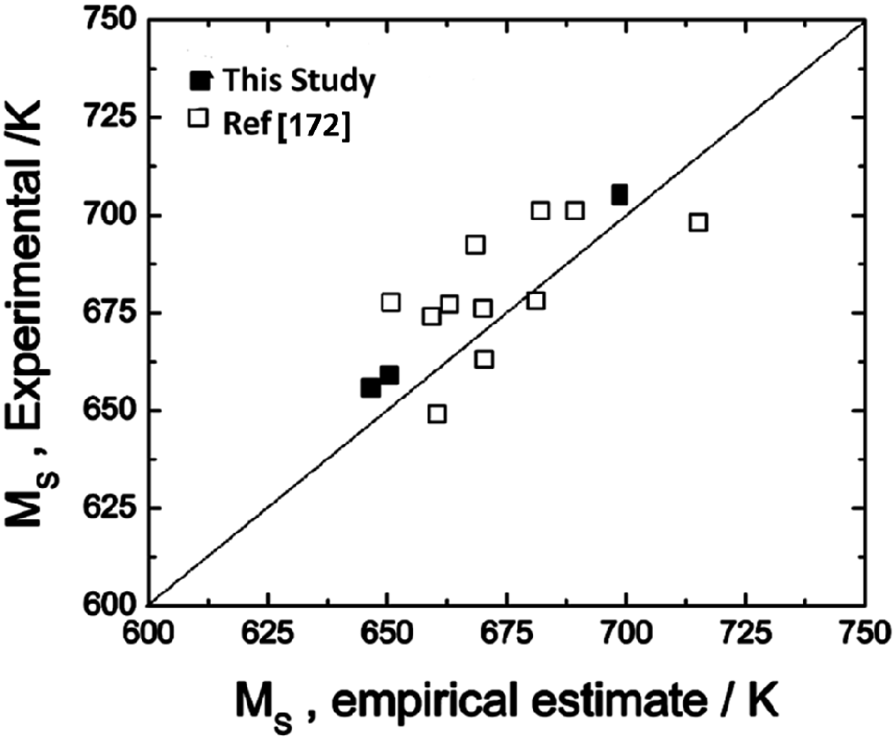

***Figure 3.16** Comparison of measured M_s temperatures [172] with empirically estimated ones using modified Finkler - Schirra formula [171].*

Elemental concentrations in the above equation are given in wt.%. The data on different 9Cr-steels were taken from the published work (indicated by open squares in the figure) of Jeyaganesh et al [172]. The data for RAFM steels (filled squares) come from this study. It is observed that by and large, the estimated M_s temperature values are in good agreement with the calorimetry measurement, for a variety of 9Cr steels, inclusive of RAFM compositions.

3.5 Simulation of Phase transformation and precipitation behaviour using JMatPro and Thermocalc

3.5.1 Simulation of Equilibrium phase transformation in 1.4W-0.06Ta steel

3.5.1.1 Transformation temperatures

Equilibrium simulation of phase transformation and precipitation behaviour of RAFM steel with varying W and Ta content has been performed using JMatPro and Thermocalc. It is well known that Thermocalc does not incorporate the effect of Ta in the calculation using TCFE6 database, the substitution of Nb in place of Ta is proved by Prat et. al. [64]. In the present study the equivalence of Ta with Nb was considered during the simulation. **Figure 3.17((a) and (b))** presents the calculated equilibrium phase fraction plot for 1.4W – 0.06Ta steel using JMatPro and Thermocalc respectively. The phase evolution sequence predicted by JMatPro and Thermocalc was found to be in agreement with the experimentally observed (**Table 3.4**) values of the steel. Both the software showed same value for Ac_1 (1080 K), while the other transformation temperatures showed mismatch of the order of 15 to 30 K as shown in the **figure 3.17((a) and (b))**. Co-existence of high temperature three phase domain namely, Liquid + γ + δ was predicted by both the software though the effect of Ta could not be incorporated in Thermocalc. However, there is a mismatch between experimentally measured transformation temperatures and those estimated, due to the assumption of full thermodynamic equilibrium.

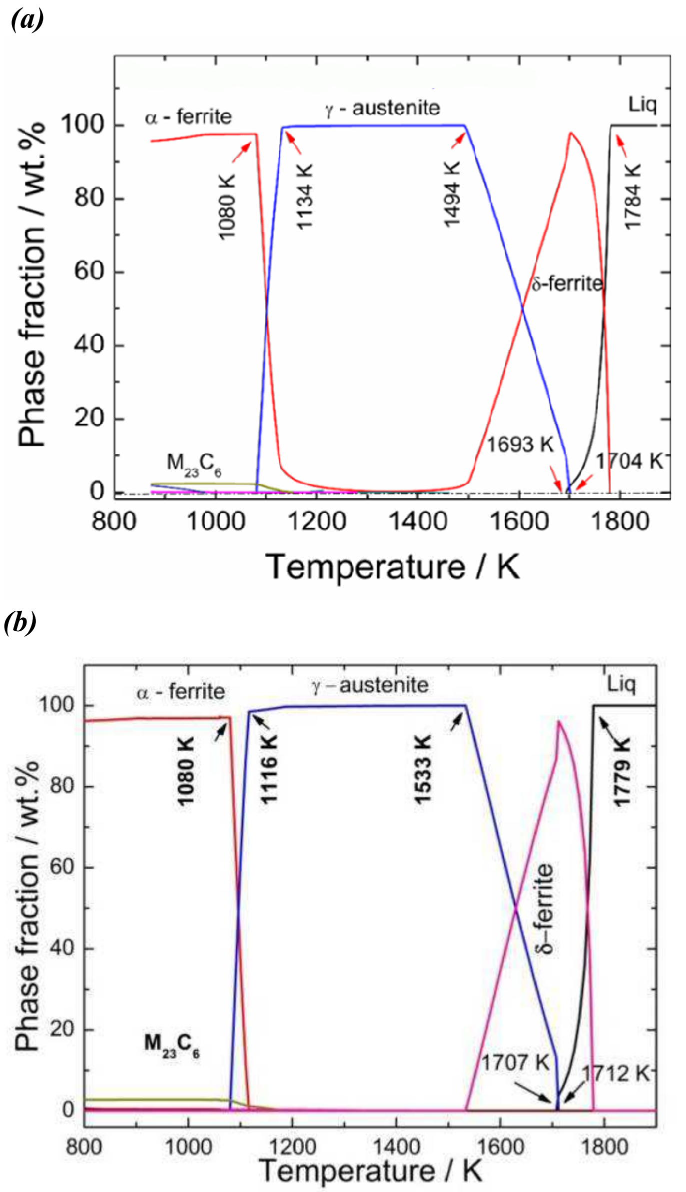

Figure 3.17. *Temperature variation of various phase fractions as estimated using (a) JMatPro; (b) Thermocalc*

Hence, it is seen that the measured solidus and liquidus temperatures for 1.4W – 0.06Ta steel, namely 1762 and 1791 K (indicated in **Table 3.4**,) are systematically higher than the predicted equilibrium values of 1693 and 1784 K by JmatPro and 1707 and 1779 K by Thermocalc respectively, indicated in **Figure 3.17(a) and (b)**. This suggests that in practice, there is an extended temperature domain of liquid phase in RAFM steel upon slow heating.

Figure 3.18 shows the comparison of measured melting point for different 9Cr steels with 1W-0.06Ta (RAFM) steel generated in our laboratory by Jeyaganesh et al.[172]. In the same figure, the corresponding estimated values using a modification of the empirical formula proposed by Hrivnak [173] (Equation 3.3) are also co-plotted.

$$T_m / K = 1808 \{50C+5Si+5Mn+5Cu+0.7Cr+1Ni+0.5Mo+0.25W+0.5V+30P+25S\} \quad (3.3)$$

Two principal conclusions emerge from **Figure. 3.18.** For different ferritic-martensitic steels belonging to generic 9Cr category, there is good agreement among measured melting temperatures for different steels. Further, the measured melting points are invariably higher than the predicted equilibrium ones. The maximum deviation is however about 15 K, which is however within the typical uncertainty limits of present thermal analysis experiments.

The experimentally measured dissolution temperatures of the MX and $M_{23}C_6$ phases (1563 and 1342 K respectively, **Table 3.4**) were also higher than the simulated values (1461 and 1153 K respectively). The difference in these values arise due to kinetic factors; since the since the dissolution of $M_{23}C_6$ and MX carbides is dependent on both their morphology and the the diffusive mobilities of substitutional solutes like Cr, W, Ta and V in γ-austenite. [174,175] The relatively slow diffusion of these solutes necessitates a little higher temperature than equilibrium temperature for the complete dissolution of carbides under continuous heating. The prediction of existence of $\gamma+\delta+L$ three phase domain (**section 3.3**), is also supported by the experimental observations of

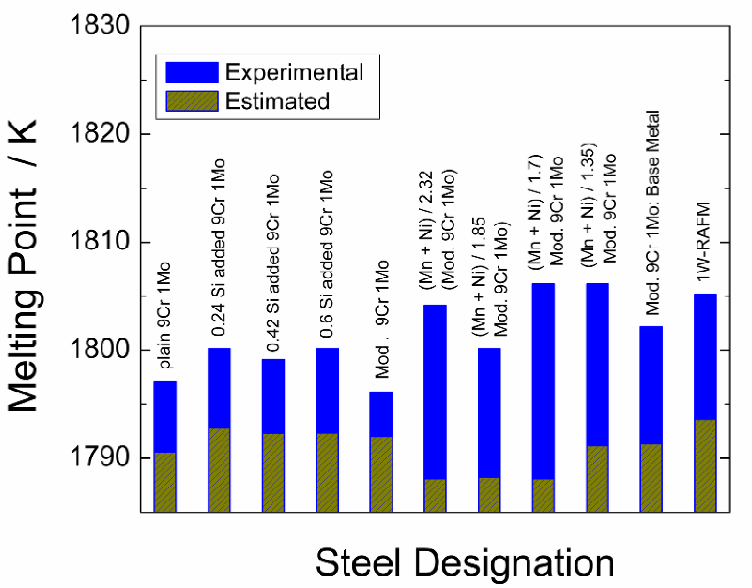

Figure 3.18 *Comparison of measured melting temperature of RAFM steel with related data on other high Cr-steels[164] The estimated values[173] are also shown*

phase transformation sequence during heating. However, as mentioned earlier, the width (ΔT) of this three phase domain in practice will be dependent on actual W content of the steel, since the extent of partitioning of W to δ-ferrite during L→δ primary solidification step is sensitive to W concentration. Since the W content of RAFM steel has not been varied extensively in this study, it is relatively difficult to speculate the role of W on the primary solidification aspects of RAFM steels.

3.5.1.2 Precipitation behaviour

In **Figure 3.19(a),** the mid-temperature domain shows the equilibrium among, $M_{23}C_6$, MX, Z and Laves phases. It may be noted that hexagonal M_2X (X=C, N) phase has not been taken into account in these equilibrium calculations; however, Z and Laves phases are taken into consideration. In **figure 3.19 (b),** the changes that are brought upon by the inclusion of M_2X phase, but neglecting Z and Laves phases, are highlighted. The detailed discussion about each phases is presented below-

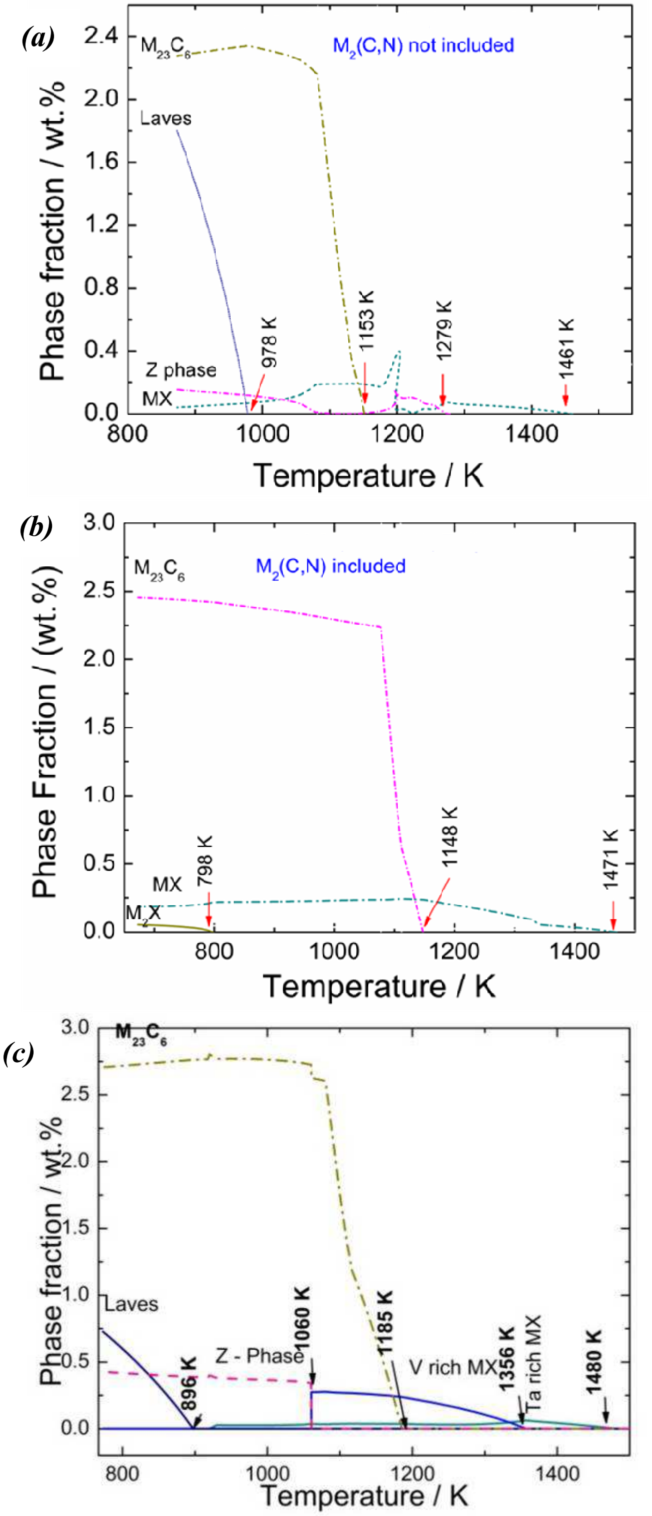

Figure 3.19 *Temperature variation of various phase fractions as estimated using JmatPro and Thermocalc (a) expanded view of figure 3.17(a) involving* $M_{23}C_6$*, MX, Z and Laves phases, but not* M_2X*; (b) same as (a), but* M_2X *included (c) expanded view of figure 3.17(b) involving* $M_{23}C_6$*, MX, Z and Laves phases.*

$M_{23}C_6$ phase:

The dissolution temperature of $M_{23}C_6$ (T_{M23C6}) observed from **figure 3.19(a-c)** is very close to the Ae_3 Temperature **(figure 3.17(a) and (b))**, suggesting that the completion of dissolution of $M_{23}C_6$ almost instantly with the transformation finish of $\alpha \rightarrow \gamma$. However, this situation is most unlikely in actual practice considering the sluggish dissolution kinetics of the $M_{23}C_6$ phase, which was discussed in the previous section. It may be noted here that, since W dissolves in $M_{23}C_6$, increasing W- content of RAFM steel will also result in an increase of T_{M23C6}. Hence, due to kinetic considerations, dissolution of $M_{23}C_6$ depends on its solute content.

M_2X phase:

The expanded view of **figure 3.17(a)** presented in **figure 3.19 (a and b)** shows the effect of nitrogen rich M_2X phase especially at low temperature (below 873 K), but at the expense of Laves (Fe_2W) and Z–phase [(Cr,Ta)(C,N)]. It is evident that the nitrogen rich M_2X phase is stable at low temperature compared to the Cr rich $M_{23}C_6$. This suggests the possibility that an additional strengthening phase can emerge during the low temperature tempering (below 873 K) of the steel, which is also supported by the existing literature [176,48]. Recent study on high Cr steel also strengthens the simulation results; a fine scale precipitation of hexagonal Cr_2N type nitride has been reported [176]. However, at longer durations, that is, during service exposure W rich Laves phase and Ta rich Z–phase compete with the M_2X precipitation. It is also reported that these phases dominate during long term thermal and stress exposure in 9Cr steel [151,48]. The formation of Laves and Z–phases were extensive in the presence of stress [48, 151]. However, the formation of Z–phase is at the expense of dissolution / conversion of fine precipitate strengtheners namely Ta rich MX. It can be concluded from the above discussion that 'there is a dynamic interplay between M_2X, Z and MX phases in the low temperature zone'. It is clear from JMatPro calculations that the consideration of Z–phase and MX did not allow M_2X to be a probable phase. In the case of RAFM steels, the presence of N is restricted due to radiological safety considerations [114,178]. Hence, the possibility of additional or second, relatively low temperature tempering treatment to precipitate M_2X phase is not expected. However, Haribabu et al. [97] recently reported the formation of M_2X phase in a similar steel (Eurofer 97) heat treated at 773 K, which contains N concentration of 0.015 - 0.045 wt. % similar to the RAFM steel studied in this thesis. However, the stability of the observed secondary M_2X phase was not discussed clearly. The above evidence strengthens the argument on the simulated results of JMatPro.

MX phase:

Both JMatPro and Thermocalc simulations show a small amount of MX phase, dissolution temperature of this phase (T_{MX}) is very far from Ae_3, which suggests that the phase is stable over a long range of temperature (**figure 3.19 (a-c)**). The stability of MX phase was also predicted (**table 3.4)** through experiments. Like $M_{23}C_6$, the dissolution temperature of MX also has a significant influence on Ac_1 and Ac_3. However, the effect could not be clearly demonstrated due to the nonspecific trend in the phase fraction of MX with temperature (figure 3.18 (b)) in the $\alpha + \gamma$ phase field.

3.5.2 Simulation of transformation temperature and precipitation behaviour with varying W and Ta content

3.5.2.1 Transformation temperature

The experimentally determined transformation temperatures were discussed in **Section 3.3**. Simulation studies in this direction were also carried out using JMatPro and Thermocalc, which showed (**Figure 3.20 (a) and (b)**) consistency with the experimental results. It is to be noted that the transformation temperatures namely, solidus and liquidus calculated using JMatPro do not exhibit considerable change with W content of the steel. A slight increase in Ae_1 and Ae_3 is seen with W content. However, Thermocalc showed a small decrease in solidus and liquidus temperature, which is not consistent with the experimental observation.

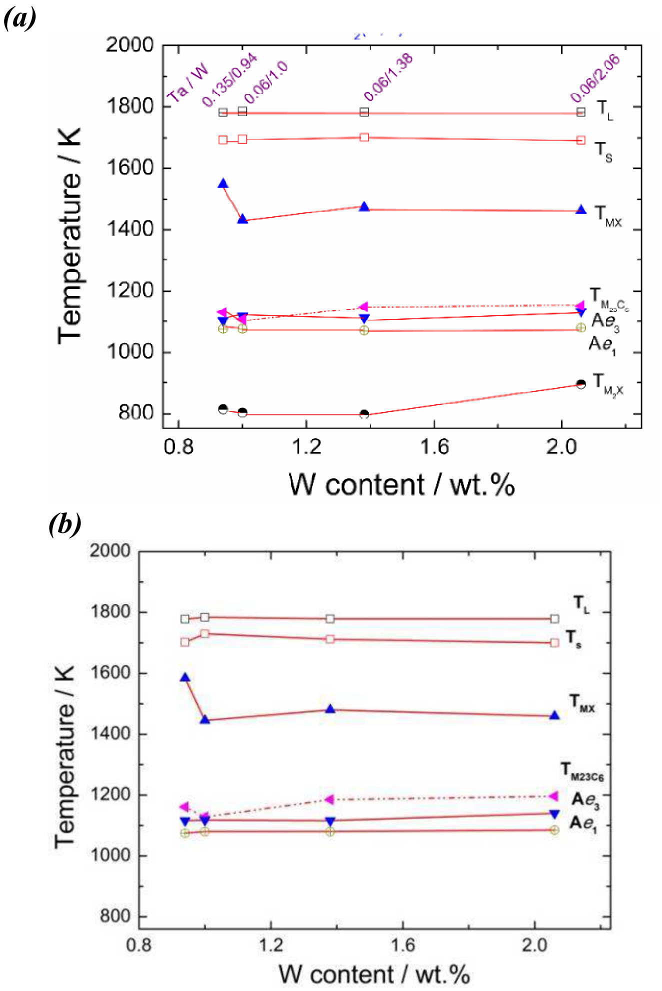

Figure 3.20. *Variation of transformation temperatures with W content for Ta=0.06 wt.%; (a) JMatPro and (b) Thermocalc simulations*

3.5.2.2 Precipitation behaviour

The incomplete dissolution of $M_{23}C_6$ with higher W content of the steel is also observed. The important observation from JMatPro is the stabilisation of M_2X at higher temperature, which is attributed to the increase in W content. This is due to the enhanced solubility of W in hexagonal M_2X structure and thereby stabilizing it further. However, the formation of M_2X phase is not predicted by Thermocalc.

Dissolution temperature of MX (T_{MX}) namely TaC carbide phase was found to increase with Ta content of the steel as observed from **Figure 3.21.** Otherwise, within the range of about 0.2 wt.% Ta, no substantial influence of its effect on other transformation temperatures has been established. It is reported that Ta forms very fine TaC phase thereby contributing to fine austenite grain size due to the pinning effect [113]. Detailed simulation for the effect of Ta using Thermocalc has not been attempted due to the difficulties in incorporating the effect of Ta (Chapter 2).

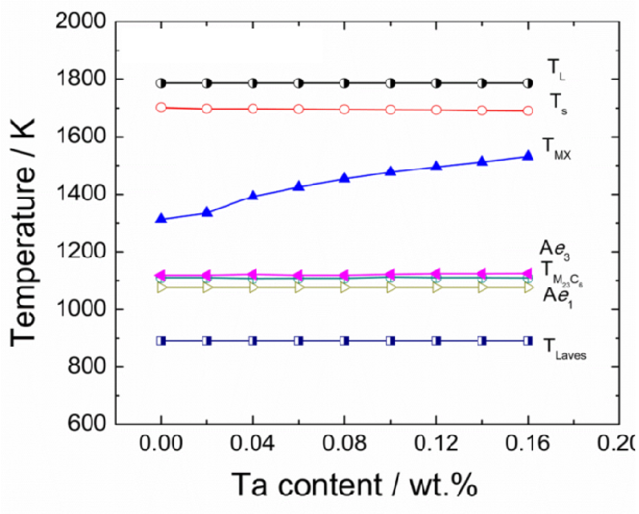

Figure 3.21. *Variation of transformation temperatures with Ta content for W=1.4 wt% simulated using JMatPro.*

Simulation results of composition of $M_{23}C_6$ and MX is presented in **Figure 3.22**. The graph (**Figure 3.22 (a-b))** shows the variation of composition of two phases estimated using JMatPro. Similar studies were also performed using Thermocalc, which showed the similar behaviour in the temperature range chosen, the results of which is presented in **Figure 3.22 (c-e)**. From **Figure 3.22(a) and (c)**, it is observed that a small amount of W dissolves in Cr rich $M_{23}C_6$ phase followed by appreciable amount of solubility of Fe.

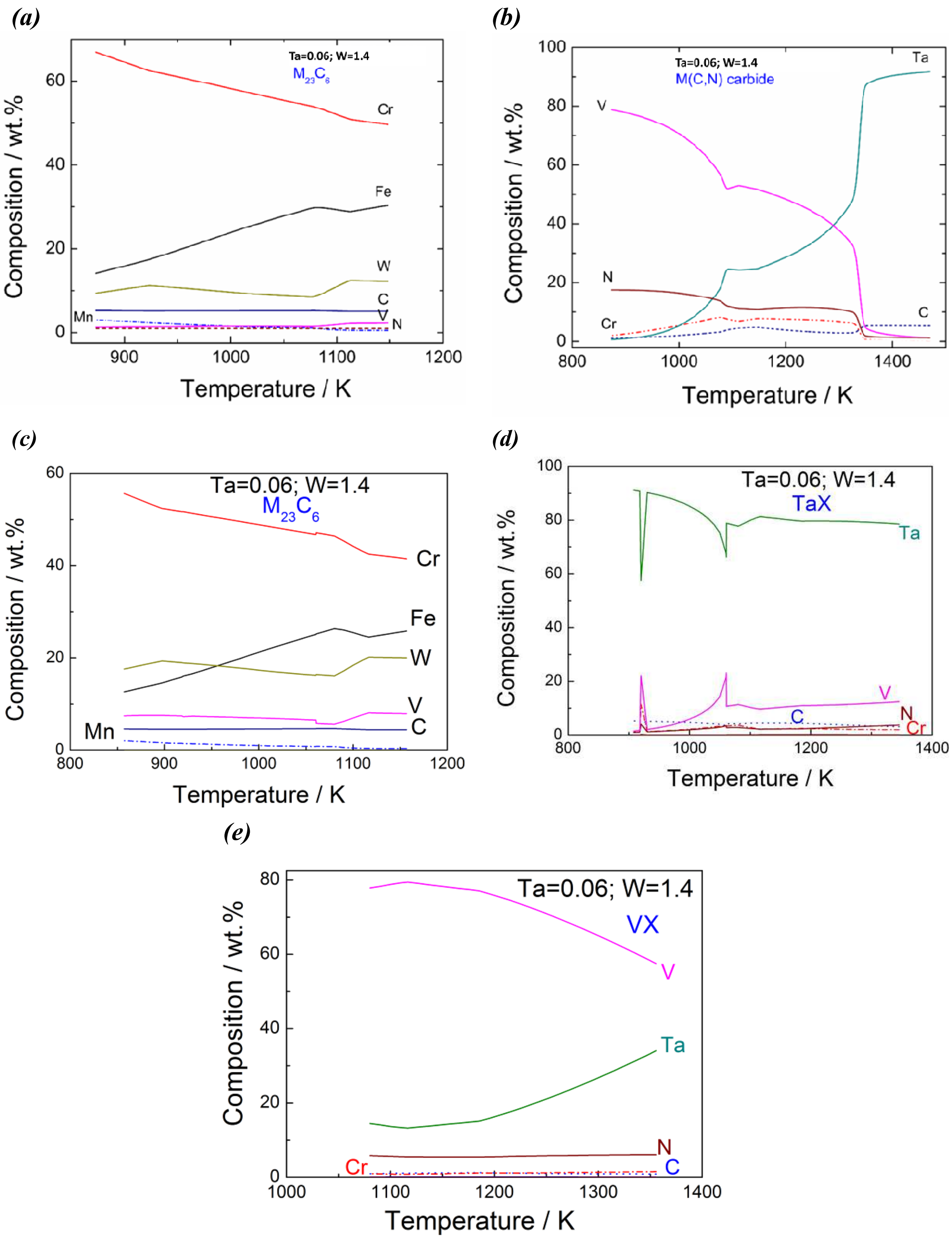

Figure 3.22. *Temperature dependence of composition of (a) $M_{23}C_6$ and (b) MX phases evaluated by JMatPro; (c) $M_{23}C_6$ (d) TaX and (e) VX estimated by Thermocalc*

However, with increasing temperature, $M_{23}C_6$ carbides which are in equilibrium with α-ferrite become gradually destabilized, and as a result, there is repartitioning of W from

$M_{23}C_6$ into the matrix α-ferrite phase. The NaCl type MX carbide phase, on the other hand does not dissolve W; but instead contains V and Ta as major metallic species. It is interesting to note that at the low temperature domain, the NaCl type cubic [48] MX phase is essentially consisting of a phase mixture of VN and TaC.

The possibility of a low temperature phase separation of two types of MX namely V rich and Ta rich MX phases is not directly evident from JMatpro simulations (JMatpro does not give polythermal sections of complex phase diagrams); but on the other hand supported both by microscopy findings and other reported data in literature [48,67]. Besides, Thermocalc equilibrium phase stability simulations (**figure 3.22 (c-e)**) also support the possibility of low temperature miscibility gap in the MX phase [48]. The possibility of two types of MX phases with one rich in Ta and the other V has been predicted. The stability regime of both the phases was found to be distinct, the dissolution temperature of V rich and Ta rich MX evaluated as 1356 and 1480 K respectively (**Figure. 3.19(c)**). This difference in solubility of two different MX phase suggest the high stability of Ta rich MX. Yet another observation to be noted here is that, the maximum volume fraction of Ta rich MX was calculated to be in the zone of dissolution temperature of V rich MX, which suggests that Ta rich MX grows / forms at the expense of V rich carbides and hence there should be a little solubility of Ta in V rich MX. Supporting the Thermocalc observation, the simulation of chemistry of MX by JMatPro also showed a considerable solubility of Ta in V rich end of temperature regime, whereas in the Ta rich regime, the solubility of V is limited. The reason for the observation is understood in terms of the relative solubility of C and N. Though both V and Ta exhibit full solubility for carbon and nitrogen in the form of MX phases at high temperatures (that is isostructural VN, VC, TaC, TaN compounds exist) that are in equilibrium with high temperature γ-austenite over a fairly large temperature interval

[151], their relative stabilities differ at low temperatures. Based on solubility product considerations TaC is more stable at high temperatures as compared to VN and vice versa [48, 3,151,].

Thus in a ferritic-martensitic steel having both V and Ta(Nb) with C and N, there is a reversal of stability among individual MX phases, with decreasing temperature. This eventually manifests in phase separation of the homogeneous high temperature MX phase into MX#1 (rich in VN) and MX#2 (rich in TaC) phases. Such phase separation has also been proposed for the α-ferrite matrix at low temperatures [179,180].

3.6 Conclusions

Effects of W and Ta on phase transformation characteristics of 9Cr- RAFM steels have been investigated using high temperature calorimetry, metallography and thermodynamic simulations. The following major findings have been identified.

(i) Phase transformation sequence on-heating has been established for RAFM steel upon slow heating of a normalized and tempered steel, which is represented as: α-ferrite(ferromagnetic)+ $M_{23}C_6$+MX → α-ferrite(paramagnetic)+$M_{23}C_6$+MX → γ-austenite + $M_{23}C_6$ + MX → γ + MX→ δ + γ +MX→ γ + δ → γ + δ + L → δ + L → L. This transformation sequence is fully supported by equilibrium thermodynamic simulations. W and Ta content of the steels in the narrow band of composition investigated did not vary the sequence.

(ii) The complete dissolution of $M_{23}C_6$ carbides requires significant superheating above Ac_3 temperature, in γ-austenite phase field; while dissolution of MX requires temperatures of the order of 1563 K. The liquidus and solidus temperatures for 1.4W RAFM steel are found to be 1794 and 1788 K respectively. These temperatures do not vary appreciably with W and Ta contents in the range of composition investigated in this study. However, the dissolution temperature of MX is found to depend on Ta concentration.

(iii) The critical cooling rate for $\gamma \rightarrow \alpha'$-martensite formation is found to be close to 40 K min^{-1} for all the RAFM steels investigated. The martensite transformation kinetics is found to be significantly influenced by the state of high temperature austenite. The presence of undissolved carbide precipitates is expected to play an important role in deciding the martensite transformation kinetics.

(iv) Electron microscopy investigations showed that there are two type of MX carbonitrides, *viz*., Ta rich TaX and V rich VX. $M_{23}C_6$ is found to be constituted of Cr, W and Fe in its metallic sub-lattice; while the MX phase did not show any presence of W, which was supported by the simulation studies carried out using JMatPro and Thermocalc.

(v) Both experiments and thermodynamic simulations showed the possibility of $L+\gamma+\delta$ three phase region during equilibrium heating and cooling of W-added RAFM steels. Further, the metallographic analysis of post solidification samples suggested that appreciable partitioning of W to δ-ferrite occurs upon slow cooling from liquid.

(vi) The M_f temperature exhibited nonlinear dependence with cooling rate for low cooling rates ($\beta \leq 40$ K min^{-1}). This is attributed to the heterogeneous character of austenite at high temperatures after the solutionising treatment at 1253 K. The measured M_s temperature of the RAFM steels are found to be in reasonable agreement with values estimated using empirical calculations.

Chapter 4

Decomposition modes of high temperature austenite and characteristics of martensite in 9Cr RAFM steels

4.1 Introduction

9Cr ferritic steels are known to be air hardenable [181] after normalization above Ac_3 temperature. It is also known that high Cr ferritic/martensitic steels with a low carbon content (<0.15%) form a lath martensite with a dislocation substructure and are associated with high M_s temperature in the range of 523-623 K [1,182]. In fact RAFM steels with W and Ta addition are reported to have higher M_s and M_f temperatures compared to their unmodified counterparts [1].

A few studies on high Cr ferritic steels have reported the formation of M_3C precipitates within the martensite laths after air cooling from the austenite (γ) phase field, The mechanism of such precipitation has not been clearly understood, since it is attributed to different causes like autotempering of martensite or para equilibrium precipitation [82,183-186]. However, such a precipitation in normalised steel results in an inhomogeneous microstructure. This can lead to a reduction in the hardenability of the steel, which is otherwise achievable in an industrial process. The heterogeneity in microstructure also arises in the weld and heat affected zone of a weldment, more so for thick plates [187,188] and components of complicated design and large dimensions [189]. In such cases, it is necessary to adopt appropriate welding methods and post weld heat treatments. Hence, the mechanism of decomposition of austenite and the resultant microstructural variations on cooling from the austenite phase field need to be understood, as a necessary step to optimise the processing and heat treatment conditions for RAFM steels.

The steels are employed in the normalised and tempered condition, wherein it derives its strength from the solid solution strengthening effects of W, the fine martensitic substructure and the fine precipitates that form on tempering of the martensite [3]. The common strengthening precipitates in 9 Cr ferritic steels are $M_{23}C_6$ and MX type of carbides / carbonitrides. It is well known that the alloy content of the steel has large influence over the kinetics of formation of these precipitates [190]. Therefore it is important to study the effect of W and Ta on the kinetics of tempering of steel.

This chapter deals with the study of decomposition modes of high temperature austenite and tempering kinetics of martensite, discussed under three major topics. **Section 4.2** presents the effect of alloy content and solution treatment conditions on the formation of martensite, describing the effect of solutionising temperature and cooling rate on formation of martensite. **Section 4.3** deals with the martensite characteristics after normalisation and tempering. The characteristics of martensite in normalized 1.4W-0.06Ta steel have been analysed by Orientation Imaging Microscopy (OIM) in TEM and Mossbauer Spectroscopy. Kinetics and mechanism of tempering of martensite has been studied in detail in **Section 4.4**. The results obtained from the experimental studies are substantiated with simulation using JMatPro calculations.

4.2 Effect of alloy content and solution treatment conditions on microstructural characteristics of normalized steels

It may be recalled from C**hapter 3** (**Figure 3.5**) that a martensite structure was observed in all the steels normalised at 1253 K. It was observed that the average Prior Austenite Grain Size (PAGS) decreases from ~25 to ~15μm with increase in W, Ta content, due to the solute drag effect. Back Scattered Electron (BSE) images of the normalised steels with W and Ta content higher than 1 and 0.06 wt. % respectively are presented in **Figure 4.1**. Steels with 1.4 and 2 wt. % W and 0.14 wt.% Ta show the presence of coarse precipitates of the size higher than 200 nm. These are identified to be pre-existing or undissolved precipitates, since the high cooling rate employed from the γ phase field precludes the formation of any such coarse precipitates during cooling. This

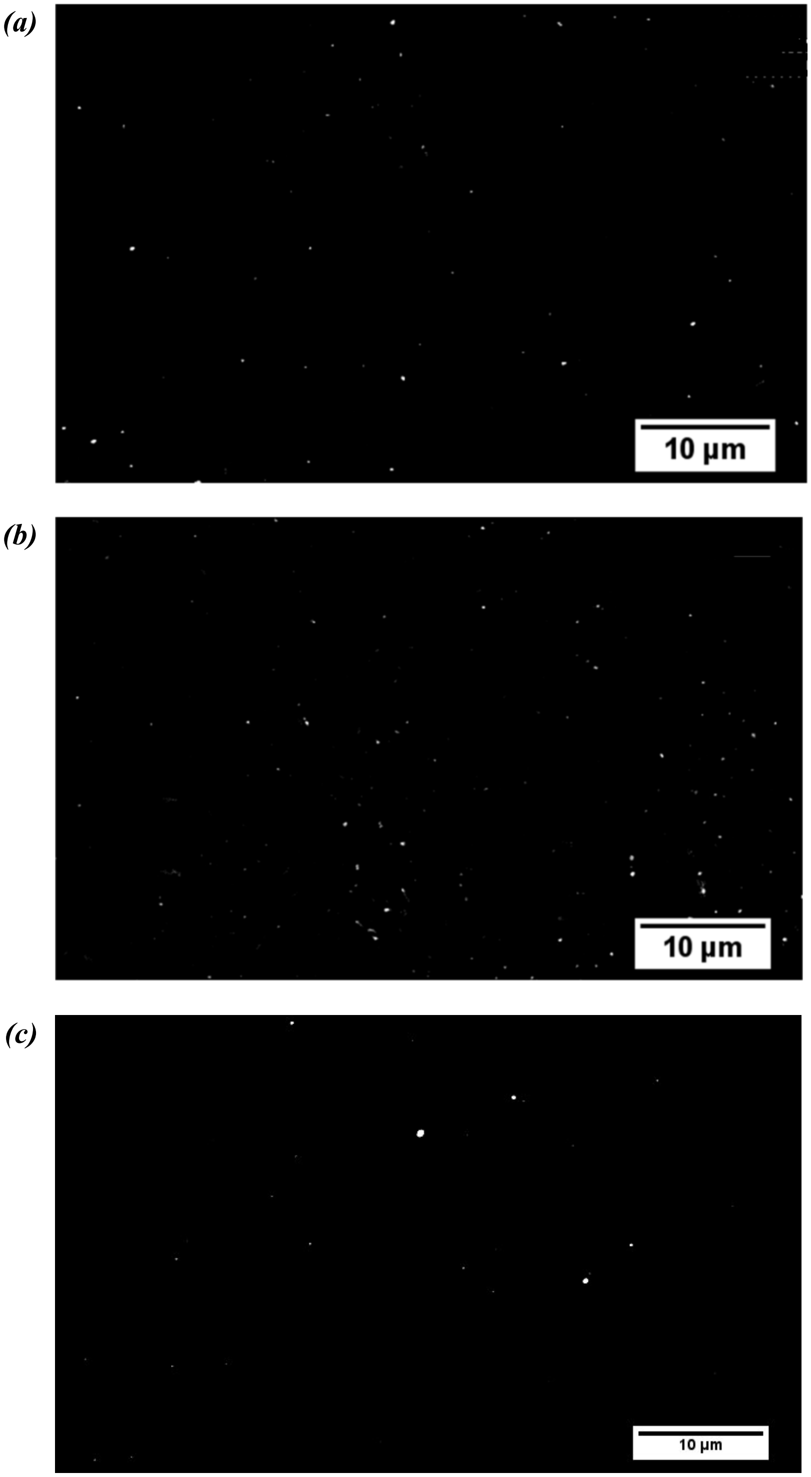

Figure 4.1. *BSE images of normalised (a) 1.4W–0.06 Ta (b) 2 –0.06 Ta (c) 1W–0.14 Ta steels showing increase in number density of undissolved precipitates with W and Ta content*

suggests that the temperature and duration of austenitisation is not sufficient to dissolve all the carbides, which is also evident from the higher dissolution temperature of $M_{23}C_6$ and MX reported in **Chapter 3** (**Table 3.4, Figures 3.9, 3.10**) than the austenitisation temperature employed in the present investigations. It is to be mentioned that the undissolved precipitates were not detected in 1W–0.06Ta steel by BSE imaging, suggesting the presence of very few undissolved precipitates.

Figure 4.2 shows the carbon replica micrograph of normalised 1.4W – 0.06Ta steel. Detailed analysis of EDX and SAED pattern showed that the undissolved carbides are Cr rich $M_{23}C_6$ and Ta and V rich MX. Similarly the increase in Ta content is expected to increase the number density of undissolved MX carbonitrides in 1W–0.14Ta steel. It is also important to recall that the carbon content of the steels varied from 0.08 wt. % for 1W-0.06Ta steel and 0.12 wt.% for the other steels. This also could be reason for the increase in number density of carbides in steels with W and Ta content higher than 1 and 0.06 wt. % respectively.

The average composition and stoichiometry of $M_{23}C_6$ present in the steels 84ormalized at 1253 K is listed in **Table 4.1**. W concentration of $M_{23}C_6$ increases with W content of the steel leading to increase in W / Cr ratio. The effect of increase in W concentration in $M_{23}C_6$ is also reflected in increase in number density of carbides (**Figure 4.1**). Hence, it can be understood that, the high cohesive energy of carbides with high solubility of W delays the dissolution of $M_{23}C_6$.

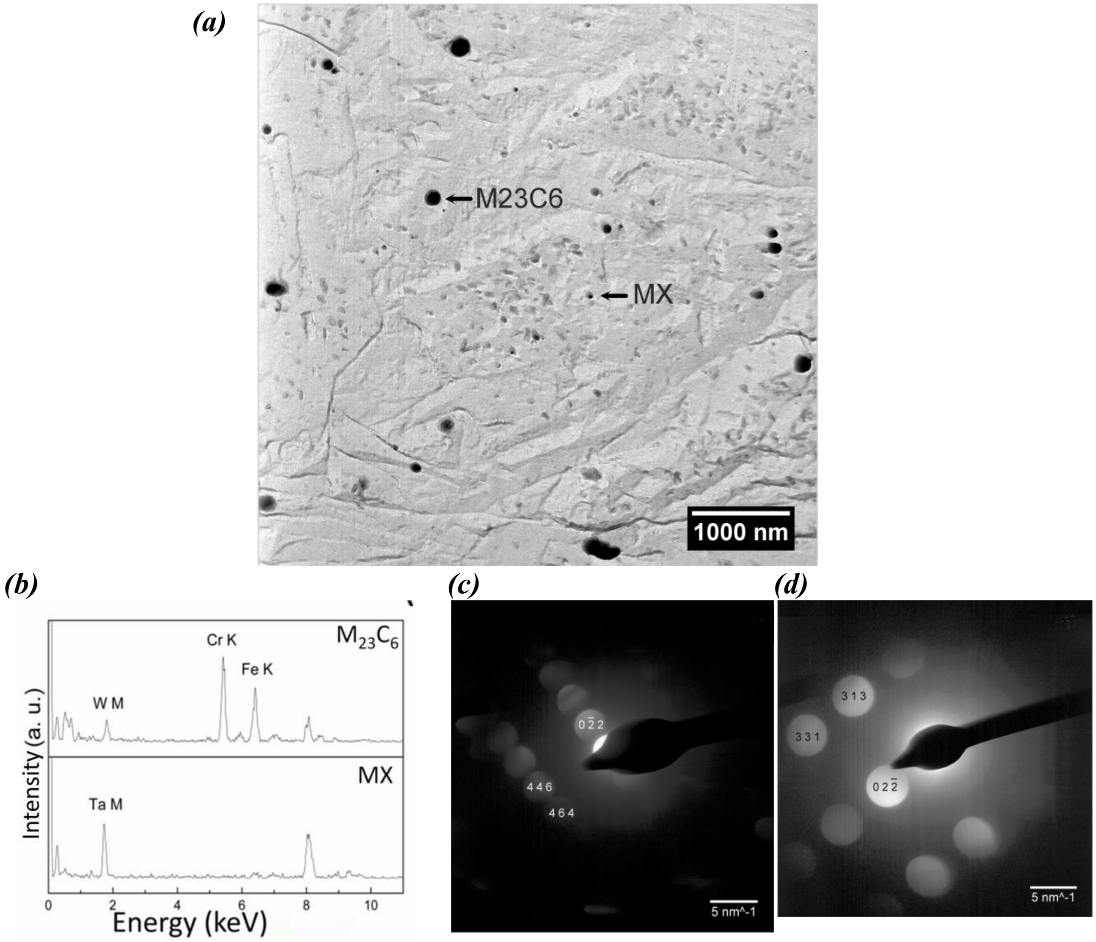

Figure. 4.2 *TEM micrograph of 1.4W-0.06Ta steel 85ormalized from 1253 K showing (a) undissolved carbides (b) EDX spectra from undissolved $M_{23}C_6$ and MX carbides (c and d) microdiffraction patterns from $M_{23}C_6$ and MX along [-5 2 2] and [4 -3 -3] zone axis respectively*

Table 4.1. *Microchemistry of $M_{23}C_6$ calculated from EDX analysis for normalised steels*

Steel	Chemical composition ±3 (wt%)			Stoichiometry
	Cr	Fe	W	
1W-0.06Ta	53.3	29.8	16.9	$Cr_{14.61}Fe_{7.16}W_{1.23}C_6$
21.4W -0.06Ta	47.6	31.6	20.8	$Cr_{13.19}Fe_{8.17}W_{1.64}C_6$
2W- 0.06Ta	46.5	28.6	24.9	$Cr_{13.33}Fe_{7.65}W_{2.02}C_6$
1W -0.14Ta	51.9	30.9	17.2	$Cr_{13.96}Fe_{7.73}W_{1.31}C_6$

4.2.1 Effect of W content and austenitisation conditions on microstructural evolution during martensitic transformation

A complete martensitic structure is observed in 1W–0.06Ta and 1W–0.14Ta steels, suggesting that the austenite is nearly homogeneous with the nominal composition of the steel, there by facilitating a complete $\gamma \rightarrow \alpha'$ transformation, which also was shown by the simulation of CCT curve for 1W–0.06Ta steel presented in chapter 3 (**Figure 3.4).** The CCT curve for the steel with high Ta content also showed a similar behaviour, which is not presented here.

4.2.1.1 Effect of cooling rate (β)

Figure 4.3 (a) shows the TEM mixrograph of the 1.4W-0.06Ta steel in normalised at 1253K. A predominantly martensitic structure with lath width varying from 200 to 250 nm, along with undissolved carbides is observed. Apart from the observed martensite structure, the formation of few fine intralath acicular precipitates was observed in a few wide laths of size about 1-2 µm, with lower dislocation density in comparison with the finer laths. Analysis of SAED pattern and EDX spectra (**Figure 4.3 (b,c)**) identified the carbides to be Fe rich M_3C. In contrast, increasing the cooling rate to water quenching resulted in a complete martensitic structure with no evidence for precipitation (**Figure 4.3(d)**). The presence of M_3C is not expected during a normalising treatment, more so in W added steels, as W addition is known to improve the hardenability of the steel. [191-193] In high Cr ferritic steels, as mentioned earlier a few studies report the formation of cementite, which has been attributed to auto tempering of martensite or precipitation of para-equilibrium cementite, resulting in a structure akin to lower bainite. M_3C is also reported [186] to form in P91 steels on air cooling from the γ phase field rather than on water quenching, similar to the observations made in 1.4W – 0.06Ta steel in this study.

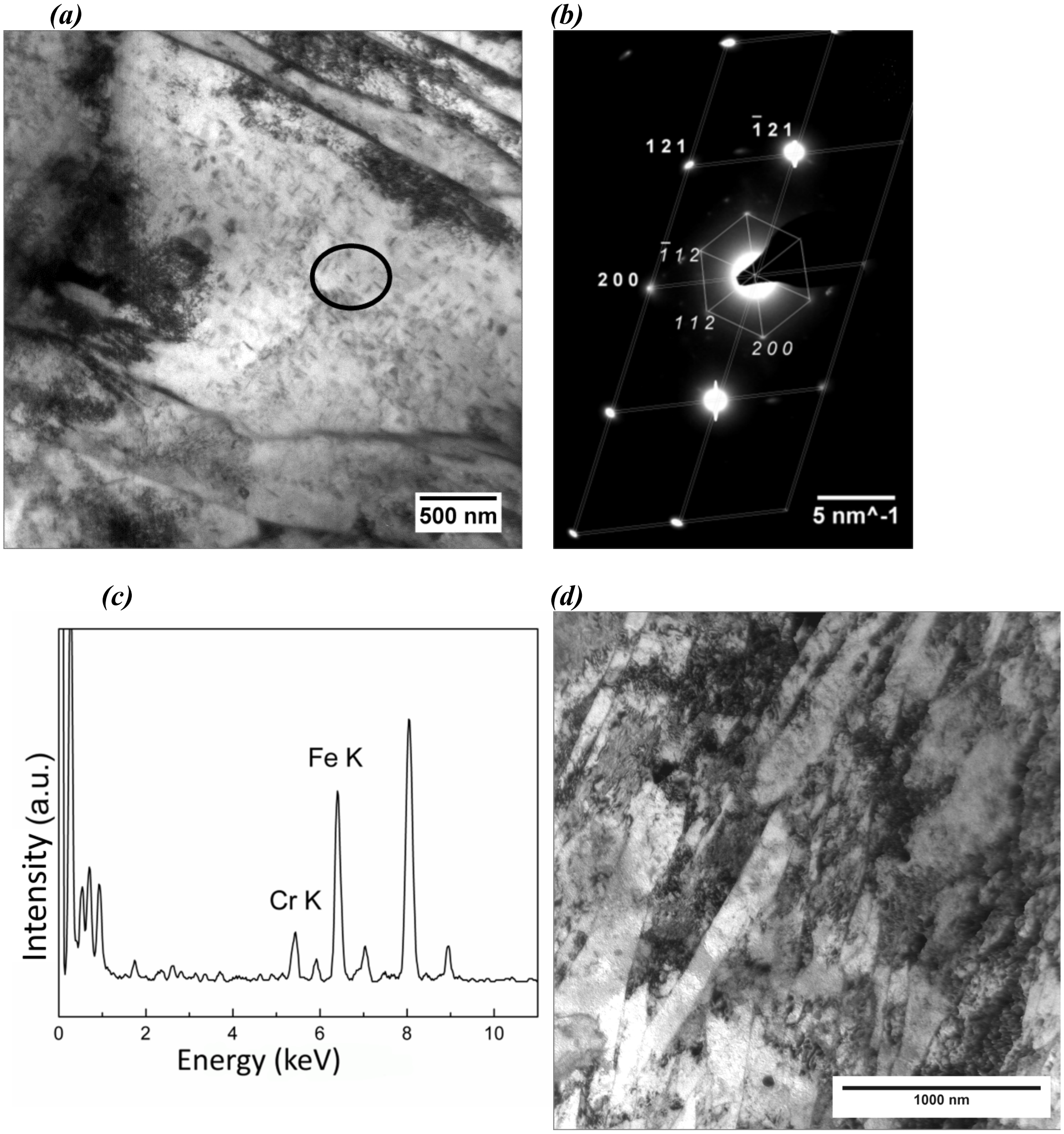

Figure 4.3 *(a) TEM micrograp of 1.4W-0.06Ta steel normalised from 1253 K showing fine carbides (circled) in a wide lath (b) SAED pattern from a precipitate confirming* M_3C *along [0 2 -1] zone axis;(c) EDX spectrum taken from one of these precipitates from carbon extraction replica of the same sample, showing its Fe rich nature (d) TEM micrograph of 1.4W-0.06Ta steel water quenched from 1253K showing martensite without any precipitation*

4.2.1.2 Effect of austenitisation Temperature (T_γ)

The 1.4W-0.06Ta steel was austenitised at 1353 K to study the effect of solutionising temperature on the martensite formation. Thin foil micrograph of both normalised and

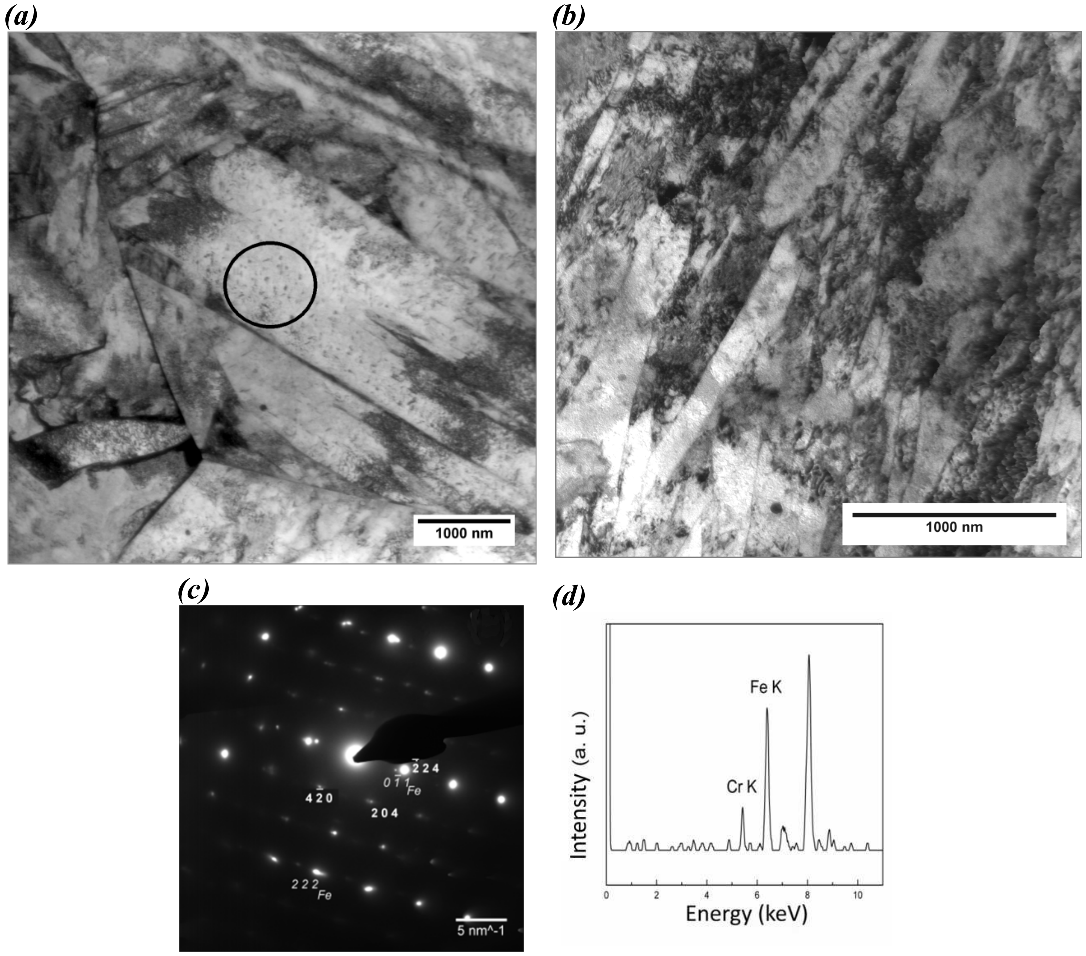

Figure 4.4 *TEM micrograph of 1.4W-0.06Ta steel (a) normalised at 1323K showing fine acicular precipitates (circled) in a wide lath (b) water quenched from 1323K showing martensite without precipitation (c) SAED pattern from a precipitate in (a) confirming* $M_{23}C_6$ *along [-2 -4 1] zone axis of (d) EDX spectrum taken from one of these precipitates from carbon extraction replica of the same sample, showing its Fe rich nature*

water quenched steel are presented in **Figure 4.4 (a, b)** respectively. It is observed that fine needles of carbides are still present in air cooled steel (**Figure 4.4(a))**, while such a precipitation was not observed in the steel water quenched from 1353 K (**Figure 4.4(b))**, suggesting that fast cooling prevented the formation of secondary carbides in steel. Identification of the precipitates by EDX and SAED analysis from the steel normalized at 1323 K **(Figure 4.4(c,d))** proved them to be Fe rich $M_{23}C_6$, in contrast to the normalised samples at 1253 K. The above results strongly suggest that, both austenitisation temperature and cooling rate influence the nature of the transformation products of high temperature austenite.

4.2.1.3 Effect of W content

The same set of heat treatments were carried out on 2W–0.06Ta steel to study the effect of W content on γ→α′ transformation during cooling. **Figure 4.5(a,b)** shows the thin foil micrographs of the steel normalised at 1253 and 1323 K respectively, which shows the presence of fine precipitates within a few wide laths. EDX analysis showed them to be Fe rich, while the analysis of the SAED patterns **Figure 4.5 (c,d)** from these intralath carbides confirmed that they are of $M_{23}C_6$ type. **Figure 4.6** shows the microstructure of the 2W-0.06Ta steel water quenched from 1253 and 1323 K. Precipitation of fine carbides (**Figure 4.6(a)**) within a wide martensite lath is observed in the steel quenched from 1253 K. Analysis of SAED pattern (**Figure 4.6(b)**) from one of the precipitates in confirmed that they are of M_3C type. The dark field micrograph in **Figure 4.6(c)** highlights the M_3C precipitates. However, no secondary carbides are observed in the sample quenched from 1323 K **(Figure 4.6 (d))**. This clearly demonstrates the dependence of γ→α′ transformation on the austenitising temperature and cooling rate. The resultant microstructure of the steels, with varying W contents is summarized in **Table 4.2**.

The formation of M_3C or $M_{23}C_6$ carbides at higher temperatures due to an auto tempering of martensite or paraequilibrium precipitation has been reported in literature.[183-186,194] However, in this study, auto tempering of martensite as a possible reason for the observed formation of carbides is strongly ruled out based on the following evidences.

(a) Temperature interval between M_s and M_f is about 100 and 50 K for 1W and higher W steel respectively (**Table 3.5**). Autotempering process if happens, should be more pronounced in 1W- 0.06Ta steel rather than in 1.4W–0.06Ta or 2W–0.06Ta steels, whereas experimental results prove the contrary. Also the observation of precipitates in few laths does not support the possibility of autotempering of martensite.

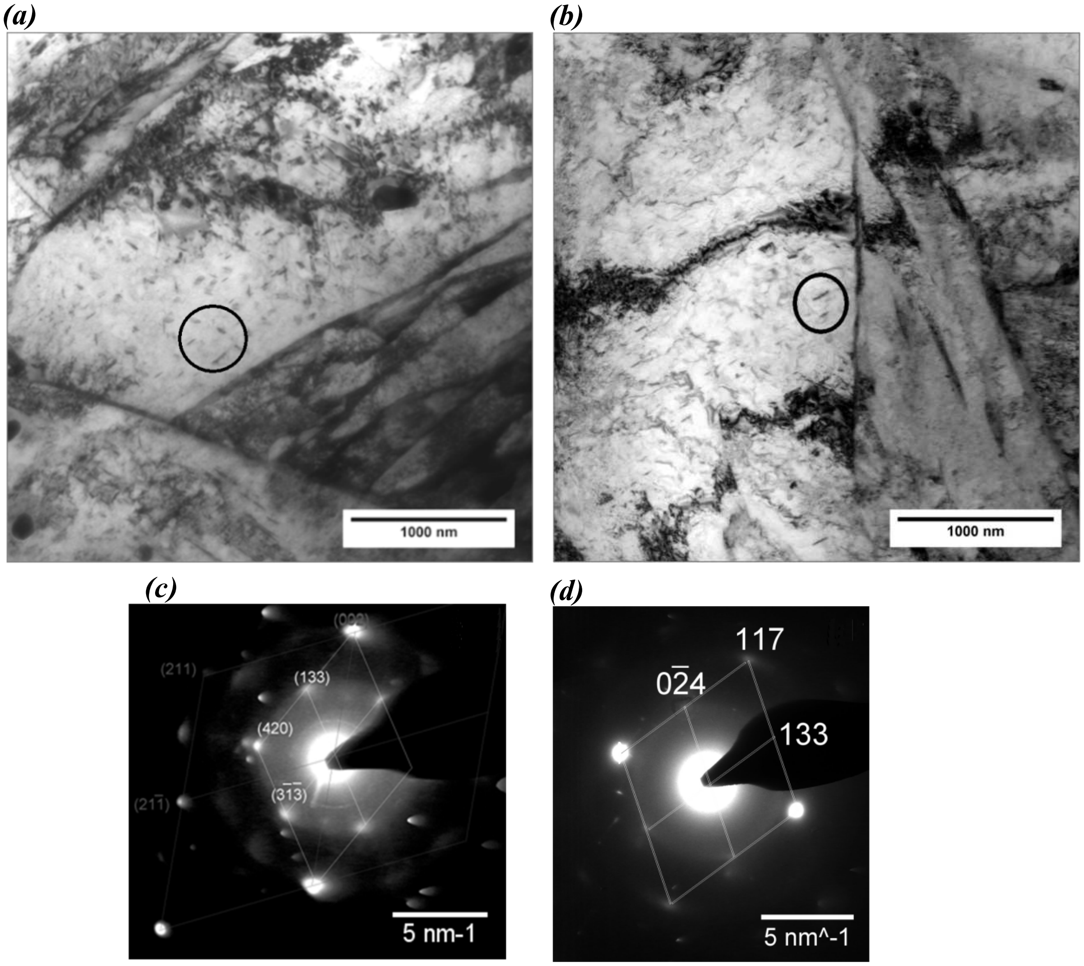

Figure 4.5 *TEM micrographs showing fine acicular precipitates (circled) in wide laths in 2W-0.06Ta steel normalised from (a) 1253K (b) 1323K; (c and d) SAED patterns confirming the presence of* $M_{23}C_6$ *in (a) and (b) along [-3 6 -5] and [-9 2 1] zone axis respectively*

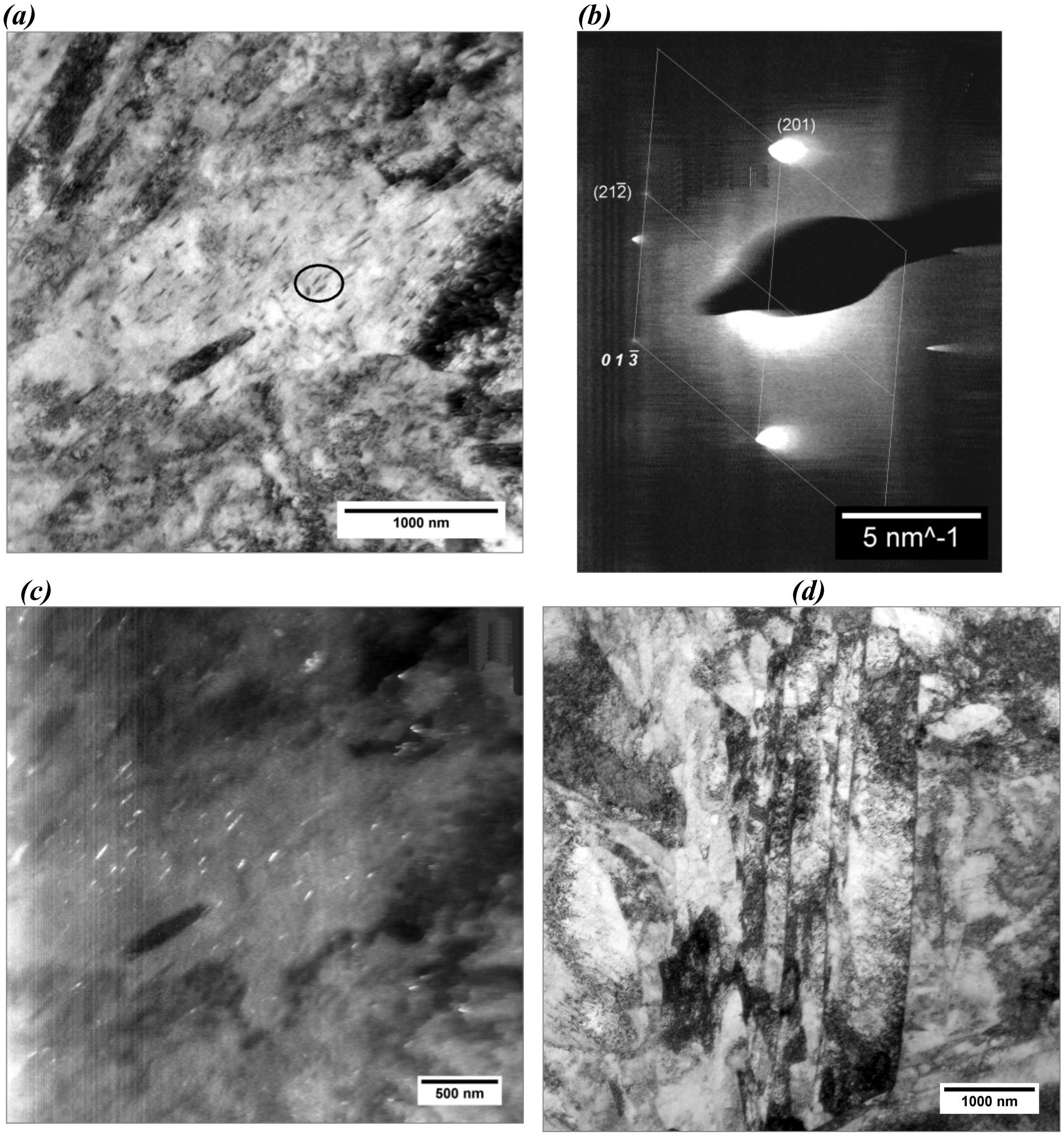

***Figure 4.6** TEM micrograph of 2W-0.06Ta steel water quenched from 1253K showing (a) fine acicular precipitates (circled) in a wide lath similar to normalised steel (b) SAED pattern from a precipitate in (a) along [-1 6 2] zone axis of M_3C, (c) DF micrograph with (2 1 -2) reflection highlighting the M_3C carbides (d) fully martensite in steel water quenched from 1323K*

(b) The presence of the carbides has been observed in relatively wide laths of low dislocation density. Formation of such wide laths implies the self diffusion of Fe and substitutional solutes, which is favoured at higher temperatures [195] and is sluggish below the M_s temperature. In our earlier study, [196] no significant coarsening of laths was observed during tempering of martensite even until 2 hours at 1023 K, a temperature far higher than M_s. Hence, the observed coarse laths correspond to ferrite formed at temperatures higher than M_s.

(c) Analysis of the SAED pattern of 1.4W steel normalised at 1253K given in **Figure 4.3(b)**, showed the presence of M_3C and α-Fe along [0 2 -1] and [0 -1 2] zone axis respectively. A stereographic analysis of the above diffraction pattern did not satisfy the Bagaryatsky orientation relationship [197,198] between ferrite and cementite.

Table 4.2. *Summary of microstructure of the austenitised steels*

Steel	***1253 K / AC***	***1253 K / WQ***	***1323 K / AC***	***1323 K / WQ***
1W – 0.06Ta	α' + UC	α' + UC	α' + UC	α' + UC
1.4W – 0.06Ta	α' + UC + M_3C	α' + UC	α' + UC+ $M_{23}C_6$	α' + UC
2W – 0.06Ta	α' + UC + $M_{23}C_6$	α' + UC + M_3C	α' + UC+ $M_{23}C_6$	α' + UC
1W – 0.14Ta	α' + UC	α' + UC	α' + UC	α' + UC

UC – Undissolved Carbides

Para equilibrium precipitation of only Fe rich M_3C has been reported in austenitised P91 steel [186], on air cooling from γ phase field. However, in the present study, M_3C and $M_{23}C_6$ form in 1.4 and 2W steels depending on austenitisation temperature and cooling rate, thus ruling out the possibility of para-equilibrium precipitation.

An attempt was made to understand the mechanism of formation of the observed Fe rich precipitates through a detailed calorimetry study in 1.4W–0.06Ta steel. The experimental conditions were chosen to be similar to the normalising conditions mentioned earlier. The results of the calorimetry study are described in the next section.

4.2.2 Thermal and microstructural analysis of 1.4W – 0.06Ta steel

The cooling DSC thermogram of 1.4W – 0.06Ta steel, cooled from 1256 K is presented in **Figure 4.7(a)**. The sample has been held at 1256 K for 15 minutes and then cooled at a uniform cooling rate of 99 K min^{-1}, the highest cooling rate possible with the instrument employed. The chosen cooling rate also corresponds to the air cooling rate of ~2 K sec^{-1}. An important observation from the DSC thermogram in the Figure is the existence of two exothermic peaks. The peak 1 with highest intensity undoubtedly corresponds to the $\gamma \rightarrow \alpha'$transformation in the steel, the M_s and M_f is estimated to be 645 and 503 K respectively. A low intensity peak is observed between 782 and 645 K (peak 2), which is above the M_s temperature of the steel. The origin of the thermal arrest at this temperature could be due to the following reasons:

- Martensitic transformation of few coarse austenite grains
- Martensite transformation of solute lean austenite grains
- Precipitation (of M_3C or $M_{23}C_6$) above M_s temperature prior to martensite transformation.

Microstructural analysis of the sample after the DSC experiment was carried out to understand the reasons for the observed peak, and is presented in **Figure 4.7(b)**. The formation of needle like precipitates is observed in few regions, which resembled the microstructure of the normalised steel discussed in **section 4.2.1**. Identification of the precipitates using SAED pattern and EDX analysis (**Figure 4.7 (c, d)**) showed that the precipitates are Fe rich orthorhombic M_3C type of carbides. The microstructural observation of the post DSC sample is in agreement with the results of normalised 1.4W-0.06Ta steel presented in **Figure 4.3(a)**. Hence the low intensity peak (peak 2)

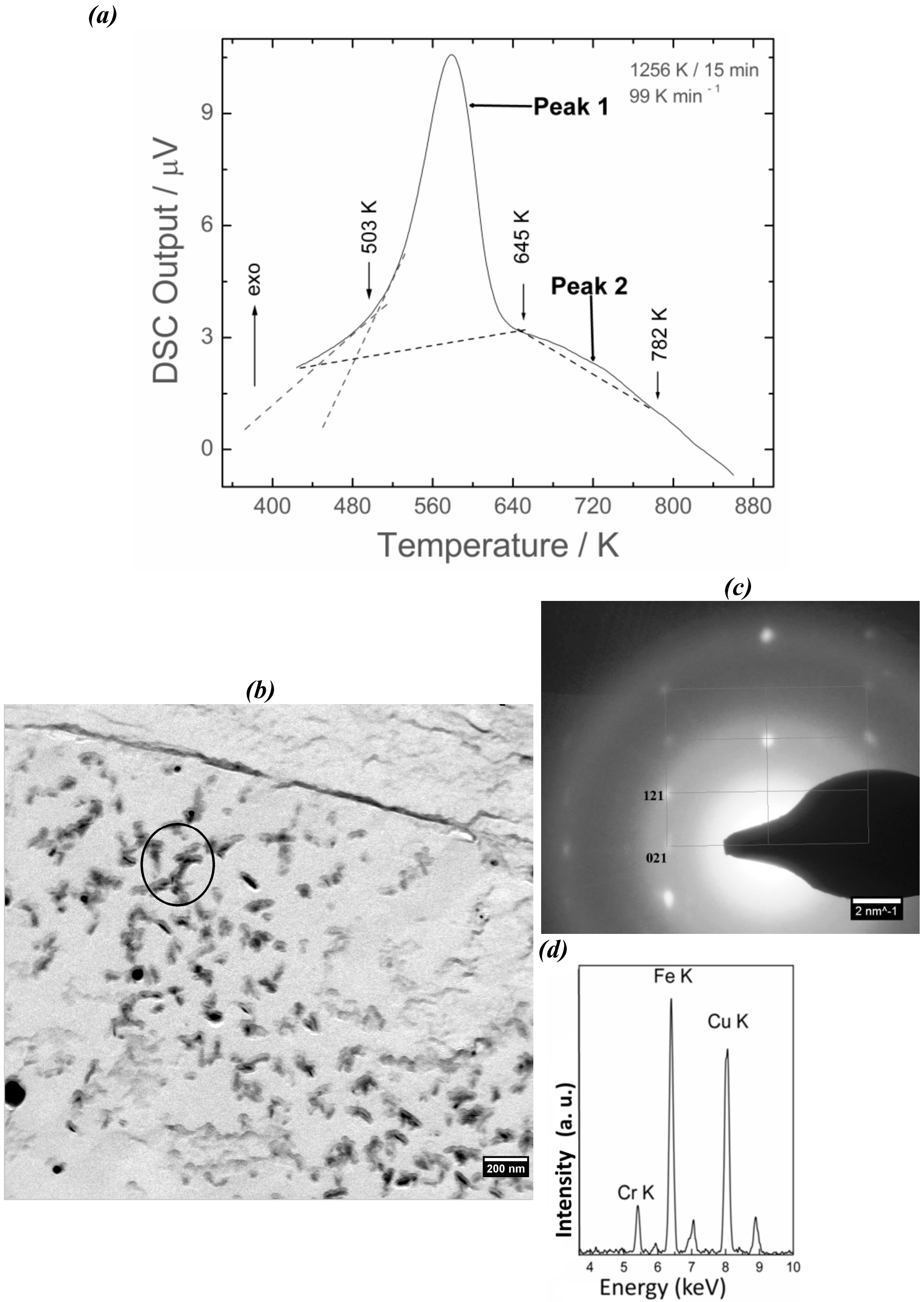

Figure 4.7.*(a) DSC profile of 1.4W-0.06Ta steel cooled at a rate of 99 K min^{-1} from 1256 K (b) TEM micrograph of the same sample showing fine acicular carbides (circled) (c) SAED pattern along [0 1 -2] zone axis of M_3C and (c) EDX spectrum showing enrichment of Fe in M_3C.*

observed in DCS thermogram (**Figure 4.7(a)**) is attributed to the formation of M_3C carbides prior to martensitic transformation in 1.4W-0.06Ta steel. M_3C precipitation prior to martensite formation is expected to reduce the C content in austenite in the steel. This partial reduction in C content would also reduce the driving force for martensite transformation in C lean austenite. Computation of M_s temperature of the steels with different PAGS showed that, M_s is not a strong function of austenite grain size, which is also reported in literature [199]. Therefore, based on the detailed TEM investigation, it is confirmed that the thermal arrest corresponding to the peak 2 is due to the precipitation of Fe rich M_3C carbides, in forming the austenite phase field prior to the martensitic transformation. The basis for such precipitation in high Cr steel is discussed further with the help of a schematic TTT diagram.

The decomposition modes of austenite not only depend on the austenitisation condition, but also on the composition of high temperature austenite, which in turn is dictated by the undissolved carbides in the austenite matrix. The sluggish diffusion of elements like Cr and W [195,200] combined with the effect of undissolved carbides during solutionising, it is highly probable that two types of austenite emerge in the steel which are designated as γ_1 and γ_2. γ_1 is the austenite transformed from ferrite/ tempered martensite regions around the undissolved precipitates, while γ_2 is the predominant austenite solid solution resulting from the regions devoid of precipitates. By mass balance considerations, the composition of γ_2 itself may not be same as that of the nominal composition of the steel, but slightly lower due to the locking up of solutes in the precipitates [201]. However, the composition of γ_2 is much higher than γ_1 and is conducive for the formation of α' in all the steels under the different austenitisation conditions. It is the composition of the solute lean γ_1 that is responsible for the observed precipitation of Fe rich carbides in the steels, which varies with W concentration and the austenitisation conditions.

Low enrichment of W in $M_{23}C_6$, in case of 1W – 0.06Ta steel [196] was the reason for the complete dissolution of carbides in this steel and hence a complete martensite structure is observed. The addition of Ta did not alter the composition of $M_{23}C_6$ and hence the observed undissolved carbides in 1W-0.14Ta steel correspond to Ta rich MX. The change in number density of MX did not show significant change in the lath martensite microstructure in 1W – 0.14Ta steel. The observed full martensite structure in both the cases is attributed to the absence or presence of very negligible amount of solute lean austenite.

The steel with highest W and C content namely 2W – 0.06Ta steel, showed the highest amount of undissolved carbides (**Figure 4.1**), specially the Cr and W containing $M_{23}C_6$ after austenitisation at 1253 K. Hence γ_1 that formed in the vicinity of these undissolved $M_{23}C_6$ will be depleted of W, Cr and C compared to the γ_2 forming in the matrix away from undissolved carbides. Thus, the solute lean γ_1 exhibits higher M_s temperature compared to that for the steel. Therefore the driving force for the martensite formation is reduced for γ_1. As a consequence, the C curve of the TTT diagram is shifted towards shorter times and can be intercepted by the cooling curve corresponding to air cooling and even water quenching. However, type and amount of precipitate is governed by the 'time of stay' in the temperature regime of concern. The formation of a small amount of Fe rich M_3C during water quenching and Fe rich $M_{23}C_6$ with a small amount of Cr during normalising at 1253K can be understood in the light of 'time of stay', which is a function of the cooling rate. This is also evident from the higher amount of $M_{23}C_6$ formed with the increased time of stay as W increases, though it was difficult to quantify due to the small areas probed in TEM. The prevalence of coarse laths with precipitates on air cooling rather than on water quenching can also be understood along the same lines. A schematic representation of the secondary precipitation on cooling of γ_1 from 1253 K in 2W-0.06Ta steel is shown in **Figure 4.8**. It is also to be mentioned that the Ac_3 and Ac_1 temperatures of γ_1 is dictated by the net effect of the concentration of α and γ stabilisers. The prediction of Ac_3 and Ac_1 temperatures for such an austenite would be difficult and for the sake of simplicity, this variation with T_γ or W, C concentration is ignored.

In view of the higher dissolution of precipitates in 1.4W-0.06Ta than 2W-0.06Ta steel on austenitisation, it is expected that the solute concentration of γ1 in 1.4W-0.06Ta steel would be relatively higher than that of the 2W–0.06Ta steel. Hence, a smaller shift in C-curve is expected in 1.4W-0.06Ta steel. Further the M_s temperature of the steel is expected to be lower. The higher temperature interval (ΔT) between T_γ and M_s in turn increases the driving force for $\gamma \rightarrow \alpha'$ transformation. Therefore, there is less possibility of the cooling curve intercepting the C-curve on water quenching thus supporting a fully martensitic structure as observed in this study. The conditions for formation of Fe rich M_3C on air cooling is also depicted in **Figure 4.8**.

As the austenitisation temperature is increased to 1323K, the increased dissolution of the carbides suggests that γ_1 would also be richer w.r.t the solutes Cr, W and C. Hence, for such an austenite, the M_s temperature is suppressed, the driving force for martensite formation is enhanced and the C-curve shifts further towards higher times as compared to 1253K. The slope of the cooling curves also decreases, the decrease being higher for air cooling. When water quenched, any secondary precipitation from γ_1 is suppressed,

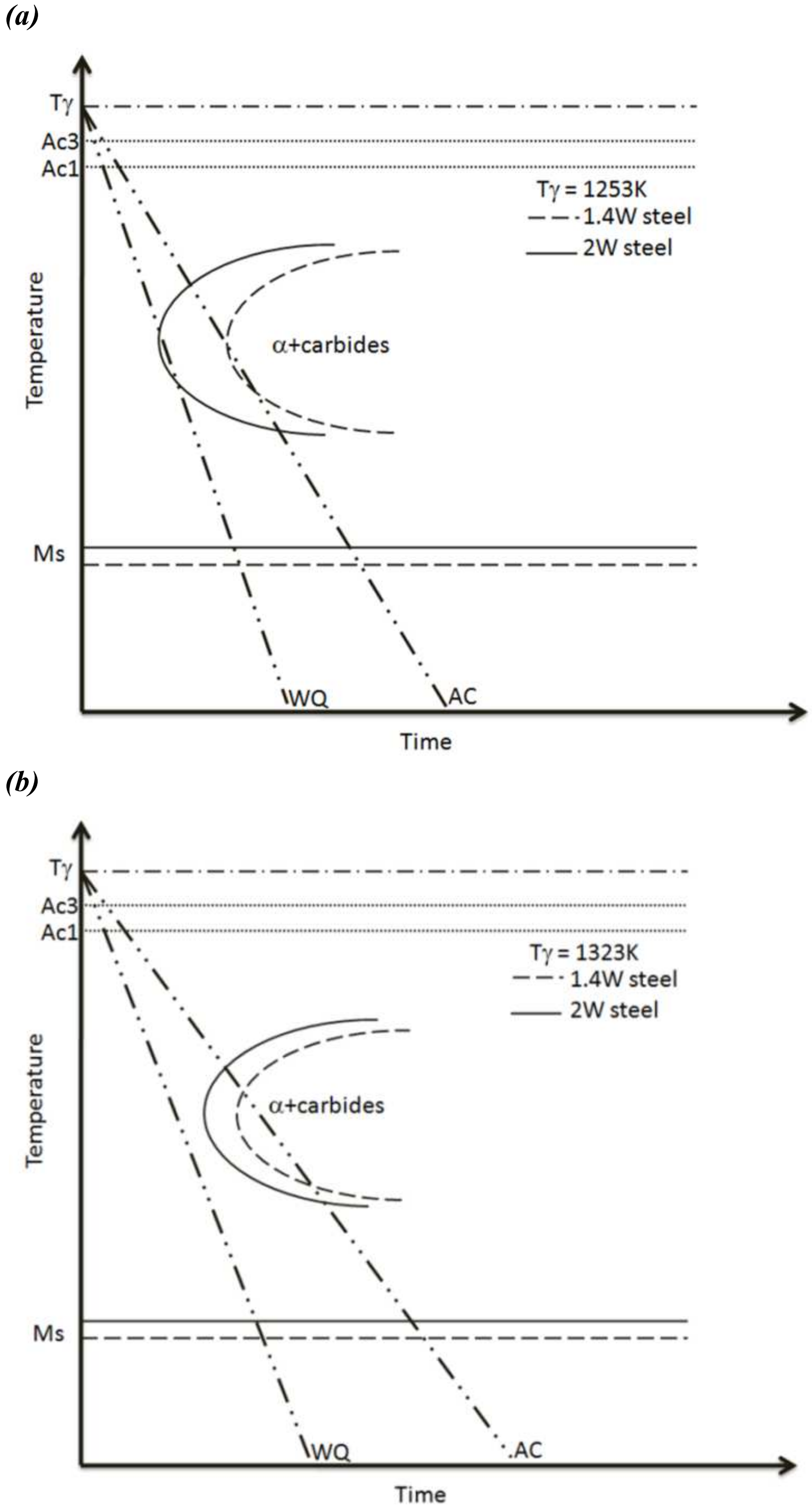

Figure 4.8. *Schematic TTT diagrams of 1.4W and 2W steels with superposition of cooling curves to illustrate the precipitation from solute lean* γ_1*, for austenitisation at (a) 1253K and (b) 1323K*

while on air cooling, due to a finite time of stay within the C-curve, precipitation of $M_{23}C_6$ takes place in both steels. Precipitation of $M_{23}C_6$ has also been reported in plain 9Cr-1Mo-0.07C steel normalised from 1323 K [201]. The same scenario prevails for RAFM steels, when austentised at 1323K, but with a lower extent of right shift of the C-curve and depression of M_s temperature for the 1.4W steel. **Figure 4.8**(b) shows a schematic depiction of precipitation on cooling of γ_1 from 1323 K in 1.4–0.06Ta and 2W–0.06Ta steels.

Hence based on strong microstructural evidences and DSC analysis, it is concluded that the inhomogeneity in composition of the austenite caused by the sluggish dissolution of W enriched carbides is responsible for the shift in the transformation characteristics, mainly the C-curve and change in M_s temperature, thus altering the driving force for martensitic transformations.

4.3 Study of martensite characteristics

The characteristics of martensite in 1.4W-0.06Ta steel have been studied by both Mossbauer spectroscopy and Orientation Imaging Microscopy in TEM. Mossbauer spectra of normalised 1.4 W-0.06Ta steel and after tempering are shown **Figure 4.9 (a,b**) respectively. It is observed that the spectrum corresponding to the normalized steel in **Figure 4.9(a)** could be deconvoluted into three six line patterns, implying that the majority of the Fe atoms are exposed to magnetic interaction and the matrix is ferromagnetically ordered with hyperfine field value of ~ 33 Tesla lying close to the Fe atoms occupying Fe matrix [202]. In addition, Mossbauer spectrum obtained in the normalized sample showed a single line pattern with a relative area of 6%. Based on the relative area of the spectrum resulting in six line pattern, it could be deduced that close to 94% of relative fractions of Fe atoms are exposed to magnetic interactions.

This implies that about 6% of Fe atoms experiencing only electric monopole interaction and do not experience any magnetic interaction. This is understood to be due to Fe atoms associated with non magnetic cubic phase with a fcc structure, which could be retained austenite or the undissolved primary carbides of $M_{23}C_6$ and MX.

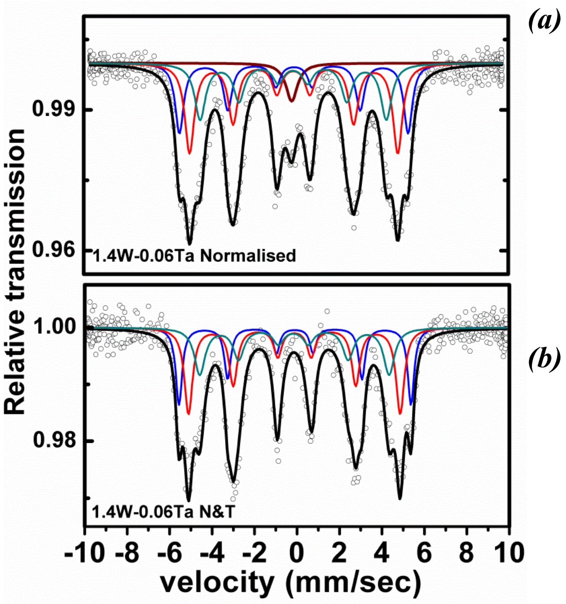

Figure 4.9 *Mossbauer spectra of the 1.4W-0.06Ta steel in the (a) normalized condition showing the presence of a single line pattern due to low amount of retained austenite and (b) normalized and tempered condition showing only ferromagnetic ordering*

In order to identify the non magnetic cubic phase, the Mossbauer spectrum of the normalized and tempered steel was also obtained and is shown in **Figure 4.9(b).** The spectrum could be deconvoluted only into three six line patterns without any single line pattern, indicating complete ferromagnetic ordering. It is well known that the amount of $M_{23}C_6$ and MX is higher in tempered steel than the normalized steel with a fully martensitic structure, as shown in the previous sections. This suggests that the single line pattern observed in the normalized steel is due to retained austenite and not due to the precipitation of $M_{23}C_6$ and MX. The absence of the singlet in the Mossbauer spectrum of tempered steel is in fact a strong evidence for the decomposition of retained austenite during tempering.

Conventional TEM and XRD experiments did not provide evidence for the presence of retained austenite in the normalized 1.4W-0.06Ta steel, which is attributed to its low volume fraction. However, synchrotron XRD analysis showed a strong asymmetry of the $(110)_\alpha$ peak, which could be deconvoluted to show a small peak corresponding to $(111)_\gamma$, which was not observed in the pattern from the tempered steel. This observation supports the conclusions drawn from the Mossbauer spectroscopy analysis. Crystal orientation map of the steel obtained by EBSD in **Figure 4.10(a)** shows the orientation of the martensite laths in different austenite grains in the normalized steel, which provided no evidence for retained austenite. Further, automated Crystal Orientation Imaging Microscopy (OIM) studies were carried out in TEM, on thin foils of the steel in both conditions. The crystal orientation map from a microscopic region obtained by OIM in TEM in **Figure 4.10(b)** also shows the different orientations of martensite in three austenite grains. **Table 4.3** lists the possible orientation relationship for fcc to bcc transformation [202 -204]. The analysis of orientation relationship is beyond the scope of the present work, although it is reported that, Kurdjumov-Sachs (K-S) or Nishiyama-Wassermann (N-W) OR is followed in low carbon steels, which are related to each other through small rotations [205, 206]. From **Figure 4.10 (a and b)** it is clearly observed that several orientations of the martensite packets nucleated from the 4 {111} planes of γ suggesting no variant selection. This can be understood in terms of the high cooling rate adopted.

Based on inputs on unit cell parameters and space group details of bcc α-Fe, fcc γ-Fe and fcc $M_{23}C_6$, for the TEM OIM mapping, the reliability maps in **Figure 4.10 (c and d)** show higher reliability for fcc γ-Fe than fcc $M_{23}C_6$, which is also significantly different in chemical composition. The analysis of the phase map in **Figure 4.10(e)** provides unambiguous evidence for the presence of low amount of retained austenite (~ 2%).

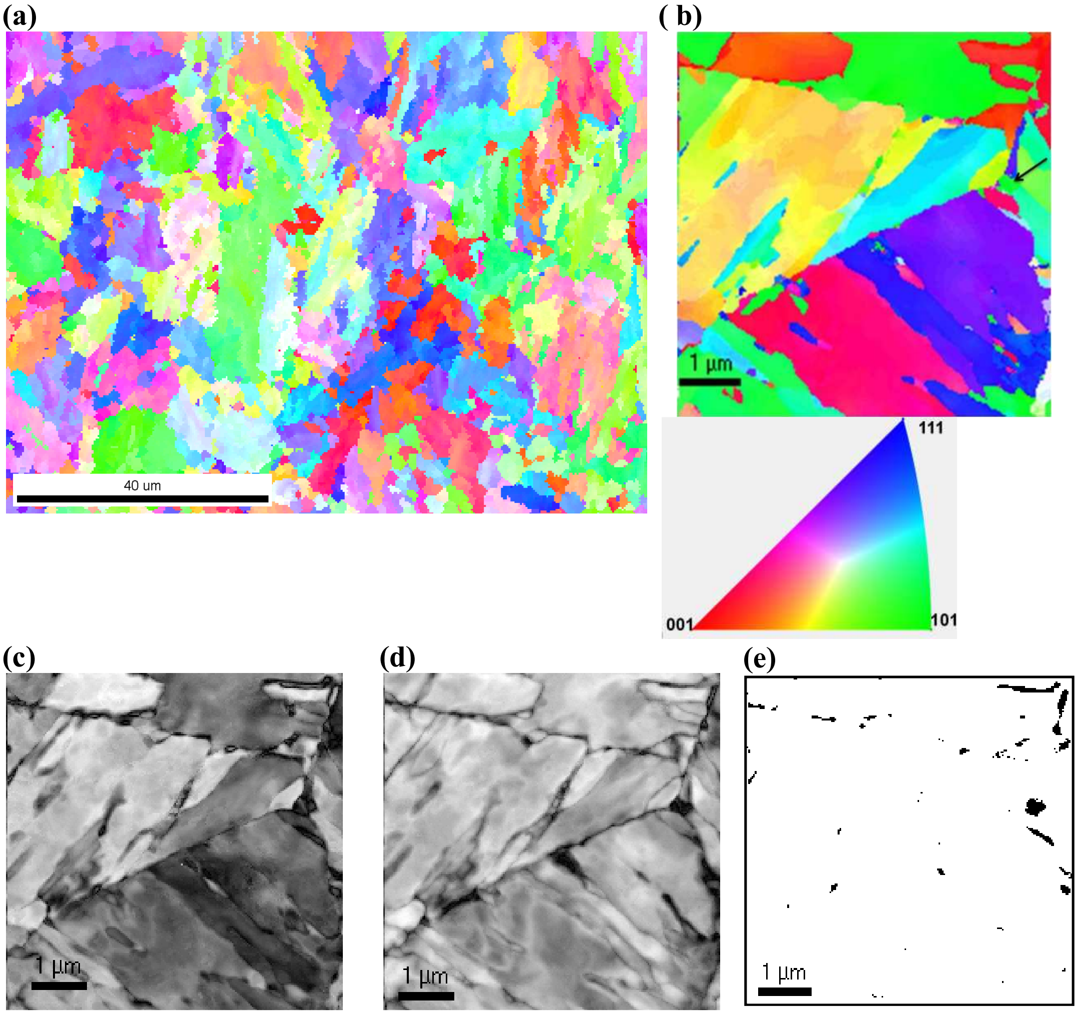

Figure 4.10 *(a & b) Orientation imaging of 1.4W-0.06Ta steel showing different orientation of martensite laths,(c & d) Reliability maps of the fcc γ and fcc $M_{23}C_6$ phases respectively and (e) phase map showing retained γ*

Table 4.3 *Four most commonly used γ/α orientation relationships*

OR	Plane	Direction
Bain	$\{010\}_\gamma \| \{010\}_\alpha$	$< 001>_\gamma \| <101>_\alpha$
Kurdjumow-Sachs	$\{111\}_\gamma \| \{110\}_\alpha$	$<110>_\gamma // <111>_\alpha$
Greninger-Troiano	$\{111\}_\gamma \sim 1^\circ \| \{110\}_\alpha$	$<12,17,5>_\gamma \| <17, 17, 7>_\alpha$
Nishiyama-Wassermann	$\{111\}_\gamma \| \{110\}_\alpha$	$<011>_\gamma \| <001>_\alpha$ or $<112>\gamma \| <110>_\alpha$

9Cr ferritic martensitic steels are known to be air hardenable with high M_s and M_f temperatures and retention of austenite is rather unexpected. However, the presence of retained austenite has been reported in few low Cr steels, which has been understood in terms of the mechanical stabilization of austenite by transformation stresses, especially in weldments [207]. The observation of retained γ along with α' facilitates the direct determination of Orientation Relationship, unlike in cases where a restitution procedure has been adopted [205].

4.4 Kinetics and mechanism of tempering of martensite

Tempering of martensite was studied for all the compositions at three different temperatures, namely 923, 973 and 1033 K. The tempering kinetics was studied using hardness and micro strain analysis from XRD measurements. The microstructures that evolved were correlated with the kinetic data. The results are discussed below.

4.4.1 Variation of hardness with temperature and time

Tempering the steel decreases the hardness and is known to increase the ductility and toughness of the steel. The change in hardness during tempering is the result of a complex interplay between the change in solid solution strengthening, substructural changes and precipitation. Decrease in solid solution strengthening and recovery decreases the hardness. Softening of the matrix takes place due to the depletion of elements like C, Cr, W, Ta and V in the matrix as a result of precipitation of secondary phases, while fine precipitate phases can also strengthen the matrix by pinning the dislocations. The overall change in hardness is dictated by the dominant mechanisms. The change in hardness as a function of temperature and time of tempering is plotted in **Figure 4.11** for all the steels. As observed in earlier studies, a decreasing trend of hardness is observed with temperature and time of tempering, indicating softening of the matrix. The data has been found to fit to the following expression-

$$H_t = A \exp(-kt) + H_{sat} \qquad \text{---------(4.1)}$$

Where, H_t is hardness at any time t, H_{sat} is saturation hardness and A, k are constants.

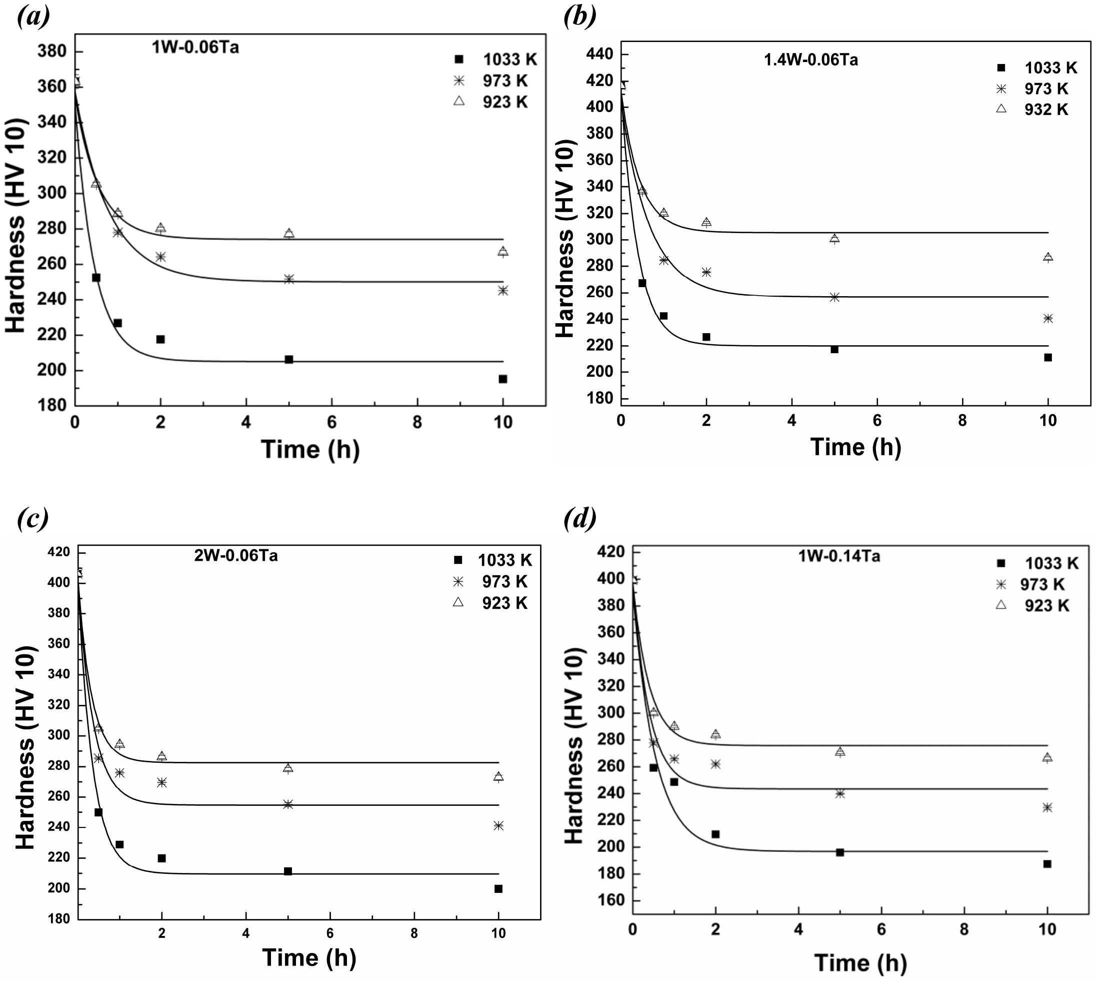

Figure 4.11 *Variation of hardness in steels with different W and Ta content (error associated is ±4 HV 10)*

Analysis of hardness variation with time at different temperatures showed the following features:

- A steep decrease in the hardness up to about 2 hours, beyond which saturation is observed.
- The decrease in hardness was highest at 1033 K indicating the higher rate of recovery of martensitic substructure.
- The saturation value of hardness was highest for 1.4W-0.06Ta steel and lowest for 1W- 0.14Ta steel, despite its high initial hardness in the normalized condition, suggesting that addition of W up to 1.4 wt. % is beneficial in strengthening the steel in contrast to Ta. Further addition of W up to 2 wt. % did not show appreciable change in hardness. This may be due to the decrease in solid solution strengthening due to the possible excess precipitation. The effect of precipitation is discussed further in this chapter.

Though an increase in hardness during initial stages of tempering is expected due to the formation of fine precipitate phases, the actual decrease in hardness observed during tempering suggested that the decrease in solid solution strengthening and dislocation annihilation dominates over precipitation strengthening. Detailed description of the supporting microstructural features is essential to understand the process, which will be discussed later.

4.4.1.1 Identification of optimum tempering conditions

The factors to be considered for the optimization of tempering parameters were discussed previously. Based on the hardness data presented in **Figure 4.11** and the detailed analysis of the observed hardness trends, an exponential decrease of hardness is evident. The optimum tempering time was fixed to be 60 – 90 minutes, which is close to the saturation value of hardness. Further, the temperature was fixed to be 1033 K due to the higher recovery of martensitic substructure, which provides microstructural stability during service. Hence in industrial practice, the tempering temperature is 1033 K and duration is 60 to 90 minutes. In the present study the tempering time is fixed as 60 minutes followed by air cooling, due to the small size of the sample used.

4.4.1.2 Kinetics of Tempering - Arrhenius analysis

In the present study, rate of change of hardness ($\Delta H/\Delta t$) was taken as a parameter to study the kinetics of tempering of martensite [208,209]. The plot of $\ln(\Delta H/\Delta t)$ vs $1/T$ is presented in **Figure 4.12**. A linear behavior with a constant slope is observed, which follows the Arrhenius equation-

$$k = A \exp(-Q / RT) \tag{4.2}$$

Where k is rate constant, T the absolute temperature (K), A is the pre-exponential factor, Q is the activation energy, and R is the universal gas constant. In the present study equation 4.2 can be written as –

$$(\Delta H/\Delta t) = A \exp(-Q / RT) \tag{4.3}$$

Hence the rate of change of hardness has been fitted to the equation

$$\ln(\Delta H/\Delta t) = (-Q / RT) + \ln B \tag{4.4}$$

where B is the proportionality constant

Activation energy (Q) for the overall tempering reaction has been calculated from the plot for all the four steels. The calculated values of activation energy are presented in **Table 4.4**. The calculated values of Q (~ 0.7-1.1eV) correspond to the activation energy for the diffusion of C in α-Fe (0.83 eV) [210-212]. Hence, it is evident that the dominant reactions taking place during tempering depends on the interstitial diffusion of C in the matrix to form the precipitates namely $M_{23}C_6$ and MX. The formation of these carbides and their chemistry is discussed later in this chapter. Since the diffusion of substitutional alloying elements are sluggish in nature, it is expected that $M_{23}C_6$ form initially with higher solubility of Fe, which eventually is replaced by the Cr atoms. It is observed that the activation energy shows a small change with W and Ta content of the steel.

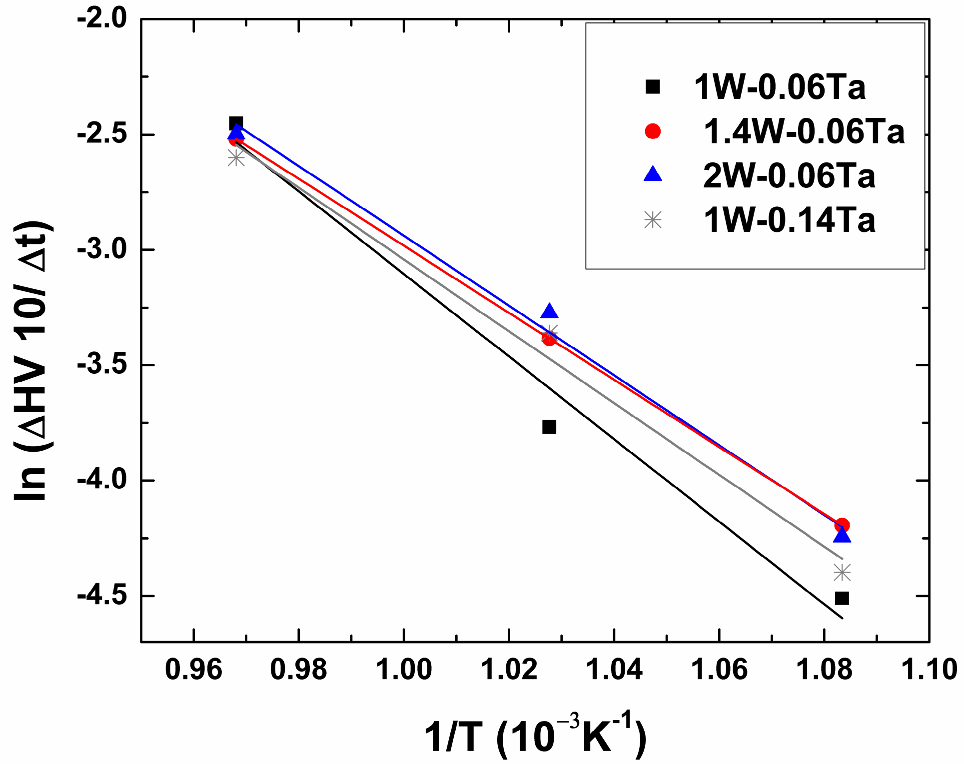

Figure 4.12. *Arrhenius plot for the steels with different W and Ta content.*

Table 4.4. *Activation energy for the tempering process in RAFM steels*

Steel	**Q (eV)**
1W-0.06Ta	1.09
1.4W-0.06Ta	0.73
2W-0.06Ta	0.74
1W-0.14Ta	0.93

4.4.1.3 Microstrain analysis

It is known that, when martensite in normalized steel with a high dislocation density is tempered, the dislocation density decreases due to the recovery of martensite [213]. The degree of tempering will also manifest as a variation in microstrain of martesnite. Hence in addition to the hardness analysis, the variation of microstrain of the normalised steel during tempering has been studied using X-Ray Diffraction. A case study has been performed for 1.4W-0.06Ta steel normalized at 1253 K followed by tempering at different temperatures from 923 to 1033 K. The full width at half maxima (FWHM) for the prominent (2 0 0) and (2 2 0) peaks of α- ferrite in the normalized steel and after tempering at different temperatures is listed in **Table 4.5**.Decrease in percentage strain in the steel has been taken as the measure to study the tempering kinetics. The martensite strain has been calculated using the equation –

$$S = (\Delta \text{ FWHM} / \text{FWHM}_{\text{ref}}) \times 100 \qquad \text{----------} \quad (3.5)$$

Where Δ FWHM refers to the difference in FWHM value between the heat treated steel and reference, FWHM_{ref} refers to that of normalized (1253K / 30minutes) and tempered (1033K / 1hour) steel. A decrease in FWHM was observed in the thermally exposed samples as compared to the normalised steel, indicating a decrease in strain in the matrix due to tempering of martensite.

Table 4.5. *FWHM for the prominent (200) and (220) peaks of α-ferrite showing decrease with time/ temperature*

(hkl)	*FWHM* $_{(200)}$			*FWHM* $_{(220)}$		
Temperature (K) → Time (h) ↓	923	973	1033	923	973	1033
0	0.72	0.72	0.72	0.78	0.78	0.78
0.5	0.645	0.643	0.561	0.698	0.644	0.606
1	0.629	0.649	0.472	0.692	0.633	0.488
2	0.574	0.575	0.577	0.636	0.605	0.587

The plot of S vs exposure time (**Figure 4.13(a)**) shows an exponential behaviour similar to hardness changes. An Arrhenius plot of ΔS / Δt vs. 1 / T is presented in **Figure 4.13(b)**. Activation energy (Q) for the overall tempering reaction has been calculated to be 0.5 eV. The activation energy corresponds to the interstitial diffusion of C in α-Fe, although the value is lower than that arrived from the hardness data. Hence, from the above studies it can be concluded that the strain relief in the matrix is due to the carbon diffusion from the matrix to the prior austenite grain / lath boundary to form carbides. Since the tempering process depends on the diffusion of interstitial carbon in ferrite, it therefore is the rate controlling step for the tempering process.

4.4.2 Mechanism of tempering

Hardness variation during short time heat treatment is a resultant of the synergistic effect of the following reactions:

1. Decrease in hardness due to annihilation of martensite induced dislocations at the grain and lath boundaries
2. Initial increase in hardness due to nucleation and growth of fine secondary phases ($M_{23}C_6$ and MX), which subsequently decreases the hardness as precipitates coarsen.
3. Decrease in hardness due to loss of solute elements from ferrite matrix.

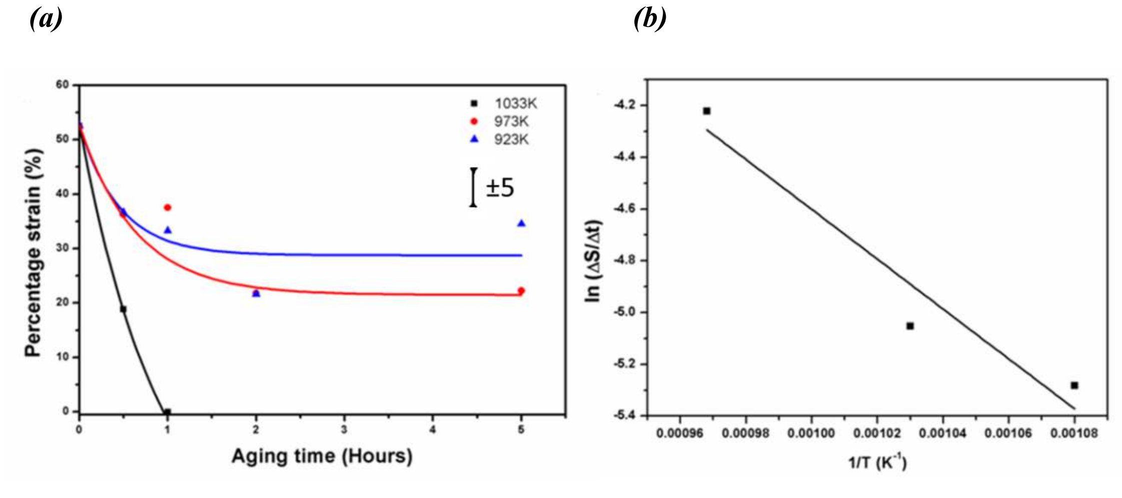

Figure 4.13 *(a) Variation of strain with time and temperature in 1.4W-0.06Ta steel showing an exponential decrease (b) Arrhenius plot for determining activation energy*

The overall effect of decrease in hardness suggested that the dislocation annihilation and loss of solute elements from the matrix over rides the effect of precipitation strengthening during tempering. An attempt has been made to understand the mechanism of tempering through the study of microstructural changes in the steel, which is discussed in the next section.

4.4.3 Evolution of microstructure during tempering:

4.4.3.1 Effect of temperature

Figure 4.14 shows TEM thin foil micrographs of 1.4W–0.06 Ta steel tempered for 30 minutes at 923, 973 and 1033 K respectively. A lesser extent of recovery of martensite is evident from the micrograph at 923 and 973 K, which is also expected from the observed change in hardness. With increase in tempering temperature to 1033 K, the recovery is rapid due to the higher mobility of dislocations. The detailed analysis of micrographs at three different temperatures showed the following features –

- Fine laths with high density of dislocations and fine precipitates at lath boundaries suggested a slow recovery of martensitic laths at 923 and 973 K.
- Laths with comparatively low dislocation density and coarse precipitates than that observed at low temperature tempering suggested the faster recovery of substructure at 1033 K. Formation of subgrains was also evident from the micrograph.
- No significant variation in lath width with temperature.

The observed large change in hardness at 1033 K is attributed to the change in dislocation density and softening of matrix due to the coarse precipitates at the lath boundaries and prior austenite grain boundaries. Similar observations have been made in the other steels. The comparison between four steels will be discussed in the subsequent section of this chapter.

Figure 4.15 shows the carbon extraction replica of the 1.4W-0.06Ta steel tempered at 923 K for 30 minutes. The micrograph shows a high number density of fine precipitates. Presence of coarse globular / acicular precipitates on the grain and lath boundaries suggested the faster nucleation and growth of precipitates at the boundaries than within the laths. This is in line with the faster diffusion of solute atoms along the grain boundary. **Figure 4.15 (b, c)** show the SAED patterns corresponding to a fine, intralath

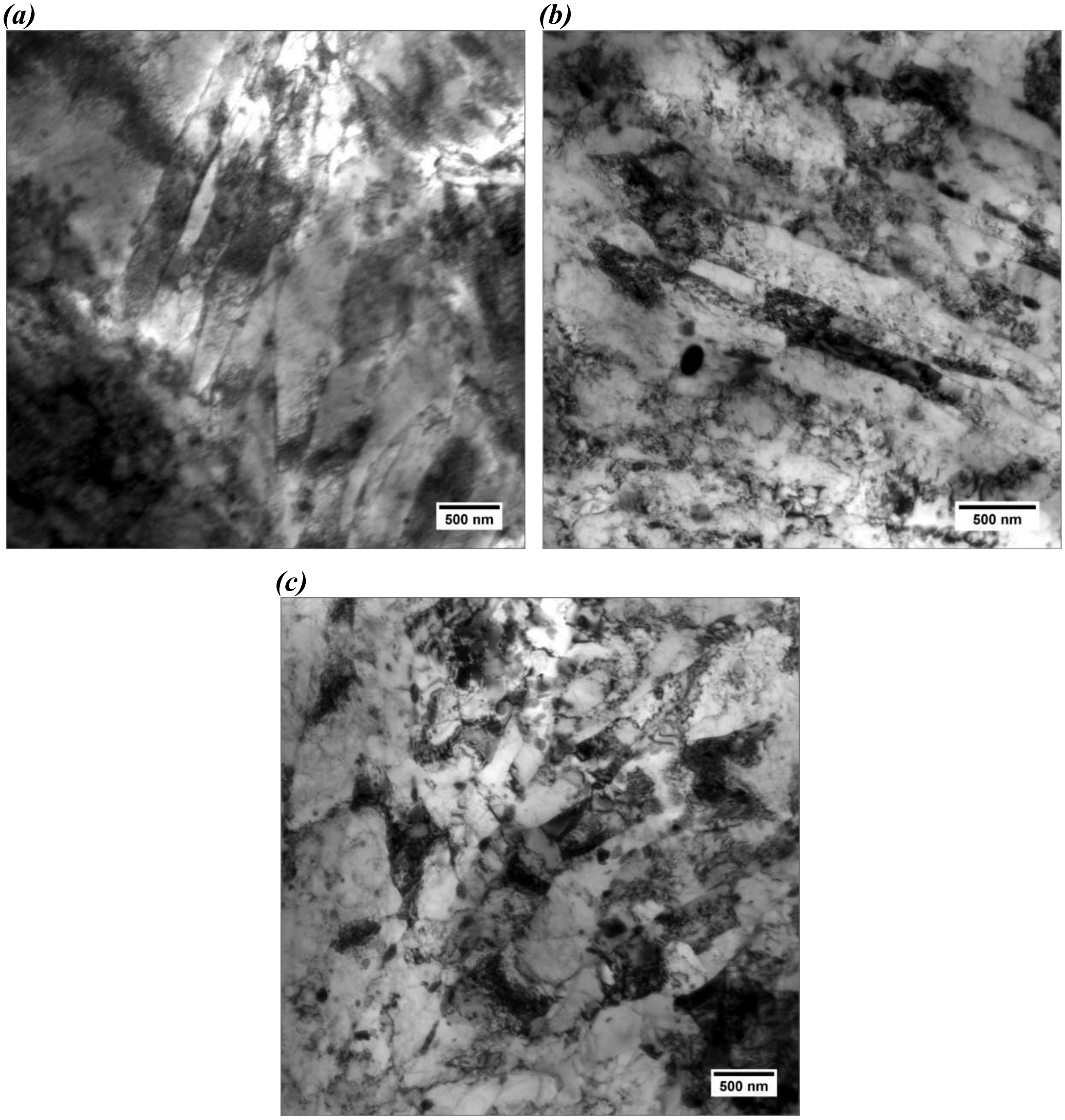

Figure 4.14 *TEM thin foil micrographs of 1.4W-0.06Ta steel tempered for 30 minutes at (a) 923, (b) 973 and (c) 1033 K showing lath structure*

MX and a coarse, acicular interlath $M_{23}C_6$ respectively. **Figure 4.15(d)** shows the EDX spectra from these carbides, in addition to that of a fine, acicular Fe rich intralath $M_{23}C_6$. Presence of Fe rich $M_{23}C_6$ precipitates were not detected in the samples tempered at 973 and 1033 K after 1 h. Coarse $M_{23}C_6$ precipitates with acicular / globular morphology and fine V or Ta rich MX precipitates were evident from TEM studies, which indicates the instability of Fe rich $M_{23}C_6$ at higher temperature. Presence of Fe rich $M_{23}C_6$ precipitates at lower temperature was more prevalent in steels with higher W content of the steel, which dissolved at higher temperatures.

4.4.3.2 Effect of exposure time at 923 K

Figure 4.15(a, b) shows respectively the thin foil micrograph and carbon extraction replica of 1.4W-0.06 Ta steel tempered at 923 K for 10 h. Presence of few coarse carbides and lath structure with comparatively reduced dislocation density after 10 h of thermal exposure is observed (**Figure 4.15(a)**) suggesting a recovery at slow rate, which is in contrast to the insignificant recovery after 30 minutes of thermal exposure at the same temperature **(Figure 4.14)**. However, lath width remained around 300 nm, similar to that in normalized condition and no evidence could be obtained for the formation of subgrains. EDX analysis of the precipitates in **Figure 4.15(b)** did not show the presence of Fe rich $M_{23}C_6$. This observation suggests that Fe rich interlath $M_{23}C_6$ observed after 30 minutes of exposure at 923 K (**Figure 4.14**) eventually dissolves more Cr as it grows. Typical composition of the precipitates marked is also listed in **Table 4.6,** which shows that $M_{23}C_6$ is enriched with Cr**.** The evolution of the precipitates during tempering at 923 K in the 1.4W-0.06Ta steel can therefore be represented as –

$$\alpha' + M_{23}C_6\ (undissolved) + MX\ (undissolved)$$

$$\downarrow\ 30\ min.$$

$$\alpha + M_{23}C_6\ (undissolved) + MX\ (undissolved) + Fe\ rich\ M_{23}C_6 + Cr\ rich\ M_{23}C_6 + MX$$

$$\downarrow\quad after\ 10\ h$$

$$\alpha + M_{23}C_6\ (undissolved) + MX\ (undissolved) + Cr\ rich\ M_{23}C_6 + MX$$

The same behaviour was observed in other steels with different W and Ta content.

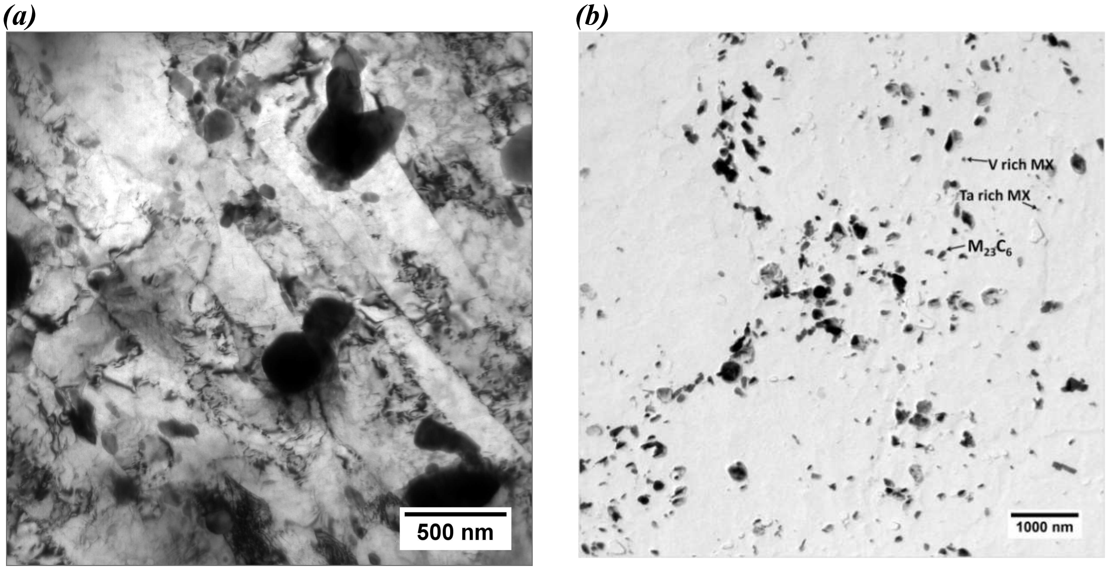

Figure 4.15 *(a) Thin foil micrograph of 1.4W-0.06 Ta steel tempered at 923 K for 10 h showing retention of lath structure even after 10 h and (b) carbon extraction replica micrograph of the same steel showing different types of precipitates*

Table 4.6. *Composition of precipitates marked in* ***Figure 4.15***

wt.%	Cr	Fe	W	Ta	V
$M_{23}C_6$	52.99	24.99	22.02	-	-
Ta rich MX	-	6.03	-	72.90	21.07
V rich MX	-	-	-	39.21	60.79

4.4.3.3 Effect of exposure time at higher temperatures of 973 and 1033 K

Figure 4.16 (a,d) shows the carbon extraction replica micrographs of 1.4W–0.06 Ta steel after tempering at 973 and 1033 K for 30 minutes and 10 h. respectively.

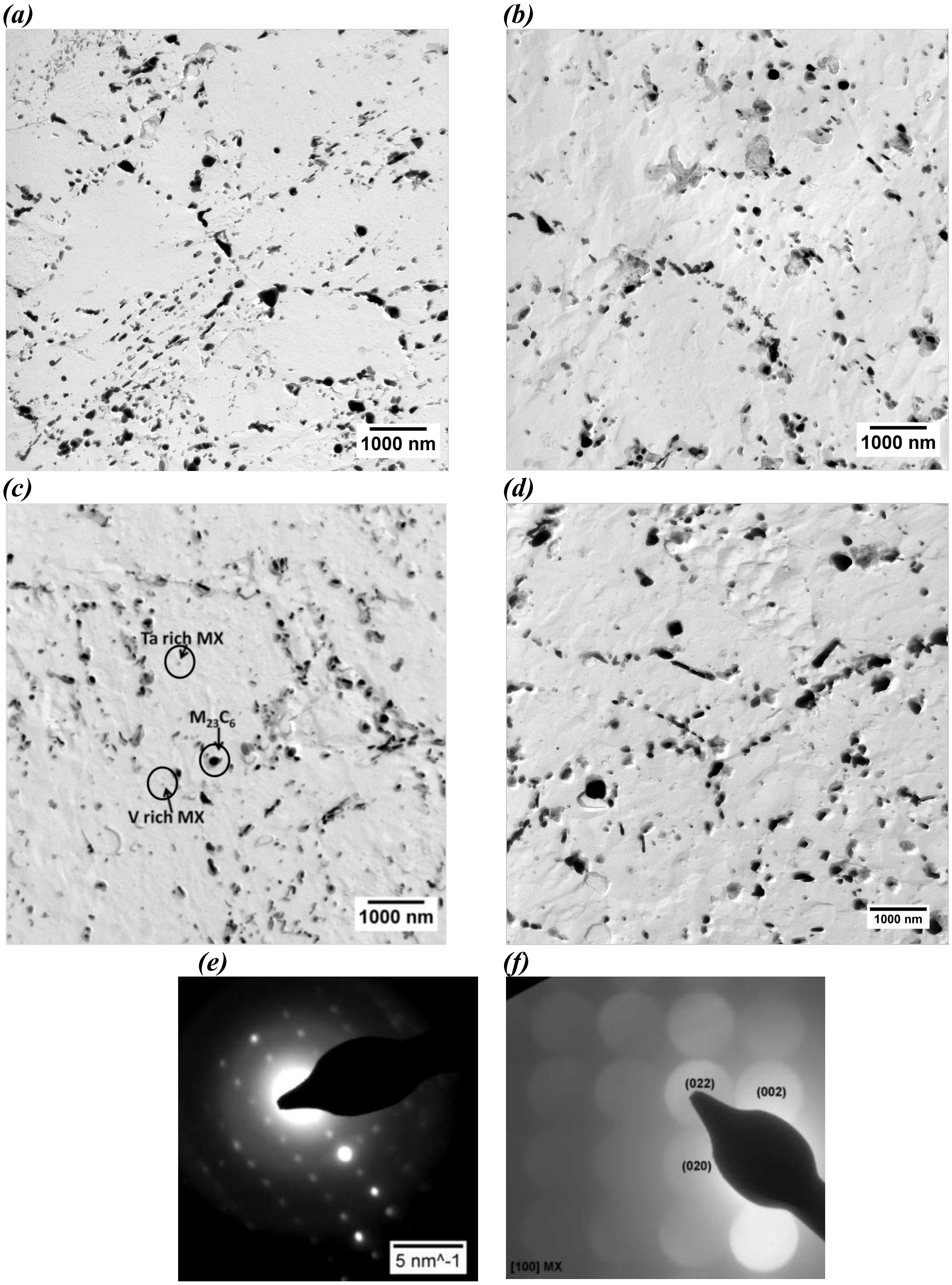

Figure 4.16. *Carbon extraction replica micrographs of 1.4W-0.06 Ta steel tempered at (a) 973 K for 30 minutes, (b) 973 K for 10 h, (c) 1033 K for 30 minutes, (d) 1033 K for 10 h showing $M_{23}C_6$ and MX precipitates; Electron diffraction patterns of (e) $M_{23}C_6$ along [0 1 -1], and (f) MX along [1 0 0] zone axis marked in (c)*

Table 4.7. *Composition of precipitates marked in* ***Figure 4.16(c)***

	Cr	Fe	W wt.%	Ta	V
$M_{23}C_6$	55.18	26.59	17.42	-	-
Ta rich MX	-	6.94	-	64.87	28.20
V rich MX	-	-	-	29.28	70.72

Tempering at 973 and 1033 K showed similar microstructural features though there was a significant change in the hardness, which is attributed to the size distribution of the precipitates as observed from **Figure 4.16((a, b) and (c, d))**. Micrographs presented clearly shows the presence of $M_{23}C_6$ and MX phases, the microchemistry of which based on EDX quantified values is given in **Table 4.7**. Presence of Fe rich $M_{23}C_6$ as observed at low temperature tempering was not observed. However, the coarsening of $M_{23}C_6$ was evident after 10 h, which was also supported by the decrease in hardness with time as a result of softening of the matrix. Hence, the evolution of precipitates at 1033 K during tempering can summarised as-

$$\alpha' + M_{23}C_6 \text{ (undissolved)} + MX \text{ (undissolved)}$$
$$\downarrow > 30 \text{ min} - 10\text{h}$$
$$\alpha + M_{23}C_6 \text{ (undissolved)} + MX \text{ (undissolved)} + \text{Cr rich } M_{23}C_6 + MX$$

Figure 4.17 shows the size distribution of the precipitates at 1033 K as a function of time. Coarsening of precipitates was observed as a shift in the peak distribution. Presence of very fine MX precipitates after 10 h suggested the stability of fine MX precipitates with tempering time. The presence of fine MX is known [4] to provide strength to the matrix during service exposure. Stability of the size of MX contributes to the high temperature mechanical properties for prolonged service. It is clearly observed that the coarsening predominantly happens for the $M_{23}C_6$ carbides.

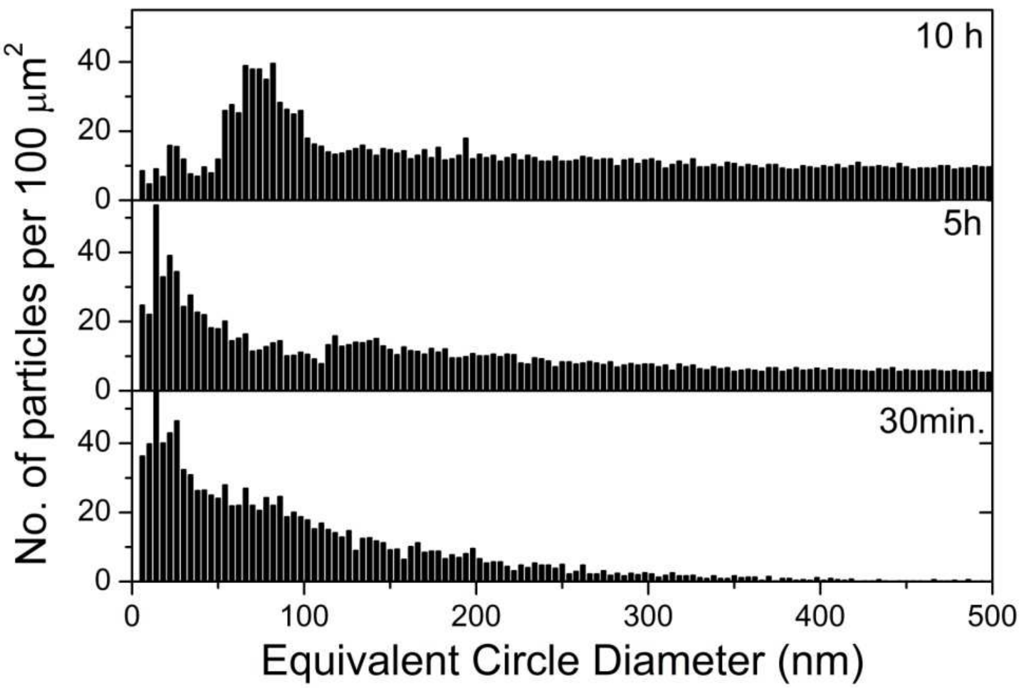

Figure 4.17 *Size distribution of the precipitates at 1033 K for 1.4W-0.06Ta steel as a function of time showing coarsening of carbides*

From the analysis of hardness variation (section 4.4.1) and the above discussion on microstructural evolution of 1.4W – 0.06Ta steel on tempering at different temperatures in the range of 923-1033K, it is observed that tempering at 1033 K for 1 h is adequate to produce a stable microstructure. Therefore further discussion on microstructural changes on tempering steels with different W and Ta content is confined to thermal exposure at 1033 K for 1 h.

4.4.4. Variation of microstructure and microchemistry with W and Ta content

4.4.4.1 Effect of W and Ta on substructure

Thin foil micrographs of the four steels tempered at 1033 K for 1 h presented in **Figure 4.18** shows partial recovery of martensite. The variation of lath width of the steel in normalised condition and after tempering is listed in **Table 4.8**. It is observed that there is a slight coarsening of the laths on tempering in all steels. However, the coarsening of

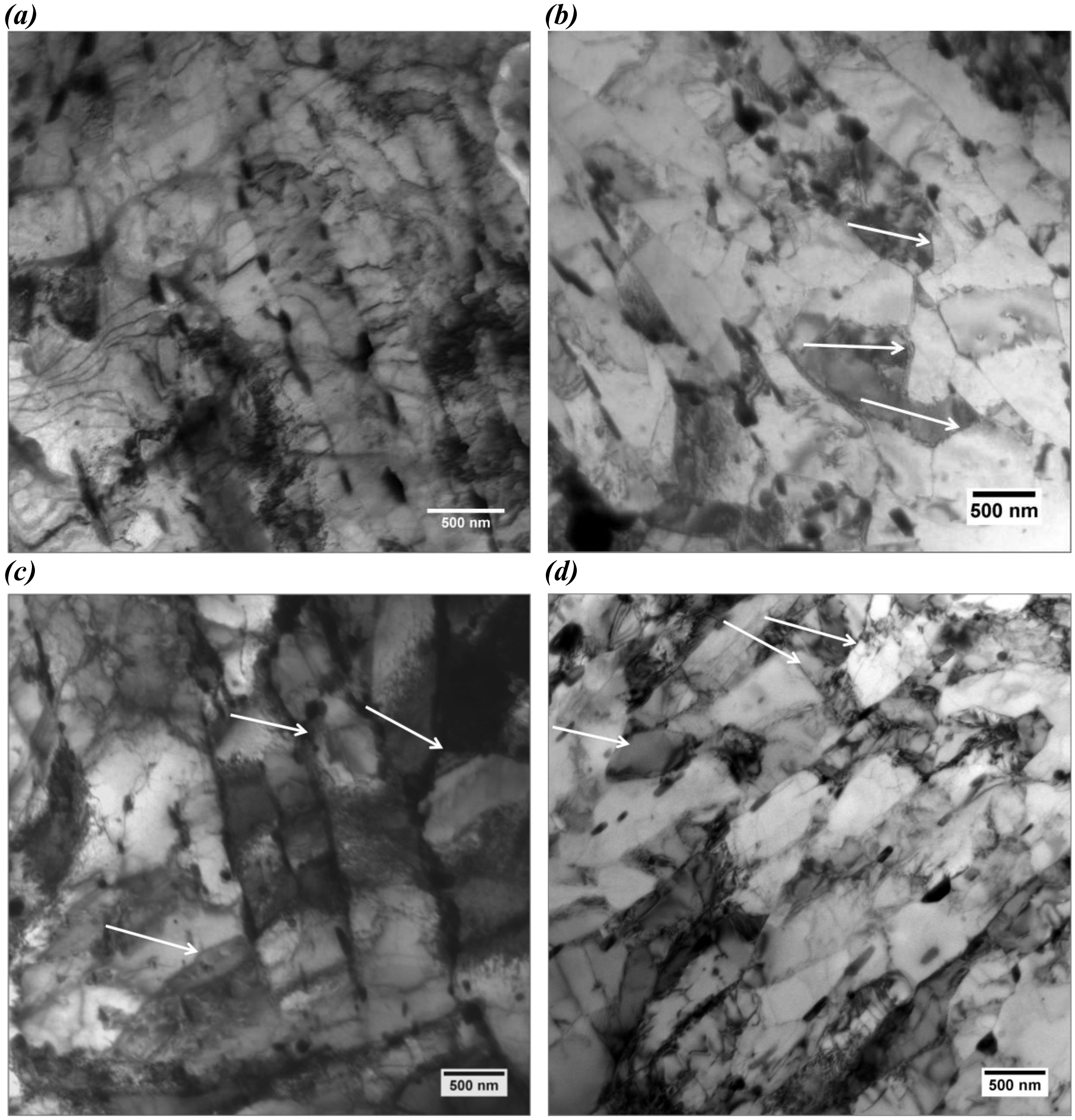

Figure 4.18. *Bright field TEM micrograph of steels tempered at 1033K for 1h (a) 1W – 0.06Ta, (b) 1.4W – 0.06Ta, (c) 2W – 0.06Ta, (d) 1W – 0.14Ta steel showing partial recovery in steels with higher W and Ta content*

laths on tempering is controlled more effectively by W than Ta. The substructure recovery was found to be a function of W and Ta content of the steel. 1W-0.06Ta steel showed recovery to less extent, while with increase in W and Ta content, formation of subgrain was evident as marked (arrow) in the micrograph. SAED pattern and EDX

Table 4.8. *Average values of lath width before and after tempering at 1033K*

Steel	*Normalised (±30) nm*	*Normalised and tempered (±30) nm*
1W-0.06Ta	*366*	*388*
1.4W-0.06Ta	*242*	*255*
2W-0.06Ta	*247*	*261*
1W-0.14Ta	*372*	*390*

analysis of a large number of precipitates showed the presence of coarse, interlath globular / acicular $M_{23}C_6$ precipitates and fine, intralath globular MX carbonitrides. The lower grain size in 1.4W–0.06Ta, 2W–0.06Ta and 1W–0.14Ta steels is expected to aid the recovery of dislocations. But, the dominant effect of precipitation of fine MX carbonitrides in the later stages of tempering retards the recovery by pinning the dislocations against the annihilation process, which enhances the long term microstructural stability.

4.4.4.2 Effect of alloy content on precipitation behavior

Figure 4.19 shows the frequency distribution of carbides as a function of size in the four steels after tempering at 1033 K for 1 h. Analysis of the size distribution of the carbides revealed that there are three different populations. In conjunction with the microstructural data, it is understood that the carbides on the prior austenite grain boundary were in the size range of 80 – 200 nm, those on lath boundary (LB) carbides had an average size range of 55 – 120 nm and majority of the very fine ones with a size < 75 nm corresponded to the intralath precipitates, though it was noted that all fine carbides were not the intralath carbides. Further, majority of such fine intralath carbides were found to be Ta and V rich MX carbonitrides, [4] essential for retention of mechanical properties during long term thermal exposure. The actual distribution was observed to be sensitive to the composition of the steel. It is seen that, with increase in

W and Ta concentrations of the steel, the size range of prior austenite grain boundary and lath boundary and intralath carbides shifts towards lower limits, while their number density increased.

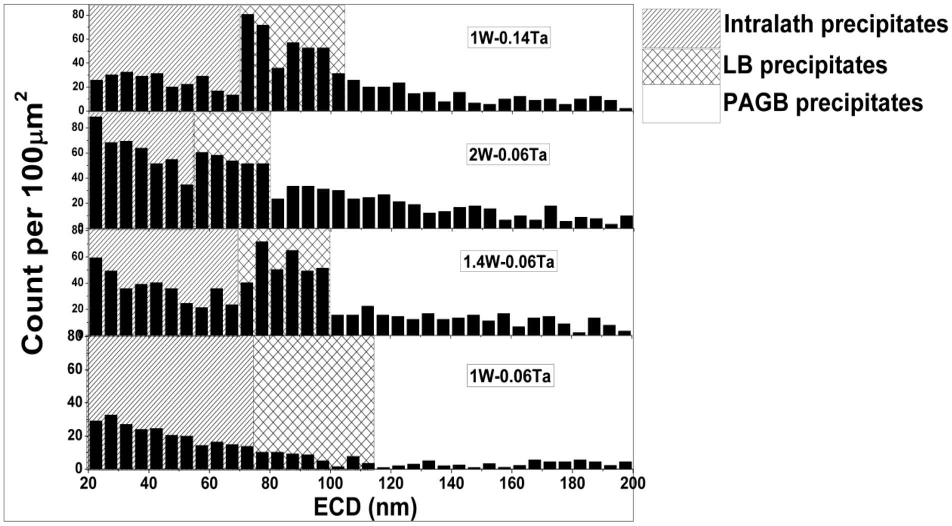

Figure 4.19. *Size distribution of precipitates in the four steels with W and Ta content after 1h of tempering at 1033 K*

An X-ray mapping has been carried out to identify and quantify the chemistry of the precipitates in 1.4W-0.06Ta steel, which is presented in **Figure 4.20**. It is clearly seen that the $M_{23}C_6$ precipitate is richer in Cr with the solubility of W and Fe, a negligible / small quantity of V also identified. MX precipitates were identified to be consisting of two types, one richer in V and the other richer in Ta marked as blue and white arrow in the **Figure 4.20(a)** respectively. Such an existence of two types of MX phases was also shown from the experimental and simulation studies in Chapter 3.

Microchemical variation of $M_{23}C_6$ and MX was studied for the other steels also. Definite trend for the chemical variation of MX could not be derived due to the large scatter in the data. However, the Ta rich MX showed 80 – 90 wt. % of Ta and a little solubility of V and Fe (few particles showed negligible amount of V and Fe), while V

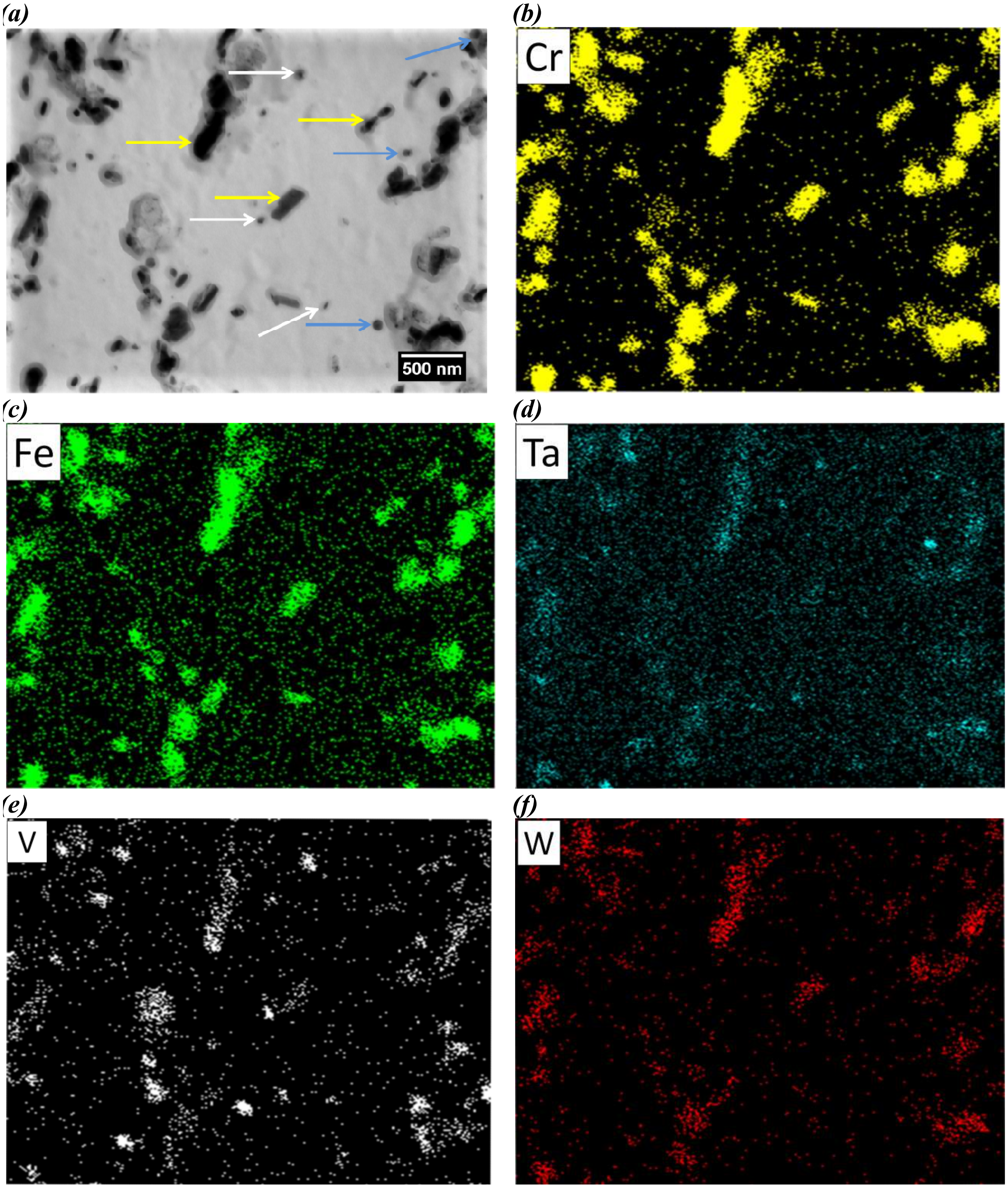

Figure 4.20. *(a) Carbon extraction replica micrograph of the 1.4W-0.06Ta steel tempered at 1033 K for 1h showing (b to f) X-ray maps of different elements corresponding to the different types of carbides present in the same region*

rich MX exhibited 50 – 70 wt. % V with about 30 – 40 wt. % Ta. The microchemical analysis of $M_{23}C_6$ is presented in **Table 4.9** shows the quantified values (in wt. %) of chemical entities namely Cr, Fe and W. Though there was a very small amount of V in very few coarse $M_{23}C_6$, those spectra were not considered for the quantification due to the lack of statistics. The variation in Cr, W and Fe listed in the table showed that there is a decrease in Fe and increase in W concentration of $M_{23}C_6$ with W content of the steel, while the concentration of Cr remained constant. The above result suggests that the increase in W content of the steel modifies the chemistry of $M_{23}C_6$. Literature [4,214] on the W added RAFM steels reported that the addition of W also delays the coarsening of $M_{23}C_6$ precipitates. The enrichment of W in $M_{23}C_6$ is also beneficial to delay the formation of W and Fe rich Laves phase, which is known to be beneficial when it is fine during nucleation and degrades the mechanical properties due to the rapid coarsening kinetics [4].

Table 4.9. *Microchemistry of $M_{23}C_6$ calculated from EDX analysis for normalised and tempered steels*

Steel	Chemical composition ±3 (wt.%)			Stoichiometry
	Cr	Fe	W	
1W-0.06Ta	53.9	27.7	18.4	$Cr_{14.6}Fe_{6.98}W_{1.41}C_6$
1.4W -0.06Ta	52.7	25.4	21.9	$Cr_{14.7}Fe_{6.56}W_{1.74}C_6$
2W- 0.06Ta	49.7	23.9	26.4	$Cr_{14.4}Fe_{6.44}W_{2.16}C_6$
1W -0.14Ta	57.2	26.2	16.4	$Cr_{15.25}Fe_{6.51}W_{1.23}C_6$

4.4.5 Simulation of evolution of secondary phases during tempering

Figure 4.21 shows the amount of different phases that evolve during thermal exposure at 1033 K, simulated with JMatPro for 1.4W-0.06Ta steel. The austenitisation temperature for the steel was 1253 K for the simulation. It is observed that M_3C, M_2X and M_7C_3 that form during initial stages, are not stable beyond 15 minutes of tempering, while after 1 h of tempering, the existence of $M_{23}C_6$ and MX phases are observed. The volume fraction of $M_{23}C_6$ and MX phases did not change significantly with time.

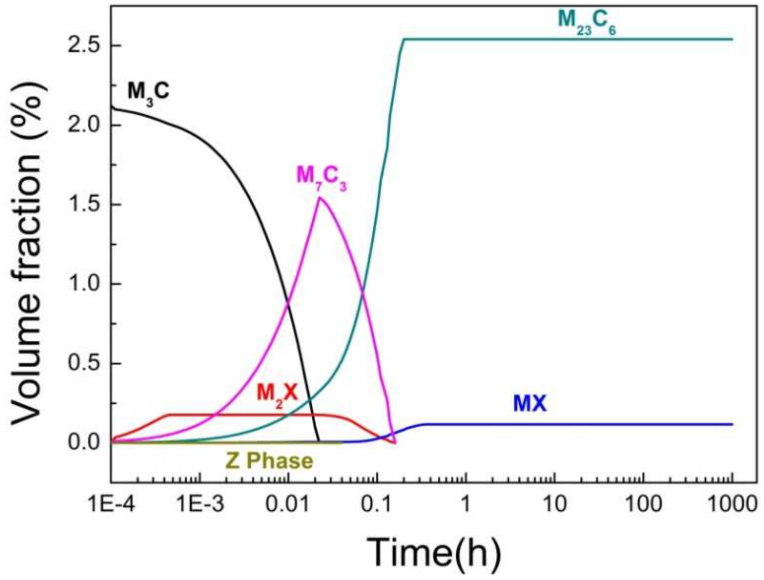

Figure 4.21. *Evolution of secondary phases in 1.4W-0.06Ta steel with time on tempering at 1033 K simulated using JMatPro*

To understand the effect of W and Ta, similar calculations were carried out for other steels with different W and Ta content, the results of which are tabulated in **Table 4.10**. Simulations showed that the volume fraction of $M_{23}C_6$ increased for the steels with higher W and Ta. Additionally, as mentioned earlier, the carbon concentration of such steels is high (0.12 wt.%) compared to that of 1W-0.06Ta steel (0.08 wt.%), which could also be responsible for the increase in volume fraction of carbides. This is also evident from the

(i) significant change in the volume fraction of $M_{23}C_{6,}$ when the W content of the steel increases from 1 to 1.14 wt. % and the Ta content of the steel increases from 0.06 to 0.14 wt.%.

(ii) slight increase in the amount of $M_{23}C_6$ with increase in W from 1.4 to 2 wt.%, where the carbon concentration of the steels is same.

However volume fraction of MX carbonitrides did not show significant variation with the alloy content, specifically even with increase in Ta content. This suggests that the addition of Ta to the steel increased the solid solution strengthening rather than precipitation of fine stable Ta rich MX, which is also reported in the literature [38,215].

***Table 4.10**. Phase fraction (in volume %) of carbides after 1 h of tempering at 1033 K simulated using JMatPro*

Steel	*$M_{23}C_6$*	*MX*
1W-0.06Ta	1.667	0.113
1.4W-0.06Ta	2.540	0.116
2W-0.06Ta	2.551	0.105
1W-0.14Ta	2.442	0.119

The above analysis of phase fraction of MX and $M_{23}C_6$ does not provide any information about the size distribution or microchemical variation of each type of precipitates. Hence no direct correlation with the experimental data has been attempted.

4.5. Conclusions

Role of alloy content on solution treatment condition and martensite characteristics have been studied under two different themes. The conclusions of the chapter are presented as follows –

- Microstructural parameters like PAGS, amount of undissolved precipitates and hardness of the steels show a systematic variation with W and Ta content.
- Solution treatment at 1253 and 1323 K resulted in complete martensitic structure in steel with 1 wt.% of W after air cooling and water quenching. Addition of W resulted in carbide precipitation in steels with 1.4wt. % of W or higher, though the predominant structure was martensite.
- The formation of such carbides has been attributed to the transformation of a solute lean austenite forming in the vicinity of the undissolved carbides during austenitisation. The solute concentration of such an austenite depends on the extent

of dissolution of the pre-existing carbides, which is dictated by the composition of the steel and temperature of austenitisation.

- The nature of precipitation from the solute lean austenite on cooling from the austenite phase field, has been understood based on the shift in the C-curve corresponding to the α+carbide precipitation, the consequent interception of the cooling curve and the ‘time of stay’ in the temperature regime far above the M_s temperature of the steel. This has also been supported by microstructure and calorimetry evidences.
- Presence of a low amount of retained austenite in the normalized 1.4W – 0.06Ta steel was confirmed by Mossbauer Spectroscopy studies and OIM. Multiple variants of martensite form from austenite obeying K-S orientation relationship.
- Activation energy for the tempering process is found to be in the range of 0.7 to 1.1 eV, which corresponds to the activation energy for the interstitial diffusion of C in α-Fe. Increase in W and Ta content of steels accelerates the initial tempering due to increased precipitation, which was more significant with increase in W than Ta.
- Extent of subgrain formation on tempering at 1033 K was higher with increase in W and Ta content of the steel.
- Fe-rich $M_{23}C_6$ carbides were observed at low temperatures and durations, the extent of which increased with W content of the steel. Increase in W content of steel modifies the chemistry of $M_{23}C_6$ on thermal exposure and controls its coarsening.
- JMatPro simulations showed the possibility of M_3C, M_2X and M_7C_3 precipitation at 1033 K below 10 minutes of tempering, while after 1 h of tempering $M_{23}C_6$ and MX precipitates were stable. Volume fraction of $M_{23}C_6$ was found to increase with W content of the steel, while amount of MX was not sensitive to the Ta content of the steel.

Chapter 5

Microstructural evolution in 9Cr RAFM steels on long term exposure - Effect of composition, temperature and stress

5.1 Introduction

The microstructural changes during short term thermal exposure of the normalised 9Cr RAFM steels with a martensite microstructure was described in detail in Chapter 4, which also led to the optimisation of conditions for the tempering treatment. It is well known that these steels are employed in the normalised and tempered condition for industrial applications. Study of microstructural stability of normalised and tempered steels is crucial to understand the performance of the steel for long term applications [1,17] and to identify the limits of the service conditions. Hence, it is essential to carry out detailed microstructural studies by varying the temperature, time and stress conditions simulating the service exposure. In order to realise the changes within a short time in the laboratory, accelerated aging has been carried out at higher temperatures and stress. These studies are also useful for remnant life assessment or evaluating the thermal history of the steel. It is well understood that the mechanical properties are influenced by the microstructural changes taking place in the steel on prolonged thermal exposure, like coarsening of $M_{23}C_6$ and Laves phase [1,39,83,90], which particularly occur at service temperature [90]. It is also important to mention that R&D efforts towards increasing the service temperature are in progress [1,90], in order to increase the efficiency of the power plants. In this context, the aging experiments have been carried out in the temperature range of 773 to 923 K, which encompasses the temperature domain of interest for the structural components of ITER [1].

This chapter describes the effect of long term thermal and stress exposure on microstructural evolution for the four RAFM steels in the temperature range of 773 to 923 K. In **section 5.2**, the effect of prolonged thermal exposure on hardness and the microstructural changes in 1W-0.06Ta steel are discussed in detail. **Section 5.3** discusses the effect of W and Ta on the evolution of microstructure and secondary phases on accelerated aging at high temperatures, including the coarsening of $M_{23}C_6$ and formation of Laves phase. The combined effect of thermal and stress exposure on microstructural evolution in steels with different W and Ta content is discussed in **section 5.4**. The details on the mechanism of formation of Laves phase in RAFM steels are discussed in **section 5.5**. The results of JMatPro simulation carried out to understand the secondary precipitation in the four steels is presented in **section 5.6. Section 5.7** summarises the results of this chapter.

5.2 Effect of thermal exposure on microstructural parameters in 1W-0.06Ta steel

The effect of thermal aging on microstructural evolution has been studied extensively in 1W-0.06Ta steel at different temperatures as mentioned in **Table 2.2.** The microstructure of the 1W-0.06Ta steel normalised at 1253 K and tempered at 1033 K is given in **Figure 5.1.** As expected, the microstructure consists of a tempered martensite structure **(Figure 5.1(a))** with coarse $M_{23}C_6$ precipitates along the boundaries and fine intralath V or Ta rich MX, as identified from the EDX and the electron diffraction pattern analysis **(Figure 5.1(b-d))**.

Metallography examination of the thermal exposed steel in the range of 773 to 923 K did not show significant change in microstructure compared to that of the initial normalised and tempered steel. However, the measured hardness was found to be sensitive to the aging time and temperature, which is discussed below.

5.2.1 Variation of hardness

Figure 5.2 shows the variation of hardness as a function of time at different temperature of thermal exposure. At 773 K, a decrease in hardness is observed as a function of time. Prolonged exposure at 823 K also showed a similar trend, with lower hardness

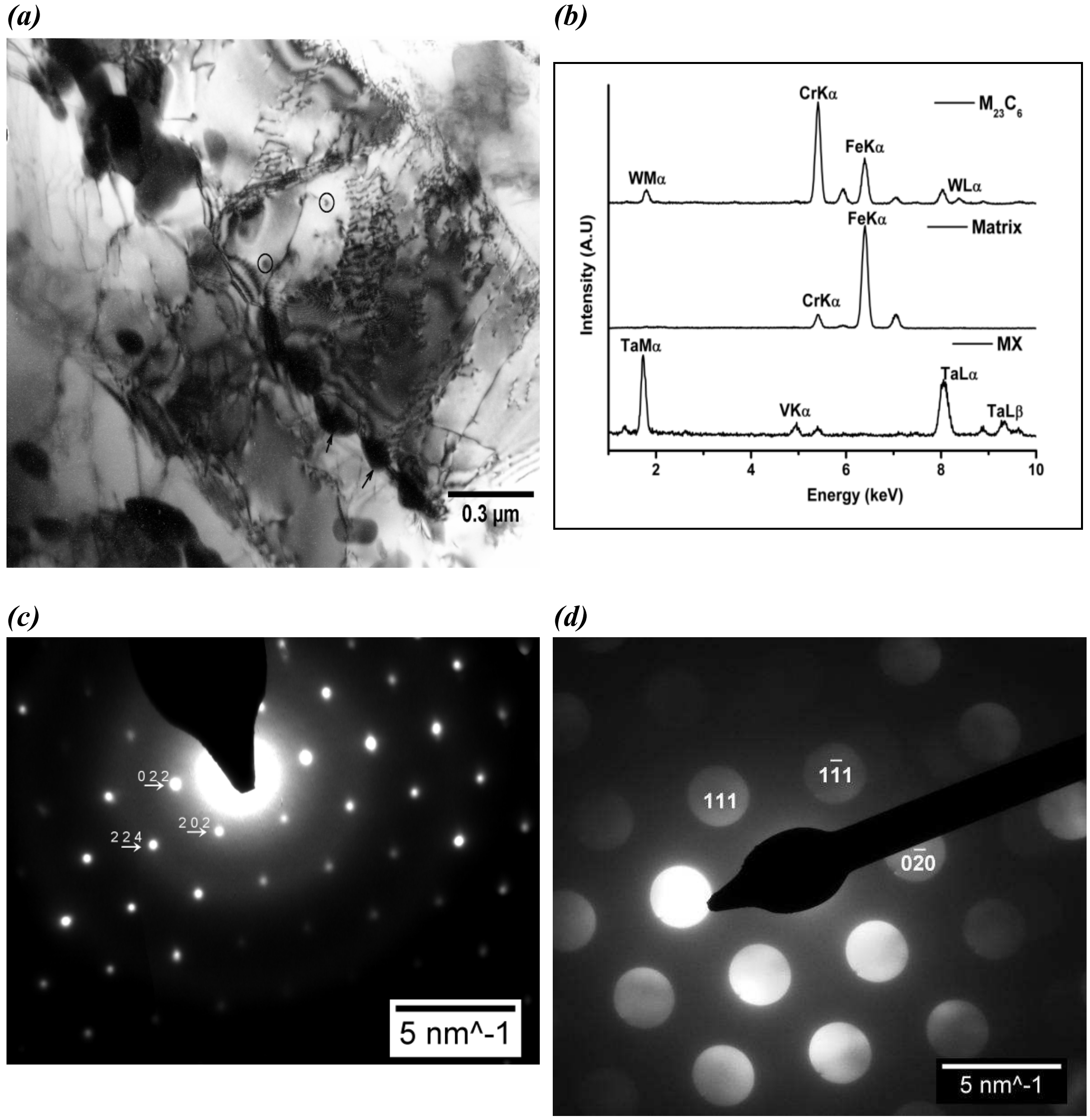

Figure 5.1. *(a) TEM thin foil micrograph of normalised and tempered 1W-0.06Ta steel showing the presence of inter (arrow marked) and intra lath (circled) precipitates, (b) EDX spectra of corresponding phases and (c and d) Electron diffraction patterns of* $M_{23}C_6$ *and MX phases along [11-1] and [10-1] zone axis respectively*

compared to that at 773 K. The decrease in hardness is associated with microstructural changes in the martensite substructure and coarsening of precipitates in the normalised and tempered steel, which will be illustrated in subsequent sections. At 873 K, a secondary hardening is observed after 5 h of thermal exposure, followed by a decrease in hardness at longer time, but higher values than at 823 K. This observation is rather unexpected, since the kinetics of recovery of martensite and coarsening of precipitates are expected to be accelerated with increase in temperature. This observation suggests the possibility of a fresh precipitation at shorter durations. These fresh precipitates do not coarsen on prolonged exposure, which could aid in controlling the recovery of matrix. In order to rationalise the observed trends in hardness, detailed TEM studies were taken up, the results of which are discussed in sections 5.2.2 and 5.2.3.

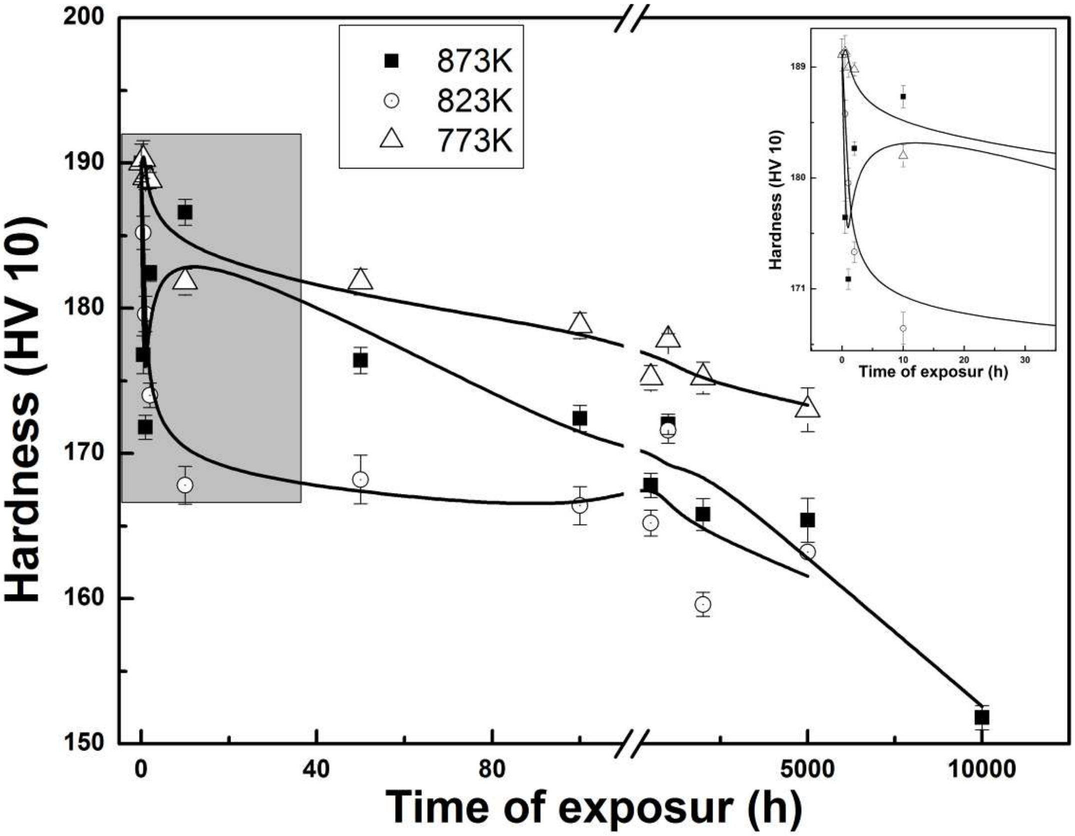

Figure 5.2. *Variation of hardness of 1W-0.06Ta steel with aging time at different temperatures*

5.2.2 Substructural changes on prolonged aging in 1W–0.06Ta steel

Figure 5.3 presents the thin foil micrographs of 1W-0.06Ta steel exposed to different temperatures for a duration of 5000 h. Careful observation showed no significant change in the microstructure between normalised and tempered steel and that aged at

773 and 823 K **(Figure 5.3 (a and b)**. Formation of subgrains in the range of 300-400 nm was observed on exposure to 873 K **(Figure 5.3 (c))** suggesting an accelerated recovery and recrystallisation. With increase in the aging time to 10000 h, partial recrystallisation along with the retention of lath structure in a few regions **(Figure 5.3(d))** is observed**.** There was no significant change in the lath width as compared to the normalised and tempered steel, while formation of equiaxed subgrains

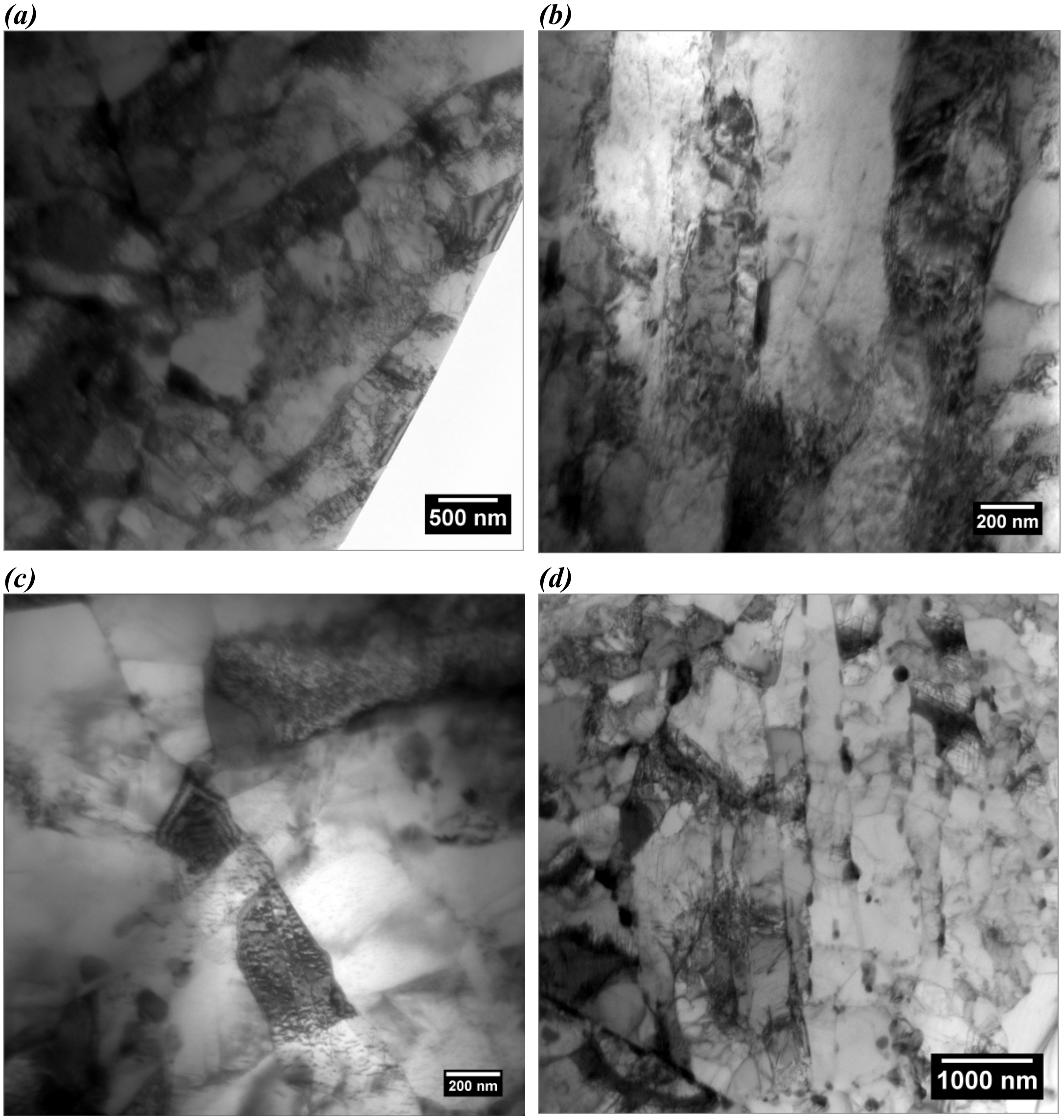

***Figure 5.3** Thin foil micrograph of 1W-0.06Ta samples exposed for 5000h to (a) 773 K, (b)823 K and (c) 873 K; (d) after 10000 h at 873 K showing enhanced recovery at high temperature*

suggested the continued evolution of microstructure. The presence of fine subgrains is attributed to the pinning effect of fine precipitates, which is also manifested in the increase in hardness at 873 K, discussed in section 5.2.1. However, as expected, recovery and recrystallisation is enhanced after aging beyond 5000 h at higher temperatures, which is also reflected in the low values of hardness, ~150 VHN, while the slow recovery of substructure below 873 K even after prolonged exposure is in line with slow diffusion kinetics of substitutional elements and self diffusion of Fe [200,216].

Figure 5.4 shows the thin foil TEM micrograph of 1W-0.06Ta steel aged at 923 K for durations of 5000 and 10000 hours. Although considerable extent of substructure changes associated with the higher temperature is witnessed, no significant change in subgrain size was observed between 873 and 923 K.

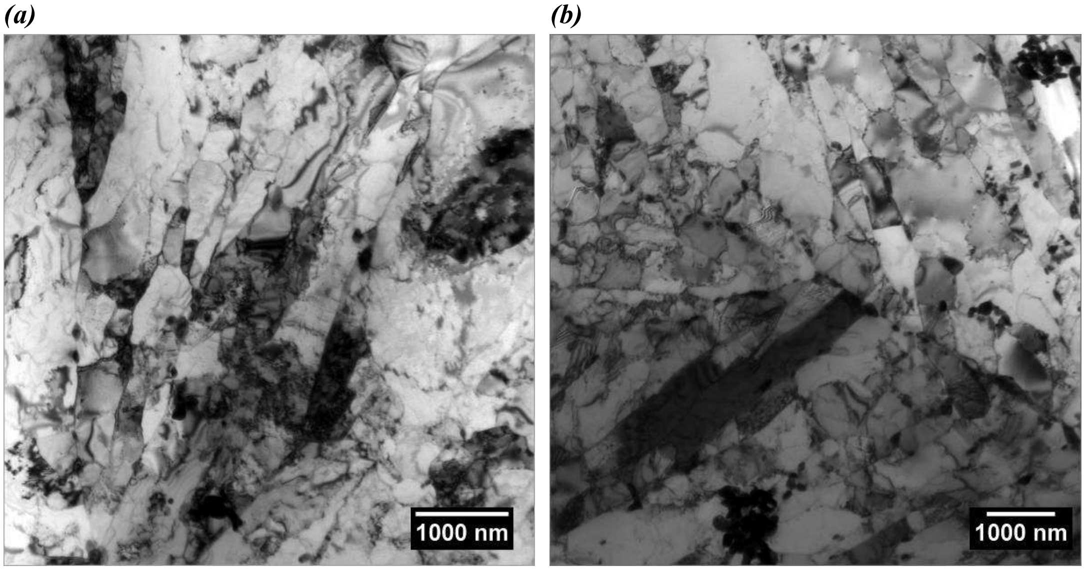

Figure 5.4. *TEM image of 1W-0.06Ta steel after thermal exposure at 923 K for (a) 5000h and (b)10000 h showing higher extent of recovery, compared to 873 K.*

5.2.3 Evolution of secondary phases on long term thermal exposure in 1W–0.06Ta steel

Prolonged thermal exposure was found to influence the precipitate characteristics in 1W-0.06Ta steel. The variation of size distribution and microchemistry of carbides on aging at different temperatures are discussed in this section.

5.2.3.1 Size distribution of precipitates

Figure 5.5 shows the typical micrographs from carbon extraction replica of steel in normalised and tempered condition and aged for 5,000 h at 773 K. An increased precipitation is clearly observed with long term aging. Analysis of electron diffraction patterns and EDX spectra confirmed the precipitates to be Cr rich $M_{23}C_6$ and V or Ta rich MX, which has already been reported in normalized and tempered steel in **section 5.2**. Existing literature on Eurofer steel [38,217] also reported the formation of two types of MX carbonitrides.

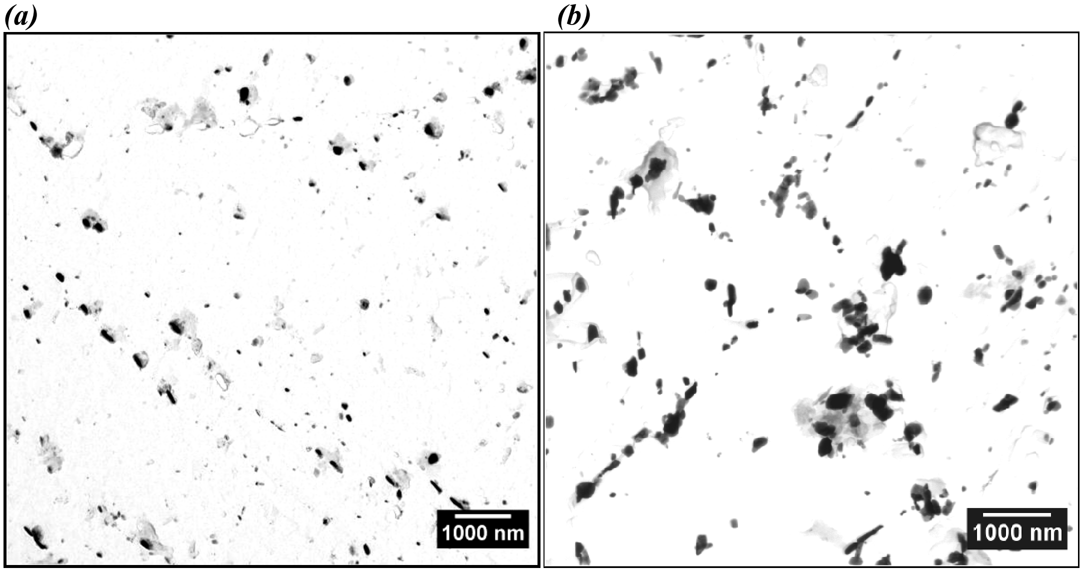

Figure 5.5. *Micrograph of extraction replica of (a) normalised and tempered steel (b) aged for 5000 h at 773 showing increased precipitation on aging*

Figure 5.6 shows the carbon extraction replica micrograph of 1W-0.06Ta steel aged at 823 K for durations ranging from 2 to 5000 h. Although there is an observable coarsening of the precipitates as compared to the normalised and tempered steel, the rate of coarsening is not significant with progress in time. This clearly demonstrates that the microstructure is stable until 823K for prolonged durations.

Figure 5.7 shows the carbon extraction replica micrograph of the steel aged at 873 and 923 K for 10000 h along with EDX spectra from the different types of precipitates marked (**Figure 5.7(b)**). The combined analysis of electron diffraction patterns and EDX spectra showed distinct features with respect to the site of nucleation, size and microchemistry of the precipitates. Majority of the coarse precipitates correspond to $M_{23}C_6$ and the fine precipitates to MX. Compared to the normalised and tempered steel with average size of $M_{23}C_6$ in the range of 150 nm, a significant coarsening of the particles up to about 200 nm was evident at 873 and 923 K, while MX precipitates did not show a significant variation in size. The formation of Laves phase was not evident even after 10,000 h of aging at 923 K. However Klueh et. al. [177] have reported the formation of Laves phase in addition to the $M_{23}C_6$ and MX phases using JMatPro calculations in a similar steel. Thomas et al, [73] have experimentally shown the formation of Fe, Mo rich Laves phase in P91 steel at 823 K after 5000 h of thermal exposure. However, in the present study there was no evidence for formation of Laves phase in the temperature range of 773 – 923 K in 1W-0.06Ta steel. Hence it can be concluded that the replacement of Mo by W in RAFM steel delays the formation of Laves phase. To understand the evolution of precipitates as a function of temperature and time, quantification of the size distribution of the precipitates was carried out, which is described subsequently.

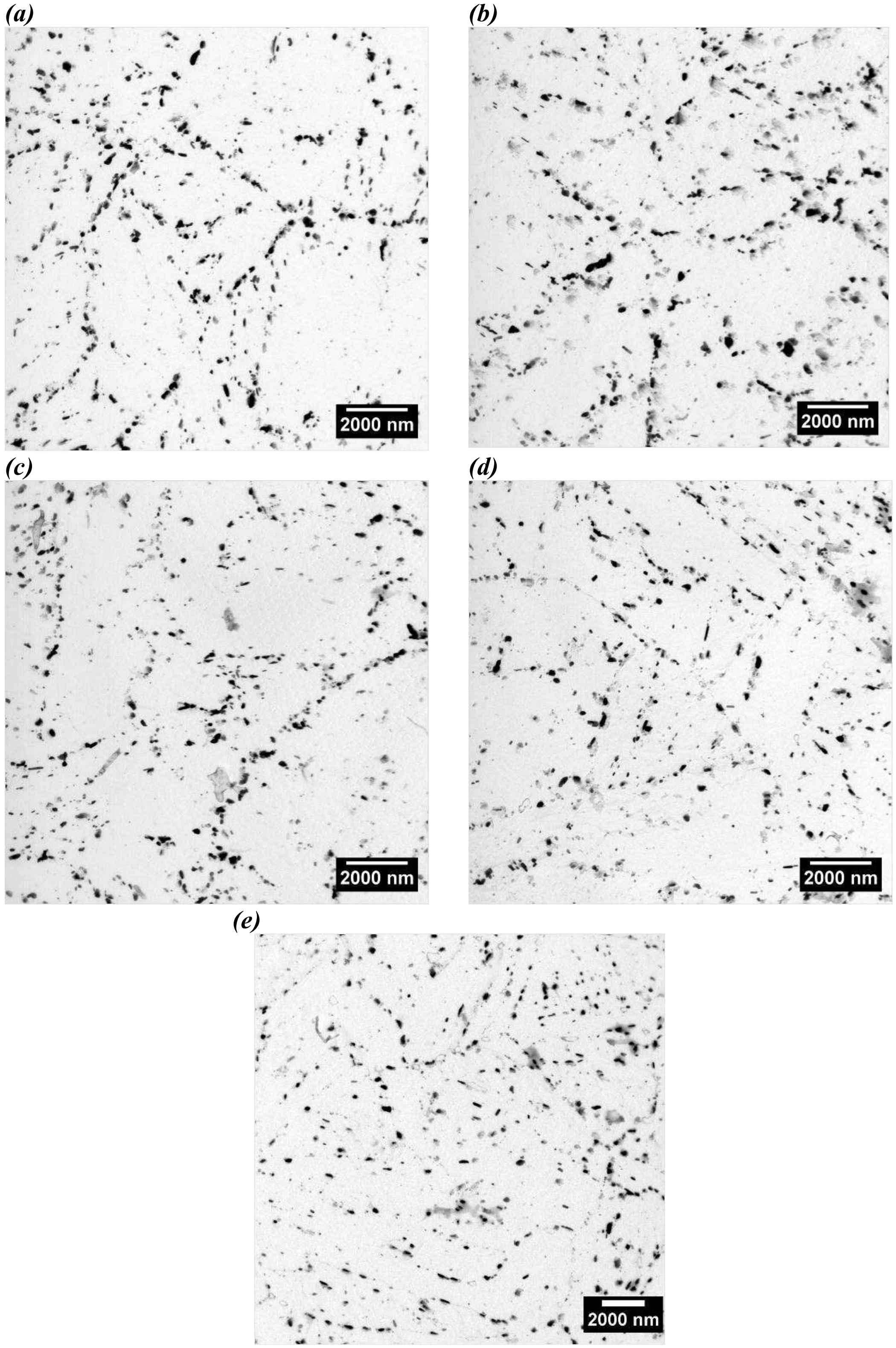

Figure 5.6 *Carbon extraction replica micrographs of of 1W-0.06Ta steel aged at 823 K for (a) 2 h (b) 10 h (c) 100 h, (d)1000h and (e) 5000 h showing negligible precipitate coarsening with time of exposure*

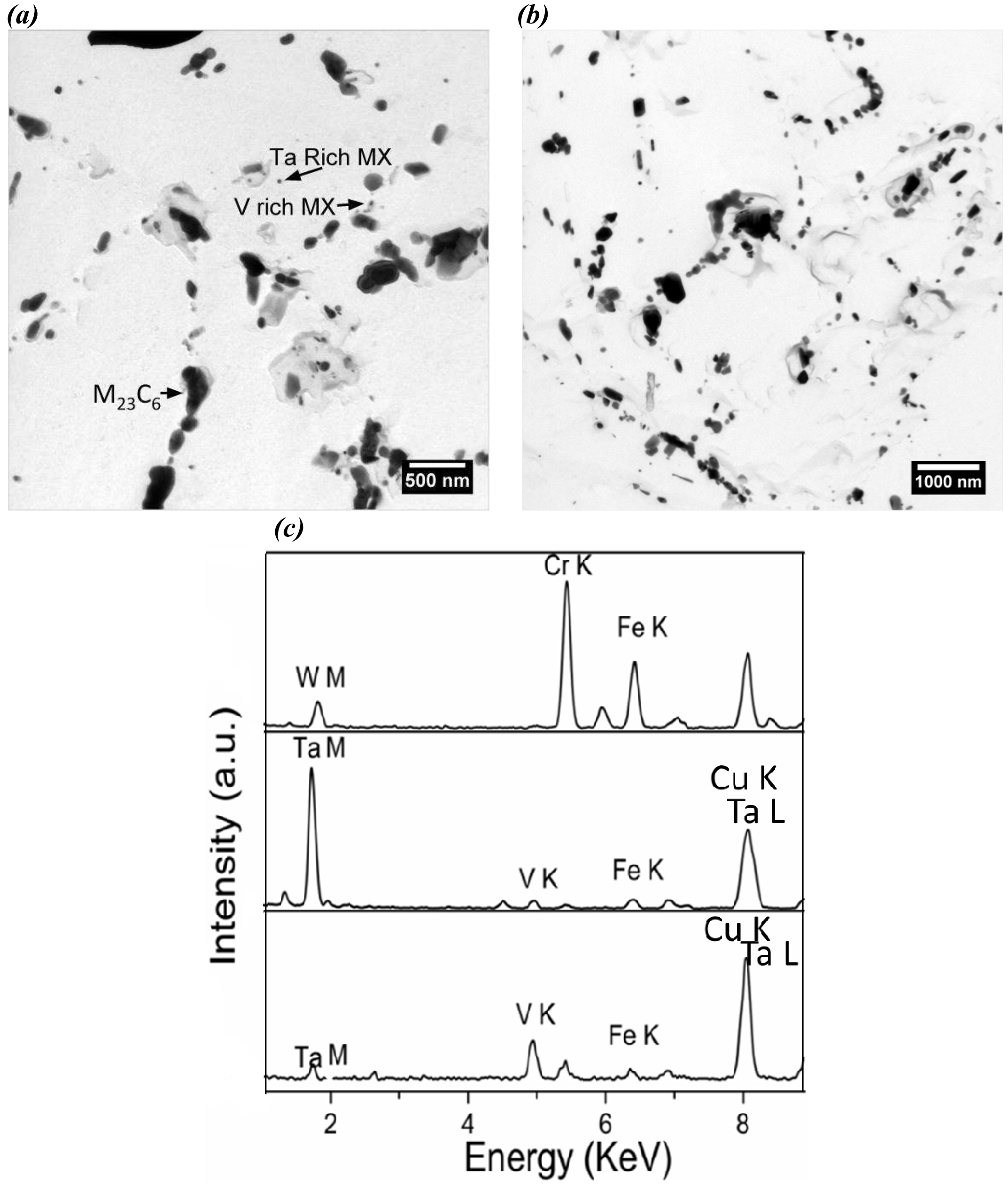

Figure 5.7. *Micrograph of carbon extraction replica of 1W-0.06Ta steel exposed to(a) 873 K (b)923 K showing the distribution of precipitates after 10000 h, (c) EDX spectra from the three types of precipitates marked in (a)*

A comparison of the frequency distribution of the precipitates as a function of size between the normalized and tempered steel and those aged for 5000h at different temperatures is presented in **Figure 5.8.** It is observed that with increase in temperature, the number density of precipitates decreases, while the size increases.

These observations clearly support the coarsening of precipitates, especially $M_{23}C_6$, while MX is observed to retain its size even at 923 K, the highest temperature employed in this study. Similar observations are reported for 9Cr steels in literature [73,119,218,219].

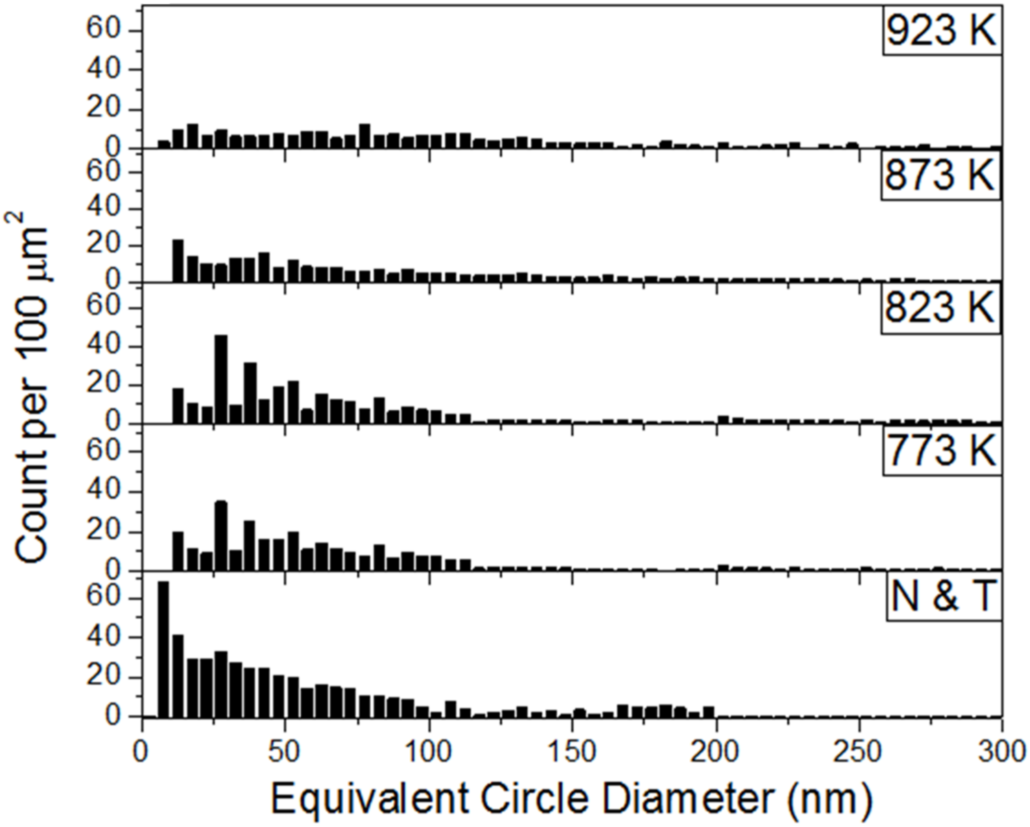

Figure 5.8. *Frequency distribution of precipitates as a function of size in 1W-0.06Ta steel after 5000 h of thermal exposure at different temperatures*

Figure 5.9 shows the effect of time on the frequency distribution of carbides of different sizes at 823 and 873 K, evaluated from carbon extraction replica micrographs. Coarsening of precipitates as a consequence of Ostwald ripening [220] is observed with aging time (**Figure 5.9 (a)**) at 823 K. Therefore, the observed decrease in hardness (**Figure 5.1)** can be clearly associated with the coarsening of precipitates, particularly $M_{23}C_6$. However, it is observed that, at 873 K, there is an increase in number density of fine carbides after about 10 h suggesting the fresh precipitation of carbides during initial stages of thermal exposure (**Figure 5.9(b))**. It is also observed that the distribution

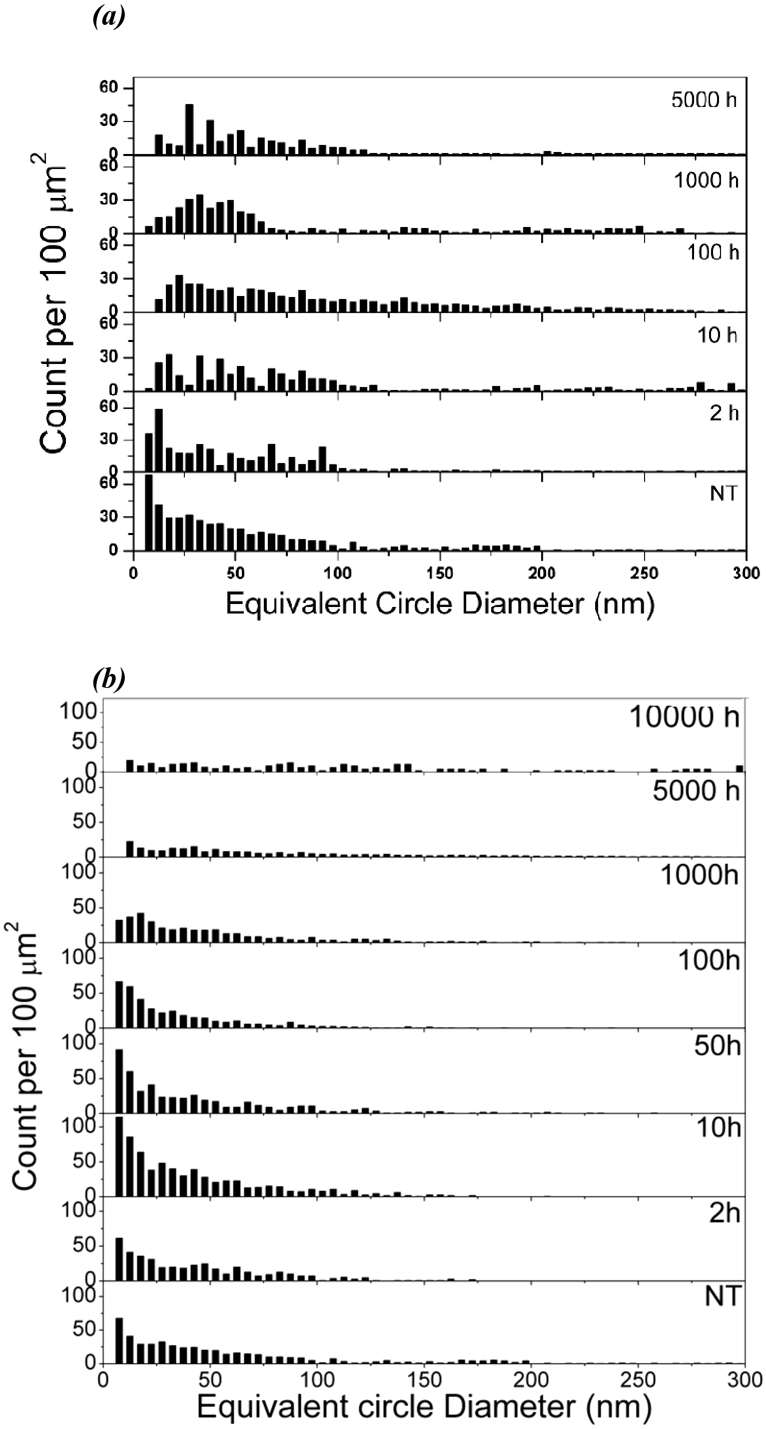

Figure 5.9. *Frequency distribution of precipitates in 1W-0.06Ta steel aged at (a) 823 and (b) 873 K showing the variation of size with time*

of carbides is nearly same up to about 1000 h. Hence, the observed high hardness for the samples aged at 873 K in contrast to that at 823 K suggests that the precipitates nucleated after 10 h could be of MX type, which strengthens the matrix during further thermal exposure rather than $M_{23}C_6$. The variation of the microchemistry of the carbides with aging is discussed below.

5.2.3.2. Microchemical variation of coexisting phases

EDX analysis of $M_{23}C_6$ **(Figure 5.10)** carbides obtained after thermal exposure at 773 and 823 K showed that the microchemistry did not change appreciably with aging time, although the Cr concentration in the precipitates is expected to increase [221] towards attaining the equilibrium composition of $Cr_{23}C_6$. This observation suggests that the diffusion of substitutional elements like Cr and W is slow at these temperatures. The microchemical variation of $M_{23}C_6$ as a function of time after thermal exposure at 873 K is also shown in **Figure 5.10**. An increase in Cr / Fe and W / Fe ratio is observed, especially after 1000 h of aging. This is attributed to the enhanced diffusion of Cr and W at this temperature. Similar studies performed in P91 and P9 steel [73, 201] have shown a progressive increase in Cr / Fe ratio in the temperature range of 773 to 873 K. However, the reported change in Mo / Fe ratio was insignificant at all temperatures.A perceptible trend could not be established for the microchemical variation of MX precipitates. The microchemistry of these precipitates after prolonged thermal exposure was found to be similar to that in the normalised and tempered steel presented in **Table 4.9.** Hence, it is concluded that MX precipitates are stable for prolonged durations (up to 5000 h) both in terms of size and chemistry in the range of temperatures studied.

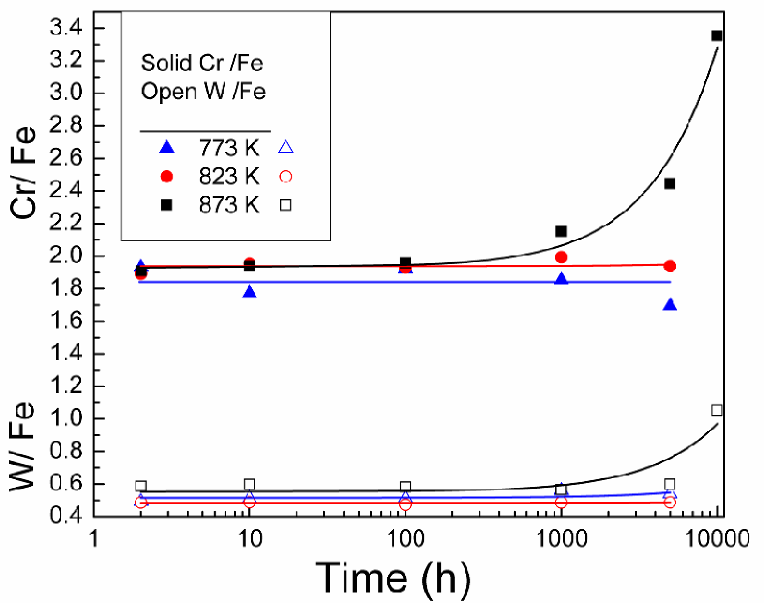

***Figure 5.10**. Variation in microchemistry of $M_{23}C_6$ with time in 1W-0.06Ta steel aged at different temperatures*

5.3 Effect of thermal and stress exposure in 1W-0.06Ta steel

Effect of stress accelerates the recovery and recrystallisation of martensite structure in 9Cr steels. Coarsening of secondary phases and formation of Laves phase is also reported to be accelerated in the presence of stress [92,119]. In this section, the effect of creep exposure on 1W-0.06Ta steel to different stress levels is discussed in detail. Subsequently, the data is also compared with that obtained for different W and Ta containing RAFM steels exposed to a stress level of 220 MPa. A detailed study on microstructural changes is taken up to understand the deformation mechanism under creep conditions. Thin foil micrograph of the steel exposed to different stress levels at 823 K is depicted in **Figure 5.11**. Extensive recovery and recrystallisation of substructure was evident in all the conditions. The comparison of subgrain and precipitate size after thermal and stress exposure is presented in **Figure 5.12**. A significant increase in both subgrain and precipitate size with stress exposure is observed. It is seen that the average width of subgrain increases from 0.5 to 0.7 µm with time of exposure, in contrast to a marginal increase during thermal exposures. This clearly indicates the role of stress in accelerating the recovery of martensite substructure as against the sluggish behaviour on thermal exposure both in terms of subgrain recovery and coarsening of $M_{23}C_6$ precipitates as reported in section 5.2.2 and 5.2.3, even at higher temperature of 923 K.

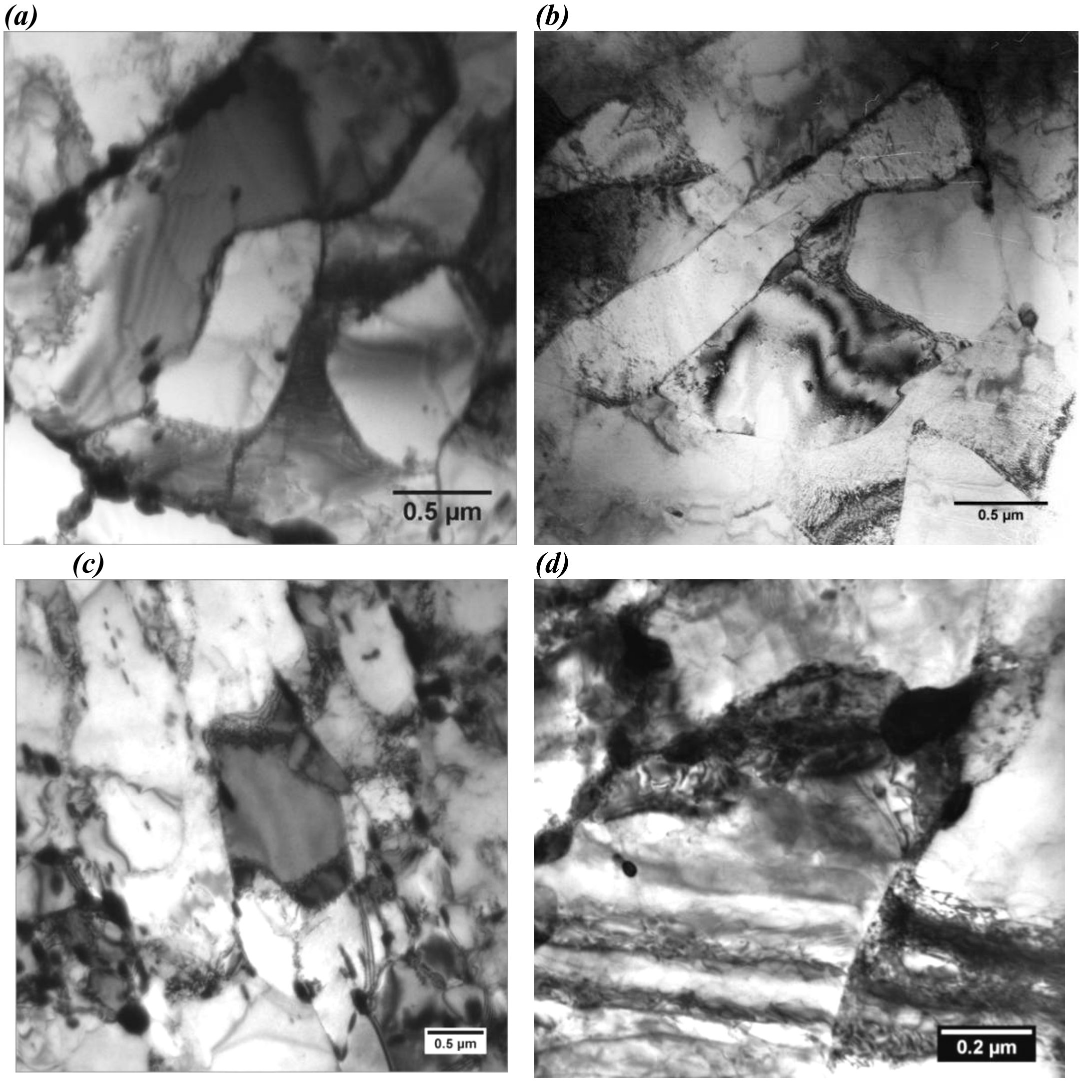

Figure 5.11. *TEM micrographs of 1W-0.06Ta steel after creep exposure at 823K at different stress levels of (a) 180, (b) 200, (c) 220, and (d) 260 MPa showing subgrain formation*

The hardness of 1W-0.06 Ta steel is reported to decrease [119] drastically in the presence of stress compared to that of the thermal exposed steel, which was also a strong function of exposure time. This decrease in hardness can therefore be understood to be due to the accelerated recovery, recrystallisation and precipitation coarsening discussed in **section 5.3** in the presence of stress. Measurements of creep rupture time by Vanaja et al [119] shows that the creep rupture time increases with W content of the steel, while addition of Ta decreases the creep rupture time. Hence it is necessary to understand the role of W and Ta in controlling the microstructure, during creep exposure, which is discussed in the next section.

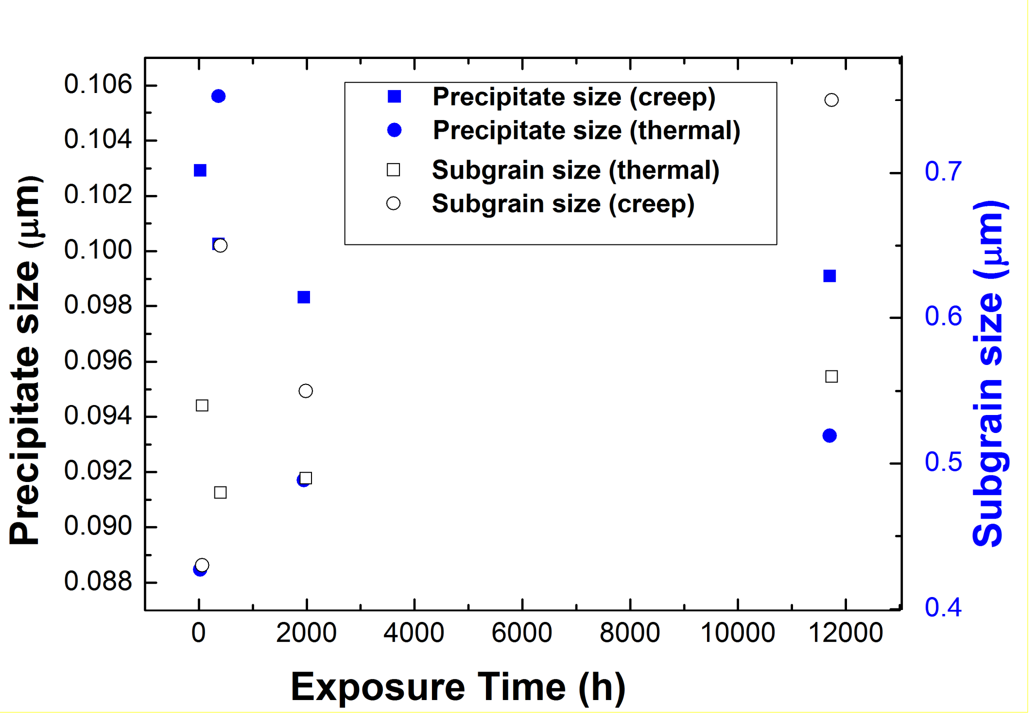

Figure 5.12. *Variation of subgrain width and precipitate size showing variation with stress exposure.*

5.4 Role of alloy content on microstructural evolution during thermal and stress exposure

5.4.1. Microstructural changes on thermal exposure and accelerated aging - Effect of W and Ta content

5.4.1.1. Substructure changes

Figure 5.13 shows the thin foil micrographs of steels with varying W and Ta contents exposed for 5000 h at 923 K. The microstructures were similar to that of 1W-0.06Ta at

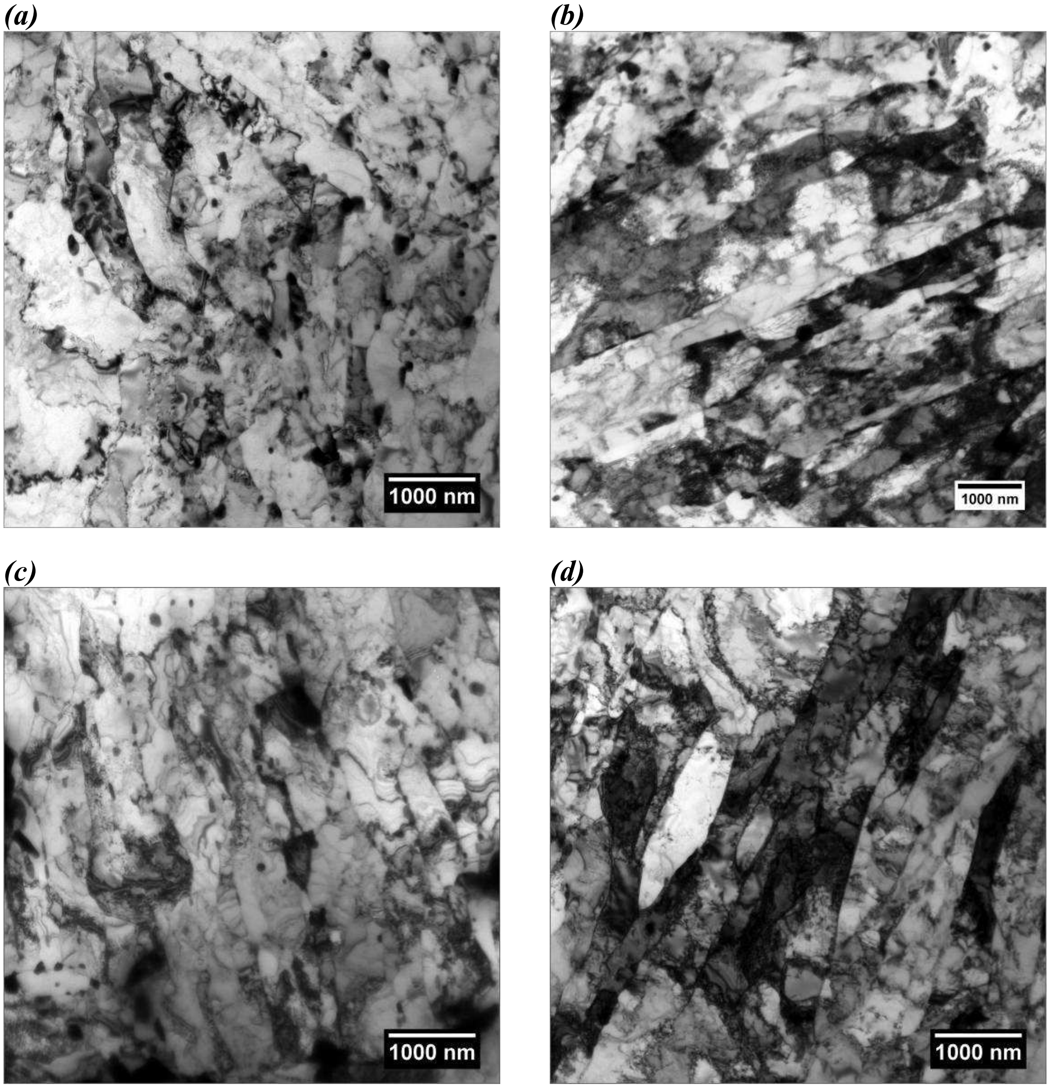

Figure 5.13. *Thin foil micrographs of (a) 1W-0.06Ta, (b) 1.4W-0.06Ta, (c) 2W-0.06Ta and (d) 1W-0.14Ta steel exposed for 5000 h at 923 K after showing partial recovery of substructure*

873 K and did not reveal any significant differences. Increasing the exposure time to 10,000 h at 923 K (**Figure 5.14)** showed considerable recovery of substructure with the formation of small subgrains in the range of 300-400 nm. However, no significant change could be observed between the four steels. The variation of the subgrain width was insignificant even after 10,000 h of thermal exposure at 923 K among different steels.

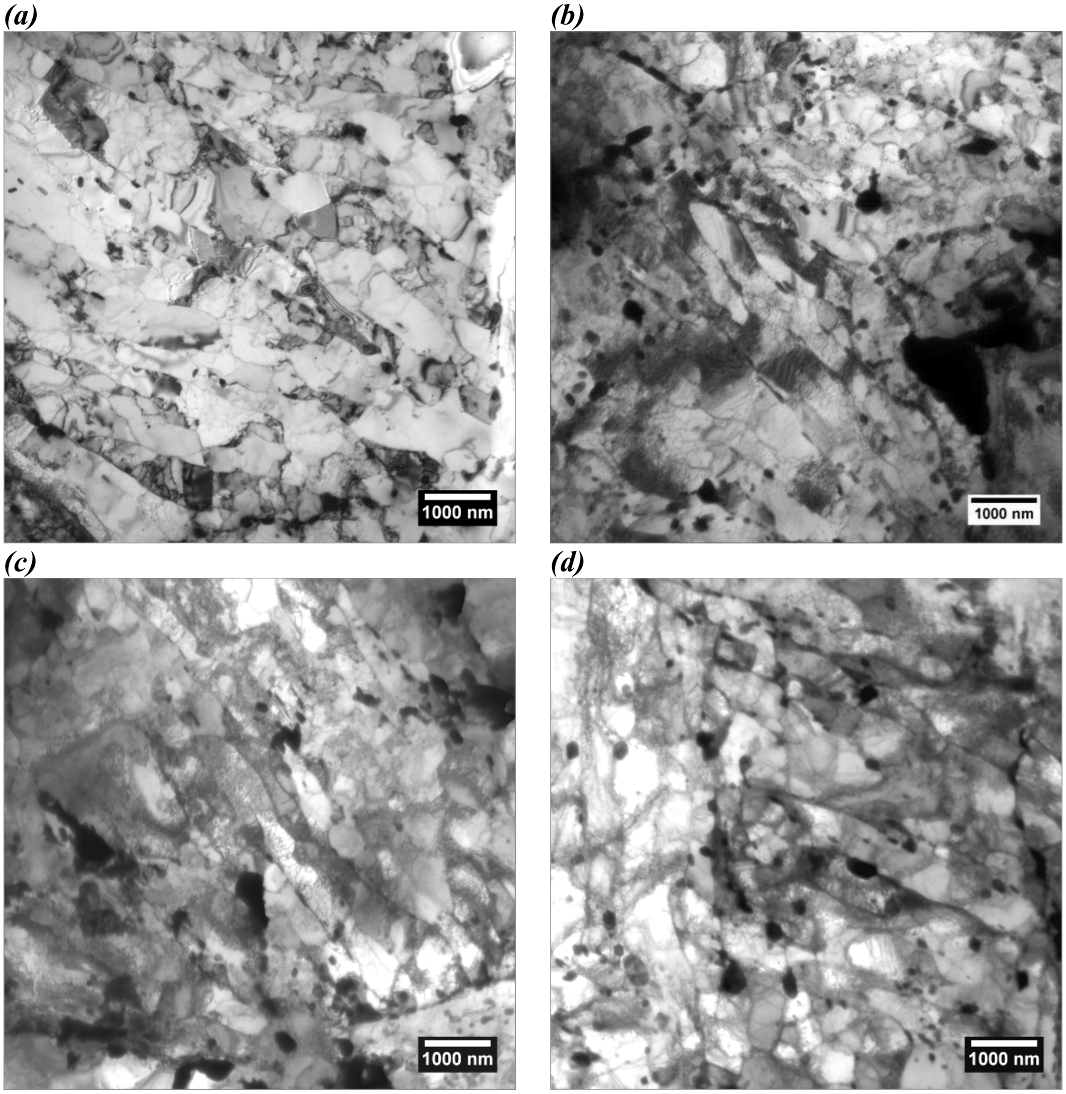

Figure 5.14. *Thin foil micrographs of (a) 1W-0.06Ta, (b) 1.4W-0.06Ta, (c) 2W-0.06Ta and (d) 1W-0.14Ta steel after thermal exposure for 10000 h at 923 K, showing increased recovery of substructure*

5.4.1.2. Evolution of secondary phases during thermal exposures- role of alloy content

Figure 5.15 shows the carbon extraction replica micrograph of the 1.4W-0.06Ta steel subjected to thermal exposure at 923 K for 5000 h. Increase in W content of the steel did not have any influence on the size of MX precipitates, which showed no solubility for W. The average particle size of $M_{23}C_6$ decreased from 200 nm to 170 nm with increase in W content of the steel from 1 to 2%, clearly showing that W controls the coarsening of precipitates, which was also reported in similar RAFM steels [220,4]. However, quantification of size distribution of the precipitates was difficult in some cases due to the agglomeration of precipitates and the formation of Laves phase, which is discussed below.

From **Figure 5.15(a)**, it is observed that in addition to $M_{23}C_6$ and MX, some regions show precipitates with a dark contrast in the close neighbourhood of $M_{23}C_6$. EDX analysis of these regions in **Figure 5.15(b)** showed that they are very rich in Fe and W in contrast to the Cr enrichment in $M_{23}C_6$. Analysis of the SAED pattern (**Figure. 5.15(c)**) obtained from such a Fe and W rich precipitate confirmed that it is Fe_2W Laves phase with HCP structure. The characteristic streaking in the SAED pattern is due to the stacking fault in the Laves phase crystal. The unique microchemistry with enrichment of Fe and W in the Laves phase facilitates its identification, though a low solubility for Ta and Cr was also observed.

Figure 5.16(a) shows the micrograph from the carbon extraction replica of the 2W-0.06Ta steel, aged at 923 K for 5000 h. With increase in W concentration of the steel to 2%, Laves phase formation was found to be more prevalent as shown in **Figure 5.16(a)** (arrow marked). A qualitative comparison of micrographs from different steel samples showed an increase in size / number of Laves phase particles with increase in W content

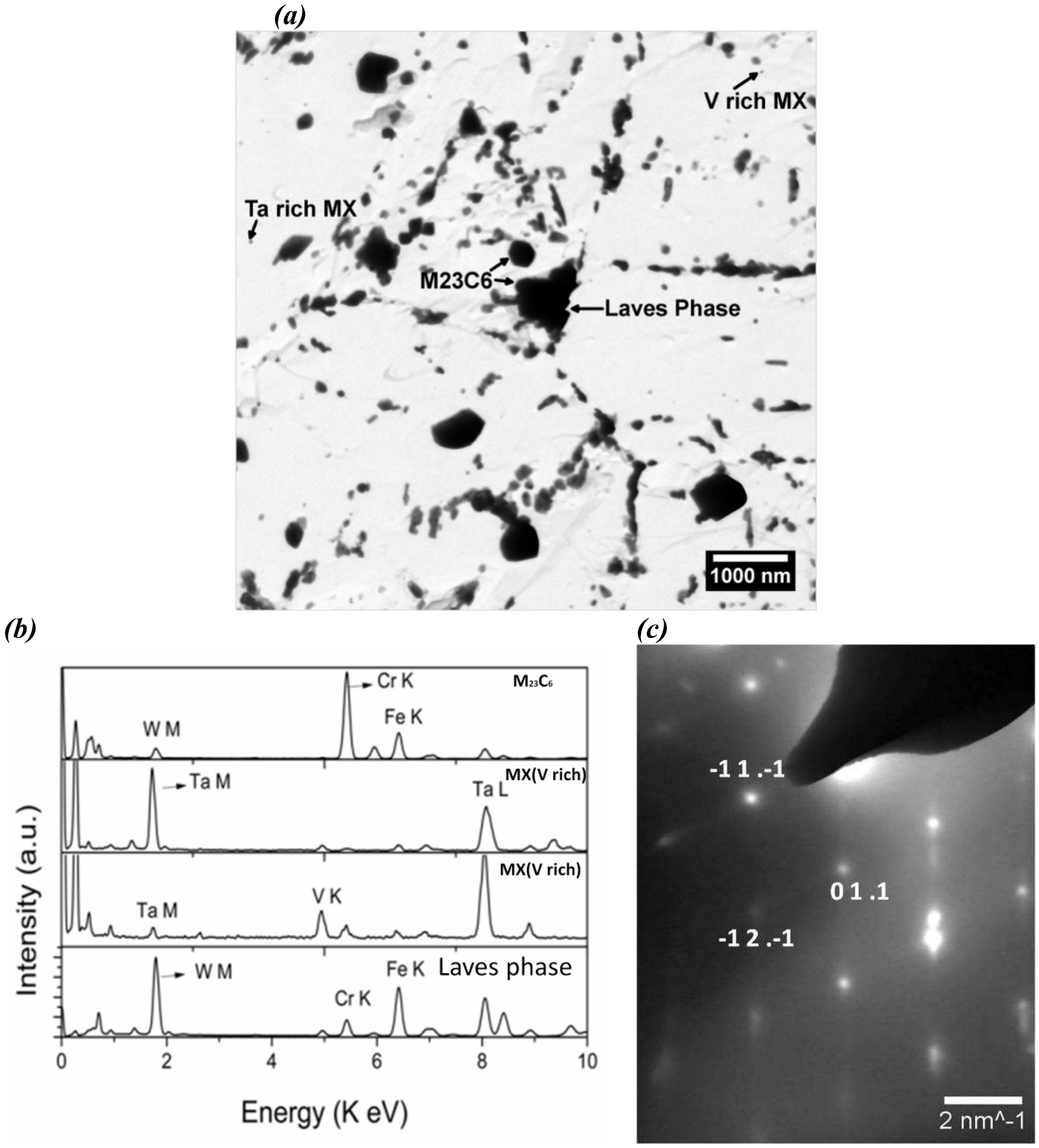

Figure 5.15. *(a) Extraction replica micrograph of 1.4W-0.06Ta steel after 5000 h of aging at 923 K; (b) EDX spectra of different precipitates marked in (a) showing the enrichment of Fe, and W in Laves phase and (c) SAED pattern of Laves phase marked in (a) along [10.-1] zone axis*

of the steel (**Figures 5.15 and 5.16**). **Figure 5.16(b)** shows the formation of a network of large Laves phase particles in 2W-0.06Ta steel with increase in aging time to 10,000 h at 923 K, suggesting its accelerated coarsening at 923 K. Presence of Laves phase like a bridge between $M_{23}C_6$ particles along the grain boundary is evident from the micrograph. The size of Laves phase particle along the grain boundary was found to be exceeding 1.5 μm.

From the above studies, it can be concluded that the formation of Laves phase, is initially delayed by addition of W as compared to Mo containing steels. However, in RAFM steels with W content exceeding 1wt%, volume fraction of the Laves phase increases, which is also supported by existing literature [39,40,222-224]. Studies on Laves phase formation in W containing steels have shown that the W addition for strengthening is effective only up to a Mo equivalent of 1.5 [225] , beyond which ductility of the steel and solid solution strengthening effect of W are drastically reduced, due to its accelerated coarsening.

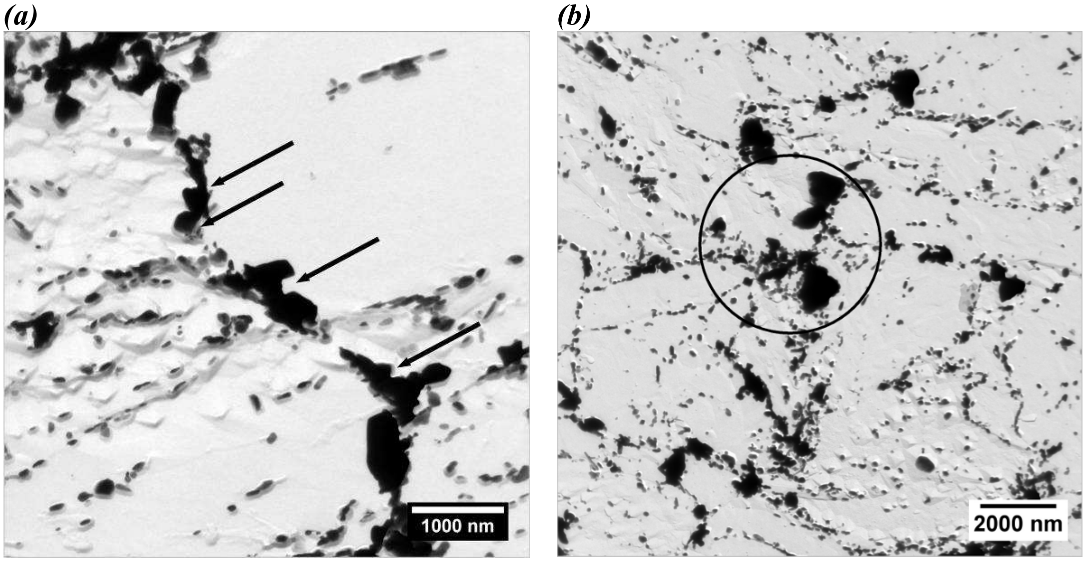

***Figure 5.16. TEM** micrographs of carbon extraction replica showing extensive precipitation of Laves phase in 2W-0.06Ta steel on aging at 923 K for (a) 5000h (arrow marked) and (b) 10000 h (circled)*

A representative carbon extraction replica micrograph of the 1W–0.14Ta steel exposed to 923 K for 10,000 h is shown in **Figure 5.17**. Careful analysis of SAED pattern and EDX spectrum showed the enrichment of Fe and W Laves phase in the steel. It was interesting to note that Laves phase in this steel also showed a small amount of Ta in addition to Cr, similar to that observed in 1.4W-0.06Ta and 2W-0.06Ta steels. This aspect of Ta dissolution in Laves phase is further discussed in detail in **sections 5.5 and 5.6**. Effect of Ta on Laves phase formation in W added steel is not reported from experimental studies in literature. However, the role of Ta in Laves phase formation in Ta added steels has been predicted by Danon et al., [48] based on thermodynamic assessment of Fe-W-Ta phase diagram [106] and by Knezevic et al., in 12Cr F-M steels [66].

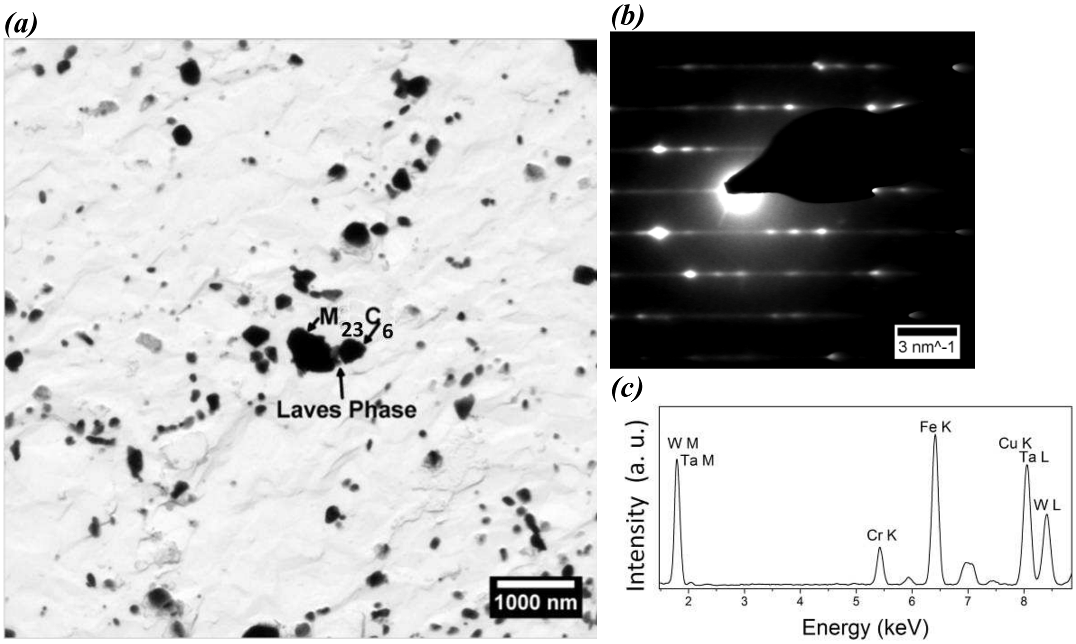

Figure 5.17. *Extraction replica micrograph of (a) 1W-0.14Ta steel showing Laves phase precipitation with increase in Ta content of the steel, (b) SAED pattern of Laves phase marked in (a) with [10.0] zone axis (c) EDX spectra from the Laves phase marked*

Formation of Laves phase in Mo containing steel is also reported to be dictated by the Mo to C ratio [105]. It is reported that formation of Laves phase is favourable only if the Mo to C ratio is greater than 5. Extrapolating this to the present study, considering the Mo equivalent expression [226], the ratio is 6.25 and 7.83 for the 1W-0.06Ta and 1W-

0.14Ta steel respectively. This value is greater than the Laves phase formation criteria; hence the formation of Laves phase should be possible in 1W-0.06Ta steel and the delay in the formation of Laves phase can only be attributed to kinetic aspects associated with the lower diffusional mobility of W in ferrite matrix as compared to that of Mo.

5.4.2 *Microstructural changes during thermal and stress exposure - Effect of W and Ta content*

5.4.2.1 Effect of thermal exposure at 823K

TEM thin foil micrograph for four steels exposed at 823 K is given in **Figure 5.18**. These samples were drawn from the grip portion of the creep tested specimens and hence represent only the influence of temperature. Partial recovery of substructure is observed for the four steels exposed to various lengths of time at 823 K and the microstructure nearly resembled the normalised and tempered steels. This indicates that the recovery is not complete. The change in substructure is observed to be insignificant with variation of W and Ta content of the steel at 823 K.

Analysis of the feature size (subgrain and $M_{23}C_6$ precipitates) is presented in **Figure 5.19** for the four steels. Coarsening of $M_{23}C_6$ precipitates in the range of 180 to 190 nm with reference to the respective normalised and tempered steels is observed, though the rate of coarsening was different for different steels. It is seen that the average size of $M_{23}C_6$ for steel with 1% W is 185 nm for an exposure time of 360 h, whereas the 2W steel showed a similar average size of $M_{23}C_6$ of 180 nm only after about 6000 h of aging. The smaller size of $M_{23}C_6$ for the steel with 2 % W again clearly shows that the addition of W restricts the coarsening of $M_{23}C_6$. Significant variation in subgrain size was not observed with varying W and Ta content which is attributed to the presence of fine carbides in the matrix.

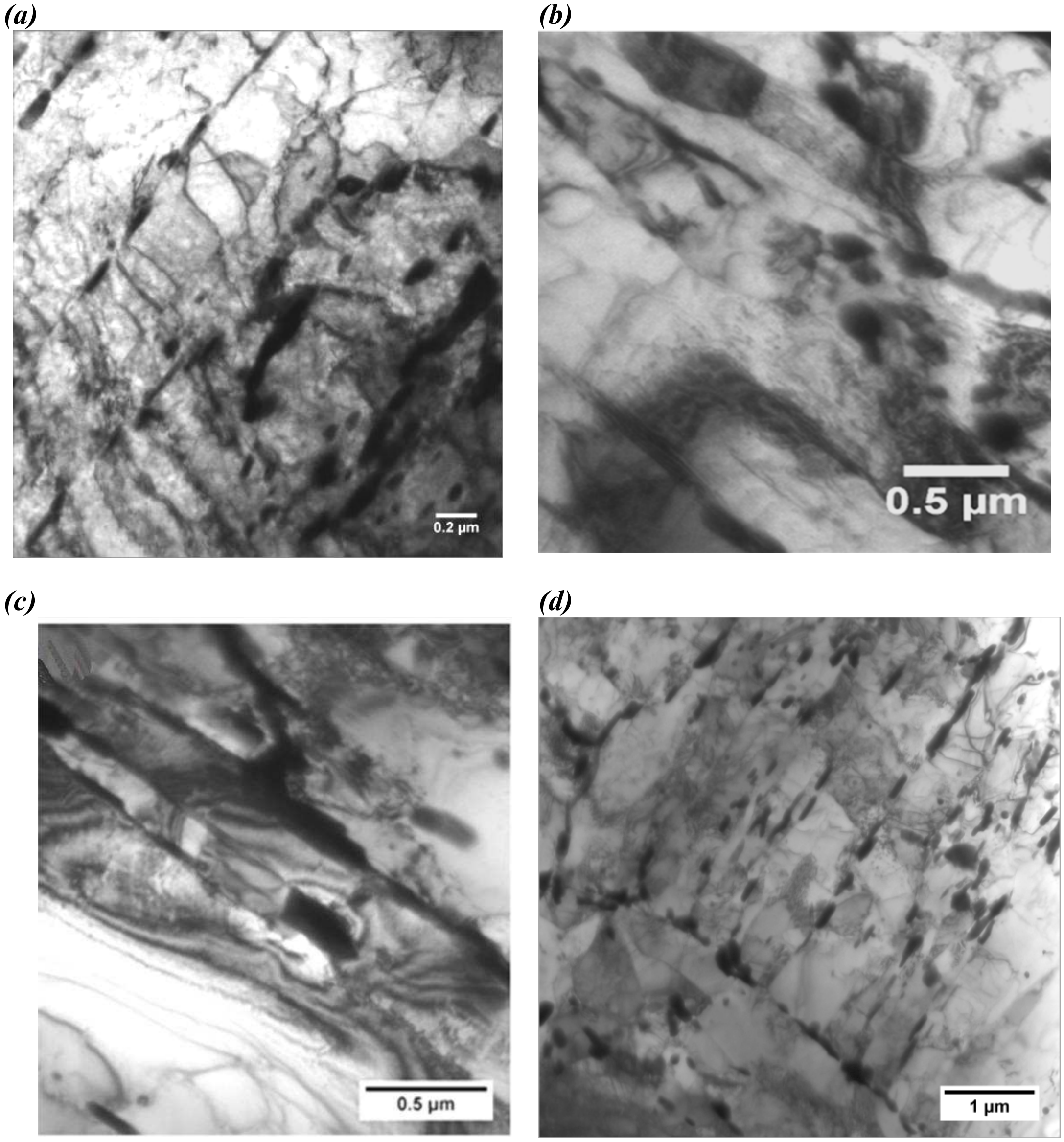

Figure 5.18 *Thin foil micrographs of (a) 1W-0.06Ta, (b) 1.4W-0.06Ta, (c) 2W-0.06Ta and (d) 1W-0.14Ta steel exposed at 823 K for different durations showing partial recovery of substructure*

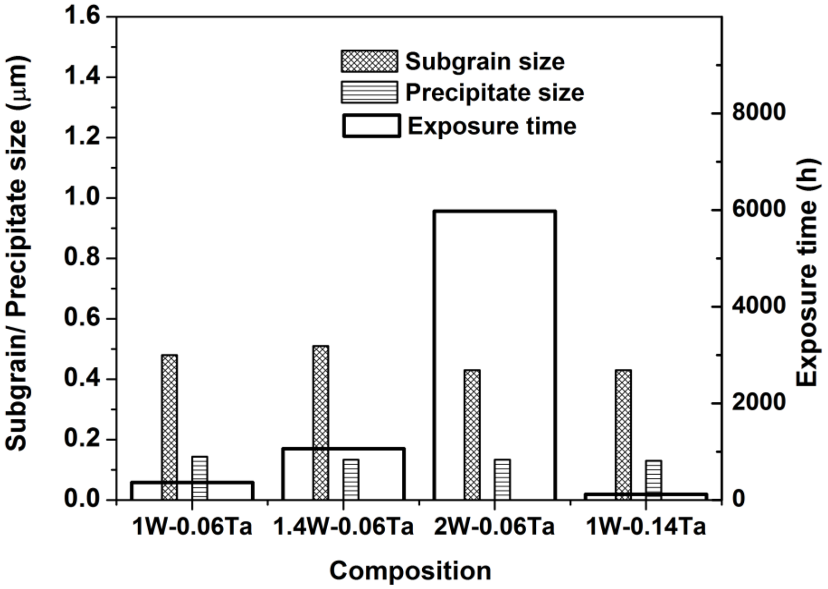

Figure 5.19. *Variation of subgrain width and precipitate size with W and Ta content of the steel at 823 K.*

5.4.2.2 Effect of stress exposure at 823 K on microstructural evolution

Creep deformation at 823K at an applied stress of 220 MPa produced significant changes both in the substructure and precipitation in the four steels. The creep rupture time is reported [119] to vary from 120 h to 6000 h with varying W and Ta content of the steel, the lowest for the 1W-0.14Ta steel and the higher for the 2W-0.06Ta steel. **Figure 5.20** shows the thin foil TEM micrographs of the creep exposed steels. An extensive recovery and recrystallisation of the martensitic substructure, together with coarsening of precipitates is observed in the steels with higher W and Ta content, similar to that reported for the 1W-0.06Ta steel (**Section 5.3**) in the presence of stress. Quantification of microstructural features in the creep exposed specimens for different W and Ta contents is depicted in **Figure 5.21**. Subgrain size of the steels was found to be higher under creep deformation than just thermal exposure, as expected during creep conditions. It is observed that for a short creep rupture time of 120h, 1W-0.14Ta steel shows a relatively high value of about 0.6μm, suggesting that the coarse primary carbides (**Figure 4.1**) are not effectively controlling the recovery of martensite [116].

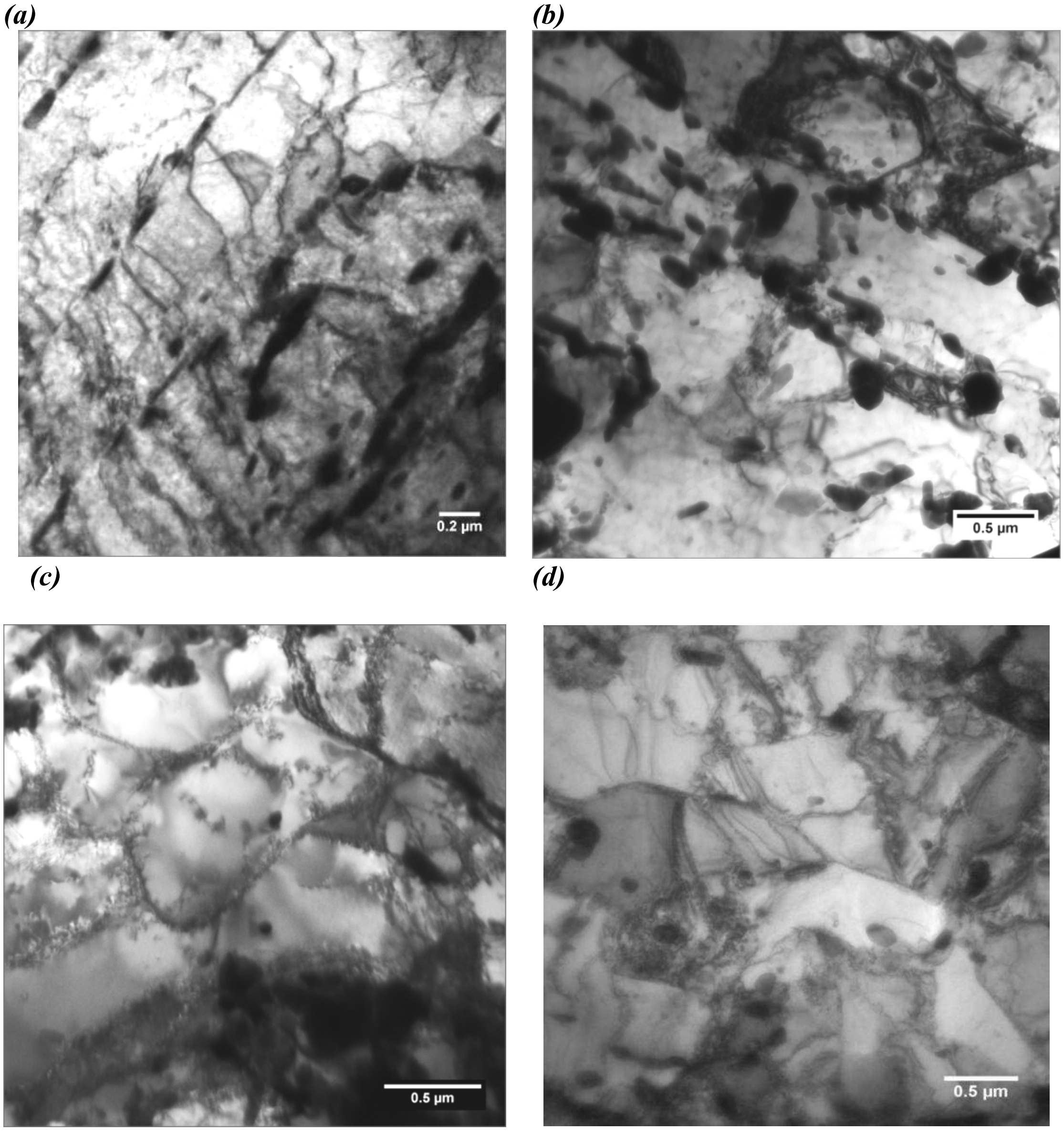

Figure 5.20. *TEM micrographs of (a)1W-0.06Ta (b) 1.4W-0.06Ta (c) 2W-0.06Ta and (d) 1W-0.14Ta steel after creep exposure at 823 K, at an applied stress of 220 MPa showing extensive subgrain formation*

The average carbide size slightly increased under stress in any steel, though it should be borne in mind that the creep exposure time also varied for the four different steels. However, the size of MX carbides did not show a significant difference between thermal and creep exposure, showing the stability of these precipitates, and its role in imparting creep resistance to the steel.

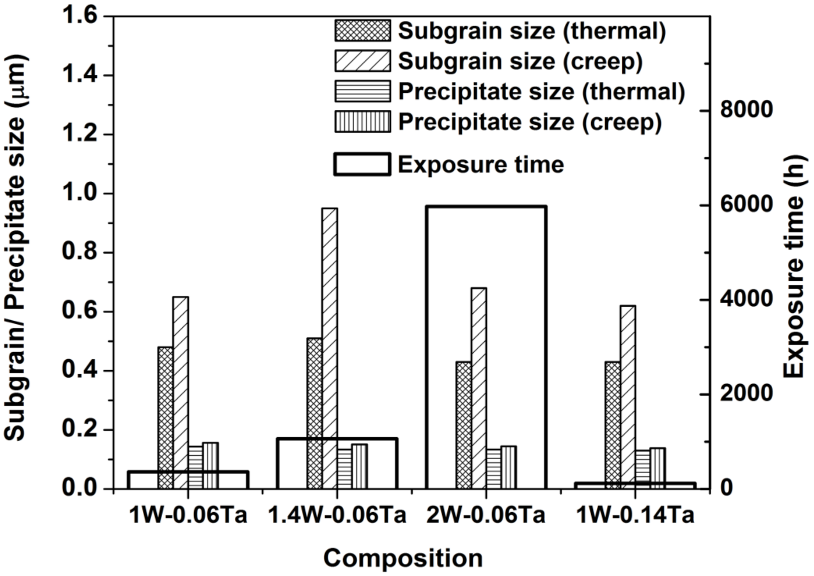

Figure 5.21. *Variation of subgrain width and precipitate size with composition of the steel in the presence of stress*

Figure 5.22 shows the carbon extraction micrograph of creep exposed 2W-0.06 Ta steel for 5978 h. Analysis of EDX spectra showed the presence of Fe and W rich Laves phase in addition to the coarse $M_{23}C_6$ and fine particles of Ta and V rich MX (EDX spectra of all the precipitates are presented). In comparison with the thermal exposed steel presented in **section 5.3**, the formation of Laves phase network along the prior austenite grain boundary at 823 K suggests the accelerated kinetics in the presence of stress.

Under the combined influence of high temperature and stress, increase in W and Ta content resulted in the following changes, which supports the creep rupture data:

- An increase in the subgrain size with increase in W content.

- Slight decrease in the average size of $M_{23}C_6$ carbides with increase in W content of the steel due to the enhanced nucleation of fresh carbides under stress, pinning the subgrain boundaries. Thus, the higher creep strength of 2W-0.06Ta steel is attributed to the synergistic effect of fine subgrains, fresh nucleation of precipitates and increase in solid solution strengthening effect of W [227].
- Higher amount of precipitation of W and Fe rich Laves phase with increase in W content.
- Increase in Ta resulted in a shorter rupture time, which shows that the presence of coarse incoherent primary carbides in the initial microstructure are not very effective in controlling the recovery of the martensitic substructure.

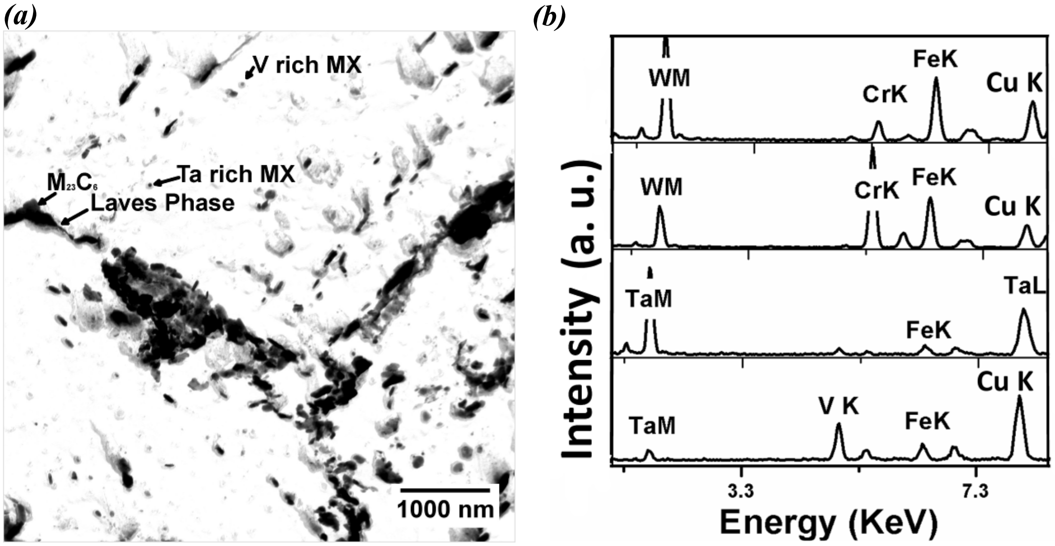

Figure 5.22. *Distribution of precipitates in creep exposed 2W-0.06 Ta steel for 5978h at 823 K showing the morphology of Laves phase*

5.5 Mechanism of formation of Laves phase

Figure 5.23 (a) shows the carbon extraction replica micrograph of the 2W-0.06Ta steel after 5000 h of thermal exposure at 923 K. A chemical mapping (X-ray mapping) performed on the same region shows the presence of Cr, Fe, W, Ta and V. Further image analysis on the X-ray maps revealed the presence of Fe and W rich Laves phase around $M_{23}C_6$ particle. It is clear from the mapped region that the $M_{23}C_6$ contains Cr predominantly along with small amount of Fe, W and V, while the Laves phase contains large amount of Fe and W, in addition to small amount of Cr and Ta. The amount of Laves phase and its composition in steels with different W and Ta content were also simulated by JMatPro, details of which will be discussed in the next section.

The above observations suggest the heterogeneous nucleation of Laves phase possibly with a chemical interaction with the existing $M_{23}C_6$ during its evolution. Evidence for the existence of isolated particle of Laves phase without the presence of $M_{23}C_6$ precipitate could not be obtained, which made the microchemical analysis difficult.

The effect of addition of W was also reflected in the increased precipitation of Fe and W rich Laves phase in the steel, a small amount of Cr and Ta found in Laves phase suggested the possibility of substitution of Cr in Fe lattice and Ta in W lattice as discussed earlier. Supportive to the observations, Thomas et al., [73] reported the solubility of Cr in Mo rich laves phase found in modified 9Cr-1Mo steel. The presence of Laves phase in close association with $M_{23}C_6$ also supported by Sawada et al, [228] leads to the following conclusions-

- Laves phase nucleates as $(Fe,Cr)_2(W,Ta)$ in the interface of matrix and $M_{23}C_6$.
- Laves phase grows by enrichment of W from $M_{23}C_6$ and Fe from the matrix during thermal aging as the phase evolves.
- Laves phase acts as a bridge for the exchange of Cr between $M_{23}C_6$ and matrix for further enrichment of Cr in $M_{23}C_6$ phase.

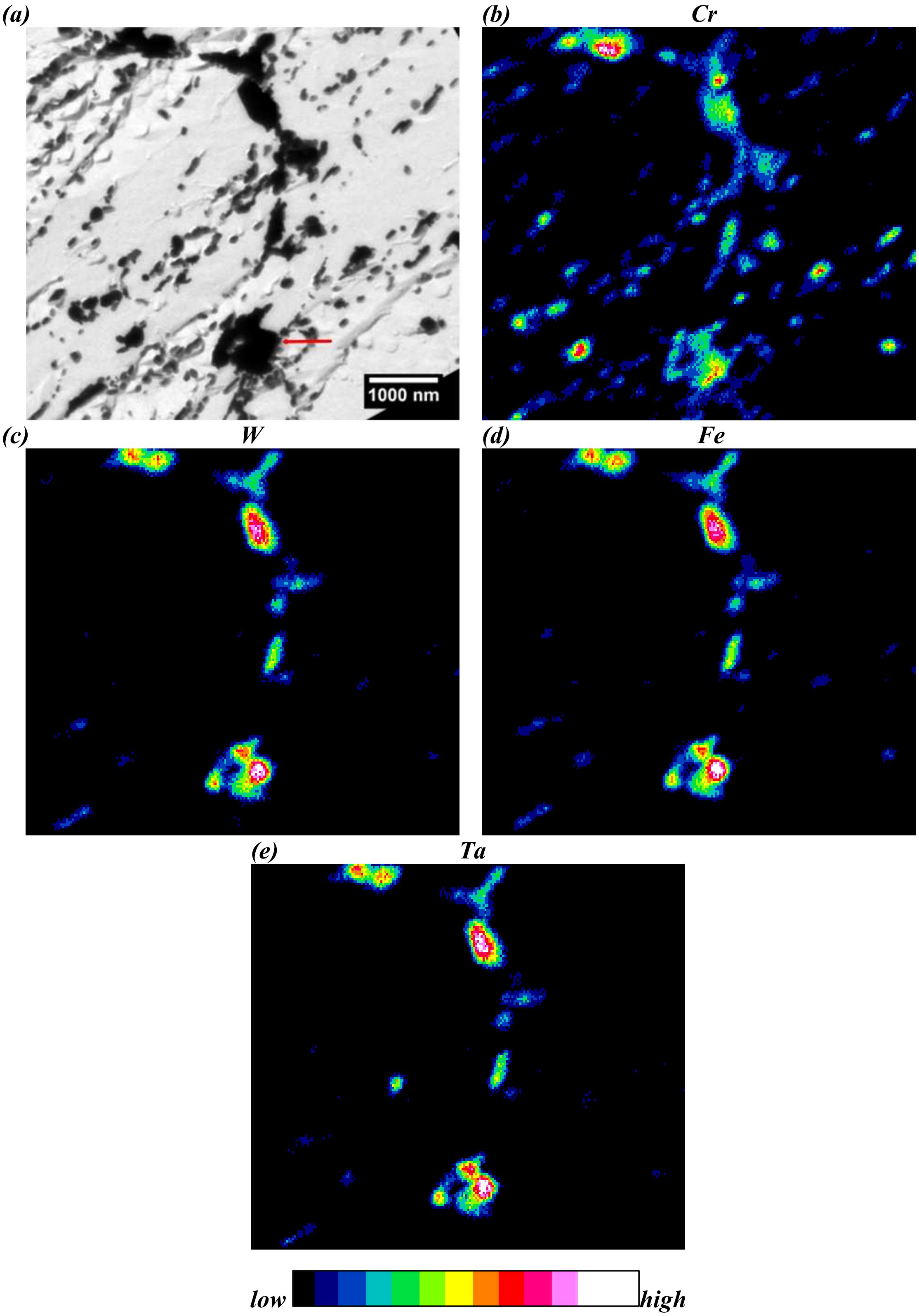

Figure 5.23. *(a) Extraction replica micrograph of 2W-0.06Ta steel aged at 923 K for 5000h, (b-e) elemental mapping showing an enrichment of W and Fe around the precipitate marked*

- Further growth of $M_{23}C_6$, which is covered with Laves phase cannot takes place due to the non-availability of C; however, significant growth of Laves phase was evident with exposure time.

Formation of Laves phase is reported to strengthen the matrix in the initial stages, which also offsets the coarsening of $M_{23}C_6$ [4]. However, the rapid coarsening of Laves phase destabilises the grain boundary [104], thus degrading the strength.

5.6 Simulation of kinetics of precipitation on thermal exposure

To understand the kinetics of precipitation on thermal exposure, simulations were carried out with JMatPro software. The initial condition was assumed to be a martensite structure obtained in quenched steel, for the simulation. The aging experiments in this study have been conducted on normalised and tempered steels, a starting condition of the steels used for any practical application. This difference in the starting microstructure has been ignored for the purpose of simulation, since the amount and composition of the phases are calculated for a given temperature at equilibrium and compared with the experimental values after long term aging. Therefore, the differences between the simulated and experimental data should be understood in the light of this background. However, such a simulation is useful since it provides valuable inputs on the possible sequence of precipitation, for a wide range of compositions and temperature, while experimental data generation over a large matrix is time consuming and difficult. Further, simulations can be done for varying time durations, where experiments have limitations due to kinetic factors. Additionally, experiments carried out for short durations of thermal exposures (eg. 1-15 minutes) may contain experimental errors associated with stability of temperature/ fluctuations etc., which can be overcome during simulations.

A kinetic simulation of the possible phases during thermal exposure up to 10000 h at 923 K in 1W-0.06Ta and 1.4W-0.06Ta steels is presented in **Figure 5.24.** Precipitation of phases

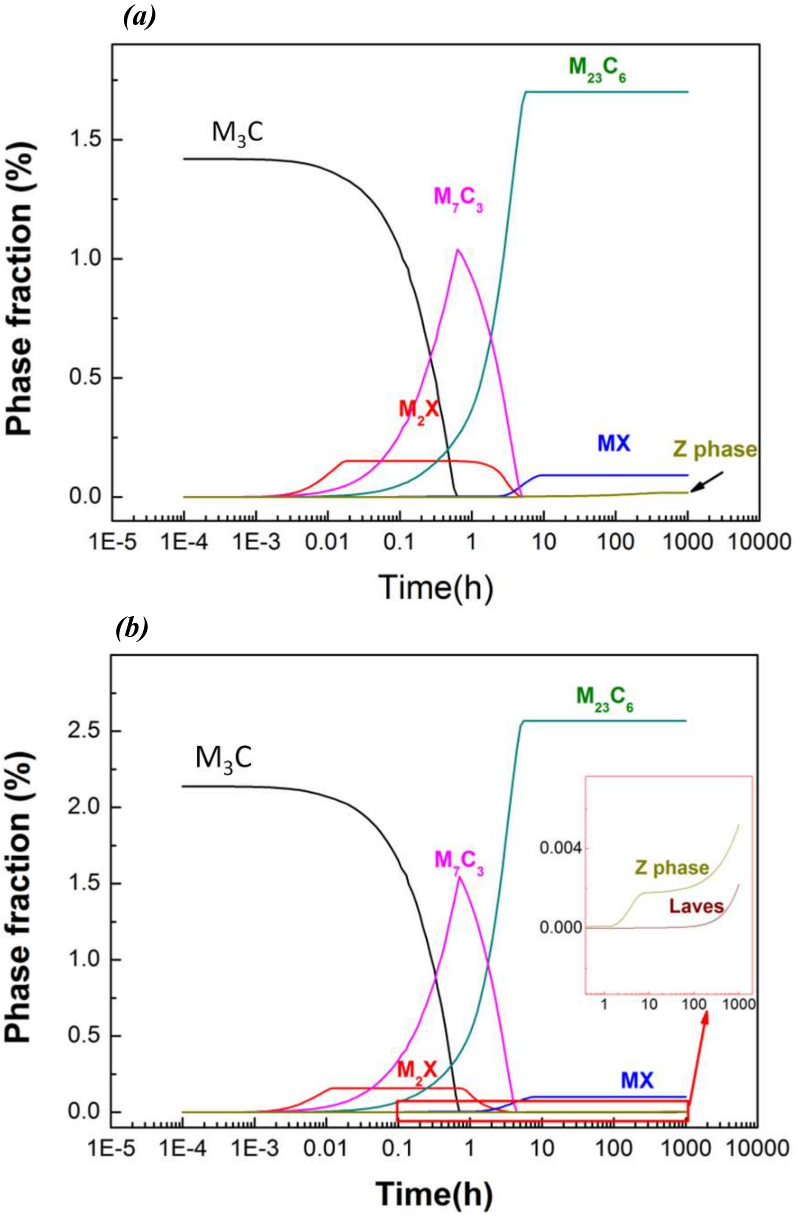

Figure 5.24. *JMatPro simulation for (a) 1W- 0.06Ta and (b) 1.4W – 0.06Ta steel showing the formation of different secondary phases on aging at 923 K*

like M_3C, M_2X and M_7C_3 were predicted below 10 h, which are unstable above 10 h. However, these phases were not observed during tempering or aging in the present study. Phases predicted by calculations beyond 10 h showed the formation of $M_{23}C_6$, MX, Z-phase and Laves phase. The increase in phase fraction of $M_{23}C_6$ and MX phase in 1.4W-0.06Ta steel as compared to that of 1W-0.06Ta steel was discussed in **chapter 3**, in the light of the difference in the carbon content between the two steels. The estimated amount of phases in the steels after 1,000 h of thermal exposure at 873 and 923 K is listed in **Table 5.1**. A very small fraction of

Table 5.1. *Estimated phase fraction (in volume %) of secondary phases in RAFM steels at 923 and 873 K after 1000 h*

Temperature	Phase	1W-0.06Ta	1.4W-0.06Ta	2W-0.06Ta	1W-0.14Ta
923 K	$M_{23}C_6$	1.7	2.568	2.578	2.469
	MX	0.092	0.102	0.092	0.102
	Z-Phase	0.018	0.005	0.001	0.020
	Laves	-	0.002	0.052	-
873 K	$M_{23}C_6$	1.705	2.576	2.583	2.466
	MX	0.086	0.092	0.089	0.108
	Z-Phase	0.022	0.012	0.002	0.015
	Laves	0.008	0.038	0.126	0.001

Laves phase has been predicted by simulation after prolonged exposure of 1000 h at 923 K for the steels with high W content, while addition of Ta did not show the formation of Laves phase at this temperature. It is to be mentioned that the Mo equivalent to C ratio as mentioned in **section 5.3** for steel with high W content (2wt.%) is greater than 10, which is well above the value required for the formation of Laves phase. The volume fraction of both Z – and Laves phase is evaluated to be high at 873 K than at 923 K, suggesting that higher temperature is not favourable for the formation of these phases. It may be recalled from chapter 3, that Z and Laves phases were predicted by JMatPro simulation to form during aging at lower temperature upto 978 K, which is also supported by Danon et al., [48] in reduced activation steels with varying W and Ta content.

In the present experimental studies Z phase has not been observed. This is in agreement with literature, where Z-phase has not been reported in Ta bearing steels [48]. However, in Nb containing steels such as P91, the formation of Cr and Nb rich Z-phase was reported both during thermal and stress exposure [228].

Simulation results at 873 and 923 K showed that the volume fraction of Laves phase is sensitive to the W and Ta content of the steel. Increase in volume fraction is observed with W content of the steel. It is interesting to note from the present simulations that the volume fraction of Laves phase increases with Ta content also, which is in agreement with the experimental observation of formation of Laves phase in 1W-0.14Ta steel in contrast to the 1W-0.06Ta steel.

Recalling the JMatPro calculations form **Chapter 3**, **section 3.5**, the formation of Laves phase is favoured only at temperatures below 978 K for steels containing 1.4 and 2 wt % W. The chemical composition of Laves phase at 873 and 923 K with equilibrium simulation by JMatPro for different steels is tabulated in **Table 5.2.** It is observed that Laves phase has a large solubility for Fe, W in addition to a low amount of Cr, Ta as shown experimentally (**Figure 5.23**). It is also seen that the W and Ta content in Laves phase shows a small increase with W and Ta content of steel. Comparison of the composition of Laves phase **(Table 5.2)** at 873 K, shows that the Ta concentration is lower than W concentration in steels with higher W concentration and vice-versa, which suggests that the W and Ta occupy the same lattice sites in Laves phase. Therefore, the stoichiometry of the Laves phase in W and Ta containing steel can be written as $(Fe,Cr)_2(W,Ta)$ as suggested by Knezevic et al. [66]. While 1W-0.06Ta and 1W-0.14Ta steels showed the formation of Laves phase only below 893 K, the chemistry of Laves phase did not vary with W content at 923 K.

Table 5.2. *Chemical variation (wt. %) of Laves phase showing the changes with W and Ta content in the RAFM steel*

	Elements	1W-0.06Ta	1.4W-0.06Ta	2W-0.06Ta	1W-0.14Ta
923 K	Cr	-	6.4	6.4	-
	Fe	-	31.1	31.1	-
	W	-	61.9	61.9	-
	Ta	-	0.4	0.4	-
	Mn	-	0.2	0.2	-
873 K	Cr	7.1	6.9	6.9	7.2
	Fe	30.3	30.6	30.5	30.4
	W	61.7	61.8	62.3	61.4
	Ta	0.6	0.5	0.1	0.7
	Mn	0.3	0.2	0.2	0.3

5.7 Conclusions

Systematic studies on the microstructural stability and phase evolution in 9Cr-W-Ta-V-C Ferritic / Martensitic steels during long term thermal exposure and stress has been carried out and the salient results of the studies show-

- 1W-0.06Ta steel showed a slower recovery at temperature below 823K, the recovery process was accelerated at 873 and 923 K. However, coarsening of subgrains was sluggish at all temperatures due to the pinning effect of finer precipitates. Replacement of Mo by W in RAFM steel retards the coarsening of $M_{23}C_6$ precipitates, which in turn retards the coarsening of the fine substructure. Presence of fine MX precipitates also helps to retard the substructural recovery.
- Replacement of Mo by W in 1W-0.06Ta steel delays the formation of Laves phase due to the slower diffusion of W in α ferrite compared to Mo. Increase in W content retards the recovery of substructure due to the finer size of $M_{23}C_6$, whereas it enhances the formation of Laves phase.

- Increase in Ta content was not effective in retarding the recovery of substructure as most of the Ta remains in the solid solution, but the formation of Laves phase was enhanced.
- Presence of stress accelerated the recovery process in all the steels. Formation of Laves phase was evident in steel containing 2 wt.% W in the presence of stress at 823 K. Increase in Ta was not beneficial to retard the recovery in the presence of stress.
- Interaction of Laves phase with the $M_{23}C_6$ during thermal exposure has been predicted. Formation of Laves phase around $M_{23}C_6$ restricts the growth of $M_{23}C_6$, where as the Laves phase coarsens rapidly. The Laves phase contained predominantly Fe and W with traces of Cr and Ta. Dissolution of Ta in Laves phase was influenced by W content of the steel.

Chapter 6

Summary and Scope for Future Work

6.1 Summary of the work

The present thesis entitled "STUDY OF TRANSFORMATION CHARACTERISTICS AND MICROSTRUCTURAL EVOLUTION IN 9Cr REDUCED ACTIVATION FERRITIC / MARTENSITIC STEELS USING ELECTRON MICROSCOPY, CALORIMETRY AND COMPUTATIONAL METHODS" is aimed at understanding the effect of alloy content, specifically W and Ta on the phase transformation characteristics and the microstructural evolution in four different compositional variants of 9Cr – W – Ta – V RAFM steel. The W content varied from 1 – 2 % and the Ta content from 0.06 – 0.14 %. The four composition studied are 1W-0.06Ta, 1.4W-0.06Ta, 2W-0.06Ta and 1W-0.14Ta. The focus of the studies was on the following three major themes, the results of which are summarised in this chapter.

- Phase transformation in RAFM steels
- Decomposition modes of high temperature austenite and characteristics of martensite
- Microstructural evolution - Effect of alloy content, temperature and stress

The first theme deals with the phase transformation characteristics of the steel using calorimetry, metallography and computational methods, evaluation of the phase transformation temperature and the sequence in 1.4W – 0.06 Ta steel, designated as IN RAFM steel. The phase transformation investigated showed the following sequence-

α-Ferrite (ferromagnetic) + $M_{23}C_6$ + MX → α-ferrite (paramagnetic) + $M_{23}C_6$ + MX → γ-austenite + $M_{23}C_6$ + MX → γ + MX → δ + γ +MX → γ + δ → γ + δ + L → δ + L → Liquid

Transformation sequence was found to be same for the four steels with varying W and Ta contents investigated in the present study. The salient results of the study are as follows:

- The dissolution temperatures of $M_{23}C_6$ and MX, were higher than the completion of $\alpha \rightarrow \gamma$ transformation (Ac_3) temperature. Therefore Ac_3 was found to be a function of dissolution rate of carbides, which in turn showed dependency on heating rate.
- Dissolution temperature of $M_{23}C_6$ was found to be independent of W or Ta content. However, the dissolution of MX was found to be a function of Ta content of the steel.
- Both experiment and simulation showed the existence of high temperature three phase field ($\gamma+\delta+L$) in the four steel compositions that were studied.
- Metallographic analysis of post solidification samples suggested that appreciable partitioning of W to δ-ferrite occurs upon slow cooling from liquid.
- M_s Temperature showed a nonlinear dependence on cooling rate.
- The critical cooling rate for $\gamma \rightarrow \alpha'$ formation is found to be close to 40 K min^{-1} for the RAFM steels investigated.

Second theme of the study deals with the results on decomposition modes of high temperature austenite and characteristics of martensite. Salient results of the study are as follows:

- The decrease in prior austenite grain size with increase in W and Ta content due to the pinning effect of undissolved carbides has been established. This decrease in prior austenite grain size was also reflected as increase in hardness of the steel.

- Formation of Fe rich M_3C and $M_{23}C_6$ has been observed in the steels containing 1.4 and 2 wt. % W during cooling from the γ phase field. This is the consequence of inhomogeneity of the high temperature austenite resulting in, solute rich and solute lean γ, the latter occurring in the vicinity of the undissolved carbides. The nature of Fe rich precipitates from solute lean γ has been understood based on the shift in the C-curve corresponding to the α+carbide precipitation and the corresponding 'time of stay' in this temperature regime far above the M_s temperature.

- Presence of a low amount of retained austenite in the normalized 1.4W-0.06Ta steel was confirmed by Orientation Imaging Microscopy (OIM) and Mossbauer Spectroscopy. Formation of multiple variants of martensite from austenite obeying K-S orientation relationship was also revealed by OIM.

- Kinetics of tempering has been studied by monitoring the rate of variation of hardness as well as X-ray diffraction based strain analysis in steels exposed to short durations of thermal exposure. The activation energy for tempering is in the range 0.5 to 1.1 eV suggesting that rate controlling step is the interstitial diffusion of C in α-Fe.

- Increase in W and Ta accelerates the initial tempering process of the steel. Formation of Fe rich $M_{23}C_6$ observed during low temperature and short durations was found to increase with W content of the steel. Simulation results on the tempering process showed precipitation of M_3C, M_2X and M_7C_3 below 10 minutes of tempering at 1033 K.

- Based on the hardness studies, the normalising and tempering treatment is optimised. The steels are normalised at1253 K for 30 minutes and tempered at 1033 K for 1 h.
- Precipitate distribution in normalised and tempered steel is found to vary with W and Ta content of steel.

Third theme comprising of the phase stability during thermal and stress exposure in the steel presents the systematic study on microstructural evolution as a function of temperature, time, stress and alloy content. Salient results of the study are listed below:

- Detailed investigation showed that the replacement of Mo by W in RAFM steel retards the coarsening of $M_{23}C_6$, thereby providing long term microstructural stability to RAFM steels.
- Existence of very fine stable MX helps to retard the recovery of martensite substructure.
- Formation of Laves phase is delayed in the steel containing ≤ 1.4 wt.% of W, compared to Mo containing steels.
- The dissolution of Ta in Laves phase has been established.
- Increase in W and Ta content was found to accelerate the formation of Laves phase.
- The rate of recovery of martensite and formation of Laves phase is found to be enhanced in the combined presence of stress and thermal exposure.

- Formation of Laves phase in the close vicinity of $M_{23}C_6$ suggested the interaction between these two phases during the phase evolution.

6.2 Scope for future work:

- Study of long term microstructural evolution in steels with higher Ta content to understand the role of Ta on mechanism of formation of Laves phase.
- Generation of Time Temperature Precipitation (TTP) diagram for the formation of $M_{23}C_6$, MX and Laves phase, since these three phases play a significant role in determining the mechanical properties of the steel.
- Behaviour of the steel during tempering/aging at low temperatures (< 773K) to obtain complete understanding of the physical metallurgy aspects of the steel.
- Substructure and micro-texture evolution during thermal and stress exposure using OIM to study the recovery and deformation mechanism of martensite.
- In-situ reversion of martensite using high temperature microscopy.

References:

1. R. L. Klueh, D. R. Harries, High-Chromium Ferritic and Martensitic Steels for Nuclear Applications, ASTM Monograph, ASTM International: West Conshohocken (2001) 3.
2. F. Abe, T. Noda, H. Araki, M. Okada, J. Nucl. Sci. Tech., 1 No.4 (1994) 279.
3. F. Abe, Sci. Tech. Adv. Mater., 9 (2008) 1.
4. R. L. Klueh, Int. Mater. Rev., 50 No.5 (2005) 287.
5. S. N. Rosenwasser, P. Miller, J. A. Dalessandro, J. M. Rawls, W. E. Toffolo, W. Chen, J. Nucl. Mater., 85-86 (1979) 177.
6. D. R. Harries, Proceedings of topological conference on ferritic steels for use in nuclear energy technologies, Eds. J. W. Davis and D. J. Michel, The Metallurgical Society of AIME, Warrendale, PA, (1984) 141.
7. Q. Huang, N. Baluc, Y. Dai, S. Jitsukawa, A. Kimura, J. Konys, R. J. Kurtz, R. Lindau, T. Muroga, G. R. Odette, B. Raj, R. E. Stoller, L. Tan, H. Tanigawa, A. -A. F. Tavassoli, T. Yamamoto, F. Wan, Y.Wu, J. Nucl. Mater., 442 (2013) S2.
8. K. L. Murty, I. Charit, J. Nucl. Mater., 383 (2008) 189.
9. R. L. Klueh, A. T. Nelson, J. Nucl. Mater., 371 (2007) 37.
10. A. Kumar, B. K. Choudhary, K. Laha, T. Jayakumar, K. B. S. Rao and B. Raj, Trans. Indian Inst. Met., 56 No. 5 (2003) 483.
11. Y. Asad, K. Dozak, M. Ueta, M. Ichimiya, K. Mori, K. Taguchi, M. Kitagawa, T. Nishida, T. Sakon, M. Sukekawa, Nucl. Eng. Des., 139 (1993) 269.
12. J. J. Fischer: ‘Dispersion strengthened ferritic alloy for use in liquid-metal fast breeder reactors (LMFBRS)’, US patent no. CA 1087879 A1, Oct 21, 1980.
13. L. Xing-gang, Y. Qing-zhi, M. Rong, W. Hao-qiang , G. Chang-chun, J. Iron and Steel Res. Int., 17 No.5 (2010) 57.

14. E. Cerri, E. Evangelista, S. Spigarelli, P. Bianchi, Mater. Sci. Eng., 245 A (1998) 285.

15. A. Czyrska-Filemonowicz, A. Zielińska-Lipiec, P. J. Ennis, JAMME., 19 No.2 (2006) 43

16. M. Tamura, Y. Haruguchi, M. Yamashita, Y. Nagaoka, K. Ohinata, K. Ohnishi, E. Itoh, H. Ito, K. Shinozuka, H. Esaka, ISIJ Int., 26 No.11 (2006) 1693.

17. R. J. Kurtz , A. Alamo, E. Lucon, Q. Huang, S. Jitsukawa, A. Kimura, R. L. Klueh, G. R. Odette, C. Petersen, M. A. Sokolov, P. Spätig, J. -W. Rensman, J. Nucl. Mater., 386–388 (2009) 411.

18. S. Hollnera, B. Fourniera, J. L. Pendua, T. Cozzikaa, I. Tourniéa, J. -C. Bracheta, A. Pineau, J. Nucl. Mater., 405 (2010) 101.

19. B. Raj, S. L. Mannan, P. R. V. Rao, M. D. Mathew. Sadhana, 27 Part 5, (2002) 527.

20. S. H. Kim, W. S. Ryu, I. H. Kuk, J. Korean Nucl. Society, 31 No.6 (1999) 561.

21. A. Morán, R. Coto, J. Belzunce, J. M. Artímez, Adv. Sci. Tech., 73 (2010) 36.

22. Y. Kohno, A. Kohyama, T. Hirose, M. L. Hamilton, M. Narui, J. Nucl. Mater., 271-272 (1999) 145.

23. R. L. Klueh, E. E. Bloom, Nucl. Eng. Des., 2 (1985) 383.

24. H. Tanigawa, K. Shiba, H. Sakasegawa, T. Hirose, S. Jitsukawa, Fus. Eng. Des., 86 No. 9-11 (2011) 2549.

25. J. Moon, C. -H. Lee, T. –H. Lee, M. –H. Jang, M. –G. Park, H. N. Han, J. Nucl. Mater., 455 (2014) 81.

26. R. Lindau, A. Möslang, M. Rieth, M. Klimiankou, E. Materna-Morris, A. Alamo, A. A. F. Tavassoli, C. Cayron, A. M. Lancha, P. Fernandez, N. Baluc, R.

Schäublin, E. Diegele, G. Filacchioni, J. W. Rensman, Schaaf Bvd, E. Lucon, W. Dietz. Fus. Eng. Des., 75-79 (2005) 989.

27. Y. B. Chun, B. K. Choi, C. H. Han, D. W. Lee, S. Cho, T. K. Kim, Y. H. Jeong, Transactions of the Korean Nuclear Society Spring Meeting, Jeju, Korea, May 17-18, 2012.
28. E. Lucon, Fus. Eng. Des., 61-62 (2002) 683.
29. F. Zhao, J. Qiao, Y. Huang, F. Wan, S. Ohnuki, Mater. Charact., 59 (2008) 344.
30. J. Sito, T. Suda, S. Yamashita, S. Ohnuki, H. Takashi, N. Akasaka, J. Nucl. Mater., 258–263 (1998) 1264.
31. M. N. Babu, G. Sasikala, B. S. Dutt, S. Venugopal, A. K. Bhaduri, T. Jayakumar, Nucl. Eng. Des., 269 (2014) 103.
32. K. Ehrlich, Fus. Eng. Des., 56–57 (2001) 71.
33. R. Lindau, A. Möslang, M. Rieth, M. Klimiankou, E. Materna-Morris, A. Alamo, A.-A. F. Tavassoli, C. Cayron, A.-M. Lancha, P. Fernandez, N. Baluc, R. Schäublin, E. Diegele, G. Filacchioni, J.W. Rensmanh, B.V.D. Schaaf, E. Lucon, W. Dietz, Fus. Eng. Des., 75–79 (2005) 989.
34. N. Baluc, D. S. Gelles, S. Jitsukawa, A. Kimura, R. L. Klueh, G. R. Odette, B. van der Schaaf, J. Yu, J. Nucl. Mater., 367–370 (2007) 33.
35. R. L. Klueh , D. J. Alexander, M. A. Sokolov, J. Nucl. Mater., 304 (2002) 139.
36. Q. Huang , C. Li, Y. Li, M. Chen, M. Zhang, L. Peng, Z. Zhu, Y. Song, S. Gao, J. Nucl. Mater., 367–370 (2007) 142.
37. K. Ehrlich, M. Gasparotto, L. Giancarli, G. L. Marois, S. Malang, B. van der Schaaf, Report of European Material Assessment Meeting, Karlsruhe, 2001.
38. R. Jayaram, R. L. Klueh, Metall. Mater. Trans., 29A (1998) 1551.
39. F. Abe, T. Noda, M. Okada, J. Nucl. Sci. Mater., 195 (1992) 51.

40. Y. De Carlan, A. Alamo, M. H. Mathon, G. Geoffroy, A. Castaing, J. Nucl. Mater., 283 – 287 (2000) 672.

41. A. Danon, A. Alamo, J. Nucl. Mater., 307 – 311 (2002) 479.

42. M. Gasparotto, R. R. Lässer, Proceedings of the Int. Conf. Nuclear Energy for New Europe, Slovenia (2006).

43. L. Scäfer, M. Schirra, J. Nucl. Mater., 271-272 (1999) 455.

44. P. H. Wang, J. M. Chen and Z. Y. Xu: 'Research and development of reduced activation ferritic/martensitic steel CLF-1 at SWIP', Proc. 23rd IAEA Fusion Energy Conf., Daejon, Korea, 2010, IAEA , FTP/P1-24

45. Y. Li, Q. Huang, Y. Wu, T. Nagasaka, T. Muroga, J. Nucl. Mater., 367–370 (2007) 117.

46. S. Li, Z. Eliniyaz, L. Zhang, F. Sun, Y. Shen, A. Shan, Mater. Charact., 73 (2012) 144.

47. K. Laha, S. Saroja, A. Moitra, R. Sandhya, M. D. Mathew, T. Jayakumar, E. Rajendra Kumar, J. Nucl. Mater., 439 (2013) 41.

48. C. A. Danon, C. Servant, ISIJ Int., 455 (2005) 903.

49. Q. Huang, C. Li, Q. Wu, S. Liu, S. Gao, Z. Guo, Z. Yan, B. Huang, Y. Song, Z. Zhu, Y. Chen, X. Ling, Y. Wu, FDS Team, J. Nucl. Mater., 417 (2011) 85.

50. B. Van der Schaaf, F. Tavassoli, C. Fazio, E. Rigal, E. Degele, R, Lindau, G. LeMarois, Fus. Engg. Des., 69, 2003, 197.

51. M. Eddahbi, M. A. Monge, T. Leguey, P. Fernández, R. Pareja, Mater. Sci. Eng., 528 A (2011) 5927.

52. K. Maruyama, K. Sawada, J. Koikea, ISIJ Int., 41 No. 6 (2001) 641.

53. A.-A.F. Tavassoli, A. Alamo, L. Bedel, L. Forest, J.-M. Gentzbittel, J.-W. Rensman, E. Diegele, R. Lindau, M. Schirra, R. Schmitt, H. C. Schneider, C.

Petersen, A.-M. Lancha, P. Fernandez, G. Filacchioni, M. F. Maday, K. Mergia, N. Boukos, Baluc, P. Spätig, E. Alves, E. Lucon, J. Nucl. Mater., 329–333 (2004) 257.

54. R. L. Klueh, D. J. Alexander, M. Rieth, J. Nucl. Mater., 273 (1999) 146.
55. B. Jeya Ganesh, S. Raju, Arun Kumar Rai, E. Mohandas, M. Vijayalakshmi, K. B. S. Rao and Baldev Raj, Mater. Sci. Tech., 27 No. 2 (2011) 500.
56. S. Raju, B. J. Ganesh, A. K. Rai, R. Mythili, S. Saroja, B. Raj, J. Nucl. Mater., 405 (2010) 59.
57. S. Raju, B. Jeya Ganesh, Arun Kumar Rai, R. Mythili, S. Saroja, E. Mohandas, M. Vijayalakshmi, K. B. S. Rao, Baldev Raj, J. Nucl. Mater., 389 (2009) 385.
58. Alamo, J. C. Brachet, A. Castaing, C. Lepoittevin, F. Barcelo, J. Nucl. Mater., 258-263 (1998) 1228.
59. A. Danon, C. Servant, A. Alamo, J. C. Brachet, Mater. Sci. Eng., 348 A (2003) 122.
60. J. -C. Brachet, L. Gavard, C. Boussidan, C. Lepoittevin, S. Denis, C. Servant, J. Nucl. Mater., 258-263 (1998) 1307.
61. S. Zheng, Q. Wu, Q. Huang, S. Liu, Y. Han, Fus. Eng. Des. 86 (2011) 2616.
62. Thermocalc: http://www.thermocalc.com/start/
63. JMatpro 4.1: http://www.sentesoftware.co.uk/
64. O. Prat, J. Garcia, D. Rojas, C. Carrasco, G. Inden, Acta Mater., 58 (2010) 6142.
65. L. Tan, D. T. Hoelzer, J. T. Busby, M. A. Sokolov, R. L. Klueh, J. Nucl. Mater., 422 (2012) 45.
66. V. Knežević, J. Balun, G. Sauthoff, G. Inden, A. Schneider, Mater. Sci. Eng., 477 A (2008) 334.
67. L. Tan, Y. Yang, J. T. Busby, J. Nucl. Mater., 442 (2013) S13.

68. C. A. Danon, C. Servant, J. Nucl. Mater., 455 (2014) 81.

69. L. Tan, J. T. Busby, P. J. Maziasz, Y. Yamamoto, J. Nucl. Mater., 441 (2013) 713.

70. T. C. Totemeier, H. Tian, J. A. Simpson, Metall. Mater. Trans., 37A, (2006) 1519.

71. S. Hari Babu, G. Amarendra, R. Rajaraman and C. S. Sundar, J. Phy.: Conf. Series 443 (2013) 012010.

72. P. Goswami, P. Eng, Advances in Materials Technology for Fossil Power Plants: Proceedings from the Sixth International Conference, 2010, Santa Fe, New Mexico, USA, 762.

73. V. Thomas Paul, S. Saroja, M. Vijayalakshmi, J. Nucl. Mater., 378 (2008) 273.

74. M. Taneike, K. Sawada, F. Abe, Metall. Mater. Trans., 35 A (2004) 1256.

75. F. Abe, T. Horiuchi, M. Taneike, K. Sawada, Mater. Sci. Eng., 378 A (2004) 299.

76. H. K. D. H. Bhadeshia, A. Strang, D. J. Gooch, Int. Mater. Reviews, 43 No.2 (1998) 45.

77. M. Tamura, H. Kusuyama, K. Shinozuka, H. Esaka, ISIJ Int., 47 No. 2 (2007) 317.

78. P. J. Ennis, A. Czyrska-Filemonowicz, Sadhana, 28 Parts 3-4, (2003) 709.

79. M. Taneike, F. Abe, K. Sawada, Nature, 424 (2003) 294.

80. J. Janovec, M. Svoboda, A. Výrostková, A. Kroupa, Mater. Sci. and Eng., 402 A (2005) 288.

81. H. C. Furtado, L. H. de Almeida, I. L. May, Mater. Charact.58 (2007) 72.

82. M. Yoshino, Y. Mishima, Y. Toda, H. Kushiama, K. Sawada and K. Kimura, ISIJ Int., , 45 (2005) 107.

83. Z. X. Xia, C. Zhang, H. Lan, Z. G. Yang, P. H. Wang, J. M. Chen, Z. Y. Xu, X. W. Li, S. Liu, Mater. Sci. Eng., 528 A (2010) 657.
84. F. Abe, M. Taneike, K. Sawada, Int. J. Pressure Vessels and Piping, 84 (2007) 3.
85. L. Yajiang, W. Juan, Zhou Bing, F. Tao, Bull. Mater. Sci., 25 No. 3, (2002) 213.
86. V. Ragunanthan, S. H. Babu, V. A. Chirayath, R. Rajaraman, G. Amarendra, S. Saroja, C. S. Sundar, A. Alamo, B. Raj, Phys. Status Solidi, C 6 No. 11, (2009) 2307.
87. M. Yoshizawa, M. Igarashia, K. Moriguchi, A. Iseda, Hassan Ghassemi Armaki, K. Maruyama, Mater. Sci. Eng., 510–511 A (2009) 162.
88. M. Tabuchi, M. Kondo, K. Kubo, S. K. Albert, OMMI, 3 No.3 (2004) 1.
89. F. Abe, Solid State Mater. Sci., 8 (2004) 305.
90. X. Xiao, G. Liu, B. Hu, J. Wang, A. Ullah, Mater. Charact., 82 (2013) 130.
91. K. Sawada, K. Kubo, F. Abe, Mater. Sci. Eng., 319–321 A (2001) 784.
92. C. G. Panait, A. Zielin´ ska-Lipiec, T. Koziel, A. Czyrska-Filemonowicz, A. –F. Gourgues-Lorenzon, W. Bendick, Mater. Sci. Eng., 527 A (2010) 4062.
93. T. Nakajima, S. Spigarelli, E. Evangelista, T. Endo, Mater. Trans., 44 No. 9 (2003) 1802.
94. S. Raju, B. J. Ganesh, A. K. Rai, R. Mythili, S. Saroja, E. Mohandas, M. Vijayalakshmi, K. B. S. Rao, B. Raj, J. Nucl. Mater., 389 (2009) 385.
95. S. H. Kim, C. H. Han and W. –S. Ryu, Solid State Phenomena, 135 (2008) 107.
96. K. Sawada, K. Suzuki, H. Kushima, M. Tabuchi, K. Kimura, Mater. Sci. Eng., 480 A (2008) 558.
97. H. B. Sata, Positron Annihilation Studies of Model Fe-Cr Alloys and Ferritic/Martensitic Steels, Ph.D. thesis submitted to Homi Bhabha National Institute Mumbai, 2013.

98. K. Sawada, H. Kushima, K. Kimura, ISIJ Int., 46 (2006) 769.

99. H. K. Danielsen, J. Hald, Energy Mater., 1 (2006), 49.

100. P. Ettmayer, Monatsh. Chem.,102 (1971) 858.

101. O. Prat, J. Garcia, D. Rojas, G. Sauthoff, G. Inden, Intermetallics, 32 (2013) 362.

102. M. Tamura, H. Hayakawa, A. Yoshitake, A. Hishinuma, T. Kondo, J. Nucl. Mater., 155-157 (1988) 620.

103. F. Abe, Mat Sci Eng., 319-321 A (2001) 770-3.

104. J. S. Lee, H. G. Armaki, K. Maruyama, T. Muraki, H. Asahi, Mater. Sci. Eng., 428 A (2006) 270.

105. O. Prat, thesis on “Investigation on diffusion-controlled transformations in creep resistant steels and grared cemented carbides”, Bochum, 2011.

106. N. Asrar, L. L. Meshkov and E. M. Sokolovskaya, J. Less-Common Met., 144 (1988), 41.

107. Y.F. Li, T. Nagasaka, T. Muroga, Q.Y. Huang, Y.C. Wu J. Nucl. Mater., 386–388 (2009) 495.

108. J. S. Park, S. J. Kim, C. S. Lee, Mater. Sci. Eng., 298 A (2001) 127.

109. S. G. Hong, W. B. Lee, C. G. Park, Scripta mater., 43 (2000) 181.

110. J. Wang, S. Lu, W. Dong, D. Li, L. Rong, Mater.Des., 64 (2014) 550.

111. F. Abe, T. Noda, H. Araki, S. Nakazawa, J. Nucl. Mater., 179–181(1991) 663.

112. J. Onoro, J. Mater. Process. Tech., 180 (2006) 137–142.

113. K. Asakura, Y. Yamashita, T. Yamada, K. Shibata, ISIJ Int., 30 No.11 (1990) 937.

114. T. Jayakumar, M. D. Mathew, K. Laha, S. K. Albert, S. Saroja, E. R. Kumar, C. V. S. Murthy, G. Padmanabham, G. A. Rao, S. N. Prasad, Fus. Sci. Tech., 65 (2014) 171.

115. B. Raj, T. Jayakumar, J. Nucl. Mater., 417 (2011) 72.

116. R. Mythili, Ravikirana, J. Vanaja, K. Laha, S. Saroja, T. Jayakumar, M. D. Mathew, E. Rajendrakumar, Procedia Eng., 55 No3–4 (2013) 295.

117. M. D. Mathew, J. Vanaja, K. Laha, G. V. P. Reddy, K. S. Chandravathi, K. B. S. Rao, J.Nucl.Mater., 417 (2011) 77.

118. J. Vanaja, K. Laha, S. Sam, M. Nandagopal, S. P. Selvi, M. D. Mathew, T. Jayakumar, E. Rajendra Kumar, J. Nucl. Mater., 424 (2012) 116.

119. J. Vanaja, K. Laha, R. Mythili, K. S. Chandravathi, S. Saroja, M. D. Mathew, Mater. Sci. Eng., 533 (2012) 17.

120. S. Saroja, A. Dasgupta, R. Divakar, S. Raju, E. Mohandas, M. Vijayalakshi, K. B. S. Rao, B. Raj, J. Nucl. Mater., 409 (2011) 131–139.

121. S. Raju, B. Jeya Ganesh, A. K. Rai, R. Mythili, S. Saroja, E. Mohandas, M. Vijayalakshmi, K. B. S. Rao, B. Raj, J. Nucl. Mater., 389 (2009) 383.

122. G. V. P. Reddy, R. Sandhya, K. Laha, M. D. Mathew, Mater. Sci. Eng., 527 (2010) 6449.

123. J. Vanaja, K.Laha, M. Nandagopal, S. Sam, M. D. Mathew, T. Jayakumar, E. Rajendrakumar, J. Nucl. Mater., 433 (2013) 4112.

124. V. Shankar, K. Mariappan, A. Nagesha, G. V. P. Reddy, R. Sandhya, M. D. Mathew, T. Jayakumar, Fus. Eng. Des., 87 (2012) 318.

125. J. Vanaja, G. Varaprasad Reddy, A. Moitra, K. Laha and M. D. Mathew, Twentieth Annual Conference of Indian Nuclear Society (INSAC-2009), January 4-6,2010, Chennai, 724.

126. A.Moitra, A. Dasgupta, S. Sathyanarayanan, G. Sasikala, S. K. Albert, S. Saroja, A. K. Bhaduri, E. Rajendra Kumar and T. Jayakumar, Proceedings of

International Conference on Structural Integrity (ICONS 2014), February 4-7, 2014, Kalpakkam, 1241.

127. M. Nani Babu, G. Sasikala, B. Shashank Dutt, S. Venugopal, A.K. Bhaduri, T. Jayakumar, Nucl. Eng.Des., 269 (2014) 103.

128. K. S. Chandravathi, C. S. Sasmal, K. Laha, P. Parmeswaran, M. Nandagopal, D. Vijayanand, M. D. Mathew, T. Jayakumar, E. Rajendra Kumar, J. Nucl. Mater., 435 (2013) 128.

129. P. Vasantharaja, M. Vasudevan, J. Nucl. Mater., 421, (2012) 117-123.

130. B. Arivazhagan, G. Srinivasan, S. K. Albert, A. K. Bhaduri, 86, No. 2-3 (2011) 192.

131. G. Srinivasan, B.Arivazhagan, S.K.Albert, A.K.Bhaduri, Fus. Eng. Des., 86, No.4-5 (2011) 446.

132. V. Thomas Paul, S. Saroja, S.K. Albert, T. Jayakumar, E. Rajendra Kumar, Mater. Charact. 96 (2014) 213.

133. http://www.esrf.eu/computing/scientific/FIT2D/

134. Powder Diffraction File: Alphabetical indexes inorganic phases, International Centre for Diffraction Data, USA, 1994.

135. G.F. Vander Voort, Metallography Principles and Practice, Mc-Graw- Hill book Company, (1984) 410.

136. http://imagej.nih.gov/ij/

137. G. Cliff and G.W. Lorimer, in: Quantitative Microanalysis with high spatial resolution, M.H. Jacobs, G.W. Lorimer and P. Daig (Eds.), The Metals Society, London, 1981.

138. S. Saroja, P. Parameswaran, M. Vijayalakshmi, V. S. Raghunathan, Acta Metall. Mater., 43 No.8 (1995) 2985.

139. E. F. Rauch, L. Dupuy, Arch. Metall. Mater., 50 (2005) 87.

140. http://www.setaram.com/SETSYS-Evolution-DTA-DSC.htm.

141. E. Gmelin and St. M. Sarge, Pure Appl. Chem., 67 (1995) 1789.

142. B. Wunderlich, Thermal Analysis, San Diego, CA, Academic Press, 1990.

143. M. Brown, Introduction to Thermal Analysis, London, Chapman and Hall, 1988.

144. G.W. H. Höhne, W. Hemminger,and H. J. Flammersheim, Differential Scanning Calorimetry: An Introduction for Practitioners, Berlin, Springer-Verlag, 1996.

145. R. Sabbah, An Xu-wu, J. S. Chickos, M. L. Planas Leitão, M. V. Roux and L. A.Torres, Thermochim. Acta, 331 (1999) 93.

146. U. Diekmann, Calculation of steel data using JMatPro, COMAT 2012: Recent Trends in structural materials, 21. (2012), Plzeň, Czech Republic, EU

147. Y. Huang, X. Chen, Z. Shen, B. Madigan, L. Yucheng, J. Zhou, J. Nucl. Mater. 432 (2013) 460.

148. K. Liu, Y. Shan, Z. Yang, J. Liang, L. Lu, K. Yang, J. Mater. Sci. Technol., 22 No.6 (2006) 769.

149. T. Hasegawa, Y. Tomita, A. Kohyama, J. Nucl. Mater., 258 (1998) 1153.

150. J. Hald, L. Korcakova: ISIJ Int., 43 (2003) 420.

151. W. Yan, W. Wang, Yi-Yin Shan, K. Yang, Front. Mater. Sci., 7 (2013) 1.

152. R. L. Klueh, N. Hashimoto, P. J. Maziasz, Scripta Mater., 53 (2005) 275.

153. A. G. Glover, J. T. McGrath, M. J. Tinkler, G. C. Weatherly, Welding Research Supplement, (1977) 267s.

154. S. Saroja, M. Vijayalakshmi, V. S. Raghunathan, J. Nucl. Mater., 27 No. 9 (1992) 2389.

155. S. Saroja, M. Vijayalakshmi, V. S. Raghunathan, Mater. Sci. Engg., 154 A (1992) 59.

156. C. R. Hutchinson, H. S. Zurob, C. W. Sinclair and Y. J. M. Brechet, Scripta Mater., 59 (2008) 635.

157. K. Chang, W. Feng and L.Q. Chen, Acta Mater, 57 (2009) 5229.

158. P. Parameswaran, S. Saroja, M. Vijayalakshmi, V.S. Raghunathan, J. Nucl. Mater., 232 (1996) 226.

159. W. Krauss, S. K. Pabi, H. Gleiter, Acta Metall., 37 (1989) 25.

160. P. R. Rios, J. R. C. Guimaraẽs, Scr. Mater., 57 (2007) 1105.

161. P. R. Rios, J. R. C. Guimaraẽs, Mater, Res., 11 (2008) 103.

162. J. R. C. Guimaraẽs, P. R. Rios J. Mater. Sci., 43 (2008) 5206.

163. J. R. C. Guimaraẽs, P. R. Rios J. Mater. Sci. 44 (2009) 998.

164. B. D. Cullity, Elements of X-Ray Diffraction, 2nd Ed., Addison Wesley 1978.

165. Ravikirana, R. Mythili, S. Raju, S. Saroja, T. Jayakumar, E. Rajendrakumar, Mater. Charact., 84 (2013) 196.

166. J. W. Elmer, S. M. Allen, T. W. Eagar, Metall. Trans., 20A (1989) 2117.

167. A. Danon , A. Alamo, , J. Nucl. Mater., 307–311 (2002) 479.

168. T. Gladman, F. B. Pickering, J. Iron Steel Inst., 205 (1967) 653.

169. H. K. D. H. Bhadeshia, R. W. K. Honeycombe, Steels: Microstrcture & Properties, Butterworth-Heinemann, 3rd Ed., Elsevier, (2006), 307.

170. J. R. C. Guimaraẽs, Mater. Sci. Eng., 476 A (2008) 106.

171. H. Finkler, M. Schirra, Steel Res., 62 (1991) 24.

172. B. Jeyaganesh, S. Raju, A. K. Rai, E. Mohandas, M. Vijayalakshmi, K. B. S. Rao, B. Raj, Mater. Sci. Tech., 27 (2011) 500.

173. I Hrivnak, *ISIJ Int.,* 1995, 35, 1148.

174. H. K. D. H. Bhadeshia, ISIJ Int., 41 (2001) 626.

175. H. K. D. H. Bhadeshia, T. Sourmail, Japan Society for the Promotion of Science, 44 (2003) 299.

176. U. A. Sachadel, P. F. Morris, P. D. Clarke, Mater. Sci. Tech., 28 (2012) 1.

177. R.L. Klueh, J. Nucl. Mater., 378 (2008) 159.

178. C. B. A. Forty, J. Fus. Energy, 16 (1997) 277.

179. M. H. Mathon, Y. de Carlan, G. Geoffrey, X. Averty, A. Alamo, C. H. de Novion, J. Nucl. Mater., 312 (2003) 236.

180. S. M. Dubiel, G. Inden, Z. Metallkd., 78 (1987) 544.

181. T. K. Kim, S. H. Kim and C. B. Lee, Ann. Nucl. Energy, 36 (2009) 1103.

182. M. N. Batista, I. Alvarez-Armas, M. F. Giordana, S. Hereñú, A. F. Armas., Mater. Sci. Tech , 2014, in press.

183. R. C. Thomson, H. K. D. H. Bhadeshia, Metall. Trans., 23A (1992) 1171.

184. W. B. Jones, C. R. Hills, D. H. Polonis, Metall. Trans., 22A (1991)1049.

185. H. D. Kim and I. S. Kim, ISIJ Int., 34 (1994) 198.

186. C. Liu, D. Zhang, Y. Liu, Q. Wang, Z. Yan, Nucl. Eng Des., 241 (2011) 2411.

187. H. Serizawa, S. Nakamura, M. Tanaka, Y. Kawahito, H. Tanigawa, S. Katayama, J. Nucl. Mater., 417, (2011) 55.

188. P. Aubert, F. Tavassoli, M. Rieth, E. Diegele, Y. Poitevin, J. Nucl. Mater., 417 (2011) 43.

189. C. Ohms, D. Neov, A. G. Youtsos, 'Evaluation of novel post weld heat treatment in ferritic steel repaira welds based on neutron diffraction', Residual Stress and Its Effect on Fatigue and Fracture', (2006) 55.

190. S. Raju, B. Jeya Ganesh, A. K. Rai, S. Saroja, E. Mohandas, M. Vijayalakshmi, B. Raj, Int. J. Thermophys., 31 (2010) 399.

191. R. L. Klueh, P. J. Maziasz, 'Metall. Mater. Trans, 1989, 20A, 373 – 382.

192. A. K. Rakhit, 'Heat treatment of Gears: A Practical Guide for Engineers', ASM International, 50, 2000, USA, Materials Park.

193. R. H. Buck, J. Warren, Douglas G. McCullough, Rochester, Mich, Alloy Steel Forging Die, US Patent 3,131,057, Published 28 April 1964.

194. G. Ghosh, C. E. Campbell, G. B. Olson, Metall. Mater. Trans, 30A (1999) 501.

195. Londolt B, 'Diffusion in solids, metals and alloys', 125, 1990, Berlin, Springer-Verlag.

196. Ravikirana, R. Mythili, S. Raju, S. Saroja, G. Paneerselvam, T. Jayakumar and E. Rajendra Kumar, Bulletin. Mater. Sci., BOMS-S-13-00580 (in press)

197. D. V. Shtansky, K. Nakai, Y. Ohmori, Phil. mag., 79 A No.7 (1999) 1655.

198. D. J. Dyson and S. R. Keown, 'Interpretation of electron diffraction patterns', 1st edn, 166, 1967, US, Plenum.

199. Ravikirana, R. Mythili, S. Raju, S. Saroja, T. Jayakumar, E. Rajendrakumar, Mater. Sci. Tech, 2014, (Accepted).

200. I. Yoshiaki, J. Phase. Equilib. Diffus., 26 No.5, (2005) 466.

201. S. Saroja, 'Study of microstructure, microchemistry and lattice strain in wrought 9Cr-1Mo steel using analytical transmission electron microscopy, convergent beam electron diffraction and thermodynamic computations', Ph D Thesis, University of Madras, India, 1999.

202. L. Herojit singh, R. Govindaraj,G. Amarendra, and C. S. Sundar, J. Phy. Chem. C, 117 (2013) 25042.

203. P. P. Suikkanen, C. Cayron, A. J. DeArdo, and L. P. Karjalainen, J. Mater. Sci. Tech., 27 No. 10 (2011) 920.

204. J. -H. Kang and H. –C. Lee, Mater. Trans., 45 No. 7 (2004) 2219

205. M. K. Dash, T. Karthikeyan, S. Saroja and M. Vijayalakshmi, Mater. Sci. Forum, 702-703 (2012) 880.

206. H. Kitahara, R. Ueji, N. Tsuji, Y. Minamino, Acta Mater., 54 (2006) 1279.

207. R. K. Shiue, K. C. Lan, C. Chen, Mat. Sci. and Eng., 287 A (2000) 10.

208. R. Mythili, V. T. Paul, S. Saroja, M. Vijayalakshmi, Proc. of Int. Seminar on Materials Ageing and Life Management “ISOMALM 2000”, 2000, Kalpakkam, 281.

209. M. Vijayalakshmi, S. Saroja, R. Mythili, V. T. Paul, V. S. Raghunathan, J. Nucl. Mater., 279 (2000) 293

210. R. Anand, C. Sudha, T. Karthikeyan, A. L. E. Terrance, S. Saroja, M. Vijayalakshmi, J. Mater. Sci., 44 (2009) 257

211. Londolt B (1990) Diffusion in solids, metals and alloys. Springer-Verlag, Berlin, 372.

212. Raghavan V, Materials Science and Engineering, Prentice-Hall, New Delhi (1984), 168

213. B. Kim, E. Boucard, T. Sourmail, D. San Martín, N. Geyb, P.E.J. Rivera-Díaz-del-Castillo, Acta Mater., 68 (2014) 169.

214. Ravikirana, R. Mythili, S. Raju, S. Saroja, T. Jayakumar, E. Rajendrakumar, Mater. Charect., 84 (2014) 196.

215. J. J. Kai, R. L. Klueh, J. Nucl. Mater., 230 (1996) 116.

216. B. Londolt Diffusion in solids, metals and alloys. Springer-Verlag, Berlin, (1990) 372.

217. P. Fernandez, A. M . Lancha, J. Lapena, M, Nernandez-Mayoral, Fus. Eng. Des.,58-59 (2001) 787.

218. P.J. Ennis, A. Czyrska-Filemonowicz, Creep Resistant Steels for Power Plant-OMMI, 1 (2002) 1.

219. P. Fernandez, A. M . Lancha, J. Lapena, , M. SerranoM. Nernandez-Mayoral, J. Nucl. Mater., 307-311(2002) 495.

220. S. Ghosh, J. Mater. Sci., 45(2010)1823

221. V. Vodarek, A. Strang, Mater. Chem. Phy., 81 (2003) 480

222. D. Dulieu, K. W. Tupholme, G. J. Butterworth, J. Nucl. Mater., 141-143, (1986) 1097

223. H. Sakasegawa, T. Hirose, A. Kohyama, Y. Katoh, T. Harada, K. Asakura ,T. Kumagai, J. Nucl. Mater., 307-311 (2002) 490.

224. K. W. Tupholme, D. Dulieu, G. J. Butterworth, J. Nucl. Mater., 179-181 (1991) 684.

225. R. L. Klueh, Elevated-temperature ferritic and martensitic steels and their application to future nuclear reactors, Oak Ridge National Laboratory, ORNL/TM-2004/176, 2004.

226. K. Ozaki, Low alloy high steel tool having constant toughness, US patent no. US7695576 B2, 13 Apr 2010.

227. K. Sawada, M. Takeda, K. Maruyama, R. Ishii, M. Yamada, Y. Nagae, R. Komine, Mater. Sci. Eng., A267 (1999) 19.

228. K. Sawada, ISIJ Int., 46 (2006) 49.